Universidad Autónoma de Madrid
Facultad de Ciencias
Departamento de Física Teórica

Sapienza Università di Roma
Facoltà di Scienze Matematiche Fisiche e Naturali
Dipartimento di Fisica

The ΛCDM model at small scales: Milky Way' satellites and cusp-core crisis

By
Arianna Di Cintio

A Thesis submitted for the degree of Doctor of Philosophy in Astrophysics

Supervisor
Prof. Alexander Knebe (Universidad Autónoma de Madrid)
Co-Supervisor
Prof. Alessandro Melchiorri (Sapienza Università di Roma)

July 21, 2014

To my sister Lorenza, my brother Guido,
my mum Elena and my dad Massimo.

Contents

List of Figures

List of Tables

Resumen y conclusiones

El modelo de materia oscura fría con constante cosmológica Λ, llamado ΛCDM, es el actual modelo cosmológico favorecido en el contexto de la formación de galaxias: formulado hace más de treinta años (White & Rees 1978), está basado en la suposición de que el universo está compuesto por un $\sim$ 68% de energía oscura, por un $\sim$ 27% de materia oscura , y sólo por un $\sim$ 5% de materia ordinaria (Planck Collaboration et al. 2013). Las partículas de la materia oscura *fría*, al tener una masa mayor del keV, no amortiguan las pequeñas fluctuaciones y pueden explicar satisfactoriamente las propiedades observacionales de las galaxias, como la gran cantidad de energía en pequeñas escalas indicadas por la función de correlación a dos puntos (Peebles 1980). La necesidad de una componente de materia oscura fría se desprende también de una serie de limitaciones observacionales, tales como, entre otras, la curva de rotación de las galaxias (Rubin et al. 1980) y la observación en *weak lensing* de colisiones entre cúmulos de galaxias (Clowe et al. 2006).

Una consecuencia directa del hecho de que la materia oscura es fría, es decir, que sus partículas son non-relativistas al tiempo de la igualdad materia-radiación, es que la formación de estructuras avanza en manera jerárquica ascendente, o *bottom-up*, desde las galaxias mas pequeñas hasta las mas grandes (Blumenthal et al. 1984). De hecho, en ΛCDM las pequeñas perturbaciones en el campo de densidad primordial pueden crecer y expandirse mediante la inestabilidad gravitacional, para luego fusionarse entre sí para crear estructuras más grandes, tales como los cúmulos y los grupos de galaxias, que vemos hoy. Las fluctuaciones primordiales de la densidad se pueden medir directamente del fondo cósmico de microondas (CMB), que es la radiación térmica remanente del Big Bang: el espectro de potencia de las anisotropías de temperatura en CMB, de hecho, refleja dichas fluctuaciones, o contraste, en la densidad de la materia en el Universo primordial (Smoot et al. 1992; Spergel et al. 2003; Planck Collaboration et al. 2013). Estas perturbaciones colapsarán para formar los - así llamados - halos de materia oscura, que son la base de la formación de todas las galaxias futuras, en un proceso altamente no lineal que puede ser descrito sólo mediante el uso

de simulaciones numéricas, tales como las simulaciones de N-cuerpos del campo de densidad cósmica (Springel 2005).

Dada una distribución de partículas inicialmente imperturbada, y teniendo en cuenta el espectro de potencia primordial como condición inicial, podemos seguir la evolución y el colapso gravitacional de las partículas de materia oscura no colisionales desde alto redshift hasta z=0, poner galaxias en los halos de materia oscura usando modelos semianalíticos (Monaco et al. 2014; Benson 2011), y comparar el resultado final con la distribución observada y las propiedades de las galaxias, por ejemplo usando la 2dF Galaxy Redshift Survey (Cross et al. 2001). Aunque las simulaciones de materia oscura hayan reproducido con éxito varias características del universo, tanto en grandes escalas, por ejemplo en las simulaciones Millenium-XXL y Multi-Dark (Angulo et al. 2012; Riebe et al. 2013) como en escalas galácticas, por ejemplo en las galaxias del Grupo Local similares a la Via Lactea (Gottlöber et al. 2010; Springel et al. 2008; Brook et al. 2012a), todavía hay discrepancias entre las propiedades observadas de las galaxias enanas y galaxias satélites con la predicción del modelo ΛCDM. En estas escalas, de hecho, el modelo se complica por la física bariónica que es importante en la dinámica de formación de las galaxias . En particular, los principales problemas que todavía afectan al paradigma ΛCDM a pequeña escala son:

- el problema de los satélites ausentes, o *missing satellite problem*
- el problema *too big to fail*
- el problema *core/cusp*

El *missing satellite problem* (Klypin et al. 1999a) es la discrepancia entre el número observado de galaxias satélite alrededor de la Vía Láctea y de la galaxia de Andrómeda y el número de subhalos en las simulaciones de N-cuerpos, el último siendo algunos órdenes de magnitud más alto que el anterior. Dentro del Grupo Local se observan solo $\sim$ 40 galaxias satélite con $M_\star > 10^{6.5}\mathrm{M}_\odot$ (McConnachie 2012; Brook et al. 2014), en comparación con los $\sim$ 1000 subhalos producidos en las simulaciones de materia oscura sin colisiones (Moore et al. 1999). Sin tener en cuenta los límites actuales de detección de las galaxias satélite menos brillante (Tollerud et al. 2008), una solución a este problema requiere la identificación de un mecanismo capaz de inhibir la formación de estrellas por debajo de una cierta masa del halo de materia oscura: la reionización en el universo primordial, que ocurre entre z=10-6, parece ser un buen candidato, ya que provoca el calentamiento del gas y evita su colapso en halos pequeños (Bullock et al. 2000; Benson et al. 2002; Somerville 2002). Por lo tanto, los halos de materia oscura menos masivos no forman galaxias visibles y permanecen desprovistos de estrellas.

Otro aspecto del mismo problema es el *too big to fail problem* (TBTF), recientemente mostrado por (Boylan-Kolchin et al. 2011, 2012; Garrison-Kimmel et al. 2014) y que se puede resumir en la siguiente manera: la cinemática de las galaxias enanas esferoidales (dShps) observadas en la Vía Láctea y en Andrómeda no coincide con la cinemática de los subhalos obtenidos en las simulaciones de N-cuerpos. La dispersión de la velocidad estelar observada al radio de media-luminosidad (*half-light radius*) de la mayoría de las dSphs es menos de 20 km/s (McConnachie 2012; Collins et al. 2014; Tollerud et al. 2014), lo cual pondría estas galaxias en pequeños halos, dejando *oscuros* los subhalos más masivos encontrado en las simulaciones; o, en otras palabras, los subhalos más masivos en las simulaciones de N-cuerpos son demasiado densos para poder explicar la cinemática de las galaxias satélites observadas en el Grupo Local.

Dado que la Vía Láctea y la galaxia de Andrómeda no parecen ser casos especiales en este sentido (Strigari & Wechsler 2012), no hay actualmente un modelo de formación de galaxias que pueda fácilmente explicar estos resultados, a menos que se acepte que la formación de las galaxias sea estocástica por debajo de una cierta escala de masa de los halos. Una solución podría ser la reducción de la densidad central de los subhalos a través de mecanismos de física bariónica tales como fugas de gas causadas por explosiones de supernovae (Governato et al. 2010; Pontzen & Governato 2012): este mecanismo hace que el perfil de densidad de la materia oscura en la parte central del halo sea mucho más plano del perfil comúnmente utilizado, el NFW (Navarro et al. 1996b). Aunque este escenario podría funcionar para las galaxias enanas más brillantes, como Fornax con su luminosidad de $L \sim 2 \cdot 10^7 L_\odot$, no está claro cómo las enanas menos brillantes, hallándose entre los objetos con el mayor contenido de materia oscura en el universo, podría desarrollar suficiente energía para crear una distribución plana (*cored*) en un halo cuya densidad inicial central es una cúspide (perfil *cuspy* o NFW) (Garrison-Kimmel et al. 2013). Además, estos resultados dependen en gran medida del tipo de feedback estelar introducido en las simulaciones: simulaciones hidrodinámicas que no incluyen las fugas de gas impulsivas conducirán inevitablemente a una contracción adiabática de la parte central de los subhalos (Blumenthal et al. 1984; Gnedin et al. 2004), provocada por el colapso de gas frío hacia el centro, dando un resultado aún peor, como se muestra en (Di Cintio et al. 2011).

Algunos estudios han demostrado, sin embargo, que la combinación de los procesos bariónicos junto con una evolución posterior de los subhalos, teniendo en cuenta los efectos de las fuerzas de marea (*tidal stripping*), podría resolver el problema (Zolotov et al. 2012; Arraki et al. 2014). Al describir el perfil de densidad de la materia oscura en los subhalos con un modelo de tipo Einasto (Einasto 1965), en lugar de NFW, se podría mejorar

el problema (Di Cintio et al. 2013; Vera-Ciro et al. 2013), ya que este modelo permite describir diferentes perfiles causados por la pérdida de material en las zonas exteriores de los subhalos por efectos de mareas (Peñarrubia et al. 2010). Por otro lado, suponiendo que la Vía Láctea tenga una masa inferior a $10^{12}M_{\odot}$, también ayuda a reducir el número de subhalos masivos que se encuentran en las simulaciones (Wang et al. 2012; Vera-Ciro et al. 2013; Di Cintio et al. 2013). Otras posibilidades serian de invocar diferentes tipos de materia oscura, como la materia oscura auto-interactiva (Vogelsberger et al. 2012) o la materia oscura templada (*warm dark matter*, WDM) (Lovell et al. 2012) (véase, sin embargo, Schneider et al. 2014).

Por último, unido al problema TBTF, es la discrepancia *cusp/core* (de Blok 2010), es decir, el hecho de que las observaciones de las galaxias muestran que el perfil de densidad de la materia oscura es *cored*, o plano, hacia el centro, en desacuerdo con las simulaciones de N-cuerpos que en lugar establecen que los perfiles de densidad de materia oscura están bien descritos por un modelo con una cúspide central, modelo *cuspy* o NFW (Navarro et al. 1996b). La cúspide central de ese perfil, $\rho_{DM} \sim r^{-1}$, está en tensión con las observaciones de las galaxias espirales y de las galaxias enanas: modelos detallados, basados en las curvas de rotación de estas galaxias, sugieren un perfil de densidad de la materia oscura de tipo *cored*, $\rho_{DM} \sim$ const (Salucci & Burkert 2000; Simon et al. 2005; de Blok et al. 2008; Kuzio de Naray et al. 2008a; Oh et al. 2011a). También se observa un *core* central entre las enanas esferoidales menos brillantes alrededor de la Vía Láctea (Walker & Peñarrubia 2011).

En los últimos años se ha ido afirmando cada vez más la idea de que esta inconsistencia *cusp/core* se deriva del haber descuidado los efectos de los bariones en las simulaciones numéricas de las galaxias. Muchos estudios han demostrado que los bariones pueden influir en la distribución de la materia oscura en las galaxias (es Tissera & Dominguez-Tenreiro 1998). El enfriamiento del gas en el centro de una galaxia, debido a la contracción adiabática, consolida las cúspides centrales y exacerba la diferencia entre las observaciones y los perfiles teóricos (es Blumenthal et al. 1986; Gnedin et al. 2004). De hecho, para conciliar las relaciones de escala observadas en las galaxias, los halos de materia oscura deben ser más bien expandidos (Dutton et al. 2007, 2013). Los bariones pueden causar una expansión de las zonas centrales de los halos a través de dos mecanismos principales (ver Pontzen & Governato 2014 para una reseña reciente): por salidas rápida de gas, producidas por feedback estelar o por los núcleos galácticos activos (AGN) (Navarro et al. 1996a; Mo & Mao 2004; Read & Gilmore 2005; Mashchenko et al. 2006; Duffy et al. 2010; Pontzen & Governato 2012; Martizzi et al. 2013), o por fricción dinámica (El-Zant et al. 2001; Tonini et al. 2006; Romano-Díaz et al. 2008; Del Popolo 2009, 2010; Goerdt et al.

2010; Cole et al. 2011).

Si por un lado la fricción dinámica es eficaz en la expansión de halos muy masivos como lo que hay en los grupos de galaxias, por otro lado el feedback estelar es más eficaz en expandir halos de baja masa (Governato et al. 2010). El gas se enfría en el centro de la galaxia, donde va a formar las estrellas que luego irán explotando como supernovae, provocando repetidos derrames de material. Estas fugas impulsivas son capaces de mover bastante masa de gas para que la densidad central del halo disminuya y se vaya creando un *core* donde originalmente había una cúspide, gracias a la respuesta de la materia oscura a los cambios en el potencial gravitacional. Peñarrubia et al. (2012) ha calculado la energía necesaria para la transformación de un perfil de densidad desde *cusp* a *core*, en función de la masa del halo. Esta transformación puede ser permanente si las salidas de gas son suficientemente rápidas (Pontzen & Governato 2012).

En recientes simulaciones de galaxias enanas (Governato et al. 2010; Zolotov et al. 2012; Teyssier et al. 2013) y de galaxias más masivas, como por ejemplo la Vía Láctea (Macciò et al. 2012), se ha mostrado que los halos de materia oscura se expanden, dependiendo del tipo de feedback estelar. Governato et al. (2012) mostró que sólo las galaxias simuladas con masa estelar mayor que $\sim 10^7 \mathrm{M}_\odot$ son capaces de desarrollar la energía suficiente para expandir sus halos. Estos autores también han demostrado que la pendiente del perfil de la materia oscura en el centro de la galaxia, γ en $\rho \propto r^{-\gamma}$, disminuye al aumentar la masa estelar, en consecuencia del aumento de la energía disponible en explosión de supenovae. Un aumento de la masa estelar puede, sin embargo, hacer más profundo el pozo de potencial en la región central del halo: hemos demostrado en Di Cintio et al. (2014b) que, por encima de una cierta masa del halo, el potencial gravitacional es tan profundo que crea una contraposición eficiente al proceso de aplanamiento.

En Di Cintio et al. (2014b) hemos propuesto que γ depende de la relación entre la masa de las estrellas y la masa del halo de materia oscura, relación que va a ser diferente para diferentes galaxias. Por $M_\star/M_{\rm halo} \lesssim 10^{-4}$ no hay suficiente energía proveniente de supernovae para cambiar de manera eficiente la distribución de la materia oscura, y el halo mantiene el perfil original del tipo NFW, con $\gamma \sim$ -1. Para valores más altos de $M_\star/M_{\rm halo}$, γ aumenta, hasta un máximo de $\gamma \sim 0$ (galaxias con densidad central *cored*) por $M_\star/M_{\rm halo} \sim 3 - 5 \times 10^{-3}$. La relación empírica entre la masa estelar de las galaxias y la masa del halo de materia oscura en el que residen (Moster et al. 2010; Guo et al. 2010) implica que este valor corresponde a $M_\star \approx 10^{8.5}\mathrm{M}_\odot$ y $M_{\rm halo} \approx 10^{11}\mathrm{M}_\odot$. En halos de masa mayor, el proceso de fuga de gas es cada vez más ineficaz en aplanar la densidad interna de la materia oscura, que vuelve a ser *cuspy* .

Mediante un conjunto de galaxias simuladas hidrodinámicamente, que cubren una amplia gama de masas y que incluyen el feedback estelar de supernovae, de los vientos estelares y de las estrellas jóvenes y masivas, hemos mostrado en Di Cintio et al. (2014a) cómo es posible obtener un perfil que describe de manera eficiente la distribución de la materia oscura en las galaxias simuladas, desde las galaxias enanas hasta las espirales como la Vía Láctea .

En la primera parte de esta tesis, me concentraré en el problema TBTF, utilizando un Grupo Local de galaxias simuladas en el proyecto CLUES[1], una simulación cosmológica de N-cuerpos presentada en Gottlöber et al. (2010), en la cual la dinámica del gas es descrita por el método de Lagrange *Smoothed-Particles Hydrodynamics* (SPH).

Los Capítulos 3 y 4 estarán dedicados al análisis de las galaxias simuladas en CLUES, correspondientes a la Vía Láctea y Andrómeda y a sus satélites. Mostraré cómo la inclusión de bariones en las simulaciones de N-cuerpos provoca un doble efecto con respecto a los subhalos: mientras que los satélites con una gran fracción bariónica sufren una contracción adiabática de sus halos, agravando así el problema TBTF, los subhalos que han perdido todo sus gas a z=0 sufrirán una disminución de $V_{\rm max}$, el pico de sus curva de rotación, hasta ser compatibles con las galaxias satélite observadas en la Vía Láctea. Veremos también cómo es posible describir el perfil de densidad de los subhalos con un modelo Einasto que, al tener un parámetro libre mas que el clásico modelo NFW, es capaz de capturar en manera mejor la distribución de la materia oscura en los subhalos: utilizando este perfil se pueden conciliar las observaciones de las dSphs y las simulaciones de los subhalos.

El número de satélites masivos que se encuentran dentro del radio virial de una galaxia depende de manera clara de la masa misma de la galaxia, por esta razón en el Capítulo 5 presentaré un método para estimar la masa de las galaxias y aplicaré este método a las galaxias simuladas en CLUES (Di Cintio et al. 2012).

En el Capítulo 6 analizaré el problema TBTF usando simulaciones de WDM, es decir, de materia oscura templada con partículas de masa ~ 1 keV, y mostraré que aunque la WDM reduce el número de las estructuras presentes a pequeñas escalas, no es, sin embargo, suficiente para explicar la discrepancia con las observaciones. Presentaré también las principales diferencias de un grupo de galaxias simuladas en un entorno ΛCDM o ΛWDM.

En el Capítulo 7, me centraré en la técnica de *abundance matching* en el Grupo Local. El uso de la función de masa de halos derivadas de simula-

[1] http://www.clues-project.org/

ciones del Grupo Local, como las simulaciones CLUES, permite ampliar la relación entre la masa estelar y la masa de los halos de materia oscura hasta las galaxias más débiles y menos brillantes, como las dSphs . Esta relación indica que la mayoría de las galaxias del Grupo Local esta contenida en halos de materia oscura de masa $\geqslant 10^{10}\mathrm{M}_{\odot}$: para conciliar los datos observacionales con esta predicción se debe asumir que algunas de estas galaxias tienen un *core* central, o sea que su halo de materia oscura es expandido.

La expansión de los halos de materia oscura y el problema *cusp/core* serán el tema central de la segunda parte de la tesis, en la cual utilizaré las simulaciones hidrodinámicas pertenecientes al proyecto MAGICC[2], que incluyen un modelo de *feedback* físicamente motivado. Estas galaxias reproducen de manera excelente la relación entre la masa estelar y la masa del halo a z=0 así como en redshift mas altos (Kannan et al. 2013), y una serie de propiedades observacionales y relaciones de escala (Brook et al. 2012b; Stinson et al. 2013).

En los Capítulos 8 y 9 describiré cómo la transformación *cusp/core* es totalmente dependiente de la relación $M_{\star}/M_{\mathrm{halo}}$ de cada galaxia, y como tal predicción se puede utilizar para hacer comparaciones con observaciones. Derivaré, además, un perfil de densidad que puede reproducir la materia oscura cuya distribución sea de tipo *cusp* así como de tipo *core*, y que es apropiado para describir las galaxias enanas y las galaxias espirales tipo Vía Láctea. Este perfil está totalmente vinculado a la eficiencia de formación estelar en cada galaxia, $M_{\star}/M_{\mathrm{halo}}$ a z=0, y representa un mejoramiento significativo sobre el perfil clásico NFW, que, siendo derivado a partir de simulaciones de N-cuerpos, no considera el impacto de la física bariónica.

La descripción completa de las simulaciones utilizadas en esta tesis será presentada en el Capitulo 2, y las conclusiones y posibilidad futuras en el Capitulo 10.

[2]http://www.star.uclan.ac.uk/∼cbb/magicc.html

Riassunto e conclusioni

Il modello di materia oscura fredda con costante cosmologica Λ, cosiddetto ΛCDM, è l'attuale modello cosmologico favorito nell'ambito di formazione di galassie: formulato più di trenta anni fa (White & Rees 1978), è basato sull'assunzione che l'Universo sia composto per il $\sim 68\%$ da energia oscura, per il $\sim 27\%$ da materia oscura e solo per il $\sim 5\%$ da materia ordinaria (Planck Collaboration et al. 2013). Le particelle di materia oscura *fredda*, avendo una massa più grande del keV, non riescono a smorzare le piccole fluttuazioni e possono quindi spiegare in maniera soddisfacente le proprietà osservative delle galassie, come la grande quantità di energia su piccole scale indicata dalla funzione correlazione a due punti (Peebles 1980). La necessità di una componente di materia oscura fredda è evidente anche da una serie di vincoli osservativi quali, tra gli altri, la curva di rotazione delle galassie (Rubin et al. 1980) e l'osservazione in *weak lensing* di collisioni tra ammassi (Clowe et al. 2006).

Una conseguenza diretta del fatto che la materia oscura sia fredda, ovvero che le sue particelle fossero non relativistiche all'epoca dell'eguaglianza materia-radiazione, è che la formazione di strutture proceda in maniera gerarchica *bottom-up*, dal basso verso l'alto (Blumenthal et al. 1984). In ΛCDM piccole perturbazioni nel campo di densità primordiale possono crescere ed espandersi via instabilità gravitazionali e poi fondersi tra di loro per creare le strutture molto più grandi, quali ammassi e gruppi di galassie, che osserviamo oggi. Le fluttuazioni primordiali in densità possono essere misurate direttamente dalla radiazione cosmica di fondo (CMB), che è la radiazione termica rimanente del Big Bang: lo spettro di potenza delle anisotropie in temperatura della CMB, infatti, riflette tali fluttuazioni, o grado di contrasto, nel campo di densità di materia dell'Universo primordiale (Smoot et al. 1992; Spergel et al. 2003; Planck Collaboration et al. 2013). Queste perturbazioni inizieranno a collassare per formare i cosiddetti aloni di materia oscura, che sono alla base della formazione di tutte le galassie future, in un processo altamente non lineare che può essere studiato solo utilizzando simulazioni numeriche come simulazioni a N corpi del campo di densità cosmico (Springel 2005).

Data una distribuzione inizialmente imperturbata di particelle, e tenendo conto dello spettro di potenza primordiale come condizione iniziale, si può descrivere l'evoluzione ed il seguente collasso gravitazionale della materia oscura non collisionale da alti redshift fino a z=0, assegnare le galassie a tali aloni di materia oscura utilizzando modelli semianalitici (Monaco et al. 2014; Benson 2011), e confrontare il risultato finale con la distribuzione e le proprietà osservative delle galassie, ad esempio utilizzando la 2dF Galaxy Redshift Survey (Cross et al. 2001). Sebbene le simulazioni di materia oscura abbiano riprodotto con successo diverse caratteristiche dell'Universo sia a grandi scale (e.g., la Millenium-XXL ed il MultiDark run in Angulo et al. 2012; Riebe et al. 2013) che a scale galattiche (e.g., il Gruppo Locale e le galassie simili alla Via Lattea come in Gottlöber et al. 2010; Springel et al. 2008; Brook et al. 2012a), esistono ancora delle discordanze tra la previsione del modello ΛCDM e le proprietà osservative di galassie nane e galassie satelliti. A tali scale, infatti, il modello è complicato dalla fisica barionica che è dinamicamente rilevante nella formazione di strutture. In particolare, le principali questioni che tuttora gravano sul paradigma ΛCDM a piccole scale sono :

- il problema dei satelliti mancanti, o *missing satellite* problem
- il problema *too big to fail*
- il problema *core/cusp*

Il problema dei *missing satellite* (Klypin et al. 1999a) è la discrepanza tra il numero di galassie satellite osservate intorno alla nostra Via Lattea e alla galassia di Andromeda ed il numero di subaloni di materia oscura trovati in simulazioni ad N corpi, quest'ultimo essendo alcuni ordini di grandezza maggiore del precedente. All'interno del Gruppo Locale si osservano soltanto $\sim$ 40 galassie satellite con $M_\star > 10^{6.5}\mathrm{M}_\odot$ (McConnachie 2012; Brook et al. 2014), contro i $\sim$ 1000 subaloni prodotti in simulazioni non collisionali (Moore et al. 1999). Trascurando gli attuali limiti di rilevabilità delle galassie satellite meno luminose (Tollerud et al. 2008), una soluzione a questo problema richiede di individuare un meccanismo in grado di inibire la formazione di stelle al di sotto di una certa massa dell'alone di materia oscura: la reionizzazione nell'universo primordiale, che avviene a z=10-6, sembra essere un buon candidato, dal momento che riscalda il gas e ne previene il collasso in piccoli aloni (Bullock et al. 2000; Benson et al. 2002; Somerville 2002). Pertanto gli aloni di materia oscura meno massivi non formeranno una galassia visibile e resteranno privi di stelle.

Un altro aspetto del problema è il cosiddetto problema *too big to fail* (TBTF), recentemente evidenziato da Boylan-Kolchin et al. (2011, 2012);

Garrison-Kimmel et al. (2014), e riassunto come segue: la cinematica delle galassie nane sferoidali (dShps) osservate nella Via Lattea ed in Andromeda non coincide con la cinematica dei subaloni prevista da simulazioni ad N corpi. La dispersione di velocità stellare osservata al raggio di mezza-luminosità, *half-light radius*, della maggior parte delle dSphs è inferiore a 20 km/s (McConnachie 2012; Collins et al. 2014; Tollerud et al. 2014), fatto che porrebbe tali galassie in piccoli aloni, lasciando *oscuri* i più massicci subaloni trovati nelle simulazioni; o, in altre parole, i subaloni più massicci in simulazioni N corpi sono troppo densi per poter ospitare molte delle galassie satelliti osservate nel Gruppo Locale.

Dal momento che la Via Lattea e la galassia di Andromeda non sembrano essere casi particolari in questo senso (Strigari & Wechsler 2012), non c'è attualmente un modello di formazione di galassie che possa spiegare facilmente questi risultati, a meno che non si accetti che la formazione di galassie sia stocastica al di sotto di una certa scala di massa. Una soluzione potrebbe essere quella di ridurre la densità centrale dei subaloni attraverso meccanismi di fisica barionica come ad esempio fuoriuscite di gas causate da esplosioni di supernovae (Governato et al. 2010; Pontzen & Governato 2012): tale meccanismo fa sì che il profilo di densità della materia oscura, nella parte centrale dell'alone, sia molto più piatto del comunemente utilizzato profilo NFW (Navarro et al. 1996b). Se da un lato questo scenario potrebbe funzionare per le galassie nane più brillanti, come Fornax con la sua luminosità di $L \sim 2 \cdot 10^7 L_\odot$, non è chiaro come le nane con una minore luminosità, essendo tra gli oggetti con il più alto contenuto di materia oscura nell'universo, possano sviluppare l'energia sufficiente a creare una distribuzione piatta (*cored*) in un alone la cui densità centrale iniziale è invece una cuspide (*cuspy*, profilo NFW) (Garrison-Kimmel et al. 2013). Inoltre questi risultati sono fortemente dipendenti dal tipo di *feedback* stellare introdotto nelle simulazioni: simulazioni idrodinamiche che non includono fuoriuscite impulsive di gas porteranno inevitabilmente ad una contrazione adiabatica della parte centrale dei subaloni (Blumenthal et al. 1984; Gnedin et al. 2004), causata dal collasso di gas freddo verso il centro, provocando un quadro ancora peggiore, come dimostrato in Di Cintio et al. (2011).

Alcuni studi hanno mostrato, tuttavia, che la combinazione di processi barionici ed una successiva evoluzione dei subaloni, tenendo conto degli effetti delle forze mareali (*tidal stripping*), potrebbe risolvere il problema (Zolotov et al. 2012; Arraki et al. 2014). Descrivere il profilo di densità della materia oscura nei subaloni con un modello tipo Einasto (Einasto 1965), piuttosto che NFW, può alleviare il problema (Di Cintio et al. 2013; Vera-Ciro et al. 2013), visto che tale modello consente di descrivere differenti profili causati dalla perdita di materiale nelle zone esterne del subalone per effetti mareali (Peñarrubia et al. 2010). D'altra parte, assumere una massa

minore per la Via Lattea aiuta a ridurre il numero di subaloni massivi (Wang et al. 2012; Vera-Ciro et al. 2013; Di Cintio et al. 2013). Altre possibilità invocano differenti tipi di materia oscura, dalla materia oscura auto-interagente (Vogelsberger et al. 2012) alla materia oscura tiepida, o *warm dark matter* WDM (Lovell et al. 2012) (vedi, tuttavia, Schneider et al. (2014)).

Infine, collegata al problema TBTF, è la discrepanza *cusp/core* (de Blok 2010), cioè il fatto che le osservazioni di galassie mostrano che il profilo di densità dei sottostanti aloni di materia oscura è *cored*, piatto verso il centro, in disaccordo con le simulazioni a N corpi che invece prevedono che tali profili di densità di materia oscura siano ben descritti da un modello con una cuspide centrale, *cuspy*, come il modello NFW (Navarro et al. 1996b). La cuspide centrale di tale profilo, $\rho_{dm} \sim r^{-1}$, è in tensione con osservazioni di galassie sia nane che a spirale, per le quali modelli dettagliati di massa basati sulle curve di rotazione suggeriscono un profilo di densità centrale della materia oscura di tipo *cored*, $\rho_{dm} \sim const$ (Salucci & Burkert 2000; Simon et al. 2005; de Blok et al. 2008; Kuzio de Naray et al. 2008a; Oh et al. 2011a). Galassie con un *core* centrale sono state osservate anche tra le meno brillanti nane sferoidali che circondano la Via Lattea (Walker & Peñarrubia 2011).

Negli ultimi anni si è sempre più andata affermando l'idea che tale incoerenza *cusp/core* derivi dall'aver trascurato gli effetti dei barioni nelle simulazioni numeriche di galassie. Molti studi hanno dimostrato come i barioni possano influenzare la distribuzione di materia oscura nelle galassie (e.g. Tissera & Dominguez-Tenreiro 1998). Il raffreddamento del gas al centro di una galassia causa contrazione adiabatica, il cui effetto consolida le cuspidi centrali e aggrava il divario tra profili teorici e osservazioni (e.g. Blumenthal et al. 1986; Gnedin et al. 2004). Per riconciliare le relazioni di scala delle galassie osservate, servirebbero piuttosto aloni di materia oscura espansi (Dutton et al. 2007, 2013). I barioni possono causare un'espansione degli aloni attraverso due meccanismi principali (vedi Pontzen & Governato 2014 per una rassegna recente): per fuoriuscite di gas prodotte da *feedback* stellare o da nuclei galattici attivi (AGN) (Navarro et al. 1996a; Mo & Mao 2004; Read & Gilmore 2005; Mashchenko et al. 2006; Duffy et al. 2010; Pontzen & Governato 2012; Martizzi et al. 2013) o per attrito dinamico (El-Zant et al. 2001; Tonini et al. 2006; Romano-Díaz et al. 2008; Del Popolo 2009, 2010; Goerdt et al. 2010; Cole et al. 2011).

Mentre l'attrito dinamico è efficace nell'espandere aloni molto massivi nei quali si trovano ammassi di galassie, il *feedback* stellare è più efficace nell'espandere aloni di piccola massa (Governato et al. 2010). Il gas, raffreddandosi al centro della galassia, andrà a formare le stelle che, esplodendo

come supernovae, provocheranno poi ripetute fuoriuscite di materiale o *outflows*. Tali *outflows* sono in grado a muovere abbastanza massa di gas da riuscire a creare un nucleo piatto di densità centrale in un alone oscuro originariamente *cuspy*, grazie alla risposta della materia oscura alle variazioni del potenziale gravitazionale. Peñarrubia et al. (2012) ha calcolato l'energia necessaria per avere la trasformazione *cusp/core* di un profilo di densità in funzione della massa dell'alone. Tale trasformazione può essere permanente se gli *outflows* sono sufficientemente rapidi (Pontzen & Governato 2012). Simulazioni di galassie nane (Governato et al. 2010; Zolotov et al. 2012; Teyssier et al. 2013) e di galassie più massive tipo Via Lattea (Macciò et al. 2012) hanno prodotto aloni di materia oscura espansi, a seconda dell'implementazione del *feedback* stellare. Governato et al. (2012) ha mostrato che solo galassie simulate con massa stellare superiore a $\sim 10^7 \mathrm{M}_\odot$ riescono a sviluppare l'energia sufficiente per espandere i loro aloni. Questi autori hanno inoltre dimostrato che la pendenza del profilo della materia oscura verso il centro della galassia, γ in $\rho \propto r^{-\gamma}$, si riduce con l'aumento della massa stellare, conseguentemente all'aumento di energia disponibile dall'esplosione di supenovae. Un aumento della massa stellare può tuttavia rendere più profonda la buca di potenziale nella regione centrale dell'alone: abbiamo mostrato in Di Cintio et al. (2014b) che, al di sopra di una certa massa dell'alone, una tale buca di potenziale si oppone al processo di appiattimento.

In Di Cintio et al. (2014b) abbiamo proposto che γ dipenda dal rapporto tra la massa di stelle e la massa dell'alone di materia oscura, rapporto che sarà differente per galassie diverse. Per $M_\star/M_{\rm halo} \lesssim 10^{-4}$ non c'è abbastanza energia da supernovae in grado di cambiare in modo efficiente la distribuzione di materia oscura, e l'alone manterrà il profilo originale di tipo NFW, con $\gamma \sim -1$. Per valori più elevati di $M_\star/M_{\rm halo}$, γ aumenterà, fino a raggiungere un massimo di $\gamma \sim 0$ (galassie più *cored*) per $M_\star/M_{\rm halo} \sim 3 - 5 \times 10^{-3}$. La relazione empirica tra la massa stellare delle galassie e la massa dell'alone di materia oscura in cui risiedono (Moster et al. 2010; Guo et al. 2010) implica che tale valore corrisponda a $M_\star \approx 10^{8.5}\mathrm{M}_\odot$ e $M_{\rm halo} \approx 10^{11}\mathrm{M}_\odot$. In aloni di massa superiore, il processo di fuoriuscita di gas diventerà sempre più inefficace ad appiattire la densità interna di materia oscura, che tornerà ad essere *cuspy*.

Utilizzando un insieme di galassie simulate idrodinamicamente, che coprono un intervallo di massa ampio ed includono *feedback* stellare da supernovae, venti stellari e stelle giovani e massicce, abbiamo ulteriormente mostrano in Di Cintio et al. (2014a) di come sia possibile ricavare un profilo che descriva in modo efficiente la distribuzione di materia oscura all'interno delle galassie simulate, dalle nane alle galassie a spirale tipo Via Lattea.

Nella prima parte di questa tesi mi concentrerò sul problema TBTF, utilizzando un Gruppo Locale simulato nell'ambito del progetto CLUES[3], una simulazione cosmologica ad N corpi presentata in Gottlöber et al. (2010), in cui la dinamica del gas è descritta con il metodo lagrangiano *Smoothed-Particles Hydrodynamics* (SPH).

I Capitoli 3 e 4 saranno dedicati all'analisi delle galassie simulate in CLUES, corrispondenti alla Via Lattea e ad Andromeda, e dei loro satelliti. Mostrerò come l'inclusione dei barioni nelle simulazioni ad N corpi causi un duplice effetto per quanto riguarda i subaloni: mentre i satelliti con una grande frazione barionica subiranno una contrazione adiabatica del proprio alone, peggiorando così il problema TBTF, i subaloni che avranno perso tutto il loro gas a z=0 subiranno una diminuzione in $V_{\rm max}$, il picco della loro curva di rotazione, risultando compatibili con le galassie satellite osservate nella Via Lattea. Farò inoltre vedere di come sia possibile descrivere il profilo di densità dei subaloni con un modello Einasto che, avendo un parametro in più rispetto al classico modello NFW, riesce a catturare meglio la distribuzione di materia oscura all'interno dei subaloni: utilizzando tale profilo è possibile riconciliare osservazioni di dSphs e simulazioni di subaloni.

Poiché il numero di satelliti massivi che si trovano all'interno del raggio viriale di una galassia dipende in maniera evidente dalla massa stessa di tale galassia, presenterò nel Capitolo 5 un metodo per stimare le masse delle galassie ed applicherò tale metodo alle galassie simulate in CLUES (Di Cintio et al. 2012).

Nel Capitolo 6 affronterò il problema TBTF utilizzando simulazioni di WDM, ossia materia oscura tiepida con particelle di massa $\sim$1 keV, mostrando che sebbene la WDM riduca il numero di strutture presenti a piccole scale, non è tuttavia sufficiente per spiegare le discrepanze con le osservazioni. Presenterò inoltre le differenze principali di un gruppo di galassie simulate in un contesto ΛCDM o ΛWDM.

Nel Capitolo 7 mi focalizzerò sulla tecnica di *abundance matching* nel Gruppo Locale. Utilizzando la funzione di massa degli aloni derivata da simulazioni del Gruppo Locale, quali le simulazioni CLUES, è possibile estendere la relazione tra massa stellare e massa degli aloni di materia oscura fino alle galassie più deboli e meno luminose, come le dSphs. Tale relazione indica che la maggior parte delle galassie del Gruppo Locale è contenuta in aloni di materia oscura di massa $\geqslant 10^{10}{\rm M}_{\odot}$: per riconciliare i dati osservativi con tale previsione bisogna assumere che alcune di tali galassie abbiano un *core*, ovvero che il loro alone di materia oscura sia espanso.

[3] http://www.clues-project.org/

L'espansione degli aloni di materia oscura ed il problema *cusp/core* saranno al centro della seconda parte della tesi, in cui utilizzerò le simulazioni idrodinamiche appartenenti al progetto MaGICC[4], che includono modelli di *feedback* fisicamente motivati. Queste galassie riproducono eccellentemente la relazione tra massa stellare e massa dell'alone sia a z=0 che a più alti redshift (Kannan et al. 2013), nonché una serie di proprietà osservative e relazioni di scala (Brook et al. 2012b; Stinson et al. 2013).

Nei Capitoli 8 e 9 descriverò come la trasformazione *cusp/core* dipenda interamente dal rapporto $M_\star/M_{\rm halo}$ di ogni galassia, e come tale previsione possa essere utilizzata per fare confronti con i dati osservativi. Deriverò, inoltre, un profilo di densità in grado di riprodurre distribuzioni di materia oscura sia di tipo *core* che di tipo *cusp*, di modo che tale profilo risulti appropriato per descrivere galassie nane così come galassie a spirale tipo Via Lattea. Tale profilo è completamente vincolato all'efficienza di formazione stellare all'interno di ogni galassia, $M_\star/M_{\rm halo}$ a z=0, e rappresenta un notevole miglioramento rispetto al classico profilo NFW, che, essendo derivato da simulazioni ad N corpi, trascura la fisica barionica.

La descrizione completa delle simulazioni utilizzate in questa tesi sarà data nel Capitolo 2, mentre il Capitolo 10 sarà dedicato alle conclusioni e prospettive future.

[4]http://www.star.uclan.ac.uk/∼cbb/magicc.html

Chapter 1

Introduction

The Λ Cold Dark Matter (ΛCDM) model is the current cosmological paradigm of galaxy formation: formulated more than 30 years ago (White & Rees 1978), it is based on the assumption that the Universe is composed by a $\sim 68\%$ of dark energy, a $\sim 27\%$ of dark matter and by only a $\sim 5\%$ of ordinary matter (Planck Collaboration et al. 2013). *Cold* dark matter particles, having a mass larger than the keV scale, do not damp small fluctuations by free streaming, and can satisfactorily explain the observed properties of galaxies, such as the large amount of power on small scales as indicated by the galaxies' two point correlation function (Peebles 1980). The need for dark matter is also evident from a series of observational constraints like, amongst other things, the rotation curves of galaxies (Rubin et al. 1980) and the weak lensing observation of a cluster merger (Clowe et al. 2006).

A direct consequence of the dark matter being cold, which means that its particles were not relativistic at the epoch of matter-radiation equality, is that structure formation proceed in a *bottom-up* hierarchical fashion (Blumenthal et al. 1984). In ΛCDM, small perturbations in the primordial density field can grow via gravitational instabilities, and then merge with each other to create the much bigger structures, like clusters and groups of galaxies, that we observe today. The primordial density perturbations can be measured directly from the cosmic microwave background (CMB) radiation, which is the relic thermal radiation of the Big Bang: the power spectrum of CMB temperature anisotropies, in fact, reflects the small perturbations, or degree of contrast, in the matter density field of the early universe (Smoot et al. 1992; Spergel et al. 2003; Planck Collaboration et al. 2013). Such perturbations will start collapsing to form the so-called dark matter haloes, which are the main seeds of all future galaxies, in a process which is highly non-linear and can only be modeled by using numerical methods, such as N-body simulations of the cosmic density field (Springel

2005).

Given some initially unperturbed distribution of particles, and taking into account the primordial power spectrum as initial condition, one can model the evolution and gravitational collapse of collisionless, dark matter only particles from high redshift to z=0, populate dark matter haloes with galaxies by using semi-analytic models (Monaco et al. 2014; Benson 2011), and compare the final result with the observed distribution and properties of galaxies, like the 2dF Galaxy Redshift Survey (Cross et al. 2001). While dark matter only simulations have successfully reproduced several features of the Universe at both large (e.g. the Millenium-XXL and MultiDark runs as in Angulo et al. 2012; Riebe et al. 2013) and galactic scales (e.g. the Local Group and Milky Way type galaxies as in Gottlöber et al. 2010; Springel et al. 2008; Brook et al. 2012a), there are still inconsistencies between the prediction of the ΛCDM model and the observed properties of dwarfs and satellite galaxies. Indeed on such scales the model is complicated by the dynamically relevant baryonic physics involved in galaxy formation. In particular, the main issues that still affect the ΛCDM paradigm at small scales are:

- the *missing satellite* problem
- the *too big to fail* problem
- the *core/cusp* problem

The *missing satellite* problem (Klypin et al. 1999a) is the discrepancy between the number of observed satellite galaxies around our own Milky Way and Andromeda galaxy and the number of simulated subhaloes found in N-body simulations, the latter being orders of magnitudes bigger than the former. Within the Local Group only $\sim$ 40 bright satellites are observed with $M_\star > 10^{6.5}\mathrm{M}_\odot$ (McConnachie 2012; Brook et al. 2014), against the $\sim$ 1000 produced by collisionless simulations (Moore et al. 1999). Apart from current detection limits (Tollerud et al. 2008), a solution to this problem requires to identify a mechanism able to inhibit star formation below a certain halo mass: reionization in the early universe happening at z=10-6 seems to be a good candidate, since it heats up the gas and prevent its collapse into small haloes (Bullock et al. 2000; Benson et al. 2002; Somerville 2002). Therefore the smallest haloes will never form a visible galaxy, remaining devoid of stars.

Another aspect of the issue is the so-called *too big to fail* (TBTF) problem, recently highlighted by Boylan-Kolchin et al. (2011, 2012); Garrison-Kimmel et al. (2014), and summarized as follow: the kinematics of observed

dwarf spheroidals (dShps) of the Milky Way and Andromeda galaxies do not coincide with the expected kinematic of subhaloes derived from N-body simulations. The observed stellar velocity dispersion at half-light radius of most dSphs is lower than 20 km/s (McConnachie 2012; Collins et al. 2014; Tollerud et al. 2014), fact that would place such galaxies into small haloes, leaving *dark* the most massive subhaloes found in simulations; or, in other words, the most massive subhaloes in N-body simulations are too dense to host the observed satellite galaxies in the Local Group.

Since the Milky Way and Andromeda galaxies do not seem to be outlier in this sense (Strigari & Wechsler 2012), no current model of galaxy formation can easily accommodate these results, unless one accepts that galaxy formation is stochastic below a certain mass scale. A solution would be to reduce the central densities of subhaloes by means of baryonic mechanisms such as supernovae driven gas outflows (Governato et al. 2010; Pontzen & Governato 2012) which will lead to an inner density profile for dark matter much shallower than the commonly assumed NFW (Navarro et al. 1996b). This scenario would work for the brightest dwarfs, like Fornax with its $L \sim 2 \cdot 10^7 L_{\odot}$, but it is not clear how the fainter dwarfs, which are amongst the most dark matter dominated objects in the Universe, could develop the energy sufficient to create a shallow *cored*-like distribution in an initially *cuspy*, NFW dark matter profile (Garrison-Kimmel et al. 2013). Moreover, these results are strongly feedback dependent: hydrodynamical simulations which do not include impulsive gas outflows will inevitably lead to an adiabatic contraction (Blumenthal et al. 1984; Gnedin et al. 2004) of the subhaloes as gas cools to its center, causing an even worse picture as we showed in Di Cintio et al. (2011).

It has been argued, however, that the combination of baryonic processes together with a subsequent evolution of the subhaloes, taking into account tidal stripping, could solve the problem (Zolotov et al. 2012; Arraki et al. 2014). Describing the subhaloes with an Einasto profile (Einasto 1965), allowing for a range of possible shape parameters as a consequence of tidal stripping (Peñarrubia et al. 2010), would solve the issue (Di Cintio et al. 2013; Vera-Ciro et al. 2013). Reducing the Milky Way's mass could also help in lowering the number of massive subhaloes that fail at forming stars (Wang et al. 2012; Vera-Ciro et al. 2013; Di Cintio et al. 2013). Other possibilities invoke self-interacting dark matter (Vogelsberger et al. 2012) or *warm* dark matter, WDM (Lovell et al. 2012) (see, however, Schneider et al. 2014).

Finally, also connected to the TBTF problem, is the *cusp/core* discrepancy (de Blok 2010), namely the fact that observations of real galaxies find cored profiles for the underlying dark matter density, in disagreement

with N-body simulations which, instead, predict that over several orders of magnitude in radius, the density profiles of dark matter haloes are well described by a cuspy, NFW model (Navarro et al. 1996b). The central cusp, $\rho_{dm} \sim r^{-1}$, of such model is in tension with observations of disc and dwarf galaxies in which detailed mass modeling using rotation curves suggests a flatter, $\rho_{dm} \sim const$, dark matter density profile (Salucci & Burkert 2000; Simon et al. 2005; de Blok et al. 2008; Kuzio de Naray et al. 2008a; Oh et al. 2011a). Cored galaxies are also found within the fainter, dark matter dominated dwarf spheroidal galaxies surrounding the Milky Way (Walker & Peñarrubia 2011).

In the last few years it has been increasingly accepted the picture in which such inconsistency arises from having neglected the effects of baryons in simulations, which are determinant on small, galactic scales. Many studies have shown how baryons can affect the dark matter (e.g. Tissera & Dominguez-Tenreiro 1998). Gas cooling to the center of a galaxy causes adiabatic contraction (e.g. Blumenthal et al. 1986; Gnedin et al. 2004), whose effect strengthens cusps and exacerbates the mismatch between theoretical profiles and observations. Rather, expanded haloes are required to reconcile observed scaling relations of both early and late-type galaxies (Dutton et al. 2007, 2013). Baryons can expand haloes through two main mechanisms (see Pontzen & Governato 2014 for a recent review): gas outflows driven by stellar or AGN feedback (Navarro et al. 1996a; Mo & Mao 2004; Read & Gilmore 2005; Mashchenko et al. 2006; Duffy et al. 2010; Pontzen & Governato 2012; Martizzi et al. 2013) or dynamical friction (El-Zant et al. 2001; Tonini et al. 2006; Romano-Díaz et al. 2008; Del Popolo 2009, 2010; Goerdt et al. 2010; Cole et al. 2011).

While dynamical friction is effective at expanding high mass haloes hosting galaxy clusters, stellar feedback is more effective at expanding low mass haloes (Governato et al. 2010). Gas cools to the galaxy centre where it forms stars that, exploding as supernovae, will drive repeated energetic outflows. Such outflows move enough gas mass to create a core in an originally cuspy dark halo, due to the dark matter response to the adjusted gravitational potential. Peñarrubia et al. (2012) calculated the energy required to flatten a density profile as a function of halo mass. The *cusp/core* change can be made permanent if the outflows are sufficiently rapid (Pontzen & Governato 2012). Simulations from dwarf galaxies (Governato et al. 2010; Zolotov et al. 2012; Teyssier et al. 2013) to Milky Way mass (Macciò et al. 2012) have produced dark matter halo expansion depending on the implementation of stellar feedback. Governato et al. (2012) showed that only simulated galaxies with stellar masses higher than $\sim 10^7 M_\odot$ expand their haloes. They also showed that the inner dark matter profile slope, γ in $\rho \propto r^{-\gamma}$, flattens with increasing stellar mass, resulting from the increase of available energy

from supernovae. An increase in stellar mass may, however, also deepen the potential well in the central region of the halo: indeed, we showed in Di Cintio et al. (2014b) that above a certain halo mass such a deepened potential well opposes the flattening process.

In Di Cintio et al. (2014b) we propose that γ depends on the stellar-to-halo mass ratio of galaxies. At $M_\star/M_{\rm halo} \lesssim 10^{-4}$ there is not enough supernova energy to efficiently change the dark matter distribution, and the halo retains the original NFW profile, $\gamma \sim -1$. At higher $M_\star/M_{\rm halo}$, γ increases, with the maximum $\gamma \sim 0$ (most cored galaxies) found when $M_\star/M_{\rm halo} \sim 3 - 5 \times 10^{-3}$. The empirical relation between the stellar and halo mass of galaxies (Moster et al. 2010; Guo et al. 2010) implies that this corresponds to $M_\star \approx 10^{8.5} M_\odot$ and $M_{\rm halo} \approx 10^{11} M_\odot$. In higher mass haloes, the outflow process becomes ineffective at flattening the inner dark matter density and the haloes have increasingly cuspy profiles.

Using a suite of hydrodynamically simulated galaxies, which cover a broad mass range and include stellar feedback from supernovae, stellar winds and young, massive stars, we further show in Di Cintio et al. (2014a) how it is possible to derive a profile that efficiently describes the distribution of dark matter within the simulated galaxies, from dwarfs to Milky Way mass.

In the first part of this thesis I am going to focus on the TBTF problem, using the Local Group drawn from the CLUES[1] project, a fully N-body+SPH simulation described in (Gottlöber et al. 2010), in which the gas dynamic is followed by means of the *Smoothed-Particles Hydrodynamics* technique.

Chapter 3 and 4 will be devoted to the analysis of the Milky Way and Andromeda galaxies and of their satellites, as derived from both the dark matter only and the baryonic run of CLUES. I will show how the inclusion of baryons in the simulations leads to a twofold effect for what concerns subhaloes: while satellites with a large baryon fraction will experience an adiabatic contraction of their haloes, thus worsening the TBTF problem, those subhaloes with a smaller baryon fraction will undergo a decrease in $V_{\rm max}$, the peak of their rotation curves, resulting in a kinematic compatible with the one of the observed dSphs. I will also show how it is possible to describe the density profile of these subhaloes with an Einasto model that, having one more free parameter than the usual NFW one, it is able to capture in a more appropriate way the distribution of dark matter within such subhaloes: using this profile it is possible to reconcile observations and simulations.

[1] http://www.clues-project.org/

Since the number of massive satellites within the virial radius of a host galaxy is strongly dependent on the mass of the galaxy itself, I will show in Chapter 5 a method to estimate such mass, and I will apply this method to the simulated galaxies in CLUES (Di Cintio et al. 2012).

In Chapter 6 I will explore the TBTF problem using WDM simulations, with a dark matter particle mass of $\sim$1 keV, showing that, although WDM is able to reduce the number of structures at small scales, it is still not sufficient to explain the discrepancy with observations. I will also present the main differences between a group of galaxies simulated within a ΛCDM and a ΛWDM context.

In Chapter 7 I will focus on the *abundance matching* technique in the Local Group. Using the halo mass function derived from Local Group simulations, like the CLUES ones, it is possible to extend the relation between stellar mass and halo mass down to the faintest galaxies, like the dSphs. This relation indicates that the vast majority of the Local Group galaxies live into dark matter haloes whose mass is bigger than $\geqslant 10^{10}\mathrm{M}_{\odot}$: to reconcile observational data with such a prediction one has to assume that some of these galaxies have a central dark matter core, i.e. their halo is expanded.

The expansion of dark matter haloes and the *cusp/core* problem will be at the center of the second part of my thesis, in which I will use the hydrodynamical simulations from the MaGICC[2] project, that include a physical motivated feedback model. These galaxies provide an excellent match to the stellar-to-halo mass relation both at z=0 and at higher redshift (Kannan et al. 2013), as well as to a range of present observed galaxy properties and scaling relations (Brook et al. 2012b; Stinson et al. 2013).

In Chapter 8 and 9 I will describe how the *cusp/core* transformation depends solely on the $M_{\star}/M_{\mathrm{halo}}$ ratio of each galaxy, and how such prediction can be used to make comparison with observational data. Moreover, I will derive a density profile able to reproduce a cored as well as a cuspy dark matter distribution in galaxies, so that it is appropriate to describe both dwarfs and spiral galaxies. This profile is completely constrained by the integrated star formation efficiency within each galaxy, $M_{\star}/M_{\mathrm{halo}}$ at z=0, and it represents a notable improvement with respect to the usual NFW profile, which, being derived from N-body simulations, does not take into account baryonic physics.

The complete description of the simulations used in this thesis will be given in Chapter 2, while Chapter 10 will be devoted to the conclusions and the future prospective.

[2] http://www.star.uclan.ac.uk/$\sim$cbb/magicc.html

Chapter 2

Simulations

In this section we present the cosmological, numerical simulations of galaxy formation used in this thesis. The first set of simulation, used in the studies presented in Chapters from 3 to 7, are part of the CLUES[1] project. The other set of simulation, used in Chapter 8 and 9, belong to the MaGICC[2] project.

2.1 CLUES simulation

The Local Group (LG) of Galaxies and its environment is the most well observed region of the Universe. Only in this unique environment we can study structure formation on scales as small as that of very low mass dwarf galaxies, resulting in the so-called near-field cosmology.

The Constrained Local UniversE Simulations, CLUES project (Gottlöber et al. 2010), are a series of constrained cosmological numerical simulations whose primary goal is to reproduce the observed large scale structures in the Local Universe, such as the local cosmic web, the Local Supercluster, the Virgo cluster, the Coma cluster, the Great Attractor and the Perseus-Pisces supercluster.

2.1.1 Initial conditions and Local Group selection

Initial conditions based on observational data of the nearby Universe have been used as constraints, in such a way that the resulting simulations closely reproduce the observed Local Universe on scales larger than

[1] http://www.clues-project.org

[2] http://www.star.uclan.ac.uk/∼cbb/magicc.html

$\approx$5 h^{-1} Mpc (Klypin et al. 2003), while the structures at smaller scales are hardly affected by the constrained initial conditions, being essentially random. The CLUES project enable to simulate structures at megaparsec and sub-megaparsec scale within the correct environment. The Local Group and its galaxies, particularly Milky Way-type objects and associated satellites, can then be studied within a preferential environment defined by the position and velocity relative to a Virgo-like cluster. Such simulations therefore serve as the ideal tool for comparing the predictions of theoretical models of galaxy formation, provided that such galaxies are embedded in the "correct" environment determined by observations.

The technique known as *constrained realizations* consists in the implementation of the Hoffman-Ribak algorithm (Hoffman & Ribak 1991), which is used to generate the initial conditions as constrained realizations of Gaussian random fields from observational data. Different observational data are used to set up the initial conditions. The first set is composed of radial velocities of galaxies drawn from the Mark III Catalog of Galaxy Peculiar Velocities (Willick et al. 1997), the surface brightness fluctuation (SBF) survey of galaxy distances (Tonry et al. 2001) and the Karachentsev (Karachentsev et al. 2004) catalog of neighboring galaxies. Peculiar velocities are less affected by non-linear effects and are used as constraints as if they were linear quantities. The other constraints are obtained from the catalog of nearby X-ray selected clusters of galaxies (Reiprich & Böhringer 2002): given the virial parameters of a cluster and assuming the spherical top-hat model one can derive the linear overdensity of the cluster, which is then imposed on the mass scale of the cluster itself as a constraint.

As already explained, since these data only constrain scales larger than a very few Mpc, it is necessary to perform a series of different realizations in order to obtain one which contains a LG candidate with the correct properties, such as two main haloes resembling Milky Way and Andromeda galaxy, with proper position relative to each-other, correct masses , negative radial velocity, etc. More than 200 realizations of low resolution simulations, with 256^3 particle, were performed and evolved since the starting redshift z=50 until present time z=0 and the one with the most suitable Local Group-like object was chosen for follow up, high resolution re-simulations. To find a LG candidate we first identify in the constrained simulation the Virgo cluster. Then we search for an object which closely resembles the Local Group and which is in the right direction and distance to Virgo.

High resolution extension of the low resolution constrained realizations were then obtained by creating an unconstrained realization at the desired resolution, FFT-transforming it to k-space and substituting the unconstrained low k modes with the constrained ones. The resulting simulation

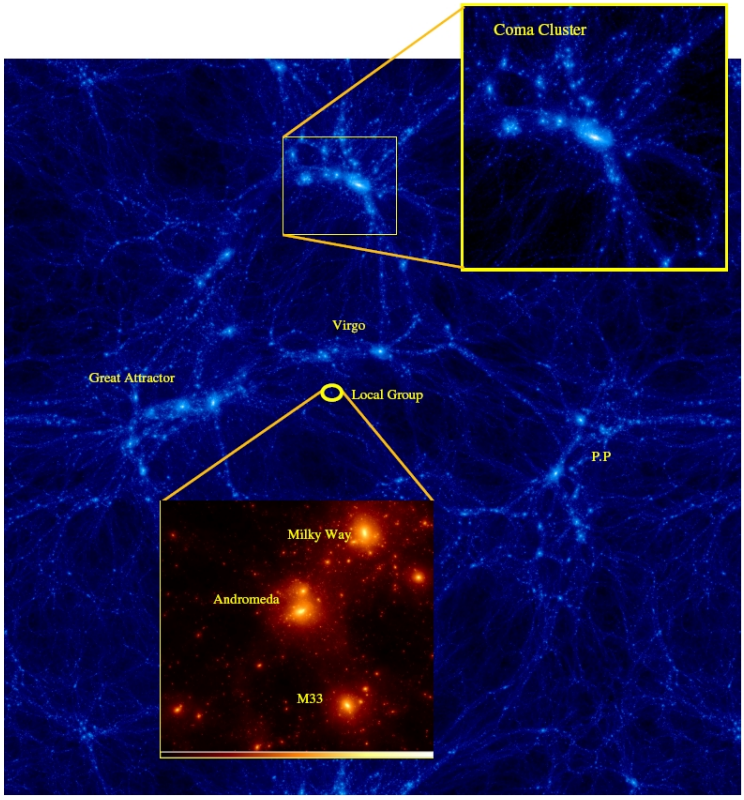

Figure 2.1: Dark matter distribution within the CLUES Local Universe. Credit: CLUES collaboration.

is thus composed of unconstrained high k modes (small scales) and fully constrained low k modes (large scales). Using this technique, we are able to both accurately constrains the super-LG scales while artificially selecting sub-LG scales as those most resembling the real LG.

We used the MPI treePM N-body + SPH code Gadget2, developed by Springel (2005), to simulate the evolution of a cosmological box with side length of $L_{box} = 64h^{-1}$ Mpc. As mentioned above the region of interest around the LG has been resimulated using high resolution. We used a full resolution of 4096^3 effective particles within a sphere of just $2h^{-1}$ Mpc centered on the LG, with a dark matter particle mass of $m_{\rm DM} = 2.95 \times 10^5 h^{-1}{\rm M}_\odot$. Exterior to the high resolution LG, the simulation box is filled with lower resolution (higher mass) particles. Fig. 2.1 shows the large scale dark matter density distribution of the Local Universe simulation, with a circle showing the position of our Local Group, and a smaller panel showing the detailed structure of the simulated Local Group.

Within the CDM scenario, we used two sets of cosmological parameters, according to a WMAP3 (Spergel et al. 2007) and a WMAP5 (Komatsu et al. 2009) cosmologies. The WMAP3 parameters are $\Omega_m = 0.24$, $\Omega_b = 0.042$, $\Omega_\Lambda = 0.76$, a normalization of $\sigma_8 = 0.73$ and a slope of the power spectrum of $n = 0.95$. The WMAP5 parameters are $\Omega_m = 0.279$, $\Omega_b = 0.046$, $\Omega_\Lambda = 0.721$, a normalization of $\sigma_8 = 0.817$ and a slope of the power spectrum of $n = 0.96$.

We use the same set of initial conditions to run two simulations, a DM only, pure N-body run and a SPH run which includes gas dynamics, cooling, star formation and supernovae feedback as in Springel & Hernquist (2003). Gas particles are included in the initial conditions by replacing each high resolution dark matter particle by an equal mass, gas-dark matter particle pair with a with a mass ratio of roughly 1:5. The dynamics of gas particles are then determined by using the lagrangian method of Smoothed Particle Hydrodynamics, built into Gadget2. The gravitational softening length is $\epsilon = 0.1h^{-1}$ kpc in both the DM only and the SPH run.

Within this environment we identified haloes and subhaloes using the AMIGA halo finder, AHF, better described in Section 2.3. The main haloes identified in the CLUES simulations formally correspond to the Milky Way and the Andromeda galaxy, whose main properties will be fully described in the next chapters of this thesis.

In Fig.2.2 we show the gas distribution within the Local Group around the three main galaxies representing the Milky Way (MW), Andromeda (M31) and the Triangulum galaxy (M33). The size of the plot is about $2h^{-1}$ Mpc across, viewed from a distance of $3.3h^{-1}$ Mpc. Within the three smaller panels we show the gas disks of such galaxies as seen from a distance of $250h^{-1}$ kpc, the size of the plot being about $50h^{-1}$ kpc. The M31 and MW disks are smaller than the disk of M33 due to major mergers which these objects had recently ($\sim$ z=0.6). The spiral features of the MW are clearly visible. Dark colors indicate low density of the gas and bright colors high density regions. The colors and density range are adjusted such that the faint structures and filaments connecting the three main galaxies, and the spiral arm features of the gas disks become visible.

To summarize, we have at our disposal a DM-only and a corresponding SPH simulation of a zoomed-in region of $2h^{-1}$ Mpc around the LG, performed within the concordance CDM model using two different sets of cosmological parameters, based on WMAP3 and WMAP5 results.

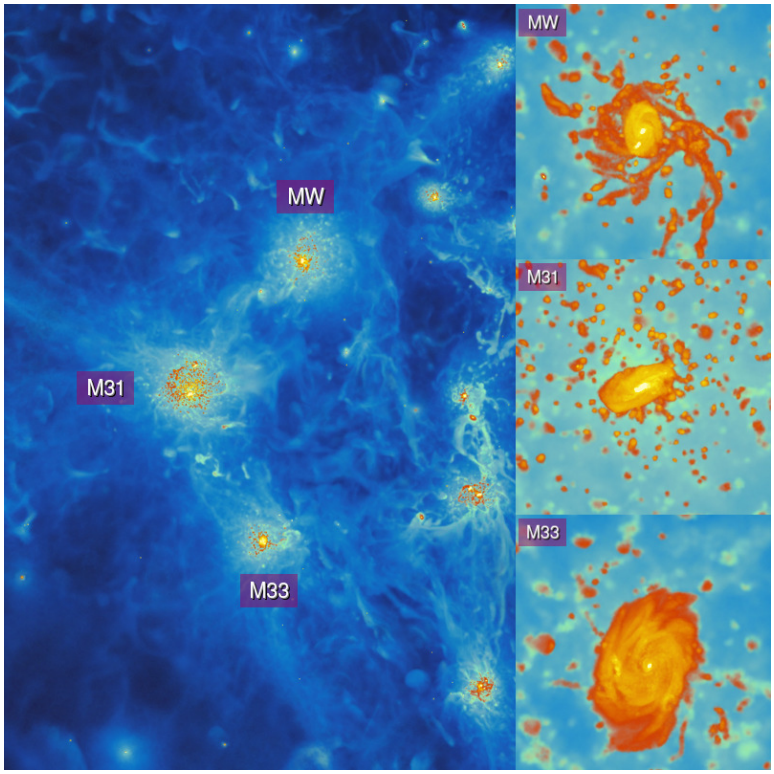

Figure 2.2: The gas distribution in the simulated CDM Local Group, for a WMAP3 cosmology. Smaller panels represent MW, M31 and M33. Credit: A. Khalatyan, using PMViewer *http://pmviewer.sourceforge.net*.

2.1.2 Star formation and feedback

In the SPH run we use the star formation and feedback rules of Springel & Hernquist (2003).

The interstellar medium (ISM) is modeled as a two phase medium composed of hot ambient gas and cold gas clouds in pressure equilibrium. The thermodynamic properties of the gas are computed in the presence of a uniform but evolving ultra-violet cosmic background generated from QSOs and AGNs and switched on at z=6 (Haardt & Madau 1996). Cooling rates are calculated from a mixture of a primordial plasma composition. No metal dependent cooling is assumed (this is slightly inconsistent as gas particles are metal enriched due to supernovae explosions). We assume that cold gas cloud formation by thermal instability, star formation, the evaporation of gas clouds, and the heating of ambient gas by supernova driven winds all occur at the same instant. Each star formation event injects energy and metals into the ISM instantaneously.

We treat star formation stochastically, in order to reproduce the Kennicut-Schmidt law for spiral galaxies (Kennicutt, 1983, 1998). The first time a gas particle undergoes star formation, we create a star particle of half the gas particle's mass, reducing the gas particle's mass appropriately. The second episode of star formation results in the gas particle converting all its remaining mass into a star particle. Thus all star particles (first and second generations) have the same mass of $m_{\rm STAR} = 2.21 \times 10^4 h^{-1}{\rm M}_\odot$while gas particles have either their full original mass of $m_{\rm GAS} = 4.42 \times 10^4 h^{-1}{\rm M}_\odot$, or half their original mass.

We assume kinetic feedback in the form of strong winds driven by SNe explosions using the stochastic approach developed by Springel & Hernquist (2003). All SPH particles in the vicinity of the star forming regions participate in the wind in a probabilistic way that is proportional to the star formation rate and the amount of supernova energy released by massive stars. We assume that a fraction of stars will explode as Supernovae. A fraction of this energy is then used to energize, kick, particles in the high density regions surrounding sites of star formation. This kinetic feedback removes low angular momentum gas from the center of DM haloes, thus allowing the formation of extended gaseous disk by preventing the so-called "overcooling problem". This mechanism has been tested and found it to be crucial in the production of stable disks containing both gas and stars.

Each star is given the metallicity of the gas particle that spawned it. We calculate a luminosity by using the stellar population synthesis model STARDUST (see Devriendt et al. (1999) and references therein). This model computes the spectral energy distribution from the far-UV to the

radio, for an instantaneous starburst of a given mass, age and metallicity. The stellar contribution to the total flux is calculated assuming a Kennicutt initial mass function (Kennicutt 1998).

2.1.3 Cold versus Warm Dark Matter CLUES

In addition to these simulations, and for the WMAP3 case, we also performed a DM+SPH run assuming a warm dark matter (WDM) scenario, specifically using a particle with m_{WDM}= 1 keV.

Within the WDM model initial perturbations below a certain mass can not collapse and the smallest structures to form out of gravitational instabilities are fairly large. This happens because the temperature of the DM particle at decoupling, specifically, whether it was relativistic or not, can cause the DM particle to escape from and erase the underlying density fluctuation. Particles with a keV mass (WDM) would become non-relativistic much later than particles with GeV-TeV mass (CDM), therefore having a bigger free-streaming length: in fact, WDM particles have a free-streaming length similar to a protogalaxy, and they are able to inhibit the formation of small structures by gravitational collapse.

In Fig. 2.3 we show the linear matter power spectrum used to set up initial conditions for the CDM and WDM models with particle mass of $\sim$1 keV, as a function of wavenumber . The k interval actually used to generate the realizations of the initial conditions is also shown, from $k = 2\pi/B$ to $k = N^{1/3}\pi/B$ where $B = 64h^{-1}$ Mpc and $N = 4096^3$. The initial conditions are generated by rescaling the CDM power spectrum and fitting it with an approximation to the transfer function representative of the free streaming effect of WDM particles (Viel et al. 2005). The free-streaming length of such a WDM particle is $0.35h^{-1}$ Mpc, which corresponds to a filtering mass of $1.1 \times 10^{10}h^{-1}\mathrm{M}_{\odot}$ (Bode et al. 2001): the WDM power spectrum, shown in Fig. 2.3, thus contains a sharp cut-off at the corresponding wavelength k free-streaming length. Smaller WDM particle masses would result in a greater suppression of the power spectrum on small scales (large k).

A comparison of the properties of MW, M31 and M33 alongside CDM and WDM simulations will be presented in Chapter 6.

2.1.4 Previous results with CLUES

The CLUES simulations have already been extensively used to study details of the Local Group of galaxies. Some of the results based on CLUES include the study of radial distribution (Libeskind et al. 2010) and radial

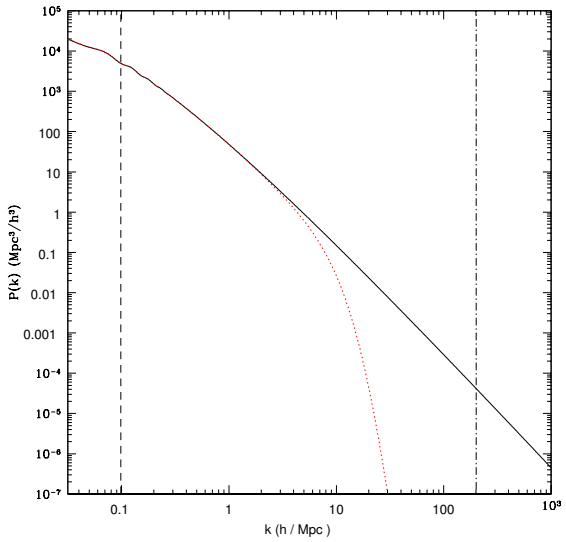

Figure 2.3: Cold (black) and warm (red) dark matter power spectrum. Credit: CLUES collaboration.

alignment of substructures (Knebe et al. 2010), the preferential infall of satellite galaxies (Libeskind et al. 2011b), the luminosities of backsplash galaxies (Knebe et al. 2011c,b), the differences between the stellar and DM halo (Libeskind et al. 2011a), the assembly properties of the Local Group (Forero-Romero et al. 2011), the the Milky Way and Andromeda progenitors visible as Lyman Alpha emitters (Dayal & Libeskind 2012) and the large scale structures' formation using a catalog of peculiar velocities (Sorce et al. 2014).

More recent studies using the CLUES simulations will be discussed through this thesis.

2.2 MaGICC simulation

The Making Galaxies in a Cosmological Context (MaGICC) project (Stinson et al. 2013; Brook et al. 2012b) is a series of numerical hydrodynamical simulation of isolated galaxies, devoted to reproduce the main observational features of galaxies spamming a wide range of masses, from dwarf size to Milky Way-like objects, i.e. low, medium and high mass galaxies.

Previous generation of hydrodynamical simulations have failed at repro-

ducing the main properties of galaxies, such as the stellar mass versus halo mass relation and the angular momentum of spirals. These issues are often referred as *overcooling problem* and the *angular momentum catastrophe*.

The main goal of the MaGICC simulations is to produce realistic galaxies, which lie on the $M_\star/M_{\rm halo}$ relation (Guo et al. 2010; Moster et al. 2010), by use of physically motivated recipes for star formation and feedback.

2.2.1 Initial conditions from MUGS simulations

The initial conditions for the galaxies are taken from the McMaster Unbiased Galaxy Simulations (MUGS), which is described in Stinson et al. 2010. MUGS is a sample of 16 zoomed-in regions where $\sim$L* galaxies form in a cosmological volume 68 Mpc on a side. MUGS used a ΛCDM cosmology with H_0= 73 km s^{-1} Mpc^{-1}, $\Omega_{\rm m}$ = 0.24, Ω_Λ = 0.76, $\Omega_{\rm bary}$ = 0.04 and σ_8 = 0.76 (WMAP3, Spergel et al. 2007).

Initially, galaxies are selected from a cosmological cube of 68 Mpc on a side containing 256^3 dark matter particles evolved to z=0. Some specific region of such a cosmological volume are then selected in order to be resimulated with higher resolution, while the surrounding volume provides the large scale density waves and impart tidal torques on the region of interest (Quinn & Binney 1992). The regions chosen for higher resolution are the ones with a mass between 5×10^{11}M$_\odot$ and 2×10^{12}M$_\odot$ which evolved at least 2.7 Mpc away from any halo more massive than 5×10^{11}M$_\odot$. Out of the 36,193 haloes found with friends-of-friends, 761 were in the right mass range, and 276 of those were sufficiently isolated. From this sample, 9 haloes are randomly selected regardless of spin parameter or merger history. Finally, particles within $5R_{\rm vir}$ of each group's center at z=0 were traced to their positions in the initial conditions, and the central region was filled with a regular grid of particles to achieve an effective resolution of 2048^3 at the center. Surrounding the non-spherical central region is a spherical region with a radius 1.2 times the maximum radius of the central region. This immediately surrounding region is populated with particles for an effective resolution of 512^3. Outside this are three spherical regions equally spread in radius with effective resolutions of 256^3, 128^3, and 64^3. The outskirts of the 68 Mpc cube are filled at an effective resolution of 32^3. Each of these regions contains progressively more massive particles corresponding to the reduced resolution. In the high resolution region, dark matter particles have a mass of 1.1×10^6M$_\odot$. The regular grids of particles in each region were perturbed using the Zel'dovich approximation with subsampled force resolutions matching the particle resolutions. This dark matter-only configuration was evolved to z=0.

The initial conditions of the medium and low mass galaxies are scaled down variants of such high mass ones, so that rather than residing in a 68 Mpc cube, they lie within a cube with 34 Mpc sides (medium) or 17 Mpc sides (low mass). This rescaling allows us to compare galaxies with exactly the same merger histories at three different masses. Differences in the underlying power spectrum that result from this rescaling are minor (Springel et al. 2008; Maccio' et al. 2008; Kannan et al. 2012). This assures us than any result derived from such sample will not be driven by the specific merger history. These DM-only runs exhibit a wide range of concentrations, from those typical of the L* to dwarf galaxies.

In addition to the collisionless, dark matter-only simulations we performed hydrodynamical, SPH simulations for each initial condition. Within the 68 Mpc box the gas particles have an initial mass of $2.2 \times 10^5 M_\odot$, while stars form with a mass of $6.3 \times 10^4 M_\odot$.

Each particle uses a gravitational softening length of 312.5 pc. Our galaxies were simulated using GASOLINE (Wadsley et al. 2004), a fully parallel, gravitational N-body + smoothed particle hydrodynamics (SPH) code. Cooling via hydrogen, helium, and various metal-lines in a uniform ultraviolet ionizing background is included as described in Shen et al. (2010).

2.2.2 Star formation and feedback

The hydrodynamical simulations use the stochastic star formation recipe described in Stinson et al. (2006), in such a way that, on average, they reproduce the empirical Kennicut-Schmidt Law (Schmidt 1959; Kennicutt 1998).

Gas is eligible to form stars when it reaches temperatures below T=15000 K and it is denser than $n > n_{\rm th}$. Two different density thresholds are used for star formation, $n_{\rm th}$=0.1 and 9.3 cm^{-3}, which is the maximum density at which gravitational instabilities can be resolved ($32 m_{gas}/\epsilon^3$) . Gas denser than n_{th} is then converted to stars in a probabilistic manner according to the Kennicut-Schmidt law:

$$\frac{\Delta M_\star}{\Delta t} = c_\star \frac{m_{\rm gas}}{t_{\rm dyn}} \tag{2.1}$$

where $\Delta M_\star$ is the mass of the stars formed in Δt, the time between star formation events (0.8 Myr in these simulations), $m_{\rm gas}$ is the mass of the gas particle, $t_{\rm dyn}$ is the gas particle's dynamical time, and $c_\star$ is the fraction of gas that will be converted into stars during $t_{\rm dyn}$. $c_\star$ is ultimately the free

parameter that sets the balance of the baryon cycle off cooling gas, star formation, and gas heating. In the fiducial runs $c_\star = 0.17$.

Stars feed energy back into surrounding gas. In hydrodynamical simulations, two methods are commonly used to model stellar feedback. One is kinetic feedback, which consists in adding velocity kicks to gas particles to remove them from the inner regions of galaxy disks (Springel & Hernquist 2003). The other method is thermal feedback, in which stars simply heat the gas particles around them and allow the adiabatic work of the particles to push other gas out of the way (Stinson et al. 2006).

Type II Supernovae (SNII) prevent more gas from collapsing, effectively regulating star formation in our simulations because of their ability to heat volumes of the interstellar medium near the site of star formation (Silk 2003) Since the blastwave shocks of SNII convert the kinetic energy of ejecta into thermal energy on scales smaller than our simulations resolve, feedback in our simulations is purely thermal. The number of supernovae produced by a star particle depends on the initial mass function of the stars that form, and in our simulations we use two different IMF, a Kroupa IMF (Kroupa et al. 1993) and a Chabrier one (Chabrier 2003). The Chabrier IMF produces two times more type SNII per mass of stars born.

Supernova feedback is implemented using the Stinson et al. (2006) blastwave formalism, depositing $\mathrm{E_{SN}} \times 10^{51}$ erg into the surrounding ISM at the end of the lifetime of stars more massive than $8\,\mathrm{M}_\odot$. The blastwave solution, based on Chevalier (1974) and McKee & Ostriker (1977), provides the maximum radius to which the blastwave explosion will extend as well as the maximum time that the blastwave will keep the surrounding gas hot. Since stars form in dense regions, the cooling times of the gas are short and the gas will quickly radiate away all the supernova energy due to the efficient cooling (Katz 1992). For this reason, cooling is disabled for particles inside a blast region of size $R = 10^{1.74} E_{51}^{0.32} n_0^{-0.16} P_{04}^{-0.20}$pc and for the length of time $t = 10^{6.85} E_{51}^{0.32} n_0^{0.34} P_{04}^{-0.70}$yr. Here, $E_{51} = 10^{51}$erg, n_0 is the ambient hydrogen density, and $P_{04} = 10^{-4} P_0 k^{-1}$, where P_0 is the ambient pressure and k is the Boltzmann constant. Both n_0 and P_0 are calculated using the SPH kernel for the gas particles surrounding the star.

Metals are ejected from Type II supernovae (SNeII), Type Ia supernovae (SNeIa), and the stellar winds driven from asymptotic giant branch (AGB) stars, and distributed to the nearest gas particles using the smoothing kernel (Stinson et al. 2006). The metals can diffuse between gas particles as described in (Shen et al. 2010).

2.2.3 Early stellar feedback

In addition to the common supernovae feedback, radiation energy from massive stars is also considered in order to provide a more complete model of stellar feedback.

The energy from high mass stars is introduced immediately after stars form based on how much star light is radiated.

Such energy could be considered using a kinetic scheme where the radiation pressure drives winds out of massive star clusters (Hopkins et al. 2011). However a kinetic implementation of feedback requires many particles to represent a molecular cloud, resolution that we do not have within the MaGICC simulations, in which only one or a few particles represent a molecular cloud. Therefore the isotropic thermal pressure is used.

During the 4.5 Myr after stars form and before the first supernova explodes, such thermal feedback from young, massive stars is implemented using a fraction, $\epsilon_{\rm esf}$, of the total luminosity emitted by the stars. The luminosity of stars is modelled with a simple fit of the mass-luminosity relationship observed in binary systems (Torres 2010):

$$\frac{L}{L_\odot} = \begin{cases} (M/\mathrm{M}_\odot)^4, & M < 10\,\mathrm{M}_\odot \\ 100\,(M/\mathrm{M}_\odot)^2, & M > 10\,\mathrm{M}_\odot \end{cases} \tag{2.2}$$

Typically, this model corresponds to the emission of 2×10^{50} erg per $\mathrm{M}_\odot$ of the entire stellar population over the $\sim$4.5 Myr between a star's formation and the commencement of SNeII in the region. These photons do not couple efficiently with the surrounding ISM (Freyer et al. 2006). To mimic this highly inefficient energy coupling, we inject $\epsilon_{\rm esf}$ of the energy as thermal energy in the surrounding gas.

Such thermal energy injection is highly inefficient at the spatial and temporal resolution of cosmological simulations (Katz 1992; Kay et al. 2002), as the characteristic cooling timescales in the star forming regions are lower than the dynamical time. Since massive young stars radiate a large amount of energy cooling is *not* turned off: after heating the gas to $T > 10^6 K$, the gas rapidly cools down to $10^4 K$, which creates a lower density medium. Though the dynamical effect is minimal, early stellar feedback effectively halts star formation in the region immediately surrounding a recently formed star, providing pressure support and increasing gas temperatures above the star formation threshold to decrease star formation. Using $\epsilon_{\rm esf} = 10\%$ limits star formation to the amount prescribed by the stellar-to-halo mass relationship.

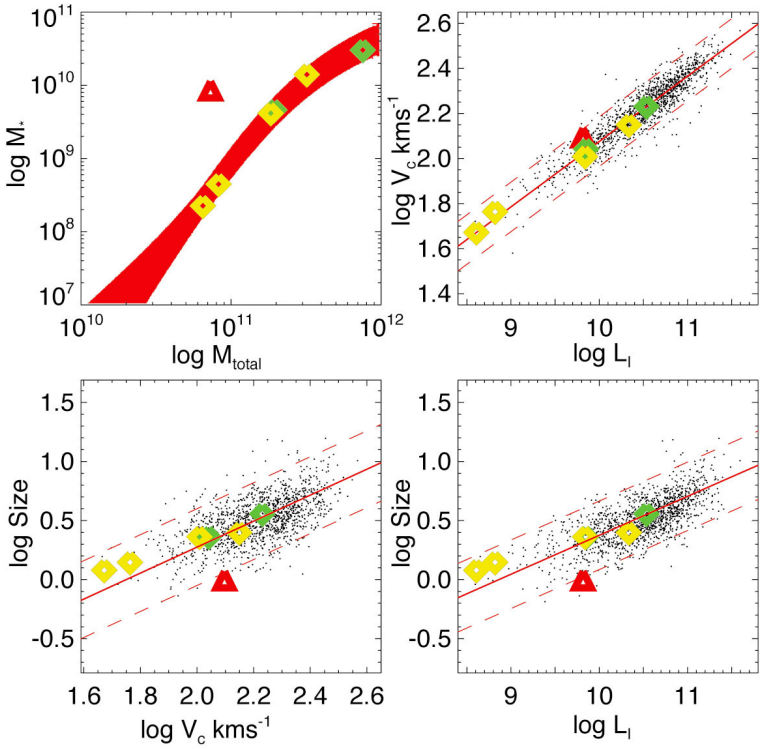

Figure 2.4: Scaling relations of the simulated galaxies superimposed on observational data from Courteau et al. (2007). From top left to bottom right: the stellar mass against total mass; the rotational velocity against luminosity in the I-band (the Tully-Fisher relation); the disc scale-length against luminosity; the disc scale-length against rotational velocity. Credit: Brook et al. (2012b)

2.2.4 Previous results with MaGICC

It has been shown in Brook et al. (2012b) that the MaGICC simulations are able to reproduce a variety of scaling relations of galaxies spanning a wide range in masses. We show such scaling relations in Fig. 2.4, where the fiducial runs are shown as yellow diamonds, the low resolution runs as green diamonds and the low feedback run as a red triangle. The low feedback case was run with a star formation threshold of 1 cm^{-3}, a Kroupa et al. (1993) IMF, 0.4×10^{51} erg deposited per supernova explosion and without early stellar feedback. It is evident how this low feedback model, which is comparable to most of the feedback implementations currently in the literature (Scannapieco et al. 2012), is not sufficient to reproduce properties of observed galaxies.

The fiducial feedback, instead, includes a Chabrier (2003) IMF, a 1×10^{51}

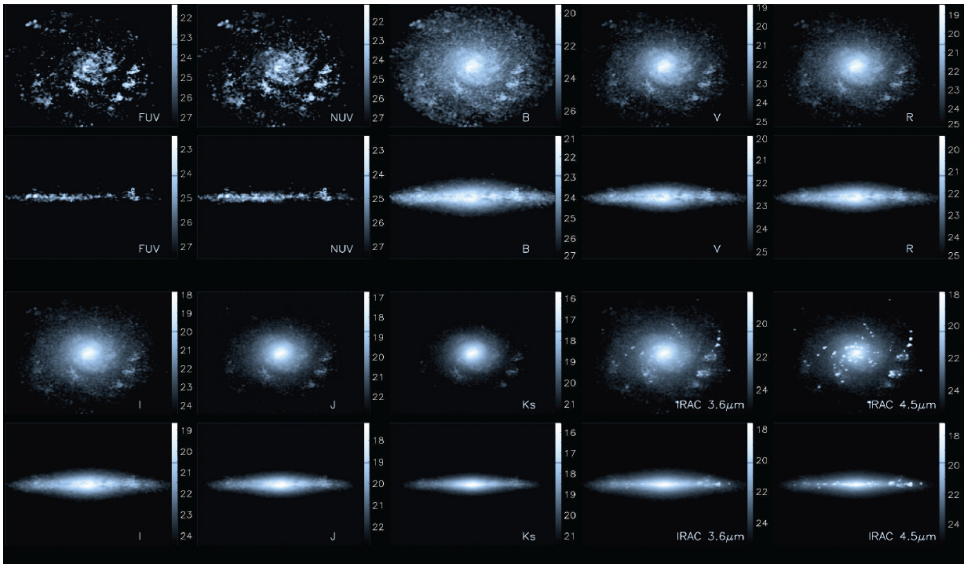

Figure 2.5: Face-on and edge-on images of the fiducial galaxy at z=0 in 8 different bands. The images are 50 kpc on a side and were obtained using the radiative transfer code `GRASIL` (Domínguez-Tenreiro et al. 2014), which includes a careful modelling of the dust component of the interstellar medium. Credit: Aura Obreja & Rosa Domínguez-Tenreiro.

erg from SNe, a $n_{th} = 9.3\mathrm{cm}^{-3}$ and 10% of early stellar feedback: it provides a perfect match to several galaxy properties. In Fig. 2.5 a galaxy of $M_\star = 2.3 \times 10^{10}\mathrm{M}_\odot$ is shown, run with such fiducial feedback. The recent transfer code `GRASIL` (Domínguez-Tenreiro et al. 2014) has been used for this image.

The MaGICC simulations, firstly run in the 2012, have been extensively used in the past two years to produce a number of studies, amongst which: the baryon cycle within galaxies (Brook et al. 2013b), the lowest metallicity stars in the LMC (Brook et al. 2013a), the effect of dark energy on galaxy formation (Penzo et al. 2014), the statistical properties of high-redshift galaxies (Kannan et al. 2012), the effects of warm dark matter in hydrodynamical simulations (Herpich et al. 2014) and the fundamental metallicity relation of galaxies (Obreja et al. 2014).

Other results coming from the MaGICC simulations will be discussed through this thesis.

2.3 AHF halo finder

In order to identify haloes and subhaloes in our simulation, both the CLUES and MaGICC ones, we have run the MPI+OpenMP hybrid halo finder AHF[3] described in detail in Knollmann & Knebe (2009). AHF is an improvement of the MHF halo finder (Gill et al. 2004a), which locates local overdensities in an adaptively smoothed density field as prospective halo centers. We would like to stress that our halo finding algorithm automatically identifies haloes, sub-haloes, sub-subhaloes, etc. and it can reliably recover substructures containing at least 30 particles (Knebe et al. 2011a). As each pair of simulations, N-body and SPH, starts with the same initial conditions (apart from the baryons) we can match individual haloes and subhaloes in the DM only simulation with a "sister" halo (subhalo) in the SPH run (see Libeskind et al. 2010). In fact, this cross identification pairs subclumps at z=0 that originated from the same overdensity in the initial conditions. The AHF MergerTree package is used to identify corresponding objects in the same simulation at different redshifts. We follow each halo (either host or subhalo) identified at redshift z=0 backwards in time, identifying as the main progenitor the halo that both shares the most particles with the present halo and is closest in mass. Subhaloes will be followed correctly along their orbits within the environment of their respective host until the point where they either are tidally destroyed or directly merge with the host. For more details on the mode of operation and actual functionality we though refer the reader to the code description paper by Knollmann & Knebe (2009), while an in-depth comparison to other halo finding techniques can be found in Knebe et al. (2011a) and Onions et al. (2012).

2.3.1 Haloes and subhaloes definition

The virial mass of each halo is defined as the mass of a sphere containing Δ times the critical matter density of the Universe $\rho_{crit} = 3H^2/8\pi G$ at z=0. Typical choices of Δ are $\Delta_{200} = 200$ or $\Delta_{\rm vir} = 18\pi^2 + 82x - 39x^2$ at z=0 (Bryan & Norman 1998), where $x = \Omega_m - 1$ depends on the selected cosmology. The corresponding halo mass will thus be defined as:

$$M = \frac{4}{3}\pi R^3 \Delta \rho_{crit} \tag{2.3}$$

where M and R indicate M_{200} and R_{200} or $M_{\rm vir}$ and $R_{\rm vir}$, according to the overdensity criterion.

[3] AMIGA halo finder, to be downloaded freely from http://www.popia.ft.uam.es/AMIGA

Subhaloes are defined as haloes which lie within the virial radius of a more massive halo, the so-called host halo. As subhaloes are embedded within the density of their respective host halo, their own density profile usually shows a characteristic upturn at a radius $r_t < r_{\rm vir}$, where $r_{\rm vir}$ would be their actual virial radius if they were found in isolation: we therefore calculate subhaloes properties using particles within such radius r_t.

Chapter 3

Massive, dense dark matter subhaloes of the Milky Way

Using Constrained Local UniversE Simulations (CLUES) of the formation of the Local Group in a cosmological context we investigate the recently highlighted problem that the majority of the most massive dark subhaloes of the Milky Way are too dense to host any of its bright satellites (Boylan-Kolchin et al. 2011). In particular, we examine the influence of baryonic processes and find that they leave a twofold effect on the relation between the peak of the rotation curve and its position ($V_{\rm max}$ and $R_{\rm max}$). Satellites with a large baryon fraction experience adiabatic contraction thus decreasing $R_{\rm max}$ while leaving $V_{\rm max}$ more or less unchanged. Subhaloes with smaller baryon fractions undergo a decrease in $V_{\rm max}$ possibly due to outflows of material. Furthermore, the situation of finding subhaloes in simulations that lie outside the confidence interval for possible hosts of the bright MW dwarf spheroidals, appears to be far more prominent in cosmologies with a high σ_8 normalisation and depends on the mass of the host. We conclude that the problem cannot be simply solved by including baryonic processes and hence demands further investigations.

3.1 Introduction

The Λ Cold Dark Matter (ΛCDM) model, first explored more than two decades ago (Davis et al. 1985), has been very successful in explaining a multitude of observations at cosmological scales, such as anisotropies of Cosmic Microwave Background radiation (CMB) Jarosik & et al. (e.g. 2011) and galaxy clustering on large scales (e.g. Cole & et al. 2005). However, on smaller, galactic scales the tests of the ΛCDM model are complicated by

the baryonic physics involved in galaxy formation. Therefore, testing the currently accepted concordance model at these scales is necessary in order to not only understand the nature of dark matter but also the accuracy of the model itself.

The validity of the ΛCDM model on galactic scales is still being questioned due to the discrepancy between the number of observed satellites and the number of predicted dark matter subhaloes. High resolution simulations of galactic-size haloes resolve a substantial number of substructures within the virial radius, as first pointed out by Klypin et al. (1999a) and Moore et al. (1999), and recently reviewed by Kravtsov (2010) and Bullock (2010).

The most popular interpretation of this so-called "Missing Satellite Problem" requires that the smallest dark matter haloes are inefficient at forming stars (e.g. Bullock 2010; Kravtsov 2010). Mechanisms such as early reionization of the intergalactic medium and supernovae feedback have been invoked to identify the halo mass scale where the galaxy formation starts to be inefficient (Bullock et al. 2000; Somerville 2002; Benson et al. 2002), partially solving the problem. Furthermore, the detection of satellites is most certainly biased because of current detection limits (Tollerud et al. 2008; Walsh et al. 2009).

There is yet another aspect of the satellite population that needs to be addressed: the mismatch between the predicted and inferred distribution of $V_{\rm max}$ values at the high-$V_{\rm max}$ end as recently highlighted by Boylan-Kolchin et al. (2011), where $V_{\rm max}$ measures the peak of the rotation curve of subhaloes. Using the Aquarius simulations (Springel et al. 2008) and the Via Lactea II simulation (Diemand et al. 2008) they found that the majority of the most massive subhaloes (i.e. the high-$V_{\rm max}$ objects) of the Milky Way are too dense to host any of its bright satellites.

There are a number of ways in which this discrepancy may be resolved: the subhalo mass function of the Milky Way could be a statistical anomaly with respect to the ΛCDM expectations (Liu et al. 2010; Guo et al. 2011), or the fundamental assumption that the luminosities of the satellites are not monotonically related to the mass of the subhaloes does not hold true.

In response to the claims by Boylan-Kolchin et al. (2011), Lovell et al. (2012) explored the possibility that warm rather than cold dark matter can provide a better match to the inferred distribution of satellite circular velocities. With a power spectrum suppressed at masses below $\sim 10^{10} M_{\odot}$ (corresponding to a warmon mass of 2 keV), they found that a warm dark matter model naturally produces haloes that are less concentrated than their cold dark matter counterparts. The attempt to explain the evolution of small scale structures in the local universe with a ΛWDM model was

already presented in Tikhonov et al. (2009). However, this is only one possible solution to the problem.

Baryonic processes will most certainly also affect the dark matter distribution. Blumenthal et al. (1986) showed that dissipative baryons will lead directly to the adiabatic contraction of the halo increasing its central density, thus being a critical ingredient to determine subhalo properties. However, the possibility that the influence of baryons will lead to a flattening of the dark matter central density cusp (through dynamical friction of infalling substructures composed of dark matter *and* baryons) has, for instance, been suggested by El-Zant et al. (2001) and further studied in Romano-Díaz et al. (2008). Another way in which the haloes' density can be reduced is through sudden mass outflows that can alter substantially the central structure, as suggested by Navarro et al. (1996a). In a recent work of Parry et al. (2012) this last scenario has been tested by following the evolution of one simulated satellite, with promising results. The same authors though also showed that the inclusion of baryons in simulations does not seem to have any correlation with the increase or decrease of the dark matter central density.

In this work we directly address the issue of the $V_{\rm max}$ problem in ΛCDM simulations by comparing two identical simulations with each other: one that is solely based upon dark matter physics and another incorporating all the relevant baryonic physics. These simulations form part of the CLUES project[1], in which the initial conditions are set by imposing constraints derived from observational data of the Local Group. The main feature of using constrained simulations is that it provides a numerical environment that closely matches our actual neighborhood.

3.2 Simulation details

In this work we use high resolution, constrained simulations of the Local Group run with a WMAP3 cosmology, with a dark matter particle mass of $m_{\rm DM} = 2.1 \times 10^5 h^{-1}{\rm M}_\odot$. For this particular study we further use a gas dynamical SPH simulation started with the same initial conditions, in which we additionally follow the feedback and star formation rules of Springel & Hernquist (2003). The gas particle mass in this case is $m_{\rm gas} = 4.42 \times 10^4 h^{-1}{\rm M}_\odot$and the star particle is $m_{\rm star} = 2.21 \times 10^4 h^{-1}{\rm M}_\odot$.

The simulations are fully described in Section 2.1 Note that the results presented through the study will only refer to the specific SF/feedback

[1] `http://www.clues-project.org`

model of Springel & Hernquist (2003): other formalisms might lead to different conclusions, and we hope to address this issue in the future.

In addition we also have at our disposal a dark matter only CLUES simulation based upon the WMAP5 cosmology (Komatsu et al. 2009) whose details have been presented already in Section 2.1 and Section 5.2; here it suffices to know that this simulation has the same formal resolution as the WMAP3 one, and it has also been re-simulated within a sphere of $2h^{-1}$Mpc radius, i.e. the primary difference between the two simulations is merely the cosmology.

3.3 Results

In order to most closely match the results presented by Boylan-Kolchin et al. (2011) and not to be contaminated by numerical effects we limited the subhaloes used throughout the study to those within 300kpc from their respective host and more massive than $M_{\rm sub} > 2 \cdot 10^8 M_\odot h^{-1}$. We further stack the data for the two most massive hosts representing our MW and M31 galaxies.

In Fig. 3.1 we show the relation between $R_{\rm max}$ and $V_{\rm max}$ for the WMAP3 simulation alongside the 1σ confidence region of the known Milky Way satellites, assuming that the mass density profile of the subhaloes containing the nine observed dwarf spheroidal follows a NFW profile (Navarro et al. 1996b): the two solid lines in Fig. 3.1 (and 3.2) thus limit the area consistent with the observed half-light radii and masses of these dwarfs, based on the work of Wolf et al. (2010). The diamonds represent the subhaloes in the dark matter only simulation while the crosses are the satellite galaxies in the SPH run. The lines connect the sister haloes, i.e. those objects that could be cross-identified in the two simulations. Please note that not all subhaloes could be cross-identified and hence only a certain number of them are connected by arrows. The results for the WMAP5 (dark matter only) data are presented separately in Fig. 3.2.

The results of these plots are quite interesting. First of all we notice that massive subhaloes (i.e. high-$V_{\rm max}$ objects) appear to be outside the observational range only in the case of the WMAP5 cosmology. This is thus in agreement with the findings of Boylan-Kolchin et al. (2011) whose Fig.2 shows both the Aquarius and Via Lactea II simulation data combined. The latter run used a $\sigma_8 = 0.74$ which is close to our WMAP3 value. Note that for this simulation the subhaloes are found only marginally outside the observational confidence interval. However, note that the actual $V_{\rm max}$ values for the subhaloes depend on the host mass and $V_{\rm max,host}$, respectively (cf.

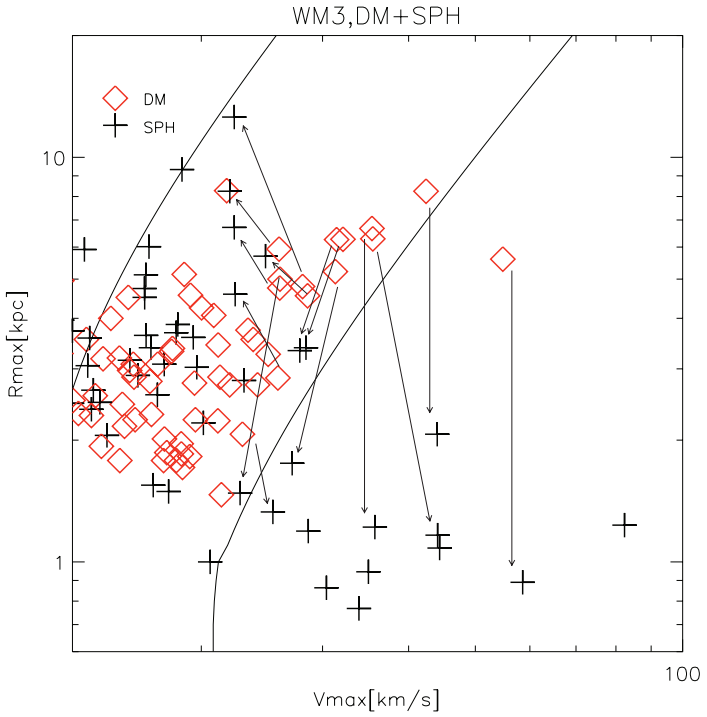

Figure 3.1: The relation between the peak of the rotation curve $V_{\max}$ and its position $R_{\max}$ for the WMAP3 simulations: the diamonds are DM only subhaloes, the cross represent baryonic SPH subhaloes. The two solid lines delimite the 1σ confidence interval of the observed bright Milky Way dwarf spheroidal galaxies, as in Boylan-Kolchin et al. (2011). The arrows connect the DM-SPH sister pairs found following the matching haloes procedure of Libeskind et al. (2010).

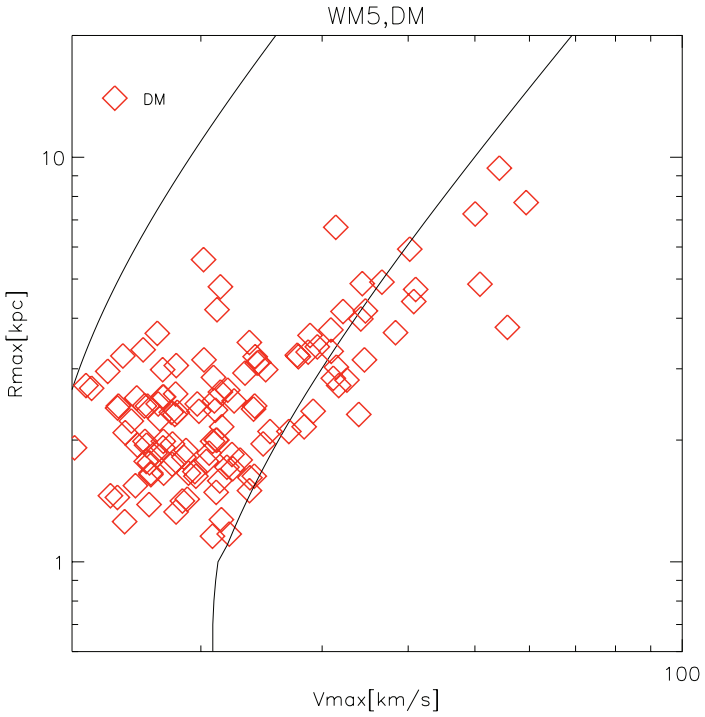

Figure 3.2: The same as Fig. 3.1 but for the WMAP5 (dark matter only) simulation.

Reed et al. 2005; Diemand et al. 2007; Springel et al. 2008). Therefore, in order to better compare the WMAP5 to the WMAP3 simulation, we scaled the subhaloes' maximum velocities, $V^{WM5}_{\rm max,sub}$, by the ratio $V^{WM3}_{\rm max,host}/V^{WM5}_{\rm max,host}$ (not presented here) where the respective values are $V_{\rm max,MW} = 131$, $V_{\rm max,M31} = 128$ for WMAP3, and $V_{\rm max,MW} = 178$, $V_{\rm max,M31} = 194$ for WMAP5 (all in km/s). We find that this re-normalization leads to a $\approx 30\%$ decrease of the $V^{WM5}_{\rm max,sub}$ values, bringing them into agreement with the WMAP3 results. In that respect, the two dark matter only simulations are in fact not too different!

More importantly, we see in Fig. 3.1 that the inclusion of baryonic physics does not solve the problem of the massive and highly concentrated dark matter subhaloes. On the contrary subhaloes with baryons appear to be down-shifted in the $R_{\rm max}$-$V_{\rm max}$ plane with respect to their dark matter counterpart, sometimes even entering the regime outside the observational constraints only in the SPH run. However, we also find that the lower-$V_{\rm max}$ objects seem to be shifted in the direction anticipated by Boylan-Kolchin et al. (2011), i.e. to the upper left of the plot. There appear to be two competing effects moving subhaloes in the $R_{\rm max}$-$V_{\rm max}$ plane.

The six SPH (sister) subhaloes that are outside the confidential range have a smaller $R_{\rm max}$ than their DM only companion: the addition of baryons causes a contraction of the halo. This effect is also visible for three SPH (sister) subhalo inside the observational area and is readily explained by the physical phenomenon of adiabatic contraction (Blumenthal et al. 1986; Gnedin et al. 2004). We confirm that the baryon fraction $f_b = \Omega_b/\Omega_m$ of those subhaloes moving downwards is higher than for the subhaloes shifted to the upper left. On average, the baryon fraction of the nine (sister) SPH subhaloes, whose $R_{\rm max}$ is reduced with respect to their DM counterpart, is $f_b/f_{b,\rm cosmic} \sim 0.314$, while the mean f_b of the SPH subhaloes inside the 1σ area whose $R_{\rm max}$ increases is $f_b/f_{b,\rm cosmic} \sim 0.006$, i.e. substantially smaller. The subhaloes with high f_b experience adiabatic contraction and the majority of these objects are the ones with the initial highest $R_{\rm max}$ – $V_{\rm max}$ pairs.

To confirm this last point, we used the `CONTRA` code (Gnedin et al. 2004) to calculate the adiabtic contraction of a dark matter halo in response to condensation of baryons. Using our numerical data as input parameters, we found that adiabatic contraction is actually efficient only for those subhaloes with sufficiently high f_b, as expected: the amount of the $R_{\rm max}$ reduction computed this way perfectly matches the observed shifts in Fig. 3.1.

Instead, for the lower $V_{\rm max}$ sister subhaloes (with substantially smaller baryon fractions) the baryonic matter has the capability to lower the maximum velocity of the rotation curves, while increasing $R_{\rm max}$. This has already

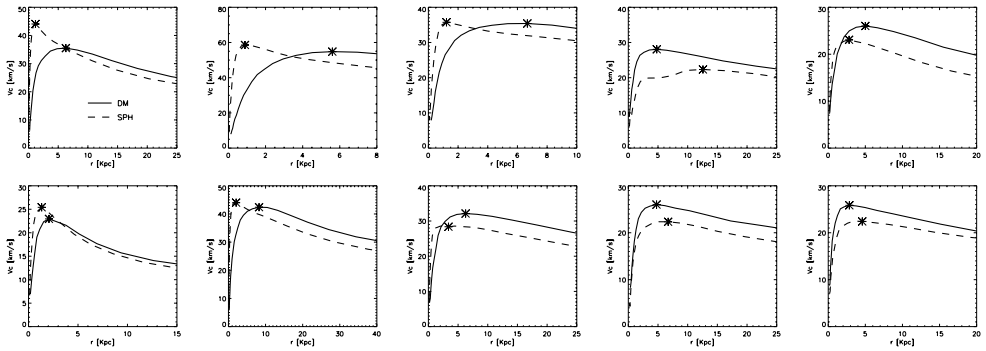

Figure 3.3: Rotation curves of ten sister pairs of massive subhaloes. In each panel the velocity profile of a pair of DM and SPH subhaloes is presented. The actual values of $V_{\max}$-$R_{\max}$ are plotted as asterisks.

been claimed in previous works and may be due to different mechanisms. In particular, we like to highlight the mass outflow model of Navarro et al. (1996a): immediate expulsion of a large fraction of baryonic material during star formation could be the cause of the creation of a central dark matter core, which will move the peak of the rotation curve to larger radii. This model has been successfully tested by Parry et al. (2012) who followed the formation history of a single stellar dominated satellite, which undergoes the sequence of events predicted by Navarro et al. (1996a). Another possible explanation to end up with less concentrated density profiles, is through the mechanism described by Mashchenko et al. (2006). A random bulk motion of gas, driven by stellar feedback, results in a flattening of the central DM cusps, thus leading to DM densities smaller than predicted by pure DM cosmological models. But why is it that those objects with low baryon fractions are the ones that require the aforementioned mechanisms? Is it that the gas expulsion has already occurred, thereby lowering the baryon fraction? Possibly the baryon fraction is only low at redshift $z = 0$ because of mass losses during the subhaloes history? Lately, Nickerson et al. (2011) explored the effect of several baryon loss mechanisms on subhaloes in SPH simulation of a Milky Way like galaxy, too: they found that for the subhaloes which ended up having (or having had) stars but no gas the most efficient mechanism of baryons removal is exactly the stellar feedback (Dekel & Silk 1986). Finally, we note that the adiabatic contraction (following Gnedin et al. (2004)) is ineffective for these subhaloes. We will address all these issue of the temporal evolution, mass loss and baryon influence in greater detail in a companion study in Chapter 5.

We close this Section with a detailed look at the rotation curves of the sister haloes in Fig. 3.3. In each plot the two sister objects are presented; the solid and dashed lines represent the circular velocity of the DM sub-

haloes in the dark matter only simulation and of the (sister) SPH subhalo, respectively. The asterisks show the $V_{\rm max}$-$R_{\rm max}$ pairs used in Fig. 3.1. We thus observe adiabatic contraction at work: the first three objects (which happen to have high baryon fraction) in that plot clearly show the centrally peaked total matter distribution in the SPH run. The plot further indicates that our measurements of the rotation curve and its peak are not contaminated by numerical artifacts (e.g. mis-identified halo centre, etc.).

3.4 Conclusions

In this work we explored the possibility that baryonic processes may solve the recently presented problem of "the puzzling darkness of Milky Way subhaloes" (Boylan-Kolchin et al. 2011). To this extent, we used dark matter only as well as full hydrodynamical simulations of cosmic structure in the context of the CLUES project. We used cosmological parameters determined from both the WMAP3 and WMAP5 data.

Our conclusions are twofold and can be summarized as follows:

- We find that when baryonic physics is included, following the feedback and star formation prescriptions of Springel & Hernquist (2003), the problem of having too dense massive subhaloes is not solved. Instead, gasdynamical simulations pose new questions regarding which mechanisms are responsible for the lowering of $R_{\rm max}$ in those subhaloes (while $V_{\rm max}$ remains more or less constant). Adiabatic contraction seems to be a reasonable explanation, as shown using the modified adiabatic contraction model of Gnedin et al. (2004): this process is effective only for some subhaloes, specifically, for those with a high baryon fraction. For the SPH subhaloes with lower baryon fractions at redshift $z = 0$, instead, we observe a general increase of $R_{\rm max}$ with respect to their DM counterpart, thus meaning that other effects are at work, e.g. the model proposed by Navarro et al. (1996a) in which a rapid expulsion of baryonic mass during star formation causes a reduction of the halo concentration, as well as naturally explaining the low baryon fraction of these objects.

- While in the WMAP5 DM only case we find dark matter subhaloes outside the confidence area (calculated following the prescription given in Boylan-Kolchin et al. (2011)) in the WMAP3 cosmology we only have one massive subhalo outside this observational range. Since the Via Lactea II and Aquarius simulations presented in Boylan-Kolchin et al. (2011) are similar cases, we conclude that the cosmology certainly

has an influence, too: the higher σ_8 of the WMAP5 scenario eventually led to higher host masses which – according to our test – are the most likely reason for the higher number of excessively centrally concentrated substructures. Note that the latest data from WMAP7 favours $\sigma_8 = 0.807$, a value between the WMAP3 and WMAP5 results: this could mean that the problem is worse than in WMAP3, but not as pronounced as in the WMAP5 case.

An issue neither touched upon by us nor other authors is the adequacy of using NFW profiles when calculating the confidence interval for possible hosts of the bright MW dwarf spheroidals. It is obvious that tidal effects will lead to severe modifications of the original NFW density profile subhaloes had upon infall into their host (Kazantzidis et al. 2004). They therefore leave an impact upon internal and kinematical properties, respectively (Lokas et al. 2010, 2011), which should be taken into account when using observed half-light radii $R_{1/2}$ and their corresponding masses $M_{1/2}$ to define the confidence interval. Further, Romano-Díaz et al. (2008) showed that adiabatic contraction makes the dark matter profile almost isothermal. However, the relevance is questionable as material will primarily be stripped from the outer regions: Peñarrubia et al. (2008) state that dSphs embedded in NFW haloes are very resilient to tidal effects until they are nearly destroyed. This is supported by Navarro et al. (2010) who found that the NFW shape holds reasonably well even for subhaloes. To roughly gauge the problem, we fitted our (SPH) subhaloes to a NFW profile, and observed that while some of them are well fitted, there are still objects whose density profile cannot be approximated by the simple NFW functional form. Taking all these considerations into account suggests that the NFW profile used to calculate the allowed region is likely not the best choice. We leave this to a companion study, presented in Chapter 5.

The interpretation of the results presented here clearly demands a closer investigation of the evolutionary tracks of the satellites, the actual influence of the SF and feedback model as well as an improved calculation of the observational confidence level, verifying the applicability of the NFW approach. We highlight here that simply the inclusion of baryonic physics does not solve the problem; it rather poses new challenges to be explored and studied in greater detail.

Chapter 4

Non-universal density profile of SPH subhaloes: implications for the Milky Way's dSphs

We use dark matter only and full hydrodynamical Constrained Local UniversE Simulations (CLUES) of the formation of the Local Group to study the density profile of subhaloes of the simulated Milky Way and Andromeda galaxies. We show that the Einasto model provides the best description of the subhaloes' density profile, as opposed to the more commonly used NFW profile or any generalisation of it. We further find that the Einasto shape parameter $n_{\rm E}$ is strongly correlated with the total subhalo mass, pointing towards the notion of a non-universality of the subhaloes' density profile. We observe that the effect of mass loss due to tidal stripping, in both the dark matter only and the hydrodynamical run, is the reduction of the shape parameter $n_{\rm E}$ between the infall and the present time. Assuming now that the dSphs of our Galaxy follow the Einasto profile and using the maximum and minimum values of $n_{\rm E}$ from our hydrodynamical simulation as a gauge, we can improve the observational constraints on the $R_{\rm max}$-$V_{\rm max}$ pairs obtained for the brightest satellite galaxies of the Milky Way. When considering only the subhaloes with $-13.2 \lesssim M_V \lesssim -8.8$, i.e. the range of luminosity of the classical dwarfs, we find that all our simulated objects are consistent with the observed dSphs if their haloes follow the Einasto model with $1.6 \lesssim n_{\rm E} \lesssim 5.3$. The numerically motivated Einasto profile for the observed dSphs will alleviate the recently presented "massive failures" problem.

4.1 Introduction

While the predictions of the current Λ Cold Dark Matter (ΛCDM) model have been widely confirmed at cosmological scales, there are still a number of discrepancies between theory and observations at galactic and subgalactic scales: one example is the well-known "missing satellite problem", first pointed out by Klypin et al. (1999a) and Moore et al. (1999). The high number of substructures resolved within the virial radius of galaxy-type objects in high resolution cosmological simulation mismatches the number of observed satellite galaxies of our Milky Way (MW) and nearby galaxies. To alleviate the problem one must invoke some mechanisms, such as early reionization of the intergalactic medium and supernovae feedback (Bullock et al. 2000; Somerville 2002; Benson et al. 2002), to suppress galaxy formation below a certain scale.

However, there is an inconsistency not only with the number, but also about the kinematics of the observed MW's dwarf spheroidals (dSphs) when compared to the velocity profiles of the most massive subhaloes found in dark matter simulations (Boylan-Kolchin et al. 2011). Assuming that these subhaloes follow a Navarro et al. (1996b,NFW herafter) profile, they have been found to be too dense to host the MW's bright satellites. This is directly related to the findings of Bovill & Ricotti (2011a,b), whose simulations showed an overabundance of bright dwarf satellites ($L_V > 10^4 L_{sun}$) with respect to the MW's dSphs.

A number of studies tried to reconcile simulations with observations.

The possibility that the MW is a statistical outlier has been ruled out by Strigari & Wechsler (2012), who used data from the Sloan Digital Sky Survey to show that, down to the scale of Sagittarius dwarf, our Galaxy is not anomalous in its number of classical satellites. Further, the analysis of Boylan-Kolchin et al. (2012), independent from the choice of actual density profile of the simulated subhaloes, demonstrates that supernova feedback is unlikely to be an explanation for the low inferred densities of dSphs, due to their small stellar masses. Different hypothesis for the nature of dark matter can naturally lead to the formation of less concentrated subhaloes in a warm dark matter scenario (Lovell et al. 2012) or in simulations of self-interacting dark matter models (Vogelsberger et al. 2012), providing an interesting alternative to the ΛCDM model. Moreover, the discrepancy between observed and simulated satellite galaxies may reflect the fact that the MW is less massive than is commonly thought: a total mass between $8{\cdot}10^{11} \lesssim M/M_{\odot} \lesssim 10^{12}$ has been argued in Vera-Ciro et al. (2013) and Wang et al. (2012). However, lowering the mass of the MW still do not explain why its dSphs (as well as many isolated dwarf galaxies), seem to live in

haloes whose mass is smaller than the current expectation from abundance matching models (Ferrero et al. 2012).

The inclusion of baryons in simulations has also been explored, and it has been found either to have negligible effects on the dark matter density of subhaloes (Parry et al. 2012) or to have a twofold effect on their density profile (Di Cintio et al. 2011). In fact, recognizing that at galactic scales baryonic processes are expected to play a crucial role, it has been investigated in Di Cintio et al. (2011) the effect of the inclusion of baryons in SPH simulation within the CLUES project.[1] These simulations are designed and constrained, respectively, to reproduce as closely as possible the actual observed Local Group with its two prime galaxies MW and Andromeda (hereafter also referred to as M31) and hence serve as an ideal testbed for investigating the dynamics and kinematics of the satellite populations of the real MW and M31. In this previous study it has been found that, while in some cases the baryons are able to lower the central density of subhaloes, through mechanisms such as gas outflows driven by star formation and supernovae (Navarro et al. 1996a; Governato et al. 2012), there are still substructures whose density is increased, as expected from the adiabatic contraction model of Blumenthal et al. (1986).

The underlying assumption in many previous works is that the satellite galaxies of the MW are embedded in subhaloes whose mass profile is described by the NFW model: it is still a matter of debate, however, if this profile is the best choice in modeling the dSphs' density.

On one hand, Walker & Peñarrubia (2011) constructed a method for measuring the slope of the mass profiles within dSphs directly from stellar spectroscopic data, independently from any dark matter halo model and velocity anisotropy of the stellar tracers, and showed evidence for the profile of the Fornax and Sculptor dSphs to be consistent with cores of constant density within the central few-hundred parsecs of each galaxy, thus ruling out a cuspy profile such as the NFW one. On the other hand, Wolf & Bullock (2012) used a Jeans analysis to show that, even in the limiting case of an isotropic velocity dispersion, not all of the dwarfs prefer to live in halos that have constant density cores. It must be noticed, however, that while the Walker & Peñarrubia (2011) method is insensitive to orbital anisotropy and underlying halo potential, the Wolf & Bullock (2012) results are dependent from these yet unknown quantities.

Regarding simulations, Di Cintio et al. (2011) pointed out that the NFW profile may not be appropriate to describe the subhaloes' density. While computing the subhaloes' circular velocities Boylan-Kolchin et al. (2012)

[1] http://www.clues-project.org

used an Einasto profile to model the density distribution of subhaloes at small radii, in order to correct for the effects of the force softening, and the raw particle data at higher radii.

The three-parameter Einasto profile (Einasto 1965), indeed, has been found to more accurately describe the halo density in dark matter only simulations (e.g. Navarro et al. 2004; Merritt et al. 2006; Prada et al. 2006; Gao et al. 2008; Hayashi & White 2008; Navarro et al. 2010; Ludlow et al. 2011; Reed et al. 2011), reducing the residuals of the fits by 20% with respect to the corresponding NFW models.

In this work we mainly focus on hydrodynamical simulations and, after a brief explanation, in Section 4.2, of the CLUES project simulations, we study the mass profile of substructures within the two main haloes of the simulated Local Group, formally calling them Milky Way and M31. In Section 4.3 we focus on the quality of several analytical models in describing the density profile of galactic subhaloes showing that, also in hydrodynamical simulations, the Einasto profile provides the best description. In Section 4.4 we then show that the corresponding profile shape parameter $n_{\rm E}$ scales with the virial mass of the subhalo. We finally discuss the implications for the mismatch between the kinematics of the observed MW's dSphs and the simulated substructures in Section 4.5, before concluding in Section 4.6.

4.2 Simulation details

We used the same set of CLUES simulations already described in Section 2.1 and Section 3.2 based upon a WMAP3 cosmology. There are two runs available, one with dark matter only (DM run) and one hydrodynamical (labelled SPH run) in which we additionally follow the feedback and star formation rules of Springel & Hernquist (2003), as well as a uniform but evolving ultra-violet cosmic background (Haardt & Madau 1996).

The stellar population synthesis model STARDUST (see Devriendt et al. 1999,and references therein for a detailed description) has been used to derive luminosities from the stars formed in our simulation. This model computes the spectral energy distribution from the far-UV to the radio, for an instantaneous starburst of a given mass, age and metalicity. The stellar contribution to the total flux is calculated assuming a Kennicutt initial mass function (Kennicutt 1998).

All the subhaloes used in this particular study are selected in order to be more massive than $M_{\rm sub} \geqslant 2 \times 10^8 h^{-1} M_\odot$, with a peak in the velocity curve $V_{\rm max} \gtrsim 10$km/s, and to lie within 300 kpc from each host's center, the latter being either the MW or M31. The masses of the SPH hosts, defined as the

Table 4.1: Quality of the fits for several density profile models. The results for SPH and DM subhaloes are listed, together with the mean value of the shape parameter n, the inner slope γ and the outer slope β, respectively.

	SPH		DM	
Profile	$\overline{\Delta^2}$	shape	$\overline{\Delta^2}$	shape
NFW	0.043	$\gamma = 1.00$	0.042	$\gamma = 1.00$
M99	0.030	$\gamma = 1.50$	0.032	$\gamma = 1.50$
$(1, 3, \gamma)$	0.014	$\overline{\gamma} = 1.98$	0.015	$\overline{\gamma} = 1.53$
$(1, \beta, 1)$	0.014	$\overline{\beta} = 3.80$	0.013	$\overline{\beta} = 4.40$
P&S	0.013	$\overline{n}_{\rm PS} = 3.35$	0.013	$\overline{n}_{\rm PS} = 3.15$
Einasto	**0.011**	$\overline{n}_{\rm E} = 4.80$	**0.012**	$\overline{n}_{\rm E} = 3.79$

masses within a sphere containing $\Delta_{vir} \simeq 390$ times the cosmic mean matter density, are $M_{\rm MW} = 4.0 \times 10^{11} h^{-1} M_\odot$ and $M_{\rm M31} = 5.47 \times 10^{11} h^{-1} M_\odot$. When stacking the data from the two hosts together, we found a total of 56 SPH and 66 DM subhaloes in this WMAP3 simulation. Note that our selection criterion assures that within each host a subhalo contains a minimum of 1000 particles.

4.3 The density profile of SPH and DM subhaloes

4.3.1 Theoretical Models

While it is widely accepted that a Navarro et al. (1996b,NFW) profile provides a good description of DM haloes, it has been already pointed out in Di Cintio et al. (2011) that this universal profile may not be the best choice when used to fit *sub*-halo densities. We will thus study different profiles and apply them to our simulated substructures, with particular emphasis on the density profile of subhaloes in hydrodynamical simulations.

Double-power law profiles A generalisation of the NFW profile is the so-called (α, β, γ), or double power-law model:

$$\rho_{\alpha,\beta,\gamma}(r) = \frac{\rho_s}{\left(\frac{r}{r_s}\right)^\gamma \left[1 + \left(\frac{r}{r_s}\right)^\alpha\right]^{(\beta-\gamma)/\alpha}} \tag{4.1}$$

where r_s is the scale radius and ρ_s the scale density, characteristic of each

halo and related to its formation time and mass (e.g. Prada et al. 2012; Muñoz-Cuartas et al. 2011; Macciò et al. 2007; Bullock et al. 2001). It is a five-parameter model in which the inner and outer region have logarithmic slopes $-\gamma$ and $-\beta$, respectively, and the α parameter regulates the sharpness of the transition. The choice $(\alpha, \beta, \gamma) = (1, 3, 1)$ provides the NFW profile, while $(\alpha, \beta, \gamma) = (1.5, 3, 1.5)$ gives the model presented in Moore et al. (1999,M99 hereafter). Besides of the NFW and M99 profiles we will also investigate the case of leaving the central slope as a free parameter, i.e. a $(1, 3, \gamma)$ model.

Einasto profile In addition to these double-power law profiles we test the Einasto profile (Einasto 1965), identical in functional form to the $2D$ Sérsic model (Sérsic 1963; Sérsic 1968), but used instead to fit a spacial mass density:

$$\rho_{\rm E}(r) = \frac{\rho_{-2}}{e^{2n\left[\left(\frac{r}{r_{-2}}\right)^{\frac{1}{n}}-1\right]}} \tag{4.2}$$

Here r_{-2} is the radius where the logarithmic slope of the density profile equals -2 and n, also referred to as $n_{\rm E}$, is a parameter that describes the shape of the density profile. r_{-2} is equivalent to the scale radius r_s of a NFW profile, and the density $\rho_{-2} = \rho(r_{-2})$ is related to the NFW one through $\rho_{-2} = \rho_s/4$. This profile gives a finite total mass and its logarithmic slope decreases inwards more gradually than a NFW or M99 profile. When $n_{\rm E}$ is large, the inner profile is steep and the outer profile is shallow. Typical values of $n_{\rm E}$ found in dark matter only simulations for haloes more massive than $10^{10} M_\odot$ are $4 \lesssim n \lesssim 7$.

Prugniel–Simien profile Finally, following the study of Merritt et al. (2006), we use the analytical approximation of the deprojected Sérsic law, given in Prugniel & Simien (1997,P&S hereafter):

$$\rho_{\rm P\&S}(r) = \frac{\rho_{-2}}{\left(\frac{r}{r_{-2}}\right)^{p} e^{n(2-p)\left[\left(\frac{r}{r_{-2}}\right)^{\frac{1}{n}}-1\right]}} \tag{4.3}$$

where n, or $n_{\rm P\&S}$ where appropriate, is again a parameter describing the curvature of the density profile and the quantity p is a function of $n_{\rm P\&S}$ chosen to maximize the agreement between the P&S model and the Sérsic law. A good choice for p, when $0.6 \lesssim n \lesssim 10$, is $p = 1.0 - 0.6097/n +$

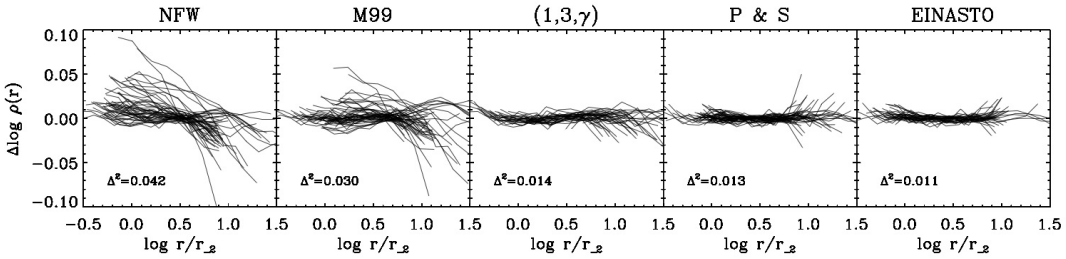

Figure 4.1: Residuals of the density profiles of all SPH subhaloes for each of the fitted models. The mean goodness-of-fit $\overline{\Delta^2}$ is indicated, providing the Einasto model to be the best one. The radial dependence of the residuals is the same for the DM only run, thus not shown here.

$0.05463/n^2$ (Lima Neto et al. 1999), used in our fitting routine. We must highlight that the shape parameter $n_{\rm E}$ of the Einasto profile is not the same as $n_{\rm P\&S}$ of the P&S model, although they follow the same functional form. The Einasto profile, the P&S one and the modified NFW profile $(1, 3, \gamma)$ are all 3-parameters models.

4.3.2 Application to Subhaloes

We now apply all the above models to fit our subhaloes' density profiles.[2] The density profiles are given in radial bins logarithmically spaced from the inner radius compliant with the convergence criterion of Power et al. (2003) out to the subhaloes' edge, defined as in Knollmann & Knebe (2009). The number of bins varies from 7 for the least massive objects to 16 for the most massive ones; by this we assure to minimize the Poissonian noise always having at least 150 particles per bin, and a minimum of 1000 particles in total in each subhalo. We verified that the convergence criterion as defined in Power et al. (2003) is suitable also for subhaloes, and thus fully applicable to our simulation. Specifically, we used a lower resolution, 2048^3 particles DM-only run with three times higher softening length $\epsilon = 411$ pc, to show that the density profile of subhaloes converges for $\sim 4.8\epsilon$. This value is always equal or less than the radius found using the Power et al. (2003) criterion: all our trusted radii are thus fully converged according to the most conservative criterion possible and are not affected by two-body relaxation effects.

We define the goodness-of-fit as

[2]We use the IDL routine MPFIT

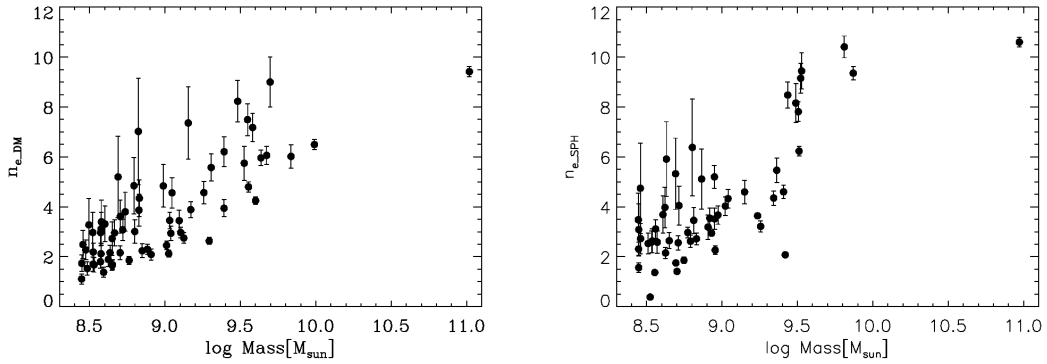

Figure 4.2: Correlation of the shape parameter $n_{\rm E}$ with the subhaloes' masses in the DM only simulations, left panel, and SPH simulation, right panel. The error bars associated to the shape parameter are indicated for $n_{\rm E}$, as provided by the fitting routine. The 1σ statistical error committed in the evaluation of $n_{\rm E}$ is, on average, the 15% of the $n_{\rm E}$ itself. The evident correlation between $n_{\rm E}$ and the subhaloes' masses in the DM only as well as in the SPH run is attributed to the dynamical effects of tidal stripping. The additions of baryons can ulteriorly modify the density profile, specifically in its inner part.

$$\Delta^2 = \frac{1}{N_{\rm bins}} \sum_{k=1}^{N_{\rm bins}} (\log_{10}\rho_{\rm sim,k} - \log_{10}\rho_{\rm fit,k})^2, \tag{4.4}$$

whose average value over the total number of subhaloes $\overline{\Delta^2}$ gives an indication of the fit performance.

The results are presented in Table 4.1 for a WMAP3 cosmology, where we list the quality of fit values $\overline{\Delta^2}$ alongside the mean value of the shape parameter $n_{\rm E}$, $n_{\rm P\&S}$ or the inner (outer) slope γ (β) in the case of considering the double power-law models. A first consideration regards the differences between the DM only and the SPH runs: we observe that the mean shape parameters in the SPH run are systematically higher than in the DM counterpart, which implies a more cuspy central slope, indicating that the net effect of the inclusion of baryons is a steepening of the subhaloes' density. Our results appear to be in agreement with the prescription of an adiabatic contraction model (Blumenthal et al. 1986), as shown already in Di Cintio et al. (2011) for the most massive and most luminous subhaloes. We must remark that we are listing the average n over the total set of subhaloes: there are cases, as discussed in Di Cintio et al. (2011), in which the SPH subhaloes with the lowest baryon fraction, instead, undergo an expansion,

therefore lowering their n. An higher shape parameter in the SPH run is also indicative of a less steep outer profile with respect to the DM only run, which means that tidal stripping effects are stronger on the DM only substructure, as reported in Libeskind et al. (2010) (see discussion below).

We also notice that the mean shape parameter of the P&S profile, $n_{\rm P\&S}$, is lower than the corresponding Einasto parameter, $n_{\rm E}$, in the same run: this is expected, and found also in Merritt et al. (2005). A few words on the steep central slopes γ found for the $(1, 3, \gamma)$ model: this model imposes the outer slope to be equal to 3, which is not the case for subhaloes where the profile drops even faster (cf. Oh et al. 1995; Peñarrubia et al. 2009), causing the fitting routine to provide high values of γ when trying to adjust the density profile. Leaving the outer profile index β as a free parameter, i.e. using a $(\alpha, \beta, \gamma) = (1, \beta, 1)$ model, we found indeed that on average the outer slope of SPH subhaloes is $\bar{\beta} = 3.8$ while in the DM only case $\bar{\beta} = 4.4$. This is in agreement with the average values obtained for the Einasto shape parameter, which is higher in the SPH case with respect to the DM only scenario: the higher $n_{\rm E}$ found in the SPH subhaloes indicates a cuspy inner profile, as expected if adiabatic contraction is acting on the central part of the structures, but also an outer density profile less steep than in the DM case, as confirmed by the $(1, \beta, 1)$ model.
The outer profile of subhaloes in the CLUES gas-dynamical run is shallower than in the pure dark matter case because of the influence of tidal stripping whose effects, being present in both runs, are stronger in the DM case. Tidal stripping, which mainly acts on the outer part of the density profile, is able to remove more mass from a pure dark matter subhalo than an SPH one, owing to the deepening of the potential in the latter case, as shown in greater detail by Libeskind et al. (2010).

Finally, we also used the exponentially truncated profile, introduced by Kazantzidis et al. (2004) to deal with the divergence of the cumulative mass distribution of haloes as $r \to \infty$, but we did not obtain improvements over the Einasto or P&S profiles.

To further highlight the quality of the different models, in Fig. 4.1 we present the residuals between the fits and the data for each subhalo in the SPH simulation as a function of $\log(\mathrm{r}/\mathrm{r}_{-2})$ (the plots look akin for the DM simulation and hence are omitted). Note that for the $(1, 3, \gamma)$ model the point where the logarithmic slope of the density profile equals -2 occurs at a radius $r_{-2} = (2 - \gamma) r_s$ for $\gamma < 2$: thus, for a NFW profile $r_{-2} = r_s$ and for a M99 profile $r_{-2} = r_s/2$.

Neither the NFW, M99, or $(1, 3, \gamma)$ profiles are well fitted over the whole radial range: while the $(1, 3, \gamma)$ with a steep central slope may describe the data in the inner regions, it fails so in the outer parts. On the contrary, the

radial dependence of the residuals in the Einasto model is clearly minimized with respects to all the other models, being consistent with zero at every radial bin. The case could be made that the $(1, 3, \gamma)$ model performs as well as the Einasto model in the inner region of the density profile (which is also the region of interest with respect to the observations of the MW's dSphs). In order to assess the degree to which these results are affected by the choice of the radial range, we calculate the residuals, for every model, for only the innermost bins with $r < r_{-2}$, and found that the Einasto is still the best profile overall.

We conclude that the Einasto model outperforms all the other proposed profiles in terms of quality of fit, giving, over the full radial range, an average value of $\overline{\Delta^2} = 0.011$ in the SPH run and $\overline{\Delta^2} = 0.012$ in the DM only run. We note that the the P&S model also provides good results, though not as good as the Einasto model.

While it is somehow obvious that these 3-parameter models perform better than the 2-parameter ones (such as the NFW or M99 model), we are reassured by the fact that even after fixing the shape parameter $n_{\rm E}$ ($n_{\rm P\&S}$) of the Einasto (P&S) profile to its mean value, therefore reducing the free parameters to two, we still obtain a mean goodness-of-fit which is lower than any other 2-parameter model (the Einasto profile, for example, provides $\overline{\Delta^2} = 0.025$ for the SPH run and $\overline{\Delta^2} = 0.028$ for the DM run). Thus, the better performance of the Einasto profile is not just an artifact of having one free parameter more. Furthermore, our results are in agreement with those of other workers in the field (e.g. Springel et al. 2008).

In light of this we state that the need of a shape parameter n to fully specify the mass profile of simulated DM and SPH subhaloes is an indication of the non-universality of their density profiles, as will be highlighted in the next section.

4.4 Shape parameter – subhalo mass relation

In Table 4.1 the average values of the Einasto shape parameter $n_{\rm E}$ are shown. However, this shape parameter varies from subhalo to subhalo, spanning quite a large range $0.4 \lesssim n_{\rm E} \lesssim 10.4$ in the SPH run (with a similar spread in the DM model). This naturally raises the question of whether this variation follows some rule or is random.

In Fig. 4.2, the fitted Einasto shape parameter $n_{\rm E}$ is plotted against subhalo mass for both the DM only run (left) and the SPH run (right). A clear correlation is immediately visible. This result forms one of the main

findings of this study: *the Einasto shape parameter correlates directly with subhalo mass*. To quantify the $n_{\rm E}$-mass correlation, the Spearman rank coefficient[3] S_r (Kendall & Gibbons 1990) is calculated, yielding $S_r = 0.70$ for the SPH run, with a significance of practically zero confirming a strong correlation: the most massive objects have a higher value of the shape parameter, while less massive ones have smaller values. In other words, low mass substructures are well fit by a inner density profile shallower than a NFW one, with a steep outer slope, while the higher mass objects are fit by a steep, cuspy-like inner profile. Convergence studies (wherein the number of radial bins used for profile fitting is drastically increased) have been performed in order to ascertain the applicability of an Einasto profile to our subhaloes. These tests have revealed that our fitting procedure is robust and not a result of the sampling. Similar results and S_r values are found for the DM only run. One might argue that the subhalo's mass may be seen as a rather ill-defined quantity, and a better proxy for mass (e.g. Knebe et al. 2011b) should be the peak of the rotation curve $V_{\rm max}$: when replacing the mass on the x-axis of Fig. 4.2 with $V_{\rm max}$ we actually do not find any substantial change in the correlation, strongly confirming it.

Since Fig. 4.2 shows the same $n_{\rm E}$-mass relation for both the DM only and the SPH run, we conclude that the mechanism responsible for this relation must be dynamical and hence is likely to be tidal stripping. To determine the influence of tidal stripping, the properties of subhaloes at infall time, defined as the last time a subhalo crossed a sphere of physical radius 300kpc from the host's center [4], have been examined.

At infall time the subhaloes' density is well described by both an Einasto and a NFW profile, as expected for field haloes. Using an Einasto profile, we find that the more mass lost since $z_{\rm infall}$, the lower the value of $n_{\rm E}$ at $z = 0$, as presented in Fig. 4.3 for the SPH case. There is thus an evident correlation between the amount of stripped material and the reduction of $n_{\rm E}$ for each subhalo. Again, this relation is quantified by the Spearman rank coefficient, $S_r = 0.68$, and showing the best curve fit, which has a unitary angular coefficient, as a solid line in Fig. 4.3. A similar dependence is found in the DM only run, thus not shown here, corroborating our findings that tidal stripping is the main mechanism able to modify the density profile of subhaloes.

Many authors (e.g. Kazantzidis et al. 2004; Springel et al. 2008; Hayashi

[3]The Spearman rank coefficient is a non-parametric measure of correlation that assesses how well an arbitrary monotonic function describes the relationship between two variables, without making any other assumptions about the particular nature of the relationship between the variables. The closer the coefficient is to 1 the stronger the correlation between the two variables. We use the IDL routine R CORRELATE() to calculate it.

[4]Using the first infall time provides similar results.

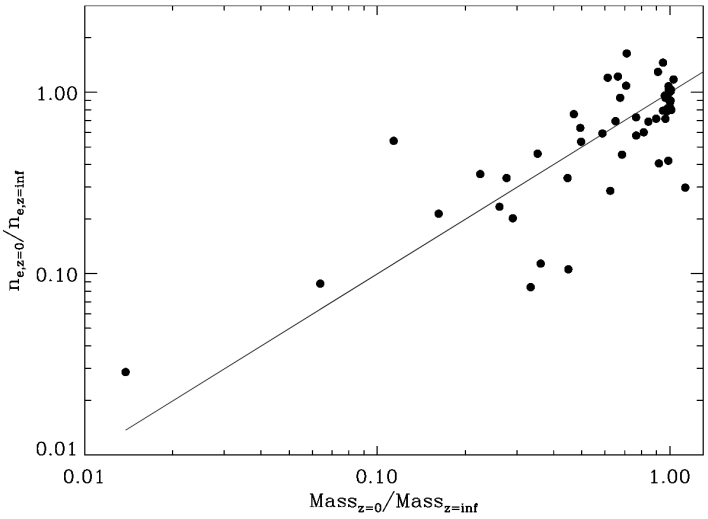

Figure 4.3: Reduction of the shape parameter $n_{\rm E}$ as a function of the mass loss between $z = 0$ and $z_{\rm infall}$ for the SPH subhaloes. A similar behavior is found in the DM only run, thus not shown here. The best fit curve, which has unitary slope, is shown as a solid line.

et al. 2003; Peñarrubia et al. 2010) have shown that tidal stripping acts mainly to modify the outer region of a profile. Since a steepening of the outer profile entails a reduction of $n_{\rm E}$ exactly as observed in our simulations, we therefore conclude that the lowering of the subhaloes' shape parameter between $z_{\rm infall}$ and $z = 0$ is primarily due to stripping effects. This finding is indeed in agreement with the recent work of Vera-Ciro et al. (2013) who show that very heavily stripped objects have on average smaller $n_{\rm E}$, because of a steepening of the outer density profile. It is also worth noting that tidal stripping has been shown by Hayashi et al. (2003) to not only affect the subhaloes' outer regions: as a substructure loses mass, the central density will also decrease significantly (although the slope of the inner density profile remains unchanged).

A word of caution is necessary at this point. The Einasto model's shape parameter $n_{\rm E}$ describes simultaneously the slope of the inner and outer profile, in a single number. This can be both an advantage and a disadvantage. Indeed for some subhaloes in our simulations the value of the scale radius r_{-2} is close to the the innermost converged radius while the outer profile is resolved with many radial bins. In these cases, if the outer profile steepens yet the structure of the inner part remains unchanged, the Einasto fit would return a lower value of $n_{\rm E}$ due to the fitted profile being dominated by the

steepened outer part. This is the case, for example, of heavily stripped objects ($M_{z=0}/M_{z_{infall}} \sim 20\%$) in the DM only run, in which the inner cuspy slope of the substructure is retained after infall, while the outer profile has been steepened by tidal stripping, thus providing a small fitted $n_{\rm E}$ value. Care must be taken not to interpret these cases as becoming cored, in the inner region, due to tidal stripping. That said even in these cases, Einasto models provide accurate fits to the density profile – more accurate than any of the other models as could be seen in Fig. 4.1 and Table 4.1.

While tidal stripping is the only relevant mechanism in the DM only run, other effects such as baryonic feedback have to be taken into account in the SPH case, since they can also contribute to changes in the density profile of subhaloes (Zolotov et al. 2012; Brooks et al. 2013). Indeed, as opposed to the DM only simulation, in the SPH run we observe in some subhaloes a change to their inner structure (cf. Di Cintio et al. 2011). Since, as mentioned above, tidal stripping does not change the inner slope of substructures, the only mechanisms able to alter the density at small radii must have a baryonic origin. Di Cintio et al. (2011) showed that the inclusion of baryons has a twofold effect, increasing or decreasing its central density according to an adiabatic contraction (Blumenthal et al. 1986) or outflows (Navarro et al. 1996a; Governato et al. 2012) model.

To shed more light onto the effects of baryons, a one to one comparison of the density profiles of those subhaloes that can be cross-identified in the DM and SPH run has been performed (as in Di Cintio et al. 2011). The subhaloes which experienced an expansion in the SPH run, with respect to their DM only partner, have lost all their gas at redshift zero, and they do not show any sign of star formation between $z_{\rm infall}$ and $z = 0$. These subhaloes have an inner density profile shallower than the corresponding sister DM subhalo. On the other hand, those objects which have undergone adiabatic contraction in the SPH run (cf. Di Cintio et al. 2011) still retain some gas at $z = 0$ and their star formation appears to be on going even after infall. These subhaloes have a high value of the shape parameter $n_{\rm E}$, which is now well describing a steeper inner density profile caused by adiabatic contraction. In any case, the fits are still dominated by the outer profile, steepened by tidal stripping, where most of the bins lie and hence higher resolution simulations are needed to verify the effective creation of a core in objects with small $n_{\rm E}$ values: the interplay of these two contrasting effects, i.e. outflows vs adiabatic contraction, and a deep analysis of the repercussions on the inner density profile of substructures in cosmological simulations will be explored in detail in the future.

Some other important conclusions can now be drawn from Fig. 4.2. Firstly, there is no evidence for any universal profile in simulated substruc-

tures. Secondly, we note that the majority of the subhaloes in both runs tend to have a small $n_{\rm E}$, while only the most massive ones (mostly the adiabatically contracted ones) have a high $n_{\rm E}$, as large as $n_{\rm E}$=10.4 in the SPH run and $n_{\rm E}$=9.4 in the DM only one. This finding, as well as the goodness of the Einasto profile, has been confirmed from an observational point of view by the recent work of Del Popolo & Cardone (2012), who used high quality rotation curves data of dwarf galaxies to show that the preferred fitting function is given exactly by the Einasto model and that the majority of the dwarfs tend to have shallow profiles (their Fig. 3). Our mean shape parameter in the hydrodynamical run, $\overline{n}_{\rm E} = 4.8$, as well as their Einasto mean shape parameter, $\overline{n}_{\rm E,D.P.} = 3.05$, are both lower than the corresponding $n_{\rm E}$ for dwarf size objects found in previous dark matter simulations (Merritt et al. 2005; Navarro et al. 2004). In that regards we need to mentioned that previous results coming from such dark matter only simulations, where cluster- and galaxy-sized haloes have been studied, showed instead a decreasing of $n_{\rm E}$ for increasing halo mass (Navarro et al. 2004; Merritt et al. 2005; Graham et al. 2006b; Prada et al. 2006; Gao et al. 2008; Hayashi & White 2008; Navarro et al. 2010). Our study indicates that there is a turnover, such that the trend with mass is reversed for low mass galaxies (at least satellites), with both SPH and DM simulations having a positive correlation of $n_{\rm E}$ with mass. The main difference between previous studies and this work is, besides the less massive objects considered here, the fact that our objects are subhaloes, and thus obviously affected by tidal stripping, as mentioned above. Finally it must be noticed that the range of variation of the $n_{\rm E}$ shape parameter found in our simulation is very large, spanning the interval $0.4 \lessapprox n_{\rm E} \lessapprox 10.4$ in the SPH case: remarkably the same large range has also been found in Del Popolo & Cardone (2012), with $0.29 < n_{\rm E,D.P.} < 9.1$, as well as in the recent work of Vera-Ciro et al. (2013), based on semi-analytical models of galaxy formation. Furthermore, in the observational paper of Chemin et al. (2011), the authors used the Einasto model to fit the rotation curves of the THINGS[5] galaxies and show that the shape parameter is near unity on average for intermediate and low mass halos, while it increases for higher mass haloes, being correlated with the halo virial mass as we find in this work.

4.5 New observational constraints for the satellite galaxies of the Milky Way

We now move to a practical application of our findings, only focusing on the properties of SPH subhaloes, which are obviously closer to reality

[5]http://www.mpia.de/THINGS/Overview.html

than their DM only counterparts. In Boylan-Kolchin et al. (2011) the observational constraints, used to establish if subhaloes found in cosmological simulations are possible hosts of the known Milky Way dwarf spheroidals, were based on the assumption that the underlying dark matter halo of these dSphs follows a NFW profile. Given our findings, however, it is clear that since the Einasto model provides the best fit to the density profile of both DM and SPH subhaloes, those observational constraints have to be modified.[6] Note that in Eq.5-7, for clarity, we will omit the subscript $_E$ from the Einasto shape parameter, simply referring to it as n. The circular velocity of an Einasto profile follows

$$v^2(r) \propto \gamma(3n, x), \tag{4.5}$$

where

$$\gamma(3n, x) = \int_0^x e^{-t} t^{3n-1} dt \tag{4.6}$$

is the lower incomplete gamma function and $x = 2n(r/r_{-2})^{1/n}$. To find the radius $R_{\rm max}$ at which $dv(r)/dr = 0$ we numerically solve,

$$\gamma(3n, 2n(\frac{R_{\rm max}}{r_{-2}})^{1/n}) = 2^{3n} n^{3n-1} (\frac{R_{\rm max}}{r_{-2}})^3 e^{-2n(\frac{R_{\rm max}}{r_{-2}})^{1/n}} \quad . \tag{4.7}$$

The relation between $R_{\rm max}$ and r_{-2}, that we need in order to compute the observational constraints, varies depending from the value of the shape parameter $n_{\rm E}$ (see, for example, Fig. 2 in Graham et al. 2006a). Given the fact that the mass density profile of the faint dSphs is still uncertain (e.g. Walker & Peñarrubia 2011; Wolf & Bullock 2012) we prefer to use the conservative limits given by the highest and the lowest values of the shape parameter $n_{\rm E}$ as obtained from our hydrodynamical simulation. In the SPH run the smallest $n_{\rm E}$= 0.4 corresponds to a relation $R_{\rm max} = 1.447 r_{-2}$, while the largest $n_{\rm E}$= 10.4 gives $R_{\rm max} = 2.348 r_{-2}$. Using these constraints, i.e. the assumption of an Einasto model and the corresponding range of $n_{\rm E}$-values, we computed the curves in the $V_{\rm max}$-$R_{\rm max}$ plane for the nine brightest classical dSphs of the MW, namely CvnI, Carina, Draco, Fornax, Leo I, Leo II, Sextans, Sculptor and Ursa Minor, which all have $M_V \lesssim -8.8$ (we excluded Sagittarius as in Boylan-Kolchin et al. (2011) since it is far from dynamical equilibrium): these curves are constructed by normalizing each dwarf to its observationally derived values of half-light mass, $M_{1/2}$, and radius, $r_{1/2}$, from Wolf et al. (2010), who showed that any uncertainty on

[6] Vera-Ciro et al. (2013) reached similar conclusions, using semi-analytical galaxy formation models.

the stellar velocity dispersion anisotropy is minimized at this radius, leading to accurate estimation of $v(r_{1/2})$.

In the left panel of Fig. 4.4 we show the maximum circular velocity $V_{\rm max}$ and its corresponding radius $R_{\rm max}$ for all the SPH subhaloes, within the MW and M31 hosts, whose luminosity is at least as high as the Draco's one, i.e. $M_V \lesssim -8.8$. With respect to Fig. 4.2 we excluded here objects with a luminosity lower than Draco, but verified that the interval for the shape parameter $n_{\rm E}$ is still the same. In Fig. 4.5 we also show the numerically derived $V_{\rm max}$-mass relation for the SPH subhaloes, which is useful to derive the range of masses associated to a specific value of $V_{\rm max}$. The grey symbols in Fig. 4.4 correspond to the subhaloes that are brighter than Fornax, which is the brightest classical dwarf considered here to construct the observational constraints having $M_V = -13.2$, and the black circles indicate all the remaining subhaloes with luminosity $-13.2 \lesssim M_V \lesssim -8.8$. We also plot the newly constrained observational limits, as solid lines, coming from the assumption that the MW's dSphs are embedded in haloes that follow the Einasto profile with varying shape parameter $n_{\rm E}$ between $0.4 \lesssim n_{\rm E} \lesssim 10.4$, and, as dashed lines, the previously used constraints coming from the NFW model.

We observe that, while the employment of an Einasto profile leads to a good agreement between observations and the SPH subhaloes,[7] it still appears to be not sufficient to explain the $R_{\rm max}$-$V_{\rm max}$ pairs of the most massive SPH subhaloes which still lie in the lower right part of the plane, outside the constraints. Note that with a shape parameter varying between $0.4 \lesssim n_{\rm E} \lesssim 10.4$ we have allowed the observational constraints to cover a wider range, in the $R_{\rm max}$-$V_{\rm max}$ plane, with respect to the NFW constraints, but even this assumption is not enough to reconcile simulation and observation. However, those massive SPH objects, which we color-coded in grey, appear to have a luminosity, $M_V \lesssim -13.2$, not compatible with any of the satellites used to derive the observational constraints.

We remind the reader that the data plotted in Fig. 4.4 refer to both the MW and M31 galaxies: a total number of 14 subhaloes brighter than Fornax is thus found within the two hosts (and only 11 if we relax the magnitude cut from $M_V < -13.2$ to $M_V < -14$). For each host halo we therefore have 5 to 7 objects brighter than the classical dwarfs used to compute the observational constraints. Three of them may be associated with the Large and Small Magellanic Clouds (LMC and SMC, respectively) and the Sagittarius galaxy. In fact, objects with $M_V \lesssim -16.2$ can be conservatively considered as the analogous of the LMC and SMC: we should therefore

[7] We find a complete agreement between observations and DM only subhaloes, which are though not shown in the plot for clarity.

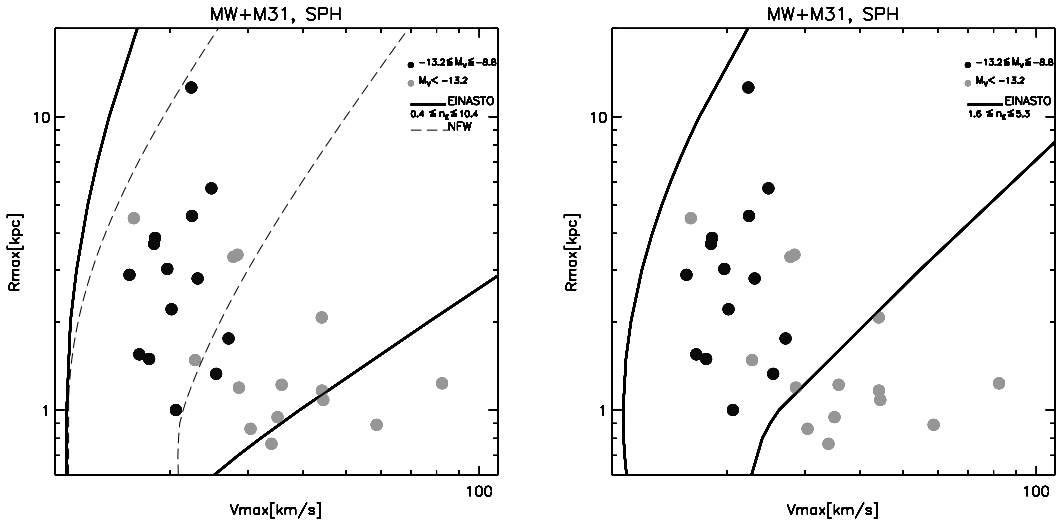

Figure 4.4: Left panel, $V_{\rm max}$-$R_{\rm max}$ pairs for the SPH subhaloes within the MW and M31 hosts. The subhaloes have been color-coded by their luminosity: in black the ones corresponding to the luminosity of the observed classical dSphs, in grey the ones which are brighter than $M_V = -13.2$. The 2σ observational constraints for the MW's dSphs are indicated as a solid line for the Einasto profile with shape parameter $0.4 \lesssim n_{\rm E} \lesssim 10.4$, obtained considering all the subhaloes with $M_V \lesssim -8.8$, and as dashed line for the NFW profile. Right panel, same criterion to color-code the subhaloes, although this time the 2σ observational constraints for the MW's dSphs are derived using an Einasto profile with shape parameter $1.6 \lesssim n_{\rm E} \lesssim 5.3$, obtained considering only the subhaloes with $-13.2 \lesssim M_V \lesssim -8.8$.

exclude these simulated subhaloes from the discussion.

With these associations there are, within each host, only two to four subhaloes left with $-16.2 \lesssim M_V \lesssim -13.2$ which do not have a counterpart in the real universe: such a small sample, i.e. the $\sim 10\%$ over the total number of objects found within each halo in the SPH run, can be explained as a statistical fluctuation due to our small number statistics. In the future, to confirm this halo-to-halo variation in the subhaloes population, it will be necessary to study many realization of a high resolution MW-like object. In this work the luminosity function, averaged over the MW and M31 subhaloes, has been shown to be in agreement with the observational data of Milky Way like galaxies (Strigari & Wechsler 2012), while slightly deviating from the Milky Way itself in the interval $-16 \lesssim M_V \lesssim -13$ (Knebe et al. 2011c) exactly because of these two to four overabundant objects in this range. Moreover, we remind that our simulation also reproduces the luminosity vs velocity dispersion correlation observed for the satellite galaxies of MW and M31 (Walker et al. 2009), as shown in Knebe et al. (2011c).

As an additional remark, we note that most of the brightest subhaloes in our simulation are the ones that experienced adiabatic contraction, being situated in the lower right part of the $V_{\rm max}$-$R_{\rm max}$ plane at redshift $z = 0$, as studied and explained in Di Cintio et al. (2011). These subhaloes are substantially different from the ones found in the work of Vera-Ciro et al. (2013), who used dark matter only simulations with semi-analytical galaxy formation models that do not show adiabatic contraction: their most luminous, brightest objects are found in the upper-right of the $V_{\rm max}$-$R_{\rm max}$ plane, contrary to what we obtained in our hydrodynamical simulations.

We now proceed to again compute the shape parameter range based only upon those subhaloes that satisfy the luminosity requirement, i.e. those objects whose M_V is within the range of the observed dSphs luminosity. We were therefore able to restrict the range, finding a shape parameter lying within $1.6 \lesssim n_{\rm E} \lesssim 5.3$, with a mean value $\overline{n}_{\rm E} = 3.2$. In the right panel of Fig. 4.4 we use the same black-grey colouring scheme for the SPH subhaloes as before, and we plot the observational limits based on the newly constrained range for the shape parameter $1.6 \lesssim n_{\rm E} \lesssim 5.3$. The result is a perfect agreement between the expected $V_{\rm max}$-$R_{\rm max}$ values of the observed dSphs and the $V_{\rm max}$-$R_{\rm max}$ pairs of the simulated subhaloes with corresponding luminosities.

We conclude that our findings, based upon self-consistent hydrodynamical simulations of a constrained Local Group in a cosmological context, strongly supports the notion that the observed satellite galaxies of the Milky Way are actually compatible with being embedded in dark matter haloes whose density profiles show considerable differences, following an Einasto

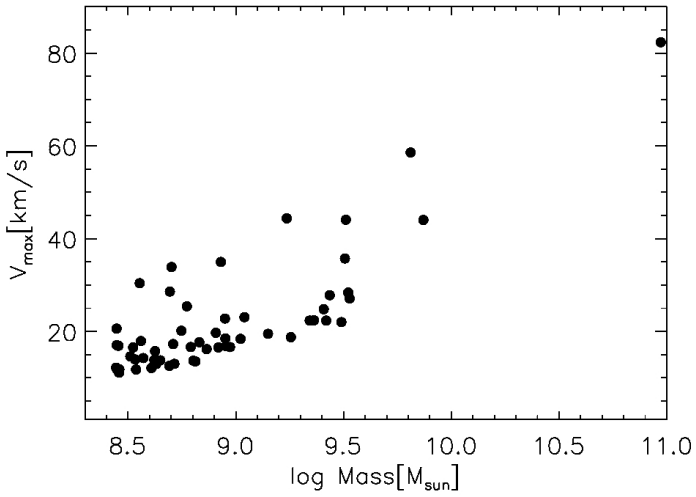

Figure 4.5: Correlation of the subhaloes maximum circular velocity with the subhaloes' masses in the SPH simulation.

model with $1.6 \lesssim n_{\rm E} \lesssim 5.3$ and mean value $\overline{n}_{\rm E} = 3.2$: the majority of the dSphs may have an inner profile shallower than the previously assumed NFW one while an outer profile steepened by tides.

4.6 Conclusion and discussion

Using a constrained simulation of the Local Group, performed within the CLUES project, it has been shown that:

- the density profile of subhaloes in both dark matter only and hydrodynamical simulations is best approximated by an Einasto profile in which the shape parameter $n_{\rm E}$ is free to vary, and that
- there is a clear trend of growing $n_{\rm E}$ with increasing subhaloes mass, in both the dark matter only and hydrodynamical run.

The structural effect associated with tidal stripping is likely the main mechanism able to modify the subhaloes' density profile: the effect of mass loss due to tidal stripping is the reduction of the shape parameter $n_{\rm E}$ between the infall and the present time. A correlation between $n_{\rm E}$ and the amount of stripped material has also been argued in Vera-Ciro et al. (2013). Differences in the inner profile of subhaloes, between the pure DM and SPH run, can instead be attributed to baryonic processes (Di Cintio et al. 2011): they

result in adiabatic contraction of the dark matter halo when gas is retained in the central regions and star formation is still on going after infall, and in expansion when gas is removed from the dwarfs due to stellar feedback and ram pressure stripping, with no signs of star formation after the subhalo has entered the host's halo. These baryonic effects, acting mainly on the inner part of the density profile, do not modify the overall $n_{\rm E}$ -mass relation which is driven by tidal stripping also in the SPH case.

The majority of our SPH subhaloes have a small $n_{\rm E}$, as reported in the right panel of Fig. 4.2: remarkably, Del Popolo & Cardone (2012) found similarly small values of $n_{\rm E}$ in observed dwarf galaxies, using high quality rotation curves. Moreover, evidences of the fact that at least some of the MW's dSphs may have a shallow profile, compatible with a small $n_{\rm E}$, are given in Walker & Peñarrubia (2011), who showed that the profiles of the Fornax and Sculptor dSphs are consistent with cores of constant density at a high confidence level. Nevertheless, the actual mass profile of the MW's dSphs is still uncertain: Wolf & Bullock (2012) claimed that, even with an isotropic velocity dispersion, not all the dSphs prefer constant-density cores and that, instead, some of them favor a cuspy inner profile. All these findings do no longer support the notion of a universal subhalo mass profile; subhaloes of differing mass cannot be rescaled to have self-similar profiles: their mass (or so to speak size) matters.

In light of these results we revisited the Boylan-Kolchin et al. (2011) observational limits for possible hosts of the MW's dSphs, assuming that the latter are embedded in haloes that follow an Einasto profile, as opposed to the earlier assumption of NFW profile, with variable shape parameter $n_{\rm E}$, and using the conservative limits $0.4 \lesssim n_{\rm E} \lesssim 10.4$ provided by our hydrodynamical simulations. While using the Einasto profile is enough to completely explain the maximum velocity of the most massive DM subhaloes, an issue still remains with respect to the most massive SPH subhaloes: these objects experienced adiabatic contraction (Di Cintio et al. 2011) and their $R_{\rm max}$-$V_{\rm max}$ pairs are still lying outside the expected observational constraints. However, these subhaloes appear to be brighter than Fornax, which is the brightest dSph used when constructing the observational constraints: thus, they should not be considered in the comparison. Once the Large Magellanic Cloud, Small Magellanic Cloud and Sagittarius galaxy analogues are removed, we still have two to four unaccounted objects per halo, whose luminosity is higher than the luminosity of the classical dwarfs: we argue that, being only 10% of the total set, they can be interpreted as a statistical deviation.

Leaving only the SPH subhaloes with $-13.2 \lesssim M_V \lesssim -8.8$, i.e. those in agreement with the luminosity of the nine classical dSphs, we show that an

Einasto profile with shape parameter $1.6 \lesssim n_{\rm E} \lesssim 5.3$ provides an accurate matching between simulations and observations, alleviating the "massive failures" problem first addressed in Boylan-Kolchin et al. (2011). The mean value of the shape parameter for them is $\overline{n}_{\rm E} = 3.2$, indicating that the majority of the MW's satellite galaxies are consistent with dark matter haloes whose profile is an Einasto one, steepened outside by the effects of tidal stripping and possibly shallower than the previously accepted NFW towards the center.

We further note that our simulated host haloes masses are at the low end of current observational estimates, and this may be one of the reason for having only a few objects in the luminosity range $-16 \lesssim M_V \lesssim -13$: Di Cintio et al. (2011) suggested that the host halo mass is directly connected to the number of massive subhaloes found in simulations, when comparing the results of dark matter only simulations based on a WMAP3 versus WMAP5 cosmology, the latter showing a higher host halo mass and consequently a higher number of massive subhaloes. The dependence of the number of "too massive subhaloes" on halo mass has been further explored and quantified by Wang et al. (2012). Boylan-Kolchin et al. (2011) extensively discussed the possibility that the reduction of the Milky Way mass could solve the problem, and recently Vera-Ciro et al. (2013) suggested that a Milky Way mass $\sim 8 \cdot 10^{11} M_{\odot}$ provides a good match between observations and semi-analytical galaxy formation models. In our simulations we have slightly lower masses for the MW and M31, between 5.5 and $7.5 \cdot 10^{11} M_{\odot}$, these values being at the low end of mass estimates obtained using different methods (Karachentsev & Kashibadze 2006; Watkins et al. 2010; Deason et al. 2012b). According to the model of Wang et al. (2012), a MW mass of $M_{MW} = 5.5 \cdot 10^{11} M_{\odot}$ will give a 84% probability of finding only three satellite galaxies with a circular velocity peak higher than $V_{\rm max} > 30$ km/s: this is what we expect since, apart from the LMC, SMC and Sagittarius, all the other classical dwarfs have been shown (e.g. Strigari et al. 2010) to inhabit haloes with a maximum circular velocity below 30 km/s. However, such a low mass for the Milky Way will reduce the probability that it hosts two satellites as the LMC and SMC; that our galaxy system is rare, with only $\sim 3.5\%$ of the MW-like candidates having two satellites as bright as the Magellanic Clouds, has been found observationally by studies using the Sloan Digital Sky Survey (Liu et al. 2011; Guo et al. 2011; Lares et al. 2011; Tollerud et al. 2011). We remark that, despite a lower Milky Way mass, subhalo density profiles should nevertheless be described by an Einasto model in order to properly match the kinematic of the observed classical dSphs with the subhaloes in hydrodynamical simulations. Finally, even assuming a small mass for the Milky Way and an Einasto profile for its satellite galaxies, there is still a problem in assigning the correct halo masses to dwarf

galaxies, as highlighted in Ferrero et al. (2012). These authors showed that the MW's dSphs, as well as many isolated dwarf galaxies with spatially resolved rotation curves and stellar mass $10^6 < M_{gal}/M_\odot < 10^7$, seem to live in haloes with $M < 10^{10} M_\odot$, which is at odds with the abundance-matching prediction of Guo et al. (2010) and Moster et al. (2010): the validity of ΛCDM at such scales is still disputable.

Chapter 5

Scale-free mass estimators applied to the Local Group

The number of satellite galaxies found in numerical simulations within the virial radius of their host halo is strongly dependent on the host halo mass itself, as highlighted in Section 3.3 (Di Cintio et al. 2011). A halo mass of about $5 - 8 \cdot 10^{11} \mathrm{M}_{\odot}$ for the Milky Way has the potential to solve the TBTF problem, as discussed in Section 4.6 (Di Cintio et al. 2013). It is fundamental therefore to have a good estimation of the mass of the host galaxy, in this case our own Milky Way and Andromeda, in order to put constraint on the expected number of bright substructures that one would find.

In this chapter, we proceed in analyzing the performance of one particular mass estimator. We use the recently proposed scale-free mass estimators (Watkins et al. 2010) to determine the masses of the Milky Way (MW) and Andromeda (M31) galaxy in a dark matter only Constrained Local UniversE Simulation (CLUES). While these mass estimators work rather well for isolated spherical host systems, we examine here their applicability to a simulated binary system with a unique satellite population similar to the observed satellites of MW and M31. We confirm that the scale-free estimators work also very well in our simulated Local Group galaxies with the right number of satellites which follow the observed radial distribution. In the isotropic case and under the assumption that the satellites are tracking the total gravitating mass, the power-law index of the radial satellite distribution $N(< r) \propto r^{3-\gamma}$ is directly related to the host's mass profile $M(< r) \propto r^{1-\alpha}$ as $\alpha = \gamma - 2$. The use of this relation for any given γ leads to highly accurate mass estimations which is a crucial point for observer, since they do not know a priori the mass profile of the MW and M31 haloes. We discuss possible bias in the mass estimators and conclude that the scale-

free mass estimators can be satisfactorily applied to the real MW and M31 system.

5.1 Introduction

Although measurements of gas rotation curves are often precise enough to constrain the inner most mass of galaxies like the Milky Way (MW) and Andromeda (M31) (within a few tens of kpc), kinematics of a tracer populations are needed to compute the mass within greater radii. These tracers can either be globular clusters or planetary nebulae (e.g. Schuberth et al. (2010);Woodley et al. (2010)), halo stars (Xue et al. 2008) or satellite galaxies (e.g. Watkins et al. (2010)). Since the kinematics of these objects are determined by the underlying host potential they allow for an estimate of the enclosed mass within their respective distances from the center of the host.

Kinematic data of galaxies in clusters have already been used to compute the mass profiles and galaxy orbits in nearby clusters (Wojtak & Łokas 2010); moreover, the mass of four Milky Way dwarf spheroidals (dSphs) satellites were constrained with high precision thanks to kinematic data sets (Łokas 2009). Line-of-sight kinematic observations enable accurate mass determinations at half-light radius for spherical galaxies such as the MW dSphs (Wolf et al. 2010): at both larger and smaller radii however, the mass estimation remains uncertain because of the unknown velocity anisotropy.

Regarding our own Galaxy, having position and proper motion data of the MW's satellite galaxies would allow one to satisfactorily apply the great majority of kinematic mass estimators to the calculus of the Milky Way's mass, including the recently proposed "scale-free projected mass estimator" (Watkins et al. 2010,hereafter W10).

In the very near future the knowledge of the full six-dimensional phase-space information for all objects, in the close Universe, brighter than $G \approx 20$ mag, is going to be dramatically improved thanks to space missions, like GAIA[1], whose goal is to create the largest and most precise three dimensional chart of the Milky Way by providing precise astrometric data like positions, parallaxes, proper motions and radial velocity measurements for about one billion stars in our Galaxy and throughout the Local Group (LG).

An et al. (2012) recently showed that new proper motions data with the targeted GAIA accuracies will be able to outperform the presently existing line-of-sight based mass estimators. But until the proper motions of these

[1] `http://www.gaia.esa.int`

satellite galaxies become available, one needs to rely on assumptions and simplifications.

One of the first estimators of the mass contained within the LG is based on the "timing" argument of Kahn & Woltjer (1959). More accurate mass estimators for spherical systems are based either on the virial theorem or on the moments of projected mass, as first introduced by Bahcall & Tremaine (1981). They assumed that only projected distances and line-of-sight velocity information were available, and demonstrated the goodness of the projected mass estimator. The main advantages of such a projected mass estimator over the virial theorem, neglecting the uncertainties in the eccentricity distribution, are that they are unbiased, their variance is known, and they converge to the real mass with an error proportional to $N^{-1/2}$, where N is the sample number. Moreover, the information from every tracer particle is equally weighted, contrary to what happens for the virial theorem case.

Previous studies successfully used these mass estimator methods to "weigh" M31; and more recently, W10 developed alternative forms of estimators that can also be applied to the calculus of the MW's mass: they rely on the assumption that both the host galaxy and its distribution of tracer objects are spherically symmetric. What is still unclear however, is the shape of the MW and M31 halo, with various authors in the literature disagreeing over whether its triaxial (Law et al. 2009) or spherical (Koposov et al. 2010).

Deason et al. (2011) and Evans et al. (2011) have demonstrated the statistical validity of the W10 mass estimators using a set of 431 parent haloes and 4864 associated satellite galaxies, taken from the GIMIC simulations (Crain et al. 2009): under the assumption of having a host profile of the type NFW (Navarro et al. 1996b), they found that the fraction of estimated halo mass which lies within a factor of two of the true mass is about 80%.

In this work we aim to gauge the quality of the method introduced in W10 by using the Local Group identified in the WMAP5 dark matter only constrained cosmological simulation of the CLUES project, a numerical laboratory for testing the applicability of such a method to the MW and M31.

Observational data of the nearby Universe are used to constrain the initial conditions of the CLUES simulations. These constrained simulations, in which the Local Group lies in the right cosmological environment, provide a complementary approach, with respect to cosmological simulations, to make a comparison between numerical results and observations. Thus, verifying the robustness of the W10 mass estimators in our unique simulated LG is an important test in addition to the more statistical methods

offered by cosmological simulations (Deason et al. 2011).

The idea is to verify whether these estimators can accurately be applied to a system such as the one found in our LG and composed of the Milky Way and the Andromeda galaxy. The arrangement and formation history of this galactic binary system, according to our present state-of-the-art of numerical simulations, is rather unique and involves preferential infall directions of their subhaloes (Libeskind et al. 2011b), a backsplash population (Knebe et al. 2011c), and even renegade satellites (Knebe et al. 2011b), i.e. satellites that change their affiliation from one of the two hosts to the other. Furthermore, the MW and M31 satellites do in fact remember the non-random nature of their infall after several orbits (Libeskind et al. 2012). We also need to mention that – when comparing constrained against unconstrained simulations – only 1-3% of the Local Group candidates share similar formation properties (Forero-Romero et al. 2011).

Moreover, the observed Milky Way satellites are found to be highly anisotropical, lying within a thin disc which is inclined with respect to the MW's one, with a minor-to-major axis ratio $c/a \approx 0.3$: this flattened distribution is not compatible with the satellites to have been randomly selected from an isotropic subset (Kroupa et al. 2005; Metz et al. 2007, 2008). Previous cosmological simulations showed anisotropy in the subhaloes population, with the brightest satellites distributed along disk-like structures, consistently with the observed MW satellites (cf. Knebe et al. 2004; Libeskind et al. 2005; Zentner et al. 2005). This anisotropy, which is also observed in our simulated subhaloes, may in principle cause a bias in the application of the mass estimator, since the hypothesis of spherical symmetry is broken.

We therefore raise (and answer) the question about the applicability of scale-free mass estimators to such a special system as the Local Group.

5.2 Simulation details

The dark matter only simulation used here forms part of the Constrained Local UniversE Simulations (CLUES) project described in Section 2.1. We used the highest resolution run in a WMAP5 cosmology (Komatsu et al. 2009) in order to reach a resolution equivalent to 4096^3 particles within a sphere of $2h^{-1}$Mpc centered on the Local Group.

Within this environment we identified two main haloes, formally corresponding to the Milky Way and the Andromeda galaxy, whose main properties are listed in Table 5.1, together with their corresponding actual observational properties. The virial mass of each halo is in units of

$10^{12} M_{\odot}$, while the virial radius and the distance between the two hosts, listed as D, are in Mpc. Both these quantities are based upon the definition $M(< R_{\rm vir})/(4\pi/3R_{\rm vir}^3) = \Delta_{\rm vir}\rho_b$ where ρ_b is the cosmological background density and $\Delta_{\rm vir} = 354$ for the considered cosmology and redshift $z = 0$. The concentration is $c_2 = R_{\rm vir}/r_2$, where r_2 denotes the "scale radius" where the product $\rho(r)r^2$ reaches its maximum value. The two axis ratios b/a and c/a are derived from the eigenvalues $a > b > c$ of the moment of inertia tensor, and the vertical-to-planar axis ratio is reported for M31. The α parameter is the exponent corresponding to a scale-free host mass profile $M(r) \propto r^{1-\alpha}$, see Section 5.3.1 for more details. The observationally derived masses are based on the work of W10, and represent the estimates of each galaxy mass assuming a virial radius of 300 kpc, using the observed anisotropy parameter β and including satellites' proper motions.

A complete summary of the characteristic of the subhaloes population of the two main haloes, MW and M31, is shown in Table 5.1, together with a comparison of the properties of their observed satellite galaxies. The haloes and sub-haloes have been identified using the `AHF` halo finder, as described in Section ahf. The $r_{\rm out}$ and $r_{\rm in}$ are the radius of the outermost and innermost tracer, respectively, in Mpc (in the case of M31 we listed the projected distances). The quantity $N_{\rm sat}$ represents the number of simulated subhaloes (or observed satellite galaxies) within 0.3 Mpc from each host center.

5.3 Scale-free mass estimators

Even though the mass estimators are derived under the assumption that the respective distributions are scale-free, they have nevertheless been successfully applied to the observed MW and M31 (W10) where the hierarchical structure formation model supports the notion that the density profile of dark matter haloes follows the functional form originally proposed by Navarro et al. (1996b), i.e. the so-called NFW profile.

Xue et al. (2008) constrained the mass distribution of the MW's dark matter halo by analyzing the kinematic of thousands of blue horizontal-branch halo stars, finding a profile that is consistent with a combination of a fixed disk and bulge model with a NFW dark matter halo. Seigar et al. (2008) have derived new mass models for M31, and found that while a NFW and an adiabatically contracted NFW profiles can both produce reasonable fits to the observed rotation curve of M31, the pure NFW model requires a halo concentration too high with respect to the range predicted by the ΛCDM cosmology, and is therefore disfavoured. Thus, it is still debatable

Table 5.1: Main properties of the two haloes (representing the MW and M31 galaxy, respectively) considered in this work, and of their respective subhaloes population. The virial mass of each halo is in units of $10^{12} M_{\odot}$, while the virial radius and the distance between the two hosts, D, are in Mpc. We listed the observational inferred quantities of MW and M31, that refer to the work of: (a) W10, (b) Law et al. (2009), (c) Banerjee & Jog (2008), (d) McConnachie et al. (2005), (e) Mateo (1998), (f) Ibata et al. (2007), (g) Martin et al. (2008), (h) Karachentsev et al. (2004).

property	MW	M31	MW	M31
	simulation		observed	
$M_{\rm vir}$	1.674	2.226	$2.7 \pm 0.5^{(a)}$	$1.5 \pm 0.4^{(a)}$
$R_{\rm vir}$	0.310	0.340	$0.300^{(a)}$	$0.300^{(a)}$
c_2	11.7	10.7	-	-
b/a	0.937	0.978	$0.83^{(b)}$	$0.4^{(c)}$
c/a	0.883	0.872	$0.67^{(b)}$	
α	-0.034	-0.052	-	-
D	0.782		$0.785 \pm 0.025^{(d)}$	
$N_{\rm sat}$	1205	1405	24	21
$r_{\rm out}$	0.309	0.340	$0.250 \pm 0.003^{(e)}$	$0.270^{(f)}$
$r_{\rm min}$	0.018	0.014	$0.023 \pm 0.002^{(g)}$	$0.005^{(h)}$

whether the Milky Way and Andromeda galaxy haloes actually follow a NFW profile.

In this Section we briefly introduce the scale-free mass estimators, which are directly taken from W10: we refer the reader to their work for a derivation of the respective formulae.

5.3.1 Theory of mass estimators

Here we present the four relevant formulae and the three parameters each formula depends on: we see that the mass estimator takes different forms according to the available informations from the tracer populations.

Full Information Estimator (FIE)

In the optimum case that the full six-dimensional phase-space information is accessible, the mass estimator can be written as:

$$M(< r_{\rm out}) = \frac{C}{G}\frac{1}{N}\sum_{i=1}^{N_{\rm tracer}} v_i^2 r_i^{\alpha}, \tag{5.1}$$

$$\text{with } C = \frac{\alpha+\gamma-2\beta}{3-2\beta} r_{\rm out}^{1-\alpha} \tag{5.2}$$

Where v and r are the velocity and distance of each individual tracer particle, $r_{\rm out}$ represents the radius of the outermost tracer, and G is the gravitational constant. The dimensional constant C is constructed out of three additional parameters determined by the host potential (α), the tracer's radial distribution (γ), and the tracer's velocity anisotropy (β), more details in Section 5.3.1 where these parameters are algebraically defined. Note that we can only estimate the halo mass contained within the outer radius $r_{\rm out}$ set by the distance to the farthest tracer. The mass is then constructed as an average of $v^2 r^{\alpha}$ over the total number of tracer objects, $N_{\rm tracer}$. We will refer to Eq. (5.1) as the Full Information Estimator or simply FIE.

Radial Information Estimator (RIE)

In the case that only the radial velocity, with respect to the center of the host galaxy, and the individual distances of the tracer population are known, v_r and r respectively, a different definition of the constant C must be used:

$$M(< r_{\rm out}) = \frac{C}{G}\frac{1}{N}\sum_{i=1}^{N_{\rm tracer}} v_{r,i}^2 r_i^\alpha, \tag{5.3}$$

$$\text{with } C = (\alpha + \gamma - 2\beta) r_{\rm out}^{1-\alpha} \tag{5.4}$$

We shall call this the Radial Information Estimator, RIE: this case applies to our own Milky Way. Since we do not have the proper motion of all of its satellites, but just of 9 of them (see for instance Metz et al. (2008)), it is safer to assume the RIE. It must be noticed that in absence of proper motion v_r may be calculated from v_{los} by using the statistical correction:

$$< v_r^2 >= \frac{< v_{los}^2 >}{1 - \beta \sin^2 \phi} \tag{5.5}$$

where ϕ is the angle between the vector from the galactic centre to the satellite and the vector from the sun to the satellite. As we can see, this correction further depends from the anisotropy parameter β. We will come back to the proper placement of the observer and the relevance of this correction, respectively, later on.

Line-of-Sight Information Estimator (LIE)

When using only projected line-of-sight velocities v_{los} and actual distances r for the tracer population, the mass estimator referred to as the Line-of-sight Information Estimator, or LIE, and may be written as:

$$M(< r_{\rm out}) = \frac{C}{G}\frac{1}{N}\sum_{i=1}^{N_{\rm tracer}} v_{los,i}^2 r_i^\alpha, \tag{5.6}$$

$$\text{with } C = \frac{3(\alpha + \gamma - 2\beta)}{3 - 2\beta} r_{\rm out}^{1-\alpha} \tag{5.7}$$

This estimator must be used, for example, when calculating the mass of the Andromeda galaxy.

Projected Information Estimator (PIE)

In the worst case scenario in which the only data available are both projected distances R and line-of-sight velocities v_{los} for the tracer population, the corresponding estimator is:

$$M(< r_{\rm out}) = \frac{C}{G}\frac{1}{N}\sum_{i=1}^{N_{\rm tracer}} v_{los,i}^2 R_i^\alpha, \tag{5.8}$$

$$\text{with } C = \frac{\alpha+\gamma-2\beta}{I_{\alpha,\beta}} r_{\rm out}^{1-\alpha} \tag{5.9}$$

where

$$I_{\alpha,\beta} = \frac{\pi^{1/2}\Gamma(\frac{\alpha}{2}+1)}{4\Gamma(\frac{\alpha}{2}+\frac{5}{2})}\left[\alpha+3-\beta(\alpha+2)\right] \tag{5.10}$$

and $\Gamma(x)$ is the gamma function. We will refer to this last equation as the Projected Information Estimator, PIE.

The parameters α, β, and γ

The ever present constant C is composed of three parameters, describing the host potential as well as particulars of the tracer population, under the assumption that they both can be sufficiently described by scale-free models. We further assume spherical symmetry for our tracer population.

The α parameter corresponds to a scale-free gravity field, which is equivalent to a host mass profile of the form:

$$M(r) \propto r^{1-\alpha} \tag{5.11}$$

or, equivalently, to a mass density that scales as $\rho \propto r^{-(\alpha+2)}$.

The β parameter is the Binney velocity anisotropy parameter (Binney & Tremaine 1987), defined as:

$$\beta = 1 - \frac{\sigma_t^2}{2\sigma_r^2} \tag{5.12}$$

in which σ_t^2 and σ_r^2 are the tangential and the radial velocity dispersions of the tracer objects. β provides information about the orbital distribution of our tracer population.

Lastly, the γ parameter represents the exponent of the power law describing the radial number density distribution $n(r)$ of the tracer population:

$$n(r) \propto r^{-\gamma}. \tag{5.13}$$

These three parameters are fundamental in describing the geometry of the system and, together with the kinematical information of the tracers, allow us to compute an accurate estimator of the mass of a host halo. It is thus absolutely essential that they are determined with the highest possible accuracy. In reality however, this is not always possible: we are often forced to make assumptions regarding the form of the underlying host potential. Moreover, the number of the known satellites of both Milky Way and Andromeda is only ~ 25, making the determination of the γ parameter relatively inaccurate. In addition, in the Milky Way's case, only 7 of these objects have accurately measured proper motions: with such a small sample the velocity anisotropy β is widely unconstrained by data. In the next Section 5.3.2 we will present the dependence of the mass estimator on each of these parameters, computing – for a specific case – the error introduced by uncertainty in α, β, and γ, respectively.

5.3.2 Dependence of the mass estimators on the parameters

Given the inherent inaccuracy in determining the three model parameters, we would like to gauge the sensitivity of the mass estimators to their uncertainties, considering an adequate set of subhaloes covering a radial range out to $r_{\rm out}$.

γ dependence

We aim to study the dependence of the mass estimator on the parameter γ, which represents the exponent describing the radial distribution of the satellites population. We therefore calculated the relative variation of the estimated mass per variation in γ:

$$\frac{\Delta M}{M \Delta \gamma} = \frac{1}{\alpha + \gamma - 2\beta} \tag{5.14}$$

We note that Eq. (5.14) is valid for the four cases of FIE, RIE, LIE and PIE, being independent from the radial distribution of satellites; it provides a tool for calculating the expected uncertainty in the mass determination given the expected errors in γ.

Assuming an isotropic distribution of orbits, i.e. $\beta = 0$, we focus on the real case scenario in which the γ parameter is $\gamma \cong 2$ (as found in W10

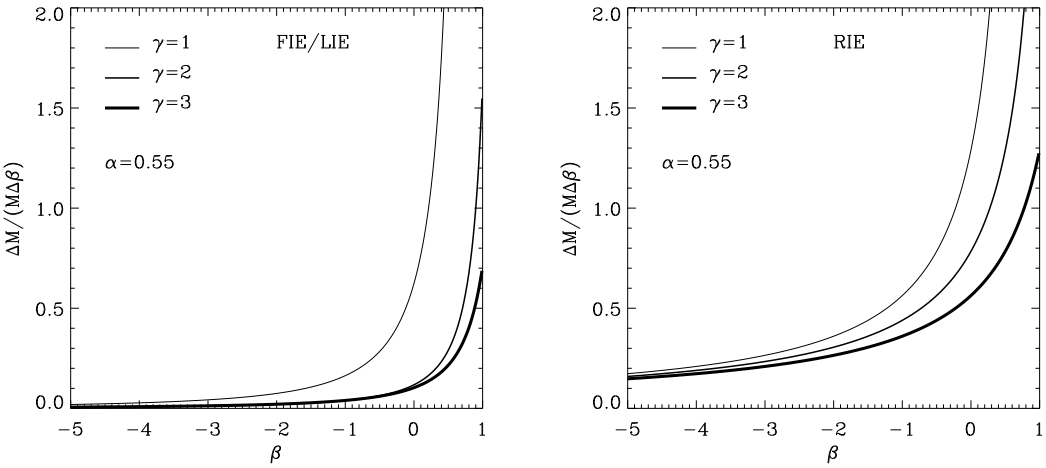

Figure 5.1: Relative variation per unit parameter change of the mass estimated as a function of the β parameter in the case of FIE/LIE (left panel) and RIE (right panel) estimators. The fractional error in the mass estimation is larger for the RIE estimator, used for MW, than for the FIE/LIE estimators, applicable to M31. See full text for more details.

for the observed satellites of MW and M31): allowing for an uncertainty of $\Delta\gamma/\gamma \sim 25\%$, and recalling the typical value for α that is around 0.55 for a NFW host (e.g., W10), we see that the error in the estimated mass is as high as $\Delta M/M \sim 20\%$. This error will be even larger when considering smaller value of γ and α, as well as for $\beta > 0$.

β dependence

Regarding the changes in the mass estimation due to the anisotropy parameter, we recall that this parameter is directly obtained from the velocities of the tracer population, computing the tangential and the radial velocity dispersion of each subhalo (as opposed to the α and γ parameter, which are derived by assuming a power law distribution). The β average value has been found to be $\beta \sim -0.3$ and $\beta \sim -0.02$ in our CLUES simulation, for the full set of subhaloes of the MW and M31, respectively. While these values of β indicate that we are close to the isotropic regime, i.e. $\beta = 0$, the MW anisotropy parameter slightly favors tangential orbits, in agreement with the measured proper motions of the known MW satellites. It is thus essential to understand how the variation in the β parameter affects the determination of the host mass. For the RIE estimator the corresponding equation reads

$$\left(\frac{\Delta M}{M\Delta\beta}\right)_{RIE} = \frac{-2}{\alpha+\gamma-2\beta} \tag{5.15}$$

whereas for the FIE and LIE cases it is

$$\left(\frac{\Delta M}{M\Delta\beta}\right)_{FIE,LIE} = \frac{2}{3-2\beta} - \frac{2}{\alpha+\gamma-2\beta} \tag{5.16}$$

finally, for the PIE scenario

$$\left(\frac{\Delta M}{M\Delta\beta}\right)_{PIE} = \frac{\alpha+2}{\alpha+3-\beta(\alpha+2)} - \frac{2}{\alpha+\gamma-2\beta}. \tag{5.17}$$

In Fig. 5.1 we present the absolute value of the fractional mass variation as a function of the β value for the FIE and LIE cases (left panel) and for the RIE estimator (right panel). We do not plot the mass changes in the PIE case, as it is practically identical to the FIE and LIE ones. As in the previous section, considering the general case of having a NFW halo, with values of β close to zero and $\gamma = 2$, which is the usual case for the hosts considered here and elsewhere (e.g., W10), we find that the error due to variations of $\Delta\beta = \pm 1$ for the FIE, LIE and PIE estimators is actually quite low and is below 10% for $\alpha = 0.55$. Moreover, Evans et al. (2011) found that for much of the radial regime covered by the tracer population, any variation of the anisotropy parameter within its physical range leads to the same estimator in the case of the PIE scenario. Thus, in the case of an external galaxy whose dark matter halo follows a NFW profile with $\alpha = 0.55$ and $2 < \gamma < 3$, we can assume to have a minor error due to β: the major uncertainty in the mass estimation comes from the assumption made on the α and γ parameters. This last statement is valid for the FIE, LIE and the PIE estimator: it does not matter if we have real satellites distances or projected ones, the biggest error on the mass does not come from the anisotropy parameter.

The situation is however, completely different for the MW galaxy, for which the RIE formula holds, i.e. we have radial information on the satellite velocities. In this case, a variation of $\Delta\beta = \pm 1$ could cause an error in the mass estimation of around 80% if we have $\gamma = 2$ and $\alpha = 0.55$. Therefore, the β parameter is unfortunately the greatest concern in the calculus of the mass of our own Galaxy. Please note that if we knew the three dimensional velocities of the MW satellites as opposed to only the radial ones, we would

be dealing with Eq. (5.16), thus being in the regime in which the correct evaluation of the β parameter will only have a subordinate influence.

We close by remarking that this discussion perfectly agrees with the previous study of the influence of the β parameter on the mass estimation as presented in W10.

α dependence

Finally, we computed the amount or error introduced by uncertainties in the α parameter, which is directly connected to the potential of the host halo. The fractional variation of the estimated mass, for the FIE estimator, is:

$$\left(\frac{\Delta M}{M\Delta\alpha}\right)_{FIE} = \frac{1}{\alpha+\gamma-2\beta} - \ln(r_{\rm out}) + \frac{\sum_i v_i^2 r_i^\alpha \ln(r_i)}{\sum_i v_i^2 r_i^\alpha} \tag{5.18}$$

where the summation, as usual, is performed over the total number of tracers $N_{\rm tracer}$ and $r_{\rm out}$ is the radius of the outermost subhalo. Eq. (5.18) is formally identical for the RIE and LIE case as well, after substituting the full velocity v with the radial velocity v_r or the line-of-sight v_{los} one, respectively.

When dealing with the PIE scenario, instead, the error can be calculated through the following equation :

$$\left(\frac{\Delta M}{M\Delta\alpha}\right)_{PIE} = \frac{1}{\alpha+\gamma-2\beta} - \ln(r_{\rm out}) + \frac{\sum_i v_{los,i}^2 R_i^\alpha \ln(R_i)}{\sum_i v_{los,i}^2 R_i^\alpha} + \\ + \frac{\Psi(\frac{\alpha}{2}+\frac{5}{2})}{2} - \frac{\Psi(\frac{\alpha}{2}+1)}{2} - \frac{1-\beta}{\alpha+3-\beta(\alpha+2)} \tag{5.19}$$

where $\Psi(x)$ is the digamma function, defined as the derivative of the logarithm of the $\Gamma(x)$ function.

Unlike the other cases, we can not give a generalized estimation of the error introduced by the α parameter, it being dependent on the radial distribution of the satellites population: this uncertainty varies for every specific scenario and needs to be calculated individually.

5.4 Application to the CLUES simulation

We now move to the application of the scale-free mass estimators to a situation as close as possible to our Local Group. To this extent we use the CLUES simulation introduced in Section 5.2. While we are certain that the scale-free approximation leads to credible results as shown by W10, Evans et al. (2011) and Deason et al. (2011), it remains to be seen whether the uniqueness of the Local Group with its binary host system and particular formation history involving preferential infall (Libeskind et al. 2011b), renegade satellites (Knebe et al. 2011b) and anisotropically distributed subhaloes (not explicitly shown here) will effect the mass estimate. Moreover, we would like to gauge the accuracy of these mass estimators when fewer tracers are used, as in the real LG.

From now on we will refer to the case of an observer that is placed at the center of our Galaxy and looking towards the MW's satellites or to the nearby M31's ones. The choice to put the observer in the galactic center instead that at the solar radius may affect the determination of v_r from v_{los}, given the fact that the radial velocity should be computed with respect to the sun. However, this is practically identical to the radial velocity with respect to the galactic center for distant tracers, for which $\sin\phi \sim 0$, which is the case for our subhaloes. Moreover, the anisotropy parameter β, which appears in the correction factor of Eq. (5.5), has always been found to be very close to zero in our simulations (as reported in Section 5.3.2). Nevertheless, when applying the different mass estimators we also used the correction factor given by Eq. (5.5), placing the observer on a sphere of radius 8 kpc from the galactic center, and we verified that the affect of this correction is at the $< 0.5\%$ level. We will thus refer, through this study, to the case of an observer placed in the galactic center.

5.4.1 Obtaining the parameters α, β and γ

In order to apply the mass estimator method to our simulated galaxies, we need to calculate the three unknowns α, β and γ that appear in Eq. (5.1),(5.3),(5.6) and Eq. (5.8).

The satellite parameters: γ and β

The γ parameter is simply obtained by fitting the radial number distribution $N(< r)$ of each host's subhaloes to the functional form

$$N(< r) \propto r^{3-\gamma}, \tag{5.20}$$

assuming that the number density $n(r)$ follows Eq. (5.13).

The velocity anisotropy parameter β, as defined in Eq. (5.12), is obtained by first calculating the radial velocity dispersion of the subhaloes, projecting their velocities along the radial axis, then by computing the tangential component of σ through the relation

$$\sigma_t^2 = \sigma_{tot}^2 - \sigma_r^2 = (\sigma_x^2 + \sigma_y^2 + \sigma_z^2) - \sigma_r^2. \tag{5.21}$$

While β and γ can be directly computed in the FIE and RIE cases, in order to calculate them in the LIE scenario we first need to derive the line-of-sight component of the velocity vectors of the subhaloes. The line-of-sight velocity depends on the viewing angle of the host which is unknown in our simulations. We thus randomly rotate each host and its subhaloes $N_{rot} = 5$ times, taking the mean of all these resulting line-of-sight velocity to compute β. We perform a small number of rotations of the whole system since otherwise, by averaging over a higher number of rotations, we converge to the FIE case. The same methodology has been applied to the PIE case where we additionally had to project the distances of the tracers objects into the observers plane in order to obtain the γ parameter.

The host halo parameter: α

To get the value of α, we must recall that since our haloes are not scale-free but rather follow a NFW profile (Navarro et al. 1996b), the applicability of a power-law is limited. While for a pure scale-free model it is irrelevant whether we fit the gravitational potential, the density or the mass profile of the host halo (see W10), it will most certainly lead to differences when the scale-invariance is broken. Recall that for a scale-free model:

$$\phi(r) \propto r^{-\alpha} \quad \Leftrightarrow \quad \rho(r) \propto r^{-\alpha-2} \quad \Leftrightarrow \quad M(r) \propto r^{1-\alpha}. \tag{5.22}$$

For a NFW object however, we must identify which quantity is the most suitable to be fitted, and we decided to use the cumulative mass profile $M(r)$ since this is the least noisy from a numerical point of view.

Furthermore, since our halo does not follow a scale-free profile (either in mass or in potential), the actual value of α depends on the radial range

Table 5.2: Value of the α parameter and its fractional error $\Delta\alpha/\alpha$ obtained by fitting the numerical mass profiles of the MW and M31 over different radial ranges.

	MW		*M*31	
Radial Range	α	$\frac{\Delta\alpha}{\alpha}$	α	$\frac{\Delta\alpha}{\alpha}$
$[0,1]R_{\rm vir}$	-0.034	70 %	-0.052	60%
$[0.4,1]R_{\rm vir}$	0.302	8%	0.266	9%
$[0.8,1]R_{\rm vir}$	0.398	3%	0.402	7%

used to fit it, i.e. $\alpha(r) \neq const.$
We thus provide, in Table 5.2, the numerically fitted values of α, obtained by fitting the total mass halo profile in different radial ranges, specifically in the total range, in the outermost one, and in the intermediate range, together with their fractional relative errors, where we indicate with $\Delta\alpha$ the 1σ error on α as found from the fitting routine.

As in the previous case of the γ parameter, we used a Poissonian weight $(1/N_{sub})$ to associate errors to the data during the fit: as expected, the smallest relative error is obtained in the outermost radial range, confirming that in this regime the host density profile is best approximated as being of scale-free nature.

We obtained for the MW and M31 in the total radial range a value of $\alpha = -0.034$ and $\alpha = -0.052$ respectively, as listed already in Table 5.1, while we can observe how the α value increases when we move to the outer part of the halo, as expected if the halo is following a NFW profile, since it gets steeper towards the outer part of the distribution.

While using the numerical mass profile given by the simulation data is actually a self-consistent way to obtain α, we note that an observer would require a mass model to actually determine the α parameter to be used with the mass estimators. Since an observer does not have any a-priori knowledge of the radial mass distribution (or potential) of the host halo, an analytical profile must be assumed. Note that W10 showed that for an object following a NFW profile the typical value of α is ≈ 0.55, based upon fitting a NFW potential in the range $[10, 300]$ kpc to a power-law $\phi \propto r^{-\alpha}$ and assuming to have hosts with concentration between $c = 18$ and $c = 8$. Given the uncertainty on the actual density profile of the real hosts, we decided to allow for the estimates of α in two different ways:

1. using the values derived by fitting our numerical profile at different

radial ranges, or

2. using the relation $\alpha = \gamma - 2$, which holds true if the subhaloes are tracking the total gravitating mass of the hosts.

5.4.2 Results for the simulated MW and M31

The application of the scale-free mass estimator to the (observationally) unrealistic scenario in which we have $N \sim 1000$ tracers, as found in our simulated haloes, gives excellent results for all the estimators FIE, RIE, LIE and PIE. Using the error formulae listed in Section 5.3.2, and allowing a maximum error on the calculation of the parameters α, β and γ of about $\sim 20\%$, we obtained the MW mass at the $R_{\rm vir} = 309$ kpc within a 5% of uncertainty and the M31 mass at the $R_{\rm vir} = 340$ kpc within a 3% of error, respectively (FIE estimator). However, we decided not to show these results and rather focus on more interesting and practical situations where the number of tracer objects is limited and agrees better with the actual observed Local Group. We must note however, that part of our initial questions has been already answered by this exercise: the scale-free mass estimators are even applicable to a *system* of host haloes such as the (observed) Local Group for which they were originally designed.

Matching the number of the observed satellites

As shown in Table 5.1, the total number of subhaloes found within 300 kpc in our simulations substantially differs from the number of observed satellites galaxies of the Milky Way and Andromeda within the same radius (the well known missing satellites problem, first addressed in Klypin et al. (1999b) and Moore et al. (1999)). Thus, we would like to calculate the accuracy of the mass estimators when the number of tracers is comparable to the real one, i.e. $N \sim 30$ (we explicitly chose this number to be able to have a direct comparison with the W10 results, see for example their Fig.1). Further, the real case scenario is the one for which we have the radial velocities of the MW satellites and the line-of-sight velocities of the M31 tracers: in the forthcoming analysis we will thus only use the RIE estimator for the Milky Way and the LIE one for the Andromeda galaxy.

From the total set of subhaloes we randomly selected $N = 30$ objects that covered the total range within $r_{\rm out} < 300$ kpc and computed their velocity anisotropy and their radial distribution, thus obtaining the β and γ coefficients. For this particular exercise, the α parameter was numerically evaluated using the three different radial ranges of the host mass profile

Table 5.3: Mean value and standard deviation of the Gaussian distribution of the estimated mass over the true mass for the MW and M31 hosts, using the RIE and the LIE, respectively, for the three considered values of α (cf. Table 5.2). The number of subhaloes has been limited to 30 random ones, and they have been used to compute β and γ for each realization. The average values of these parameters over the total $N = 1000$ realizations are $\gamma = 1.63 \pm 0.12$ and $\beta = -0.307 \pm 0.061$ for the MW, and $\gamma = 2.013 \pm 0.013$ and $\beta = -0.006 \pm 0.001$ for M31.

MW			*M*31		
α	μ	σ	α	μ	σ
-0.034	1.057	0.204	-0.052	1.060	0.257
0.302	0.992	0.177	0.266	0.958	0.167
0.398	0.975	0.169	0.402	0.931	0.159

listed in Table 5.2 (ignoring the option to evaluate it as $\alpha = \gamma - 2$ for the moment). For each of these values of α we performed 1000 random realization, we applied the scale-free mass estimator and we calculated the distribution of the ratio of the estimated over the actual mass, i.e. $M_{\rm est}/M_{\rm true}$; those distributions have then been fitted by a Gaussian curve eventually leading to the best-fit parameter μ and its standard deviation σ.

The results of these tests (for the α value evaluated from the total radial range, i.e. first line of Table 5.2) are summarized in Fig. 5.2 for the MW and Fig. 5.3 for M31 where we plot in the left panels the distributions of $M_{\rm est}/M_{\rm true}$ for the FIE mass estimators and in the right panels the RIE (MW) and LIE (M31), respectively. The legends of each panel further list the three parameters α, γ, and β relevant for the respective mass estimator (where β and γ represent the average value over the total 1000 realizations) alongside the peak and standard deviation of the best fit Gaussian. Note that the standard deviation is compatible with $1/\sqrt{N_{sub}}$ where N_{sub} is the number of used tracers, and it increases when only radial velocities (or line-of-sight ones) are used. Remarkably, the mean of the distribution stays always very close to $\mu = 1.0$: the mass estimators are thus unbiased with respect to the number of used objects. We repeated the above mentioned analysis for the other values of α listed in Table 5.2, and found practically indistinguishable results: the best-fit μ and σ values are given in in Table 5.3.

In summary, we found that for both host systems the mass is always recovered within a few percent of error when restricting the analysis to 30 randomly selected subhaloes each.

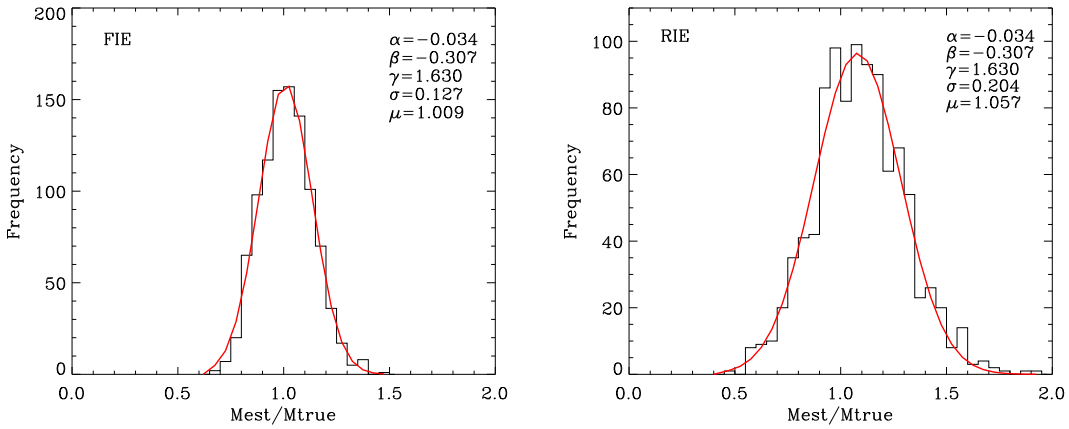

Figure 5.2: Distribution of 1000 realizations of the estimated mass over the real one for 30 subhaloes of the simulated Milky Way. The average value of the parameters β and γ obtained in each realization is shown. The best-fit Gaussian is also plotted, and its mean μ and standard deviation σ are indicated. The left panel corresponds to the FIE estimator, the right panel to the RIE one.

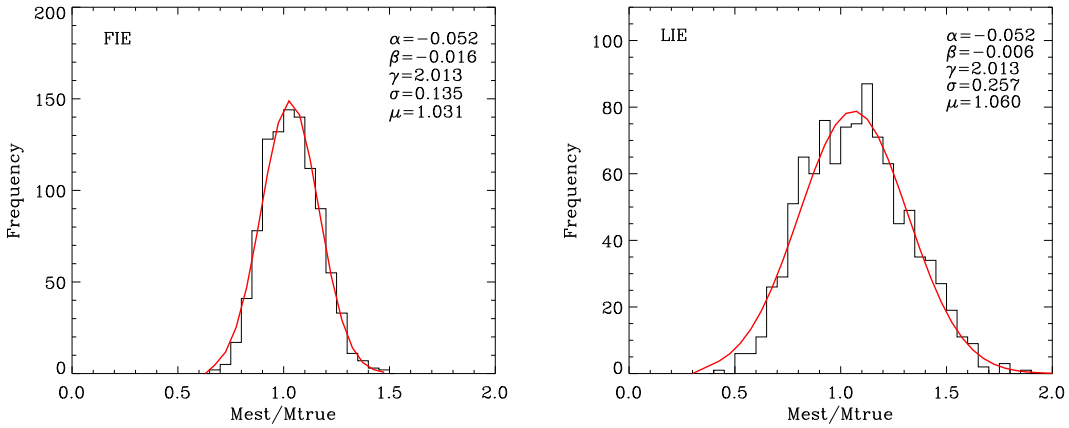

Figure 5.3: Distribution of 1000 realizations of the estimated mass over the real one for 30 subhaloes of the simulated Andromeda galaxy. The average value of the parameters β and γ obtained in each realization is shown. The best-fit Gaussian is also plotted, and its mean μ and standard deviation σ are indicated. The left panel corresponds to the FIE estimator, the right panel to the LIE one.

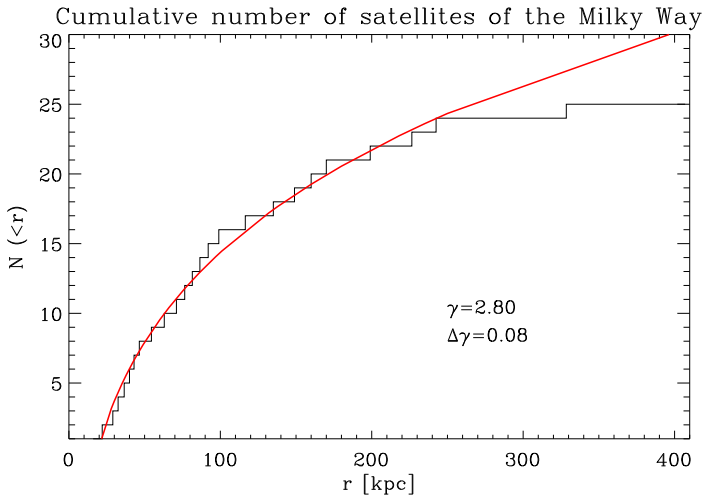

Figure 5.4: Radial distribution of the observed MW satellites and corresponding best fit in the range $r < 300$ kpc.

Matching the radial number distribution of the observed satellites

While using 30 randomly chosen subhaloes leads to exceedingly well recovered host masses, we acknowledge that our model subhaloes (for the MW) do not follow the same radial distribution as the observed ones (why this is the case is substance for yet another study and shall not be addressed here): we list in Table 5.4 the distances to all presently known MW satellites (taken from Wadepuhl & Springel 2011) alongside their masses and use this data to obtain the observed $\gamma \pm \Delta\gamma = 2.80 \pm 0.08$ by fitting the radial distribution to a power-law in Fig. 5.4. Please note that we only focus on the MW's subhaloes here, as in the case of M31 the $\gamma = 2.013$ coefficient is very similar to the one obtained from the observed satellites distribution (see W10).

From the total set of subhaloes in our numerical MW, we constructed a subset of 30 tracers by selecting those objects that follow the radial distribution $N(< r) \propto r^{3-2.8}$. Further care was taken to verify that the randomly selected subhaloes always cover the (observational) radial range up to $\sim$ 300kpc. While the $\gamma = 2.8$ is fixed by construction the β has always been derived from this subset; for the α we first used, again, the three values listed in Table 5.2, and we found a notable bias in the Gaussian distribution of $M_{\rm est}/M_{\rm true}$, as high as the 80%: this choice of α does not provide the expected host mass. Thus, we secondly decided to verify if the assumption that the tracers are tracking the total gravitating mass of the host can pro-

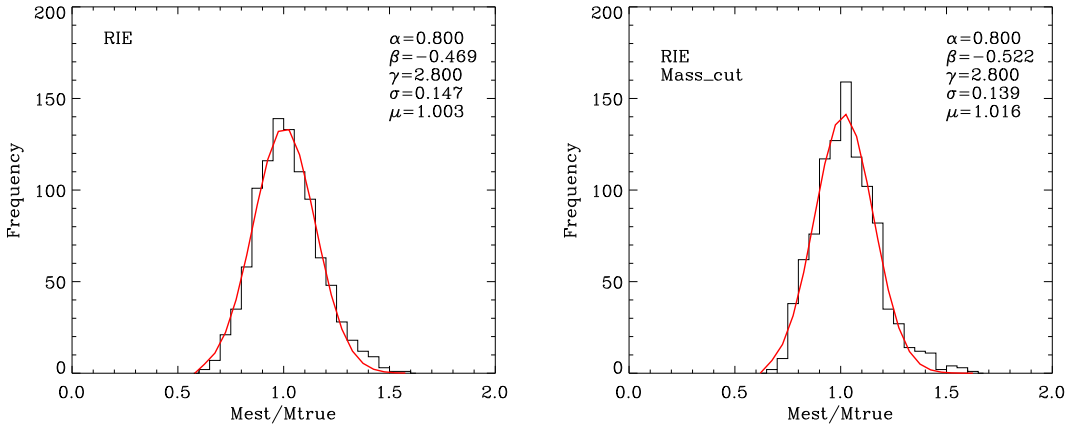

Figure 5.5: Distribution of the estimated RIE mass over the real one for 30 subhaloes of the Milky Way and 1000 realizations. The subhaloes have been selected following the power law with $\gamma = 2.8$ (left panel) as well as additionally also constraining them to lie within the observed mass range (right panel). Note that in both cases α has been determined as $\alpha = \gamma - 2$.

vide a better constrain on the value of α, i.e. using the relation $\alpha = \gamma - 2$. In this case, without making any fits to the numerical shape of the host profile, we actually found results in excellent agreement with the true mass, as shown in the left panel of Fig. 5.5. In the right panel of the same figure we show the distribution obtained when yet another additional constraint was added, i.e. we selected only those subhaloes whose mass lies between $5 \cdot 10^6 < M/M_\odot < 1 \cdot 10^8$, in order to resemble the average mass of the observed MW satellites (see Table 5.4). Also in this case we can observe that the Gaussian is peaked very close to 1.0, at $\mu = 1.016$.

We finally decided to also test and use the suggested value of $\alpha = 0.55$ (W10), but we actually obtained a Gaussian mean value for μ that is biased by approximately 30% towards large estimated masses.

In summary, even when restricting the subhaloes to follow the same power-law as the observed satellites within the same mass range, the scale-free mass estimators are capable of recovering the true mass of our constrained MW and M31 if one chooses to use $\alpha = \gamma - 2$ (being close to the isotropic regime, i.e. $\beta = 0$ and as far out as $\beta = -0.5$).

Table 5.4: List of the MW satellites used in this work, corresponding to those lying within 300kpc from the galactic center and with measured line-of-sight velocities. The Galactocentric distances D are in kpc. The values are from: (a) Martin et al. (2008), (b) Mateo (1998), (c) Belokurov et al. (2008), (d) van den Bergh (1994), (e) Belokurov et al. (2009), (f) Simon & Geha (2007), (g) Bekki (2008), (h) van den Bergh (2000).

Name	$D[kpc]$	$Mass[10^6 M_\odot]$
$BooI^{(a)}$	66 ± 3	-
$BooII^{(a)}$	42 ± 8	-
$Carina^{(b)}$	101 ± 5	13
$Com^{(a)}$	44 ± 4	$1.2 \pm 0.4^{(f)}$
$CVnI^{(a)}$	218 ± 10	$27 \pm 4^{(f)}$
$CVnII^{(a)}$	160^{+4}_{-5}	$2.4 \pm 1.1^{(f)}$
$Draco^{(a)}$	76 ± 5	22
$Fornax^{(b)}$	138 ± 8	68
$Her^{(a)}$	132 ± 12	$7.1 \pm 2.6^{(f)}$
$LeoI^{(b)}$	250 ± 30	22
$LeoII^{(b)}$	205 ± 12	9.7
$LeoIV^{(a)}$	160^{+15}_{-14}	$1.4 \pm 1.5^{(f)}$
$LeoV^{(c)}$	180	-
$LMC^{(d)}$	49	$10.000^{(g)}$
$Sag^{(b)}$	24 ± 2	$150^{(h)}$
$Sculptor^{(b)}$	79 ± 4	6.4
$SegI^{(a)}$	23 ± 2	-
$SegII^{(e)}$	35	$0.55^{+1.1}_{-0.3}$
$Sextans^{(b)}$	86 ± 4	19
$SMC^{(d)}$	58	$400^{(g)}$
$UMaI^{(a)}$	96.8 ± 4	$15 \pm 4^{(f)}$
$UMaII^{(a)}$	30 ± 5	$4.9 \pm 2.2^{(f)}$
$UMi^{(b)}$	66 ± 3	23
$Wil1^{(a)}$	38 ± 7	-

Do we require a host mass profile or simply $\alpha = \gamma - 2$?

The analysis in the previous subsection has shown that simply using $\alpha = \gamma - 2$ actually leads to excellent results for the scale-free mass estimators when applied to our constrained Local Group and a subhalo population restricted to follow the observed one as closely as possible. But can this finding be generalized, at least with respects to our simulation?

To verify that the assumption $\alpha = \gamma - 2$ holds true in general, we select the subhaloes of both MW and M31 in order to follow different radial distributions, according to $N(< r) \propto r^{3-\gamma}$, where we allowed the γ to vary between 1.5 and 3.0. The α coefficient was then calculated consequently, while the β, as usual, came from the selected satellites velocity dispersions. In this way we selected $N = 30$ subhaloes again for 1000 times and we obtained Gaussian distributions of the $M_{\rm est}/M_{\rm true}$ quantity. We show the best-fit μ, with the standard deviation σ as error bars, as a function of γ in Fig. 5.6 for the MW (left panel, RIE only) and M31 (right panel, LIE only). The anisotropy parameter was always found to be close to $\beta \sim 0$, with a maximum variation between $-0.3 < \beta < 0.1$, indicating that we are in the isotropic regime. We would like to highlight that despite other choices of α may in principle be possible, as demonstrated in Section 5.4.2, the simple assumption $\alpha = \gamma - 2$ provides always the best estimation for the host mass, whose associated Gaussian distribution has mean value μ closer to 1 and smaller standard deviation σ.

We see that the simple assumption, that the satellites track the total mass of the host halo, is sufficient to give an excellent estimation of the parameter α to be used. The suggested value of $\alpha = 0.55$, indicative of a NFW halo potential, is thus recommendable when the satellite distribution follows a power law with exponent $\gamma \sim 2.5$: these values have been already successfully used in Deason et al. (2011) and Evans et al. (2011). This is of fundamental importance for observations: without having any a-priori knowledge about the host halo density profile, we can simply use the value $\alpha = \gamma - 2$ once we have calculated γ from the satellite distribution. This condition has been verified in our constrained simulations only, in which the anisotropy parameter is always $\beta \sim 0$: care should be taken when dealing with satellite populations whose β is highly anisotropic.

In summary, we have shown that our two model hosts within the simulated constrained Local Group allow the application of scale-free mass estimators to them. And, for as long as we are in the isotropic regime in which $\beta = 0$, the simplifying assumption of $\alpha = \gamma - 2$ can be used. This alleviates the need to derive this parameter from a model of the host potential or mass profile.

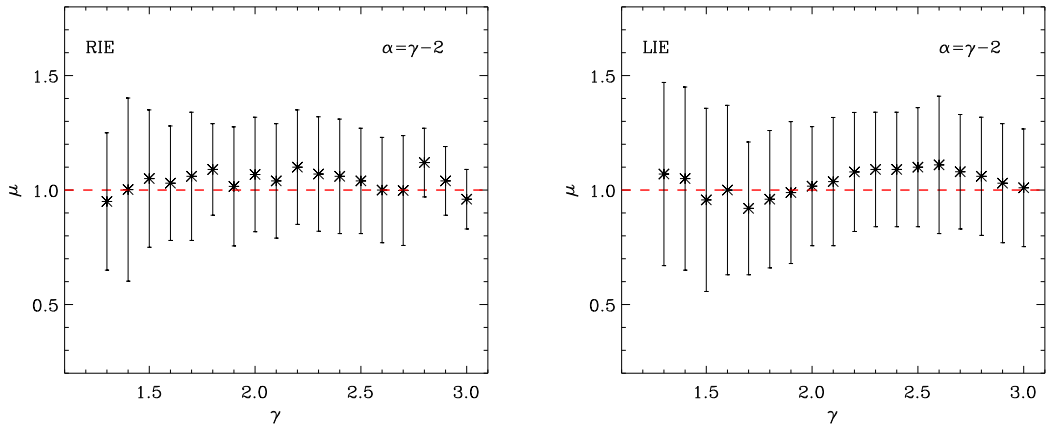

Figure 5.6: Mean value μ of the best fit Gaussian distribution for different values of γ and correspondingly $\alpha = \gamma - 2$. The anisotropy parameter lies between $-0.3 < \beta < 0.1$. The distribution is based upon 1000 realization. MW, using the RIE, left panel, M31, using the LIE, right panel.

5.4.3 Exploring the influence of the MW and M31 on each other

Subhaloes (not) facing the opposite host

The fact that the MW and M31 hosts are close to each other, forming a binary galactic system, poses the question if the mass estimators work even in the situation in which we only consider satellites in between the two haloes. To shed light on this issue we begin by separating the MW halo into two hemispheres, defined as "facing" and "non-facing" M31 (we perform the same test for the M31 halo, too). Subhaloes are then grouped by the hemisphere they sit in. We remark that this is a purely spatial cut, to investigate if the proximity of the companion host causes some bias on the mass estimator.

The facing/non-facing subhaloes of the MW are selected according to a radial number distribution $N(< r) \propto r^{3-\gamma}$ with $\gamma = 1.63$, and consequently $\alpha = \gamma - 2 = -0.37$, while the M31 subhaloes are selected in order to follow the distribution with $\gamma = 2.013$ and $\alpha = 0.013$. We chose these value to match the parameters found in Section 5.4.2, but verified that our results are not affected by the choice of the specific power law, as already expected (cf. Fig. 5.6). Finally, we randomly selected $N = 30$ subhaloes from each of the two facing/non-facing subsets, repeating the analysis 1000 times and computing each time the parameter β and the estimated mass. The anisotropy parameter, for both MW and M31 and in every subset of

Table 5.5: Milky Way and Andromeda galaxy mass estimation (RIE for MW, LIE for M31) using the subset of subhaloes facing and non-facing the companion host. The mean value μ and standard deviation σ of the Gaussian distribution of the estimated mass over the true one are shown, obtained by selecting N=30 subhaloes from the facing or not facing subsets, repeating 1000 realizations and evaluating the mass at two different $r_{\rm out}$.

Host $r_{\rm out}$	All Subs	Facing Subs	Not Facing Subs
$r_{\rm out,MW}$	$\mu \pm \sigma$	$\mu \pm \sigma$	$\mu \pm \sigma$
309 kpc	0.97 ± 0.12	1.05 ± 0.16	0.95 ± 0.24
197 kpc	0.98 ± 0.12	1.01 ± 0.12	1.03 ± 0.26
$r_{\rm out,M31}$	$\mu \pm \sigma$	$\mu \pm \sigma$	$\mu \pm \sigma$
340 kpc	1.02 ± 0.19	1.08 ± 0.19	0.92 ± 0.15
221 kpc	1.05 ± 0.19	1.11 ± 0.22	0.98 ± 0.16

objects considered, has been found to be very close to 0 again, lying between $-0.35 < \beta < 0.05$. We are hence in a situation to explore the influence of the two hosts on each other: with the β close to 0 and the subhaloes selected to follow a fixed power law (thus without errors associated to the 3 main parameters) we can affirm that any deviation in the mass estimation should now be attributed to the subhaloes facing or not the other host.

In Table 5.5 we show the results of the mean value and standard deviation of the Gaussian distribution of the estimated mass over the true one for the MW (by applying the RIE) and for M31 (using the LIE). We show the μ obtained by using the facing subhaloes, the non-facing subhaloes and also the total set. We did this exercise for two different values for $r_{\rm out}$, thus computing the host mass up to this outer radius: in this way we should be able to observe if the proximity or, on the contrary, the distance of the subhaloes population to the opposite host has some influence as well. For the MW host we can observe that the estimator performs equally well when using the facing or non-facing objects, for each of the two $r_{\rm out}$ values used. In the case of M31, instead, the non-facing population of subhaloes seems to give better results in the estimation of the host mass, while the facing objects lead to a Gaussian distribution whose mean value is slightly biased ($\mu = 1.11$) when we considered the $r_{\rm out} = 221$ kpc. Given the high uncertainties associated to this biased result however, we can conclude that each of the main galaxies does not influence the subhalo population of the other one.

Renegade subhaloes

As already discussed, we call renegade subhaloes those objects, in our simulations, that change their affiliation from one of the two prominent hosts in the Local Group to the other (Knebe et al. 2011b). We were able to identify 129 renegade objects, 57 of which belonging to M31 at z=0, and the remaining 72 belonging to the MW.

We thus examine the effect that this population of renegade subhaloes may have on the mass estimators: while in the previous studies we used the full set of subhaloes, automatically including also the renegade ones, we now want to restrict the analysis to the renegade subhaloes only in order to estimate the mass of MW and M31.

For each host we computed the anisotropy parameter and radial distribution of their respective renegade satellites, and found $\beta_{M31} = 0.86$ - $\beta_{MW} = 0.72$ and $\gamma_{M31} = 2.15 \pm 0.21$ - $\gamma_{MW} = 2.01 \pm 0.20$. The choice of the host parameter α is made considering its value in the total $[0, 1]R_{\rm vir}$ range, or using the relation $\alpha = \gamma - 2$ that we provided in the previous sections. The resulting estimated masses are shown in Table 5.6, in which we have used the FIE estimator in order to compare the effects of these renegade subhaloes in the same way for both hosts. This time, because of the small number of objects considered, we do not perform multiple realizations of the mass estimation, but only one: the errors associated with the mass are thus computed through the error propagation formula based on Eq. (5.14) - Eq. (5.19), in which we further assume that β is fixed, $\Delta\gamma/\gamma \sim 10\%$ as obtained by the fitting routine and $\Delta\alpha/\alpha$ is listed in Table 5.2. We see that in the case of using the value of α from the total radial range, the mass estimator is biased for both hosts, with a large associated error. When using the relation $\alpha = \gamma - 2$, instead, the mass of both Milky Way and Andromeda in recovered within a much smaller uncertainty. Is interesting to note how the relation between the host parameter α and the subhaloes distribution parameter γ seems to hold true also in this case, in which the anisotropy parameter β is substantially far from being isotropic. However the lack of statistic in this case, having at our disposal just one realization of a small number of renegade objects, prevents us from generalizing the finding of Section 5.4.2 to this highly anisotropic case. The fact that $\beta \sim 1$ for the renegade subhaloes means that these objects are mainly moving on radial orbits with respect to their hosts. We conclude that the computation of the host mass based upon a family of renegade subhaloes gives results in agreement with the expected ones and hence these mass estimators will not be biased in case that renegade objects also exist in reality.

Table 5.6: Estimation of the MW and M31 mass based upon renegade subhaloes only, FIE case. The parameter used are $\beta = 0.72$ and $\gamma = 2.01$ for the MW, $\beta = 0.86$ and $\gamma = 2.15$ for M31. We remind that the value of α from the total radial range is $\alpha = -0.034$ for the MW and $\alpha = -0.052$ for M31, as in Table 5.2.

	MW	M31
α	$(M_{est} \pm \Delta M_{est})/M_{true}$	
$[0,1]R_{\rm vir}$	0.92 ± 0.33	0.75 ± 0.40
$\gamma - 2$	1.00 ± 0.21	0.97 ± 0.16

Unbound subhaloes

For all previous results we did not test whether or not a subhalo is gravitationally bound to its host; we simply used a spatial criterion to determine its affiliation as this is how satellites are often defined in the observations. Now instead, we impose an additional constraint on our subhalo population: its velocity has to be lower than the local escape velocity v_{esc} of the halo at that distance. Following this criterion, we find that about the 3% of the subhaloes inside the virial radius of each host are unbound. As expected, most of them lie near by the virial radius, where the v_{esc} is lower and the effects of the proximity of the other host are more important. We thus quantify the effects that unbound subhaloes have on the mass estimators. This is an interesting test, as it corresponds to the real case scenario in which the affiliation of a tracer object is not clear and could be erroneously included into the calculation of the mass of a host.

We repeat our previous methodology by evaluating the MW and M31 mass 1000 times with a subset of $N = 30$ subhaloes, this time including one, two or three unbound subhaloes. In order to ensure an unbound subhalo is included, we explicitly substitute in each realization, one, two or three of the 30 subhaloes with an unbound one. We then computed the β and γ coefficients for each realization, and used the formula $\alpha = \gamma - 2$. We verify that the inclusion of a single unbound subhalo leads to mass estimators which are slightly biased towards larger masses: we obtained, for both M31 and MW, a Gaussian peaked at $\mu = 1.04$ with $\sigma = 0.14$. When including two unbound subhaloes, we found an higher deviation, with $\mu = 1.12$ and $\sigma = 0.13$. Finally, forcing three unbound subhaloes to be included in each 30 subhalo subsample, we obtain a Gaussian peaked at $\mu = 1.17$ and $\sigma = 0.14$. We performed the calculation using the FIE estimator but verify that our results are the same in the RIE and LIE case, giving similar values for the mean of the distribution μ, and increasing standard deviations σ with

respect to the FIE case.

We note that the results presented in the previous sections are not significantly affected by the presence of unbound subhaloes, as in that case the probability that in a given realization of $N = 30$ randomly picked subhaloes one was unbound is $P \approx 37\%$[2], due to the fact that unbound subshaloes make up just 3% of the full subhalo population. In this last test, instead, the probability that one object is unbound, over the $N = 30$ subhaloes used in each realization, is $P = 100\%$, because we deliberately replaced one random subhalo with an unbound one. Thus, we expect that the error on the mean value of the Gaussian distributions in the previous analysis, caused by the possible inclusion of one unbound object, is $100/37 \approx 2.7$ times lower than the error made here, when one subhalo is forced to be unbound. Looking at the $\mu = 1.04$ obtained in this section, for the FIE case when we used a single unbound subhalo, we see that the 4% of deviation from the expected value will be reduced of a factor 2.7, giving negligible errors. We are further reassured by having performed the analysis of Section 5.4.2 also by explicitly neglecting the unbound objects, and we have observed no significant differences in the results already presented.

To conclude, in this section we demonstrate that, being sure of having included unbound subhaloes, this inclusion causes an overestimate of the host mass, in agreement with the results of Deason et al. (2011). The more unbound objects we include into the mass estimator, the more biased the final mass is. Care should thus be taken when considering objects at the "edge" of a galaxy halo, as they may be not bound to it.

5.5 Summary & Conclusions

We verified the accuracy of the scale-free mass estimators recently proposed by Watkins et al. (2010,W10) when applied to the two dominant Local Group host haloes, the MW and M31, by using Constrained Local UniversE Simulations (CLUES). These scale-free mass estimators assume that all the relevant informations about the enclosed mass of a halo are contained in the properties of its satellites (or any other tracer population),

[2]This probability can be computed using the hypergeometric distribution, which, in our case and for the M31 and MW, respectively, describes the probability to get one unbound subhalo within $k = 30$ randomly drawn objects from a total subhaloes population of size $N = 1405(1205)$ in which the unbound objects are $n = 45(36)$, thus the $\sim 3\%$ of the total.

$$P = \binom{n}{1}\binom{N-n}{k-1}/\binom{N}{k} \tag{5.23}$$

such as distances and velocities, which can both be given as either projected or full $3D$ data. The importance of such estimators resides in the fact that the full six-dimensional phase-space information of all celestial bodies down to the very faint magnitude $G \approx 20$ mag will soon be available thanks to the upcoming GAIA mission. What makes the usage of these mass estimators so appealing? After three years of operation the Sloan Digital Sky Survey II (SDSS-II[3]) discovered eight new dwarf galaxies, seven of them orbiting our Galaxy. The SDSS, which covered more than a quarter of the sky, essentially doubled the known number of MW satellite galaxies, helping close the gap between the observed number of dwarf satellites and theoretical predictions. During its projected five-year mission, GAIA will scan the entire 41253 square degrees of the sky, obtaining astrometric parameters (angular position, proper motion, and parallax) for roughly one billion stars. Recently, An et al. (2012) further investigated the benefits that the use of all this new proper motion data will introduce in the application of mass estimators. It is thus imperative to develop and test against simulations the mass estimator based entirely upon tracer objects, such as satellite galaxies. This issue has already been partially addressed in Deason et al. (2011) and Evans et al. (2011), using the GIMIC suite of simulations, from which they selected a set of galaxies that resemble the Milky Way.

In this work we tested the scale-free mass estimators against Constrained Simulation of the Local Group, in which observational data of the nearby Universe is used as constraints on the initial conditions. These constrained simulations provide us with a unique Local Group seated in the correct environment, as opposed to un-constrained cosmological simulations, to make a direct comparison between numerical results and observations: verifying the goodness of the W10 mass estimators in our simulated LG should therefore been seen as complementary to the already published work on their credibility and as an extension to a system resembling as closely as possible the real Local Group.

Our motivation is driven by the fact that the Local Group likely is a rather special (binary) system of galaxies featuring backsplash galaxies (Knebe et al. 2011c), renegade satellites (Knebe et al. 2011b) and preferential infall: Libeskind et al. (2011b) have studied the simulated MW and M31 galaxies in the CLUES framework and have found a clear evidence for the anisotropic infall of subhaloes onto their respective hosts. This result has been recently corroborated by Keller et al. (2012), who examined the spatial distribution of the MW young halo globular clusters finding that they are anisotropically spatially distributed, sharing the same accreted origin as that of the MW's satellite galaxies. Our simulations also show

[3] `http://www.sdss.org/`

the typical anisotropy in the distribution of subhaloes population, compatible with the observed classical MW satellites (Kroupa et al. 2005; Metz et al. 2007, 2008), and as already found in other cosmological simulations (cf. Knebe et al. 2004; Libeskind et al. 2005; Zentner et al. 2005). Furthermore, when comparing constrained against un-constrained simulations – only 1-3% of Local Group (candidates) share similar formation properties (Forero-Romero et al. 2011). Thus, it is clear that our Local Group is a very special object in the Universe.

We first studied the sensitivity of the mass estimators with respect to their main parameters: α, which describes the host halo scale-free gravity field, β, which corresponds to the satellites' velocity anisotropy, and γ, representing the exponent of the power law describing the number density of the tracer population. We found that for an external galaxy, such as M31, for which only line-of-sight informations are available, the greatest error comes from the uncertainty of α and γ, whereas the mass variations stemming from the anisotropy parameter β are almost negligible in the interesting physical range. On the other hand, the greatest concern in the estimation of the mass of our Galaxy comes from the β parameter, as pointed out by W10: without precise information about the satellites' proper motions, the error introduced by using their radial velocities is sensibly high. Hopefully, future surveys (e.g. the GAIA mission) would be able to measure such proper motions, significantly improving the quality of these mass estimators.

We then applied the relevant mass estimators to the MW and M31 Local Group system as found in our constrained simulation. We found that all the estimators (FIE and RIE for the MW, FIE and LIE for M31) provide an unbiased results, with the mean of the M_{est}/M_{true} distribution close to $\mu = 1.0$ and its standard deviation scaling with $1/\sqrt{N_{sub}}$, even when a small ($N \sim 30$) number of tracer objects are used, resembling the real case scenario of the known satellites galaxies. When selecting the subhaloes in order to follow a specific radial number distribution $N(< r) \propto r^{3-\gamma}$ with different γ, we found that, in the limit of the isotropic regime (i.e. $\beta \sim 0$ and as far as $\beta = -0.5$ in our simulations) the assumption that the subhaloes are tracking the total mass of the host (i.e. $\alpha = \gamma - 2$) is sufficient to get a very good estimate of the host mass.

We thus also investigated how the mass estimators work when using subhaloes that are closer or further away from the neighboring host, by restricting the analysis to the facing and non-facing hemispheres and calculating the mass at different values for $r_{\rm out}$: we observe that the two dominant hosts of the Local Group do not appear to influence its subhalo populations – at least not when the applicability of the scale-free mass estimators is concerned.

Finally, we explored the possibility that using renegade subhaloes, i.e. subhaloes that change their affiliation from one of the two hosts to the other, in the estimation of the mass may cause a bias: we do not find evidence for this, on the contrary, we observe that the mass of both MW and M31 is recovered with a few percent of error when the assumption $\alpha = \gamma - 2$ is made, even if the anisotropy parameter in this case is $\beta \sim 0.7$, indicating that these objects are moving on radial orbits.

On the other hand, the inclusion of unbound objects, mainly found near the virial radius of each host, is able to cause an overestimate of the host mass, as high as the 20% when 3 unbound subhaloes are used out of a total of 30 objects. In this regard, care should be taken when dealing with tracer populations whose affiliation to each of the two host is not clear. As long as boundness is verified however, the unique subhaloes population in our simulations, showing anisotropy in their spatial distribution, preferential infall (Libeskind et al. 2011b) and even renegade objects (Knebe et al. 2011b), does not prevent us from always recovering a good estimation of the host mass.

Hence, the most important finding of this work is that satellite galaxies are well suited to "weigh" the MW's halo. Even with a small sample of just two dozen objects and despite anisotropic accretion, an anisotropic spatial distribution, different masses, sizes and histories, subhalo kinematics are dominated by the host potential, making satellite galaxies well suited for the problem at hand. We therefore conclude that the application of the scale-free mass estimators to either of the two dominant hosts of the Local Group provide credible results, it therefore appears safe to use it for the Local Group as already done by W10. To get a good estimation of a host mass, in the case of having the anisotropy parameter $\beta \sim 0$, we recommend the use of the parameter $\alpha = \gamma - 2$ where the γ directly come from the observation of a satellite population.

In the future, sensitive surveys and space based telescopic missions will most likely improve both the census of satellite galaxies as well as our understanding of their proper motions: these new data will enhance the mass estimators making them more accurate than they are today.

Chapter 6

Warm dark matter Local Group simulations

We explore the main differences in the formation of the Local Group by analyzing cold (CDM) and warm (WDM) dark matter simulations within the CLUES project. In the WDM case the initial power spectrum has been changed to mimic a 1 keV dark matter particle.

We firstly focus on the "too big to fail" problem and show that the WDM scenario naturally predicts less subhaloes than the CDM one. The fewer number of substructures formed, however, is not enough to accommodate all the visible subhaloes of the Milky Way; moreover, the brightest subhaloes in the WDM SPH run are still too bright to be compatible with observed dSphs.

Regarding the entire Local Group, two significant differences between the CDM and WDM run are found. While in the CDM case a group of galaxies that resembles the real LG forms, the WDM run fails to reproduce a viable LG, instead forming a diffuse group which is still expanding at z=0. This is surprising since, due to the suppression of small scale power in its power spectrum, WDM is naively expected to only affect the collapse of small haloes and not necessarily the dynamics on a scale of a group of galaxies. Furthermore, the concentration of baryons at the center of the haloes is greater in CDM than in WDM.

6.1 Introduction

Despite the many successes of CDM, we have seen that there are still issues with the small scale structures formed within such a model. This

is what motivated scientists to investigate the formation of structures by using a different type of dark matter, namely a warm dark matter particle. Invoking a warmer flavor of DM, such as a 2 keV sterile neutrino, may indeed solve a number of issues related to dwarf satellite galaxies, including the "missing satellite problem" (Klypin et al. 1999a; Moore et al. 1999) as well as the "massive failure problem" (Boylan-Kolchin et al. 2011, 2012).

In this Chapter we use again the CLUES simulations, run this time with a power spectrum changed to mimic the suppression of power at small scales caused by a 1 keV particle, as shown in Fig. 2.3. Within such WDM model initial perturbations below a certain mass cannot collapse and the smallest structures to form out of gravitational instability are fairly large. The initial condition and details of the simulations have been presented already in Section 2.1 and the SPH and star formation recipes are exactly the same as in the CDM counterpart.

In the WDM simulation, discreteness effects which can cause haloes below a specific limit mass (M_{lim}) to arise from the unphysical numerical fragmentation of filaments, is an issue. In order to protect our analysis against these artificially formed haloes we use the value of M_{lim} provided by Wang & White (2007) as the minimum trusted mass for a halo in the WDM simulation. Their expression, originally based upon Hot Dark Matter models, reads $M_{lim} = 10.1\bar{\rho}d/k_{peak}^2$, where $\bar{\rho}$ is the mean density, d is the mean interparticle separation, and k_{peak} is the wavenumber at which $\Delta^2(k) = k^3P(k)$ reaches its maximum. In our WDM run, where the power spectrum has been modified to correspond to a 1 keV particle, the values of this limiting mass is $M_{lim} \sim 2.6 \times 10^7 M_\odot/h$, which corresponds roughly to a 100 particle limit. In practice when comparing CDM and WDM simulations, only objects whose mass is greater than 500 particles are used. We note that since the simulations have identical baryonic physics, particle mass and spatial resolutions any of the differences reported here are due entirely to the nature of the DM model.

6.2 Results

The WDM simulation of the Local Group produce three dominant objects which we name galaxy A, B and C in decreasing mass. In the CDM case these closely resemble the Milky Way (MW), Andromeda (M31) and Triangulum (M33). An image of the two groups can be seen in Fig. 6.1. Two salient aspects of WDM are immediately apparent from this figure: (1) there are far fewer small substructures and (2) the two groups differ substantially, cosmographically speaking.

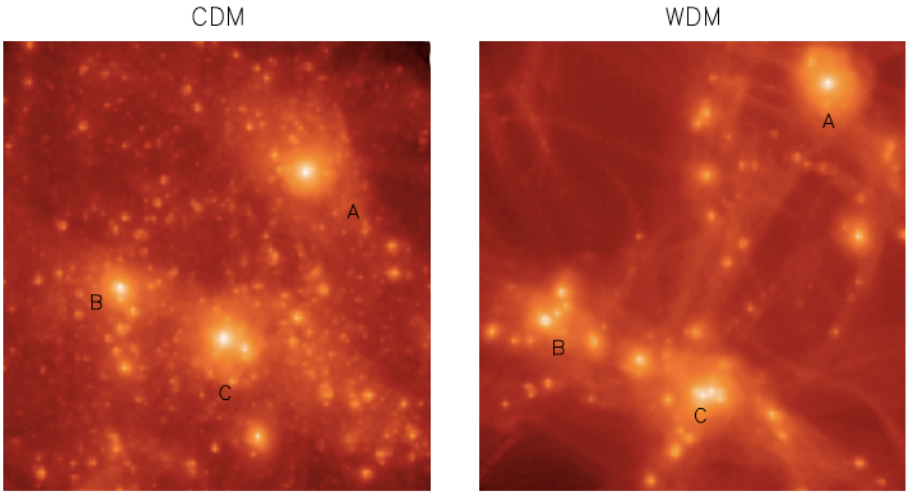

Figure 6.1: Dark matter distribution within a $2h^{-1}$Mpc sphere containing the three main haloes of the LG. CDM (left) and WDM(right). Credit: Libeskind et al. (2013)

Regarding the first point, it is clear how the number of fewer small structures observed within the main haloes in the WDM run could, in principle, solve the "massive satellite" problem. The warm, 1 keV particles are indeed able to suppress dramatically the number of such substructures within Milky Way like haloes. We show in Fig. 6.2 the total number of substructures found within the halo A and the halo B (dubbed as MW and M31, even if they do not accurately resemble some of the main features of the observed galaxies, as we will discuss later) in the $V_{\rm max}$ - $R_{\rm max}$ space, for the DM only run, as open diamonds, and SPH run, as filled circles.

We indicate as black circles those subhaloes whose magnitude is compatible with the observed dSPhs, while in light gray we show subhaloes with are "too bright" when compared to the classical dwarfs. The dashed line indicates the observational constraint coming from the assumption that the dSphs live in NFW haloes, while the solid black line is the same constraint but using an Einasto profile with variable shape parameter. We based such constraint on the analysis of subhaloes density profile in CLUES, and found that like the CDM case described in Section 4.3, such profiles can be accurately described by an Einasto model, which over performs the NFW fit.

Amongst the two hosts considered in our simulations, we found only 5 satellites brighter than the classical dwarfs, only 3 of which lying outside

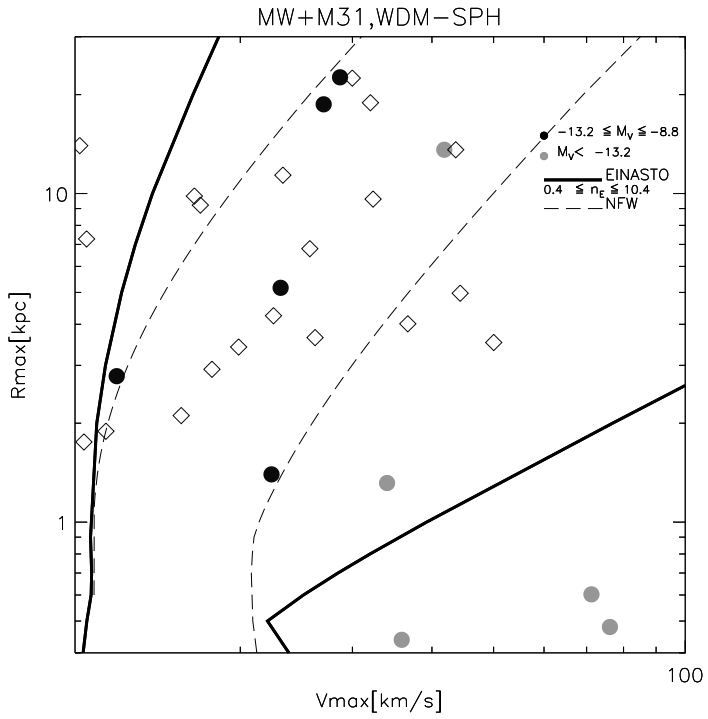

Figure 6.2: The "too big to fail" problem in warm dark matter simulations. Open diamonds indicate the subhaloes found in the DM-only run, while the filled circles indicate the SPH satellites, color-coded according to their magnitude. The satellites of the two main hosts are shown here.

the observational range. While these numbers can easily be explained by a statistical fluke, it is worrisome that the fewer number of substructures formed, however, is not enough to accommodate all the visible subhaloes of the Milky Way. Using a 2 keV particle would, possibly, solve the problem (Lovell et al. 2012). This results have been, however, recently disfavored by Schneider et al. (2014), who used the most stringent constraints on warm dark matter particle mass coming from the Lyman-α forest which provides $m_{WDM} > 3.3$ keV at the 2σ level (Viel et al. 2005). With such a realistic WDM particle mass the TBTF problem seem to be as severe as in the CDM scenario.

We conclude that simply invoking a WDM scenario is not enough to solve the TBTF problem.

We now move on in analyzing the evolution of some physical properties of the three main haloes found in WDM simulations. In Figure 6.3(a,c) we show the co-moving and physical distance between the three pairs of group

members as a function of look back time, normalized to the z=0 value. In the CDM simulation, the physical separation of each pair of galaxies reaches a maximum "turn-around" (at a look back time of around 6 Gyrs for galaxy B-A and galaxy B - C pair and around a few Gyrs later for galaxy A - C). In the WDM simulation this is not the case: the physical distance between each pair of haloes at every redshift is smaller than the corresponding distance at redshift zero, indicating that the Hubble expansion is the dominant force at every epoch and that all three pairs of galaxies have yet to begin approaching each other. Accordingly, the group is more compact in CDM than in WDM. Using these specific initial conditions, over densities that turn around and are on a collision course at a given epoch in cosmic time in CDM, have yet to approach each other in WDM: where CDM produces an attracting, collapsing group of galaxies, WDM produces a still expanding version. Using initial conditions, whose only difference is a suppression of small scale power, the defining dynamics of a group of galaxies is completely different in CDM and WDM, with the former predicting an attracting group that resembles the LG, while the latter predicting a still expanding one.

The co-moving distances (shown as the thick lines in Fig. 6.3a,c) show monotonic attractions. In the WDM case the simulated haloes are closer to each other (relative to their z=0 distances) at early times than the CDM haloes. In the CDM case, by z=0 the haloes have been brought closer. Note that the small kinks in the A -C system (CDM) and B - C system (WDM case) appear due to false identification of the main progenitor in the merger tree construction at a given snapshot.

We now examine the evolution of the three individual group members by examining the mass accretion history shown in Fig. 6.3(b,d). In both the CDM and WDM run, the two most massive galactic haloes (A and B) show jumps in the mass accretion history characteristic of merger activity occurring more or less continuously. Often, these haloes appear to lose mass after a violent major merger. This is because of the unique merger history of these objects - violent mergers may bring material into the virial radius that is bound at one redshift, but which may become unbound and flung out at a later time. The smallest halo (C) on the other hand shows little evidence of major mergers in its past.

Although the mass growth histories look similar, in fact they differ slightly. The time at which half of the z=0 mass has been assembled is shown in each plot as a filled circle. In the WDM simulation, each halo assembles 50% of its mass later with respect to the CDM model. Specifically, in the WDM run halo A, B and C accrete half-mass at a look-back time of ~ 4, ~ 6, and ~ 9.5Gyrs, respectively. In the CDM case this occurs at ~ 7, ~ 7 and ~ 10Gyrs: that is ~ 3, ~ 1, ~ 0.5 Gyrs earlier. Since B and C

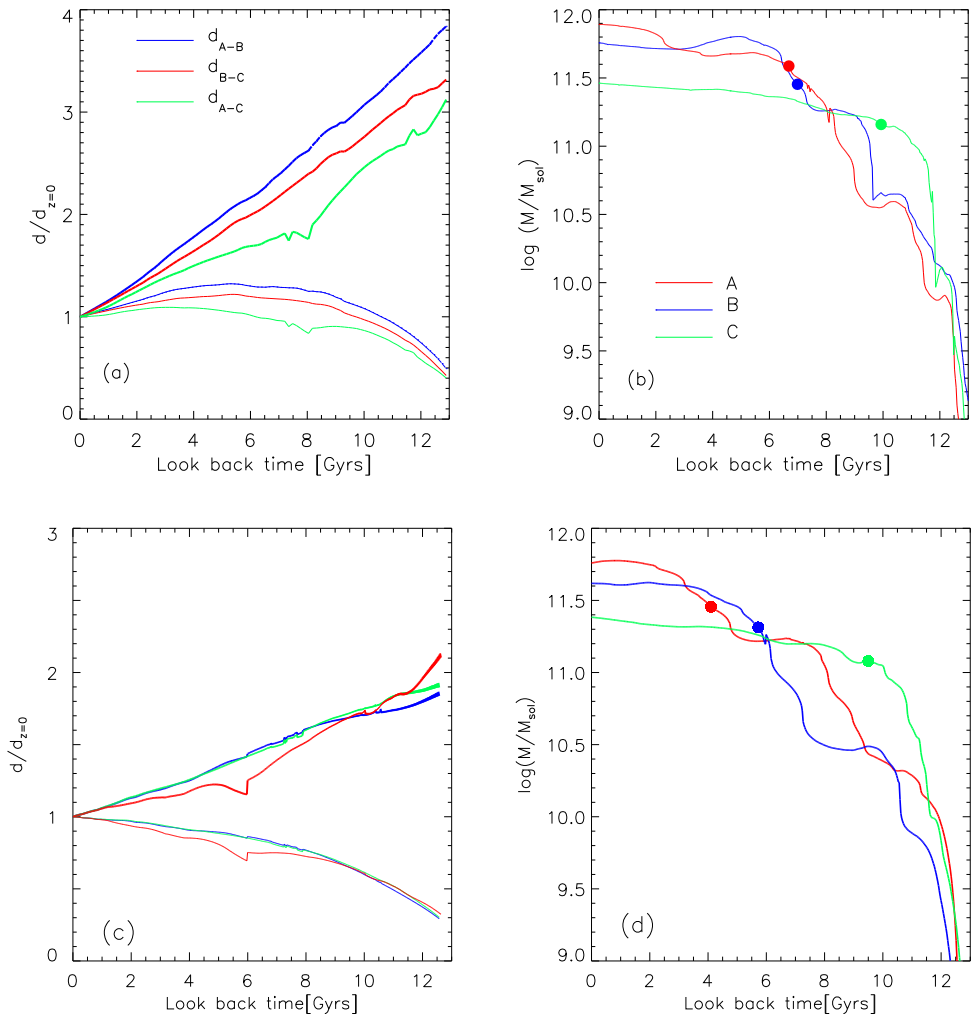

Figure 6.3: *Upper Panels:* CDM; *Lower Panels:* WDM. *Left Panels (a,c):* The physical (*thin line*) and co-moving (*thick line*) distance as a function of look back time between the three pairs of LG haloes. We show the distances between the A and B in blue, the B and C in red and A and C in green. Each curve is normalized to its z=0 value which can be found in Table 1. *Right Panels (b,d):* The mass growth for halo A (red), B (blue), and C (green) as a function of look-back time. The solid dots denote the time at which half the z=0 mass was assembled. Credit: Libeskind et al. (2013).

are smaller mass haloes, their half mass times are considerably earlier and the delay is considerably smaller than for halo A. A characteristic feature of the WDM model emerges here: the finite primordial phase-space density due to the large thermal velocities of the particles causes most of the mass to undergo gravitational collapse at later redshift ($z < 5$), resulting in the suppression of halo formation at higher redshift (Bode et al. 2001). Halo collapse is thus delayed with respect to the CDM model. Although not a new result, this finding directly informs the main differences we find between CDM and WDM.

How do the different cosmographies and histories change the internal structure of each of our three LG objects? In Fig. 6.4(a)-(c) we show the density profile of the three LG members in both WDM (dashed) and CDM (solid) simulations. All density profiles are standard NFW fits, and in all three cases the WDM is nearly indistinguishable from the CDM. That said, owing to the lower mass of the WDM haloes, their density profiles are systematically shifted to slightly lower densities.

In Fig 6.4(d)-(f) we show the cumulative baryon fraction as a function of radius. Again, WDM and CDM show broad similarities in shape and value of the baryon fraction. In the inner parts, WDM shows a systematically lower baryon fraction. At around $\sim 0.03 r_{\rm vir}$, the total fraction of internal mass in baryons is roughly the same in both cosmologies. Towards the outer parts of the halo, the baryon fraction of both cosmologies drops, reaching the cosmic mean of ~ 0.1 at the virial radius. That CDM haloes have more concentrated baryons is likely due to a number of combining factors: their earlier formation time, their greater mass and thus their deeper potential. We conclude that WDM haloes have lower baryon fractions in their inner parts where baryons dominate, than CDM haloes.

The baryonic properties of the three Local Group members are summarized in Table 2. The fraction of mass in a gaseous component is presented in Fig. 6.4(g)-(i). Although each halo shows different specific behavior, some interesting similarities exist. Firstly, the fraction of mass in gas is almost always greater in WDM than in CDM. This is true for all radii in halo A, and for radii greater than $0.03 r_{\rm vir}$ for halo B and C (although in halo B, there is more gas in CDM for $r < 0.2 r_{\rm vir}$). The higher gas fractions in WDM may inhibit infalling substructures from depositing their material in the center of the halo thereby suppressing the baryon fraction in the inner parts of WDM haloes, as seen in Fig. 6.4(d)-(f).

Finally, we close this section with an image of the gas distribution in the Local Group within such WDM scenario, in Fig. 6.5. The size of the plot is about $2h^{-1}$ Mpc across, viewed from a distance of $3.3h^{-1}$ Mpc. On the three right panels we show the gas disks of the three main galaxies as seen

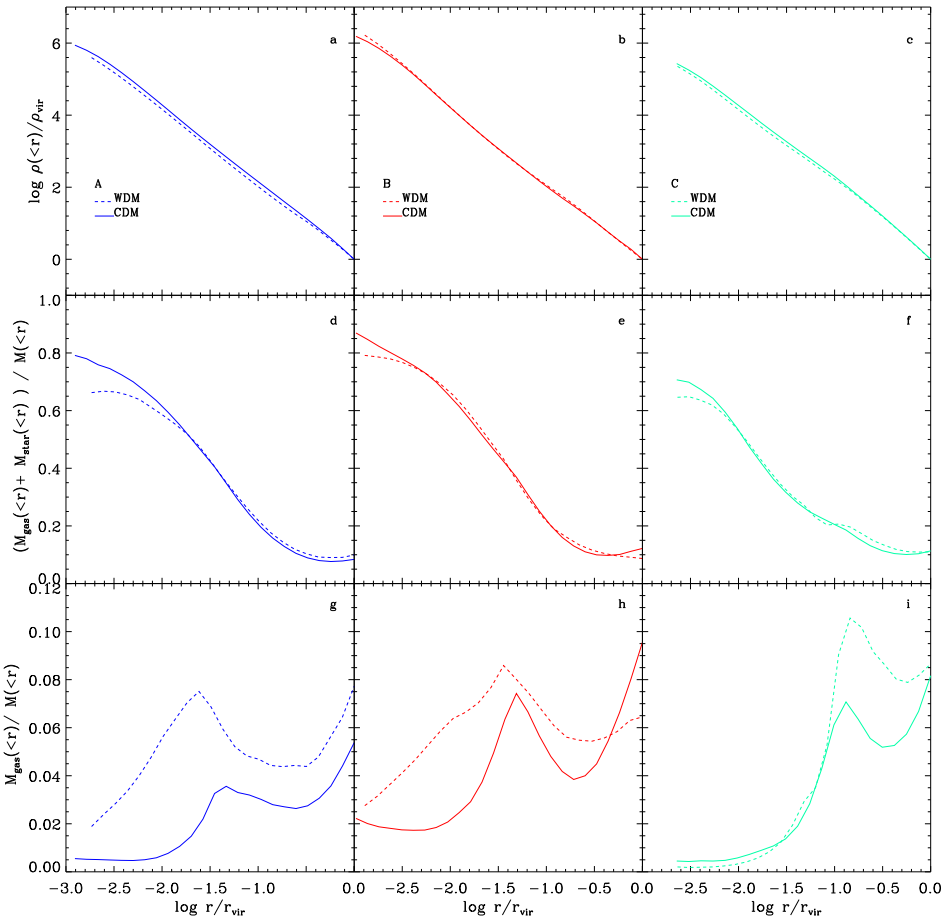

Figure 6.4: Internal properties of the three main haloes simulated as function of radius. Properties for halo A (red, left panel), B, (blue, center panel) and C (cyan, right panel) are shown for WDM (dashed) and CDM (solid). *Top row:* Density profile. *Middle row:* Baryon fraction. *Bottom row:* Gas fraction. Credit: Libeskind et al. (2013)

Halo	Property		CDM			WDM	
		TOTAL	GAS	STARS	TOTAL	GAS	STARS
A	$N_{\rm vir}$	4.2	1.3	0.65	2.9	0.66	0.43
	$M_{\rm vir}$	5.5	0.52	0.14	4.2	0.27	0.094
	$f_{\rm b,vir}$	0.12			0.09		
B	$N_{\rm vir}$	2.9	0.53	0.55	2.2	0.56	0.30
	$M_{\rm vir}$	4.0	0.21	0.12	3.0	0.23	0.066
	$f_{\rm b,vir}$	0.08			0.09		
C	$N_{\rm vir}$	1.5	0.40	0.29	1.3	0.36	0.19
	$M_{\rm vir}$	2.0	0.17	0.064	1.8	0.15	0.040
	$f_{\rm b,vir}$	0.11			0.11		

Table 6.1: Properties of the three main galaxies in the CDM and WDM simulation. For each halo we show the number $N_{\rm vir}$, in units of 10^6, and mass $M_{\rm vir}$, in units of $10^{11}h^{-1}M_\odot$, of stars, gas and all particles within the virial radius. We present the baryon fraction within the virial radius ($f_{\rm b,vir}$).

from a distance of $250h^{-1}$ kpc, the size of the plot is about $50h^{-1}$ kpc.

6.3 Summary and Discussion

Since the temperature of the DM particle at decoupling determines its ability to "free-stream" out of potential wells, it also sets the scale at which structures are able collapse. In principle this characteristic can be used to constrain DM to be either "cold", "warm", or "hot". Hot DM, such as neutrinos which travel at relativistic speeds, were at first hailed as the solution to the DM problem but have now been effectively ruled out since they can escape most potential wells and prevent structures from formation via gravitational instability. Cold DM (CDM), on the other hand, moves non-relativistically and as such is able to collapse into smaller objects. The prediction of small substructures embedded in larger objects is a generic feature of the CDM model and, since such objects are unobserved in the Milky Way, this has lead to the famed "missing satellite problem" (Klypin et al. 1999a; Moore et al. 1999), often dubbed a crisis for CDM. Astrophysical process (such as photo-evaporation of star forming gas due to UV radiation, see Benson et al. 2003) are invoked to inhibit the gas cooling into small subhaloes. These process do not erase substructures, they simply ensure that they remain non-luminous. A large population of dark subhaloes detectable via gamma ray emission from DM annihilation (Stoehr et al. 2003) or via strong gravitational lensing of background sources (Xu et al. 2009), is thus

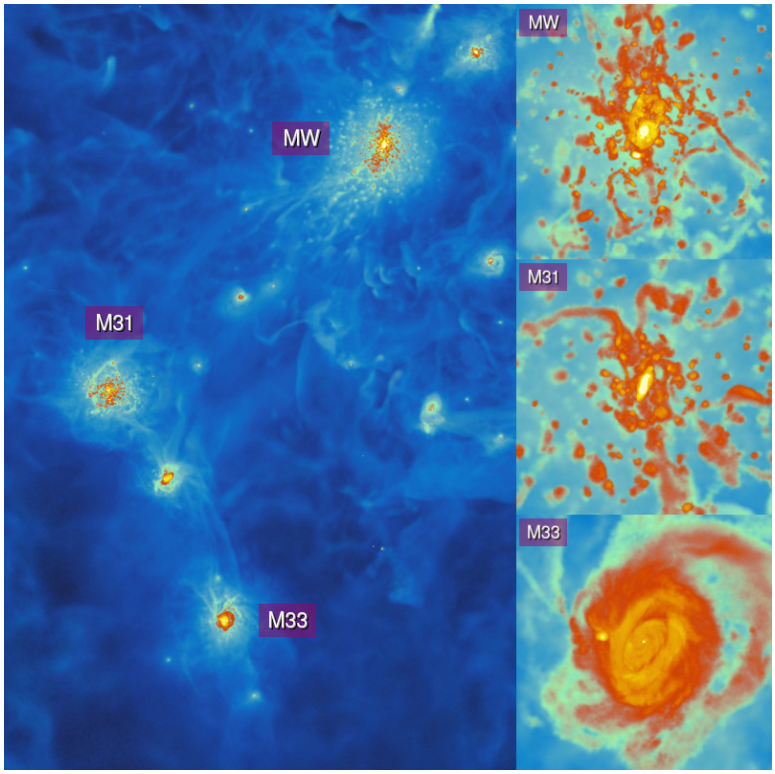

Figure 6.5: The gas distribution within the LG in a WDM scenario (for CDM see Fig. 2.2). Credit A. Khalatyan, using PMViewer *http://pmviewer.sourceforge.net*.

predicted albeit unobserved, in the Milky Way halo.

As a result of the apparent failures of CDM in over producing and HDM in underproducing the number of dwarf satellites around the Milky Way, warm DM (WDM), has recently been suggested and studied (by e.g. Bode et al. 2001; Knebe et al. 2002, 2008; Macciò & Fontanot 2010; Lovell et al. 2012; Schneider et al. 2014, among others). In this work, we have used a set of initial conditions that constrain scales unaffected by the nature of the DM to test the effect of the type of DM on a group of galaxies (i.e. $\sim$ 1Mpc). Within the scales that are still linear at z=0 (the "local environment") a group of galaxies that in CDM resembles the local group is resimulated at high resolution, with gas dynamics. In the CDM run, this local group includes three galaxies that have the same mass, geometry and kinematics as the MW, M31 and M33. Thus our simulation allows us to study in detail the merger history and internal structure of these galaxies as well as their baryonic properties. Since the local environment has been kept identical, we can directly measure the effect the type of DM has on our CDM LG.

The main difference between our CDM and WDM simulations is that structure formation is delayed in WDM. This is a direct result of the suppression of small scale power which, owing to the lack of mergers below the filtering mass, means that it takes longer for haloes to grow to a given mass. The greatest effect this has is to inhibit the collapse of a group of galaxies in WDM. All our results regarding the differences in the galaxies themselves, follow directly from this main difference.

- The number of luminous substructures formed within such a WDM scenario is not enough to reconcile simulations and observations of dSphs: there are too few subhaloes within the luminosity range of the observed classical dwarfs.

- A group of galaxies which at z=0 closely resembles the LG in CDM, is dynamically very different in WDM. Whereas in CDM the group is collapsing and is compact, in WDM it is still expanding and is much more diffuse.

- Delayed halo collapse, implies that at z=0 WDM haloes are smaller than their CDM counterparts.

- Baryons are more centrally concentrated in CDM versus WDM haloes.

Our conclusions are all consequences of the delayed formation and collapse of haloes in WDM cosmologies with respect to CDM. This simple

attribute, a direct result of the lack of small scale power due to free streaming of DM at early times, informs a myriad of physical properties, from star formation rates to bulge/disc ratios to colors.

For a more comprehensive study of the differences between a CDM and a WDM simulated Local Group we refer the reader to Libeskind et al. (2013).

Chapter 7

Abundance Matching in the Local Group

The way in which dark matter halo masses are assigned to each specific dSph within the Local Group is by mean of dynamical measurements: knowing the stellar velocity dispersion of such galaxies at a specific radius, such as the half-light radius $r_{1/2}$, and assuming that the dSphs are amongst the most dark matter dominated objects in the Universe, one can immediately derive the dark matter mass within such $r_{1/2}$ after a density profile has been chosen.

We showed already in the previous Chapters that with this procedure the brightest satellite galaxies of the Milky Way would be apparently housed by subhaloes which are smaller than expected within a galaxy formation model, the TBTF problem (Boylan-Kolchin et al. 2011). The key in solving the "massive subhaloes" problem is thus to understand what is the actual halo mass of subhaloes within which the observed satellite galaxies are embedded.

Using the abundance matching technique (e.g. Moster et al. 2010; Guo et al. 2010), it is possible to constrain the relationship between stellar mass and halo mass of galaxies. The idea is to match the cumulative number of observed galaxies with the cumulative number of dark matter haloes, the latter being derived either from theory or from cosmological N-body simulations.

In this Chapter, we use the CLUES simulations to show that a single power law halo mass distribution is appropriate for direct matching to the stellar masses of observed Local Group dwarf galaxies, allowing the determination of the slope of the stellar mass-halo mass relation for low mass galaxies. In other words, we extended the halo-galaxies abundance matching down to the completeness limit of the Local Group galaxies. Errors in

halo masses are well defined as the Poisson noise of simulated local group realizations, which we determine using local volume simulations. For the stellar mass range $10^7 M_\odot < M_* < 10^8 M_\odot$, for which we likely have a complete census of observed galaxies, we find that the stellar mass-halo mass relation follows a power law with slope of 3.1, significantly steeper than most values in the literature. This steep relation between stellar and halo masses would indicate that Local Group dwarf galaxies are hosted by dark matter haloes with a small range of mass. Our methodology is robust down to the stellar mass to which the census of observed Local Group galaxies is complete, but the significant uncertainty in the currently measured slope of the stellar-to halo mass relation will decrease dramatically if the Local Group completeness limit was $10^{6.5} M_\odot$ or below, highlighting the importance of pushing such limit to lower masses and larger volumes.

7.1 Introduction

By comparing stellar masses of galaxies from large scale surveys with masses of haloes in cosmological dark matter simulations, one can use abundance matching techniques to derive the stellar-to-halo mass relation, $M_* - M_{\rm halo}$ (e.g. Moster et al. 2010; Guo et al. 2010). More direct measurements of $M_* - M_{\rm halo}$ can also be made by measuring halo masses using, for example, galaxy-galaxy lensing (e.g. Hoekstra et al. 2004; Hudson et al. 2013) or satellite dynamics (e.g. Prada et al. 2003; More et al. 2011), with the various methods giving reasonable agreement (e.g. Leauthaud et al. 2012).

However, the range of masses that can be probed by abundance matching is limited by the luminosity down to which galaxy surveys are complete, and by variations in the halo mass functions of simulations. Large scale galaxy surveys, e.g. SDSS and GAMMA, have provided complete stellar mass functions (Baldry et al. 2008, 2012) down to $\sim 10^8 M_\odot$within volumes that are large enough such that the mass function within collisionless cosmological simulations have variations which are insignificant.

The details at the low mass end, $M_* \lesssim 10^9 M_\odot$, become less clear, as does the question as to how to extend the relation to even lower mass galaxies. For example, the stellar mass function from Baldry et al. (2008) has an upturn at the low mass end, which translates to an upturn in the $M_* - M_{\rm halo}$ relation (Behroozi et al. 2013). This implies a slope of the $M_* - M_{\rm halo}$ relation of α=1.6 at the low mass end, where $M_* \propto {M_{\rm halo}}^\alpha$. Extrapolating this relation to lower masses would imply that low stellar mass galaxies would reside in significantly lower mass dark matter haloes than predicted by extrapolating the earlier models of Moster et al. (2010) and Guo et al. (2010),

which found steeper slopes (higher values of α) for the $M_*-M_{\rm halo}$ relation.

However, Garrison-Kimmel et al. (2014) point out that extrapolating a slope of α=1.6 would significantly over-estimate the number of Local Group galaxies with $M_* \gtrsim 5\times10^6 {\rm M}_\odot$. Using updated observational data from Baldry et al. (2012), which shows less upturn in the stellar mass function and hence a steeper $M_*-M_{\rm halo}$ relation, Garrison-Kimmel et al. (2014) find a slope α=1.92 at the low mass end.

Regardless of these differences, there is no *a piori* reason to believe that the relation between stellar mass and halo mass should be extrapolated to low mass galaxies, $M_*<10^8 {\rm M}_\odot$. Further, the relation derived from large volume galaxy surveys may not be directly applicable to the particular environment of the Local Group.

In this study, we use constrained simulations of the local universe (CLUES) to show that the mass function of a volume analogous to the Local Group follows a single power law. This allows us to match the masses of dark matter haloes taken from the underlying power law mass function directly to the stellar masses of observed Local Group galaxies. We thus provide the first robust measurement of the relation between the stellar mass of Local Group galaxies and the masses of the haloes in which they are hosted, assuming a ΛCDM cosmology.

7.2 Local Group Simulations

We use here the same set of CLUES simulations already extensively described in the previous Chapters. Our fiducial dark matter only run has WMAP5 cosmology (Dunkley et al. 2009), and its two most massive haloes, taken as analogues of the MW and M31, have virial masses of $M_{\rm MW}=1.7\times10^{12}{\rm M}_\odot$ and $M_{\rm M31}=2.2\times10^{12}{\rm M}_\odot$ and are separated by a distance of 849 kpc.

To calculate *rms* errors between simulated halo masses and the underlying power law mass function, we also use a CLUES local group run with WMAP3 cosmology, and 10 simulated local group volumes from the Exploring the Local Group Volume In Simulation Suite (ELVIS, Garrison-Kimmel et al. 2014).

The `AHF` halo finder[1] (Gill et al. 2004b; Knollmann & Knebe 2009) has been used to identify all (sub-)haloes in our simulation. Virial mass is defined as the mass within a sphere containing $\Delta_{vir} \simeq 350$ times the cosmic mean matter density. We measure halo masses at their maximum mass, prior to being stripped.

[1] http://popia.ft.uam.es/AHF

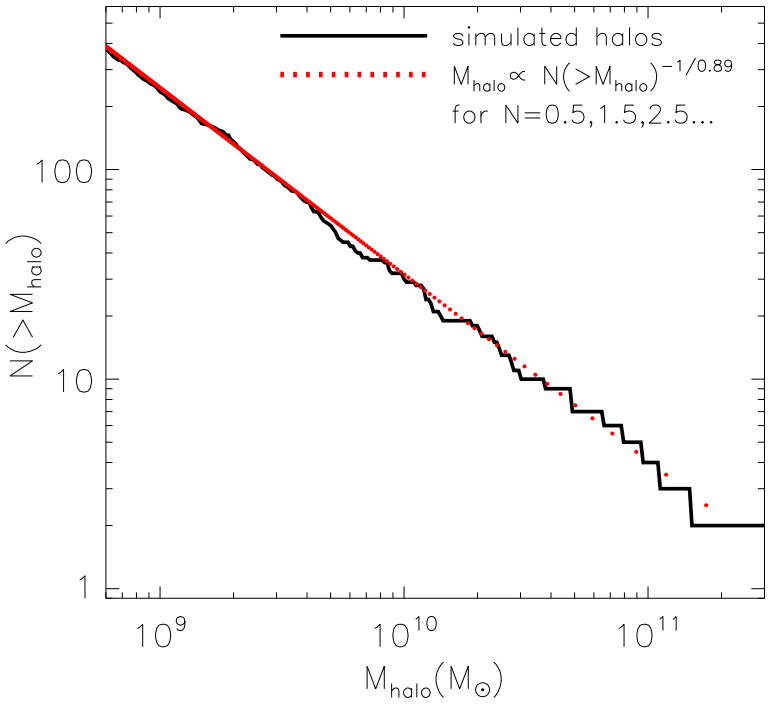

Figure 7.1: The mass function of CLUES haloes, including subhaloes, within the defined local group region (LGV, black line). The red dots follow the best fit to the halo mass function, with masses assigned to each N= 0.5, 1.5, 2.5 etc. by inverting the mass function to give $M_{\rm halo} \propto {\rm N}(>M_{\rm halo})^{-1/0.89}$. Credit: Brook et al. (2014).

7.3 Results

In what follows, the slope of the dark matter halo mass function, $\alpha_{\rm dm}$, is defined via a power law fit to the mass function, $\mathrm{N}(>M_{\rm halo}) \propto {M_{\rm halo}}^{\alpha_{\rm dm}}$. The slope, α, of the $M_*-M_{\rm halo}$ is defined by assuming a power law fit $M_* \propto {M_{\rm halo}}^{\alpha}$. The local group volume (LGV) is defined as a sphere of radius 1.8 Mpc centred on the MW analogue halo.

Figure 7.1 shows (black line) the halo mass function of the fiducial CLUES local group simulation within the LGV. Subhaloes, using their maximum mass values prior to stripping, are included within the total halo population. The LGV mass function follows a single power law with slope $\alpha_{\rm dm}=-0.89$, the same slope as the cosmological box from which the LGV is drawn, and essentially the same slope as other cosmological mass functions in the literature (e.g. Jenkins et al. 2001).

The LGV of the CLUES simulation run with WMAP3 cosmology also has a mass function slope of $\alpha_{\rm dm}=-0.89$, the same as the slope in the cosmological volume from which it is drawn. Further, the 10 LGVs surrounding paired MW/M31 analogue haloes from Garrison-Kimmel et al. (2014), follow a slope $\alpha_{\rm dm}=-0.9$. These results provide strong evidence that the mass function of Local Group dwarf galaxies is a single power law.

The red dots in Figure 7.1 are halo masses of a defined local group distribution which follows the mass function power law: masses are assigned to each N= 0.5, 1.5, 2.5 etc., according to the inverted mass function,

$$\frac{M_{\rm halo}}{10^{10} M_{\odot}} = N_0 \times N(> M_{\rm halo})^{-1.12} \tag{7.1}$$

where N_0=47.9 for our fiducial model, and N_0=38.1 for the mean of the 12 simulated LGVs.

This distribution of masses is appropriate for direct application to the observed Local Group, with the virial masses of each halo subject only to Poisson noise around the power law halo mass function.

We next match this power law halo mass distribution to observed stellar masses of Local Group galaxies, assuming a one-to-one correspondence in order of mass, as shown in Figure 7.2. Our predicted Local Group abundance matching is shown as points with error bars, while stellar-to-halo mass relations from previous studies are shown as lines. Observed Local Group galaxy luminosities are taken from McConnachie (2012), with stellar mass to light (M_*/L) taken from Woo et al. (2008). Updated distance measurements have resulted in slight changes to the Woo et al. (2008) stellar masses (see Kirby et al. 2013,for a table of updated stellar masses for most

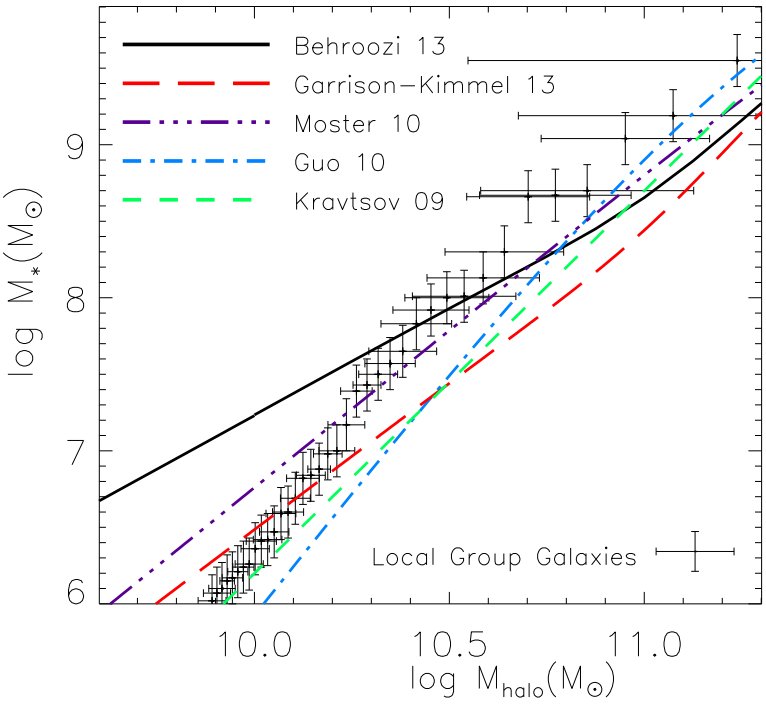

Figure 7.2: The stellar mass of observed Local Group galaxies within 1.8 Mpc of the Milky Way, assigned to halo masses from the power law fit to the halo mass function (red dots in Figure 7.1). Stellar mass errors are 0.17*dex* (Woo et al. 2008). Halo mass errors are the *rms* deviations of simulated LGV halo masses from the power law fit to the halo mass function. Also shown are the stellar-halo mass relations of Behroozi et al. 2013 (solid line), Garrison-Kimmel et al. 2013 (long-dashed line), Moster et al. 2010 (triple-dot-dashed line), Guo et al, 2010 (dot-dashed line), and the luminosity-mass relation from Kravtsov 2010 (dashed line). Scatter in the halo mass-stellar mass would only change the matching order: shifting high stellar mass galaxies into low mass haloes must be accompanied by low stellar mass galaxies being hosted by high mass haloes. The slope will not be flattened. Credit: Brook et al. (2014).

galaxies). We assume M_*/L=1.6 for galaxies not listed in either Woo et al. (2008) or Kirby et al. (2013). There are 41 galaxies in our sample with $M_*>10^6 M_\odot$ and within 1.8 Mpc of the Milky Way.

Error bars for stellar masses in Figure 7.2 are 0.17 *dex*, the quoted typical error in Woo et al. (2008). Error bars for $M_{\rm halo}$ in Figure 7.2 are *rms* errors of each simulated halo mass from the corresponding (by ordered number) power law halo mass, $M_{\rm halo} \propto N^{-1/\alpha}$, using our full suite of 12 simulated LGVs. These errors in halo mass are dominated by Poisson noise, with other sources of error coming from the different cosmologies and any sample variance being insignificant. The errors on the halo masses are reasonably small in the relevant region for this study, where $N(>M_{\rm halo})>10$. This region is relavent because there are 10 Local Group galaxies with $M_* \gtrsim 10^8 M_\odot$. so the single power law in this region can be used to match galaxies with $M_* \lesssim 10^8 M_\odot$.

Analyzing Figure 7.2 we found that the $M_*-M_{\rm halo}$ relation for the Local Group galaxies is well fit by α=3.1 in the region $10^7<M_*/M_\odot\leq10^8$. The catalogue of Local Group galaxies within 1.8 Mpc of the MW is likely complete down to $M_*=10^7 M_\odot$ and possibly down to $M_*=5\times10^6 M_\odot$ (Koposov et al. 2008; Tollerud et al. 2008). If we do increase the assumed completeness range to $5\times10^6<M_*/M_\odot\leq10^8$ we obtain a slope of α=3.5.

In this context, we note the recent discovery of satellites in the vicinity of M31 that have stellar masses of several times $10^6 M_\odot$ (Martin et al. 2013b,a), demonstrating that we are certainly not complete down to $M_* \sim 10^6 M_\odot$ in the Local Group. Even using the $M_* = 10^7 M_\odot$ limit, our derived slope of the $M_*-M_{\rm halo}$ relation, α=3.1, is nevertheless significantly steeper than most values in the literature (see the Introduction and Figure 7.2).

The normalization of the mass function coming from the total mass of the Local Group will not affect such derived value of α; instead, the effect will be to shift all points in Figure 7.2 left or right. In the region $10^7<M_*/M_\odot\leq10^8$, the $M_*-M_{\rm halo}$ relation is fit by

$$M_* = \left(\frac{M_{\rm halo}}{M_0 \times 10^6}\right)^{3.1} \tag{7.2}$$

where M_0=79.6 in our fiducial run. M_0=63.1 when using the mean power law mass function for the 12 LGVs. Similarly, systematic errors in observed stellar mass determinations, such as assuming a different initial mass function, will shift all points up or down.

In Figure 7.3, we plot the stellar mass function of observed Local Group galaxies, shown as the black line. Fixing the halo mass function slope at $\alpha_{\rm dm}=-0.89$, we examine the resultant stellar mass functions for various

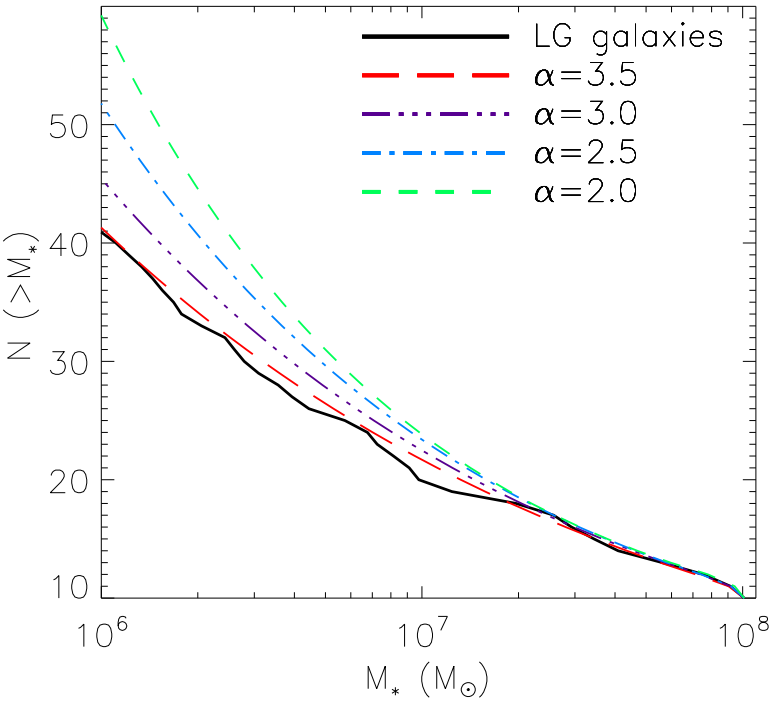

Figure 7.3: The stellar mass function of observed Local Group galaxies within 1.8 Mpc of the Milky Way (black line). Coloured lines are stellar mass functions that assume a halo mass function of slope $\alpha_{\rm dm}$=−0.89 along with various assumed slopes for a power law $M_*-M_{\rm halo}$ relation, α=2, 2.5, 3, 3.5 plotted as dashed, dot-dashed, triple-dot-dashed and long-dashed lines respectively. Normalization ensures 10 galaxies with $M_*>10^8 {\rm M}_\odot$in each case: we are interested in the shapes of the curves. Credit: Brook et al. (2014).

assumed values of the slope of the $M_*-M_{\rm halo}$ relation, α. Stellar mass functions that result from assuming α=2, 2.5, 3, 3.5 are plotted as dashed, dot-dashed, triple-dot-dashed and long-dashed lines respectively in Figure 7.3. Normalisation ensures 10 galaxies with $M_*>10^8{\rm M}_\odot$, i.e. the observed number, in each case.

The stellar mass functions for low values of α diverge from the observed function as we go to low stellar masses. Down to a completeness limit of $M_*\sim10^7{\rm M}_\odot$, values of α are hard to distinguish, with just a few galaxies separating α=2 from α=3.5. However, assuming that the completeness limit for Local Group is closer to $5\times10^6{\rm M}_\odot$, a slope of $\alpha \gtrsim 3$ is clearly favoured. As the catalogue of observed Local Group galaxies becomes complete to lower stellar masses, the stellar mass-halo mass relation will become increasingly well defined.

In Figure 7.3, no assumption of a one-to-one correspondence between halo mass and stellar mass is made, as it is in Figure 7.2. The slope of the stellar mass function, α_* is simply derived from the relation, $1+\alpha_*=(1+\alpha_{dm})/\alpha$. Any scatter around the $M_*-M_{\rm halo}$ relation, which may be large for low mass galaxies (e.g. Behroozi et al. 2013), will not affect our result for the preferred slope, $\alpha \gtrsim 3$.

7.4 Conclusions

We have extended the abundance matching relation between halo mass and stellar mass of galaxies down to the current Local Group observational completeness limit.

Supported by evidence from constrained local group simulations, we argue that a power law mass function for haloes is appropriate to be directly applied to Local Group galaxies. Poisson noise of simulated realizations provide well defined errors in halo masses. By matching such power law mass function to stellar masses of observed Local Group galaxies, we determine a slope of the $M_*-M_{\rm halo}$ relation of α=3.1 for galaxies with stellar mass $M_* \lesssim 10^8{\rm M}_\odot$. This determination of the relation for Local Group galaxies down to $M_*=10^7{\rm M}_\odot$ is significantly steeper than most values in the literature, which have generally been extrapolations of the abundance matching relation from higher masses.

Our value of α is consistent with the extrapolation of the Guo et al. (2010) relation to small stellar masses, yet the upturn in the relation at masses above $M_*=10^8{\rm M}_\odot$ (Behroozi et al. 2013; Garrison-Kimmel et al. 2014) indicates that the extended relation is likely to be more complex than a single power law for masses $M_*<10^9{\rm M}_\odot$.

The key insight of our paper comes from the fact that the halo mass function of the local group analog simulation in a volume with radius 1.8 Mpc follows a single power law slope to large enough masses to host all the local group galaxies with $M_* \lesssim 10^8 M_\odot$. Because the census of observed Local Group galaxies is well known down to $M \sim 10^7 M_\odot$ (or a little lower) within such a volume, we can match Local Group dwarf galaxies to dark matter haloes drawn from a population that follows a power law in a region where Poisson noise, which determines the uncertainties in the halo masses, is low.

On the other hand, smaller volumes, such as sub-halo mass functions of Milky Way analogue haloes, are not constrained in this manner. *On average*, such populations will also follow a single power law (e.g. Boylan-Kolchin et al. 2010), but their individual mass functions are dominated by Poisson noise. Therefore the Local Group is unique, with a volume that is large enough to have a single, well defined power law mass function, yet small enough to find faint galaxies.

Scatter in the $M_* - M_{\rm halo}$ relation appears evident in the Local Group. For example, Fornax is 100 times more luminous than Draco, but seems to have a smaller halo mass (Peñarrubia et al. 2008). However, such scatter will not flatten the slope of the stellar-to-halo mass relation that we derived, as is evident in Figure 7.3 where only slopes are considered, with no assumption made regarding how stellar masses and halo masses are matched. Nevertheless, scatter in the $M_* - M_{\rm halo}$ relation will result in some relatively high stellar mass galaxies being hosted by relatively low mass haloes, but this is only achieved in conjunction with relatively low stellar mass galaxies being hosted by high mass haloes.

As we show in Figure 7.3, surveys of Local Group galaxies that extend the the completeness limit to lower luminosities, such as `SKYMAPPER` (Keller et al. 2007) and `LSST` (LSST Science Collaboration et al. 2009) will provide increasingly strong constraints on the $M_* - M_{\rm halo}$ relation, and particularly on the slope of such relation at small masses, simply by matching observed data to a power law mass function for dark matter haloes.

7.5 Discussion

Finally, and most importantly, we have shown that the vast majority of the galaxies in the Local Group, regardless of whether they are satellites or isolated, are predicted to be housed in haloes whose mass exceeds $10^{10} M_\odot$, in evident contrast with dynamical measurements of dSphs, which would assign most of these galaxies to a halo of smaller mass. Such assignment assumes that the dark matter halo follows the density profile derived from

N-body simulations, the commonly used NFW model.

They way out of this discrepancy may reside in baryonic processes that are neglected when using collisionless simulations to make predictions about observed dwarf galaxies. If we can identify a process that is able to cause an expansion of the dark matter halo of satellite galaxies, then we will solve at the same time the "massive subhaloes" problem and the abundance matching vs. dynamical measurements discrepancy.

Indeed, some satellites will be hosted in big ($\sim 10^{10}\mathrm{M}_{\odot}$), expanded haloes, thus in agreement with the prediction of our LG abundance matching. Such haloes will also be in agreement with dynamical measurements of dSphs, as their velocity dispersion can be well fitted by a $\sim 10^{10}\mathrm{M}_{\odot}$ cored halo (or by a smaller $\sim 10^{9}\mathrm{M}_{\odot}$, cuspy NFW halo, scenario that we have seen to cause many tensions within a galaxy formation model). The TBTF problem will then be solved since such cored haloes would be much less concentrated toward the center, and they would be big enough not to leave any "massive failure": in other words, all the biggest haloes will now be populated with galaxies, with an expanded inner dark matter profile in agreement with observations of stellar velocity dispersions.

Of course, one naively expects that whatever is the baryonic mechanism that causes expansion in dark matter haloes, it would be connected to the amount of stellar, baryonic mass available in each galaxy, ultimately leading to different profiles according to the different amount of energy that each galaxy has. We do not expect, therefore, all the satellite galaxies in the LG to live within an expanded halo: there must be some case in which the "baryonic energy" is simply not enough to create a cored profile, and such galaxies will retain a cuspy, NFW halo.

The evidence for a mixed population of cored and cuspy satellite galaxies within the Local Group is strongly supported by observations (Walker & Peñarrubia 2011; Wolf & Bullock 2012).

Exploring what are the main mechanisms able to cause an expanded dark matter haloes in galaxies will be the focus of the next Chapters of this thesis, by using hydrodynamical simulations of galaxies from the MaGICC project.

A detailed study of the connection between satellite galaxies' kinematics, abundance matching in the Local Group and the core/cusp discrepancy in galaxies is an ongoing project.

Chapter 8

Cusp and cores in galaxies: the dependence of dark matter profiles on the stellar-to-halo mass ratio

We have seen in the previous Chapters the importance of studying the impact of baryonic physics on galaxy formation, particularly regarding the core/cusp discrepancy.

To explore this issue, we use a suite of 31 simulated galaxies drawn from the MaGICC project to investigate the effects of baryonic feedback on the density profiles of dark matter haloes. The sample covers a wide mass range: $9.4 \times 10^9 < M_{\rm halo}/{\rm M}_\odot < 7.8 \times 10^{11}$, hosting galaxies with stellar masses: $5.0 \times 10^5 < M_\star/{\rm M}_\odot < 8.3 \times 10^{10}$, i.e. from dwarf to L*. The galaxies are simulated with blastwave supernova feedback and, for some of them, an additional source of energy from massive stars is included. Within this feedback scheme we vary several parameters, such as the initial mass function, the density threshold for star formation and energy from supernovae and massive stars.

The main result is a clear dependence of the inner slope of the dark matter density profile, α in $\rho \propto r^\alpha$, on the ratio between stellar-to-halo mass, $M_\star/M_{\rm halo}$. This relation is independent of the particular choice of parameters within our stellar feedback scheme, allowing a prediction for cusp vs core formation. When $M_\star/M_{\rm halo}$ is low, $\lesssim 0.01$ per cent, energy from stellar feedback is insufficient to significantly alter the inner dark matter density and the galaxy retains a cuspy profile. At higher ratios of stellar-to-halo mass feedback drives the expansion of the dark matter and generates cored

profiles. The flattest profiles form where $M_\star/M_{\rm halo} \sim 0.5$ per cent. Above this ratio, stars formed in the central regions deepen the gravitational potential enough to oppose the supernova-driven expansion process, resulting in cuspier profiles. Combining the dependence of α on $M_\star/M_{\rm halo}$ with the empirical abundance matching relation between $M_\star$ and $M_{\rm halo}$ provides a prediction for how α varies as a function of stellar mass. Further, using the Tully-Fisher relation allows a prediction for the dependence of the dark matter inner slope on the observed rotation velocity of galaxies. The most cored galaxies are expected to have $V_{\rm rot} \sim 50\,{\rm km\,s^{-1}}$, with α decreasing for more massive disc galaxies: spirals with $V_{\rm rot} \sim 150\,{\rm km\,s^{-1}}$ have central slopes $\alpha \leqslant -0.8$, approaching again the NFW profile. This novel prediction for the dependence of α on disc galaxy mass can be tested using observational data sets and can be applied to theoretical modeling of mass profiles and populations of disc galaxies.

8.1 Introduction

The Λ Cold Dark Matter (ΛCDM) cosmological model has been shown to agree with observations of structures on large scales (e.g. Riess et al. 1998; Komatsu et al. 2011; Hinshaw et al. 2013; Planck Collaboration et al. 2013). According to this theory, galaxies are embedded within dark matter (DM) haloes (White & Rees 1978; Blumenthal et al. 1984), whose properties have been extensively studied in the past thanks to numerical N-body simulations (e.g. Springel 2005; Power & Knebe 2006; Maccio' et al. 2008; Kuhlen et al. 2012). Problems at small scales, however, still affect the ΛCDM model, one of which is the so-called "cusp-core" problem. A prediction of pure DM collisionless simulations is that dark matter density increases as $\rho \propto r^{-1}$ toward the halo center (Navarro et al. 1996b; Springel et al. 2008; Navarro et al. 2010). The existence of such a "cuspy" density profile is in disagreement with observations of disc and dwarf galaxies (e.g., Salucci & Burkert 2000; Simon et al. 2005; de Blok et al. 2008; Kuzio de Naray et al. 2008b, 2009; Oh et al. 2011b), where detailed mass modeling using rotation curves suggests a flatter, or "cored", DM density profile. Simulated DM haloes modeled with an Einasto (Einasto 1965) profile have a inner slope of -0.7 (Graham et al. 2006a): this value is closer to what observed in real galaxies (Swaters et al. 2003), yet not sufficient to solve the discrepancy (de Blok et al. 2003).

One possibility, without resorting to more exotic forms of dark matter (e.g. warm dark matter see Avila-Reese et al. 2001; Bode et al. 2001; Knebe et al. 2002,Macciò et al. 2012b), is that this inconsistency arises from having neglected the effects of baryons, which are irrelevant on cosmological

scales where dark matter and dark energy dominate, but may be dynamically relevant on small, galactic scales. For example, as gas cools to the central region of galaxy haloes, it adiabatically contracts dark matter to the centre (e.g. Blumenthal et al. 1986; Gnedin et al. 2004). Such adiabatic contraction exacerbates the mismatch between the profiles of dark matter haloes and the observed density profiles inferred from rotation curves. Further, theoretical models with halo contraction are unable to self-consistently reconcile the observed galaxy scaling relations, such as the rotation velocity-luminosity and size-luminosity relations. Un-contracted or expanded haloes are required (Dutton et al. 2007, 2011).

Two main mechanisms have been shown to cause expansion: supernova feedback (Navarro et al. 1996a; Mo & Mao 2004; Read & Gilmore 2005; Mashchenko et al. 2006; Pontzen & Governato 2012) and dynamical friction (El-Zant et al. 2001; Tonini et al. 2006; Romano-Díaz et al. 2008; Goerdt et al. 2010; Cole et al. 2011). Supernova feedback drives sufficient gas outflows to flatten the central dark matter density profile in simulated dwarf galaxies (Governato et al. 2010; Teyssier et al. 2013) into a "core". Dynamical friction smooths dark matter density profiles during mergers.

The analytical model of Pontzen & Governato (2012) predicts that repeated outflows, rather than a single, impulsive mass loss (as in Navarro et al. 1996a), transfer energy to the dark matter. The rapid oscillations of the central gravitational potential perturb the dark matter orbits, creating a core. Mashchenko et al. (2006) decribed a similar mechanism in which supernova-driven outflows changed the position of the halo centre, also creating a core. Macciò et al. (2012) showed that reasonable amounts of feedback in fully cosmological simulations can result in dark matter cores rather than cusps in galaxies as massive as $L^{\star}$. Governato et al. (2012) measured the inner dark matter slope in a sample of simulated dwarf galaxies, that match well the stellar-to-halo mass relation (Munshi et al. 2013), using a power law density profile $\rho \propto r^{\alpha}$. They found that the slope α increases, i.e. the profile flattens, with increasing stellar mass.

In this chapter we study dark matter density profiles in a suite of galaxies drawn from the MUGS (Stinson et al. 2010) and MaGICC projects (Stinson et al. 2013; Brook et al. 2012b). The galaxies cover a broad mass range from dwarf to massive discs, and are simulated using a variety of stellar feedback implementations. The wide mass range of our simulated galaxies, $5.0 \times 10^5 < M_{\star}/\mathrm{M}_{\odot} < 8.3 \times 10^{10}$, allows us to confirm and extend the results of Governato et al. (2012). We show that the most relevant property for the determination of the DM inner slope is actually the stellar-to-halo mass ratio, i.e. the star formation efficiency, and that the relation between α and stellar mass turns over such that the inner density profiles of more massive

disc galaxies become increasingly steep.

We present our simulations in Section 8.2, the results and predictions in Section 8.3 and the conclusions in Section 8.4.

8.2 Simulations

The hydrodynamical simulations used in this study are part of the MaGICC project, as described in Section 2.2.

All of the simulations are listed in Table 1 where they are separated into 3 mass groups: high, medium and low mass. The symbol shapes denote simulations with the same initial conditions, while the colors indicate the specific star formation and feedback model used. The medium and low mass initial conditions are scaled down variants of the high mass initial conditions, so that rather than residing in a 68 Mpc cube, they lie within a cube with 34 Mpc sides (medium) or 17 Mpc sides (low mass). This rescaling allows us to compare galaxies with exactly the same merger histories at three different masses. Differences in the underlying power spectrum that result from this rescaling are minor (Springel et al. 2008; Maccio' et al. 2008; Kannan et al. 2012). Moreover this methodology does not affect our analysis and results since we reach, at the low halo mass end where we have made the rescaling, the same conclusions as in Governato et al. (2012) whose galaxies do not have rescaled initial conditions.

In addition to the hydrodynamic, SPH simulations, collisionless, dark matter-only simulations were performed for each initial condition. These DM-only runs exhibit a wide range of concentrations, from those typical of the L* to dwarf galaxies. The concentration, c, varies between $10 \lesssim c \lesssim 15$, where $c \equiv R_{\rm vir}/r_{\rm s}$ and $r_{\rm s}$ is the scale radius of the NFW profile (Navarro et al. 1996b). Such a range is sufficient to study density profiles. Indeed, the sample includes a number of galaxies with high c at each mass range, a legacy of preferentially simulating galaxies with early formation times in order to model Milky Way formation.

The main haloes in our simulations were identified using the MPI+OpenMP hybrid halo finder `AHF`[1] (Knebe et al. 2013; Knollmann & Knebe 2009; Gill et al. 2004a). The virial masses of the haloes, $M_{\rm halo}$, are defined as the masses within a sphere containing $\Delta = 390$ times the cosmic background matter density at $z = 0$.

[1] http://popia.ft.uam.es/AMIGA

Table 8.1: Simulation parameters

	MUGS label	gas part. mass [$M_\odot$]	soft [pc]	$M_{\rm halo}$ [$M_\odot$]	$R_{\rm vir}$ [kpc]	$M_\star$ [$M_\odot$]	$E_{\rm SN}$	$\epsilon_{\rm esf}$	IMF	$n_{\rm th}$ [cm^{-3}]	sym
Low	g1536	3.1×10^3	78.1	9.4×10^9	61	7.2×10^5	1.0	0.1	C	9.3	●
	g1536	3.1×10^3	78.1	9.4×10^9	60	5.1×10^5	1.0	0.125	C	9.3	●
	g1536	3.1×10^3	78.1	9.4×10^9	61	5.0×10^5	1.0	0.175	C	9.3	●
	g1536	3.1×10^3	78.1	9.4×10^9	60	7.0×10^5	1.2	0.0	C	9.3	●
	g15784	3.1×10^3	78.1	1.9×10^{10}	77	8.9×10^6	1.0	0.1	C	9.3	▲
	g15784	3.1×10^3	78.1	1.9×10^{10}	79	7.4×10^8	0.4	0	K	0.1	▲
	g15784	3.1×10^3	78.1	1.9×10^{10}	79	8.4×10^6	1.0	0.125	C	9.3	▲
	g15784	3.1×10^3	78.1	1.8×10^{10}	75	6.0×10^6	1.0	0.175	C	9.3	▲
	g15784	3.1×10^3	78.1	1.8×10^{10}	75	1.1×10^7	1.2	0.0	C	9.3	▲
	g15807	3.1×10^3	78.1	3.0×10^{10}	89	1.6×10^7	1.0	0.1	C	9.3	■
Medium	g7124	2.5×10^4	156.2	5.3×10^{10}	107	1.3×10^8	1.0	0.1	C	9.3	*
	g5664	2.5×10^4	156.2	6.3×10^{10}	114	2.4×10^8	1.0	0.1	C	9.3	♦
	g5664	2.5×10^4	156.2	6.6×10^{10}	116	1.0×10^9	0.8	0.05	C	9.3	♦
	g5664	2.5×10^4	156.2	7.3×10^{10}	120	8.7×10^9	0.4	0	K	0.1	♦
	g1536	2.5×10^4	156.2	8.3×10^{10}	125	4.5×10^8	1.0	0.1	C	9.3	●
	g21647	2.5×10^4	156.2	9.6×10^{10}	131	2.0×10^8	1.0	0.1	C	9.3	◀
	g15784	2.5×10^4	156.2	1.8×10^{11}	161	4.3×10^9	1.0	0.1	C	9.3	▲
	g15784	2.5×10^4	156.2	1.8×10^{11}	161	2.4×10^9	1.0	0.125	C	9.3	▲
	g15784	2.5×10^4	156.2	1.9×10^{11}	164	7.1×10^9	1.0	0.1	K	9.3	▲
	g15784	2.5×10^4	156.2	1.7×10^{11}	157	8.6×10^8	1.0	0.1	C	9.3	▲
	g15807	2.5×10^4	156.2	2.9×10^{11}	189	1.5×10^{10}	1.0	0.1	C	9.3	■
High	g7124	2×10^5	312.5	4.5×10^{11}	219	6.3×10^9	1.0	0.1	C	9.3	*
	g7124	2×10^5	312.5	4.9×10^{11}	227	5.1×10^{10}	0.4	0	K	0.1	*
	g5664	2×10^5	312.5	5.6×10^{11}	236	2.7×10^{10}	1.0	0.1	C	9.3	♦
	g5664	2×10^5	312.5	5.7×10^{11}	237	4.9×10^{10}	0.4	0	K	0.1	♦
	g5664	2×10^5	312.5	5.9×10^{11}	241	1.4×10^{10}	1.0	0.175	C	9.3	♦
	g1536	2×10^5	312.5	7.2×10^{11}	257	2.4×10^{10}	1.0	0.1	C	9.3	●
	g1536	2×10^5	312.5	7.7×10^{11}	264	8.3×10^{10}	0.4	0	K	0.1	●
	g1536	2×10^5	312.5	7.0×10^{11}	254	1.1×10^{10}	1.0	0.125	C	9.3	●
	g1536	2×10^5	312.5	7.8×10^{11}	265	2.5×10^{10}	1.0	0.175	C	9.3	●
	g1536	2×10^5	312.5	7.0×10^{11}	255	1.8×10^{10}	1.2	0.0	C	9.3	●

8.2.1 Star Formation and Feedback

The hydrodynamical simulations all include star formation, with the stars feeding energy back into the interstellar medium (ISM) gas. A range of star formation and feedback parameters are used in this study: all of them employ blastwave supernova feedback (Stinson et al. 2006), and some also include "early stellar feedback", the energy that massive stars release prior to their explosions as supernovae (Stinson et al. 2013). Early stellar feedback uses a fraction, $\epsilon_{\rm esf}$, of the total luminosity emitted by massive stars. In the fiducial model used in the MaGICC simulations, $\epsilon_{\rm esf}$=0.1, which corresponds to the fraction of ionizing UV flux emitted from young stellar populations.

Two initial mass functions were used in the simulations. MUGS used (Kroupa et al. 1993,denoted K), while most of the rest used (Chabrier 2003,denoted C). Chabrier (2003) produces two times more type SNII per mass of stars born.

The fiducial feedback (red colored symbols) includes early stellar feedback with $\epsilon_{\rm esf} = 0.1$, 10^{51}erg of energy deposited per supernova and a Chabrier (2003) IMF. The early stellar feedback efficiency $\epsilon_{\rm esf}$ is increased from 0.1 to 0.125 (blue) in some simulations, while in others $\epsilon_{\rm esf} = 0$, but the energy per supernova is then increased by 20 per cent (cyan). In yellow, we include simulations with $\epsilon_{\rm esf} = 0.175$, in which diffusion of thermal energy from gas particles (Stinson et al. 2012; Wadsley et al. 2008) is allowed to occur during the adiabatic expansion phase. We also include simulations made with the original MUGS feedback, with 4×10^{50}erg per supernova, a Kroupa et al. (1993) IMF and no $\epsilon_{\rm esf}$, which systematically overproduce the number of stars at each halo mass (black). Finally, an intermediate feedback implementation with $\epsilon_{\rm esf} = 0.05$, Chabrier IMF and 8×10^{50}erg per supernova, has been also added (purple).

The reader is referred to Stinson et al. (2013) for a study of the effects of the parameters on the galaxy properties. Suffice to say that the fiducial simulations best match present observed galaxy properties (see also Brook et al. 2012b).

8.3 Results

We study the response of the dark matter distribution to different feedback schemes within this full set of simulated galaxies. Some example density profiles are shown in Figure 8.1. It shows how the dark matter density profiles of the hydrodynamic simulations can vary depending on physics

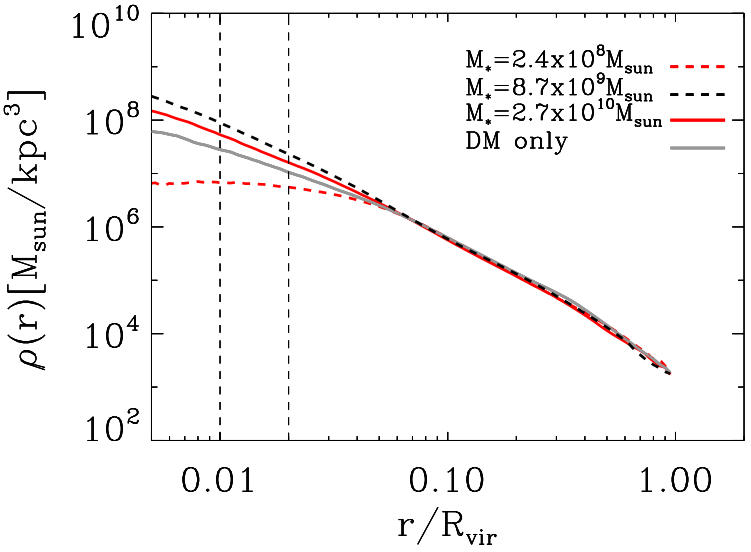

Figure 8.1: Density profiles of contracted (solid red and dashed black lines) and expanded (dashed red line) dark matter haloes, together with the corresponding DM only prediction (solid grey). The vertical dashed lines indicate 0.01 and 0.02 of the virial radius, our fiducial range to measure α.

(MUGS in black compared to MaGICC fiducial simulations, that use early stellar feedback, in red), galaxy mass (solid line at high mass and dashed line at medium mass), and how the hydrodynamic simulations compare with the dark matter only run (solid grey line).

The halo profiles are calculated using logarithmically spaced bins and the dark matter central density is subsequently fit using a single power law, $\rho \propto r^{\alpha}$, over a limited radial range. The vertical dashed lines in Fig. 8.1 show the fiducial range over which α is measured, $0.01 < r/R_{\rm vir} < 0.02$, where $R_{\rm vir}$ is the virial radius. Other radial ranges are also used to ensure the robustness of our results.

The choice of $0.01R_{\rm vir}$ as the inner most bin satisfies the Power et al. (2003) criterion for convergence even in our least resolved galaxy, as it encloses enough DM particles to ensure that the collisional relaxation time is longer than the Hubble time. This range is also straightforward to reproduce, and is not dependent on the resolution of the simulations. We also measured α between $3 < r/\epsilon < 10$, where ϵ is the softening length of each galaxy, and at a fixed physical range, $1 < r/{\rm kpc} < 2$. The choice of radial fitting range does not affect our results qualitatively, and only makes small quantitative differences which we show in our main results.

8.3.1 Inner slope as a funcion of halo mass

We first examine how α varies with stellar and halo mass. The top panel of Fig. 8.2 shows the $M_\star - M_{\rm halo}$ relation for the entire suite of galaxies with the abundance matching prediction from Moster et al. (2013) indicated as the central solid black line with the 1σ uncertainties plotted as thin lines above and below the central relationship. Each galaxy is colored according to the feedback model and symbol coded correspondingly to which initial condition was used, as described in Table 1.

Simulations are scattered around the $M_\star - M_{\rm halo}$ relation. The fiducial feedback (red) represents the best fit to the abundance matching relation at every halo mass. Increasing the early stellar feedback efficiency $\epsilon_{\rm esf}$ (blue) reduces the stellar mass by a factor of two at the high mass end, while leaving the total amount of stars relatively unchanged at the low mass end, compared to the fiducial feedback. When early stellar feedback is not included the energy per supernova must be increased to $E_{\rm SN} = 1.2$ in order to lower the stellar mass to the Moster et al. (2013) relation (cyan). We note that the star formation history using such feedback is quite different from the fiducial runs, with more star formation at high redshift (see Stinson et al. 2013,for details). The yellow simulations that include high $\epsilon_{\rm esf}$ have systematically lower stellar-to-halo mass ratios, and also have high late time star formation. Finally, the original MUGS feedback (black) systematically forms too many stars at each halo mass.

The bottom panel of Fig. 8.2 shows α as a function of halo mass, where $M_{\rm halo}$ comes from the full hydrodynamical simulation[2]. The solid black line shows the theoretical expectation of α as a function of halo mass for the DM only case, as in Maccio' et al. (2008) assuming a WMAP3 cosmology; the thin solid lines represent the scatter in the c-$M_{\rm halo}$ relation.

At fixed halo mass, α varies greatly, depending on the feedback strength. The simulations that most closely follow the $M_\star - M_{\rm halo}$ relationship show a notable flattening of inner profile slopes as mass increases, as in Governato et al. (2012). This flattening is due to the increasing energy available from SNe explosions, as derived in Peñarrubia et al. (2012). Indeed, all the galaxies in our sample whose inner slope is shallower than the corresponding DM run, have had an energy injection from SNe equal or higher than the conservative values found in Peñarrubia et al. (2012). We note, however, that in our simulations the core creation process does not only depend on the total amount of energy available: in the g15784 MUGS dwarf galaxy (black triangle), for example, the energy from SNe is higher than in the

[2]Using $M_{\rm halo}$ taken from the dark matter only run provides similar results, as the halo mass amongst DM and SPH simulations changes by only a few percent.

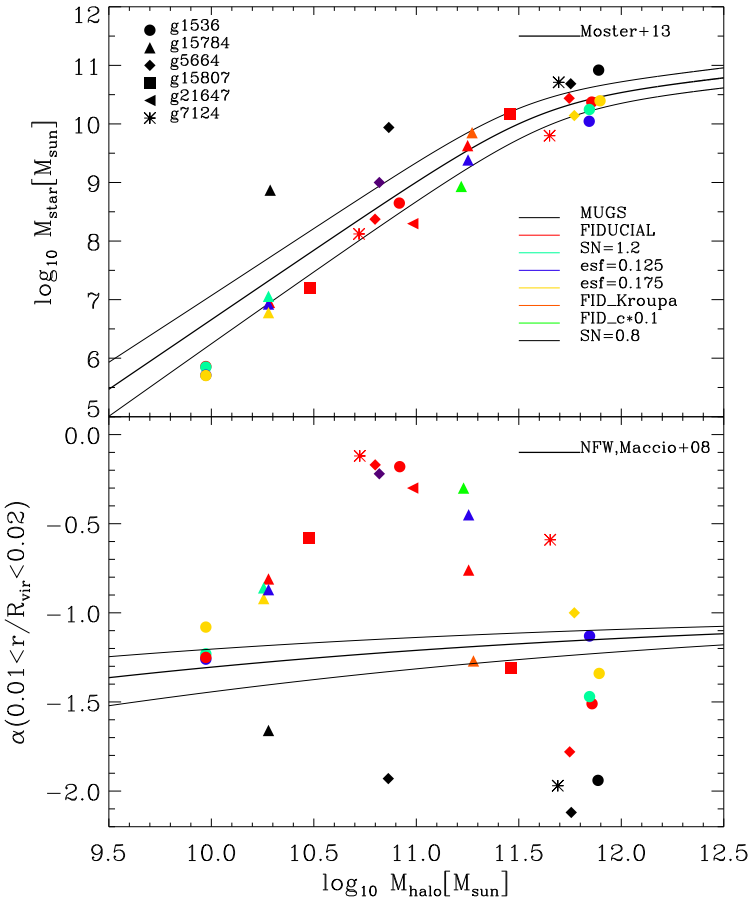

Figure 8.2: Top panel: The abundance matching relation for our suite of simulated galaxies. The feedback schemes are indicated with different colors, while the different galaxies are represented with symbols. The thick solid line corresponds to the abundance matching prediction from Moster et al. (2013) and the thin lines are the 1σ uncertainty on it. Bottom panel: The inner slope of the dark matter distribution, measured between 0.01 and 0.02 of each galaxy's virial radius, as a function of total halo mass. The solid lines are the theoretical expectation for dark matter haloes from Maccio' et al. (2008) with its scatter.

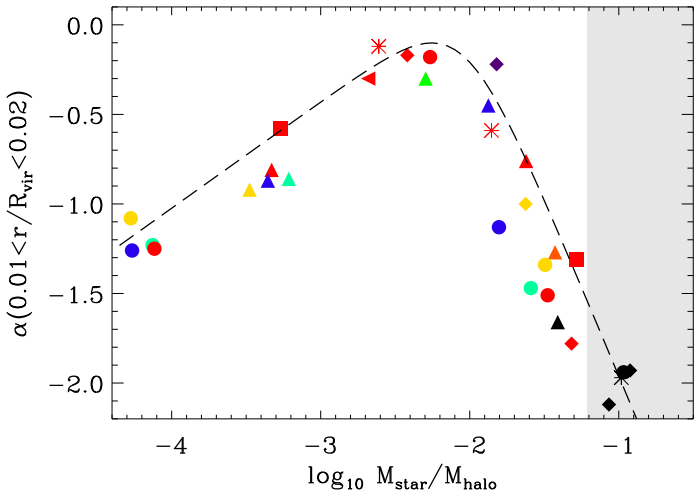

Figure 8.3: The relation between dark matter density profile slope, α, measured between $0.01 < r/R_{\rm vir} < 0.02$, and the stellar-to-halo-mass ratio of each galaxy. Colors and symbols are the same as in Fig. 8.2. The best fit function of Eq. (8.1) is overplotted as a dashed line. The grey area on the right side indicates the 1σ peak in the $M_\star/M_{\rm halo}$ abundance matching.

g15784 dwarfs of the same mass that had an expansion, yet this galaxy is strongly contracted. What we observe is the interplay between the energy from stellar feedback and the increased potential well caused by the high number of stars at the galaxy center (see next section for more details).

The profiles are flattest around $M_{\rm halo} \sim 10^{11}{\rm M}_\odot$.

At higher masses, however, the inner profiles steepen again. All the simulations above the $M_\star - M_{\rm halo}$ relationship have inner slopes $\alpha < -1.5$, i.e. a contracted halo steeper than the DM expectation at each halo mass. These simulations are all black colored indicating that they were part of the MUGS simulations.

Thus, depending on the feedback and the halo mass used, the dark matter haloes may expand, contract or retain the initial NFW inner slope. It seems that the inner slope of the dark matter density profile does not show a clear dependence on halo mass (or equivalently stellar mass) when different feedback schemes are included.

8.3.2 Inner slope as a funcion of stellar-to-halo mass

While there is not a well defined relation between α and stellar or halo mass individually, Fig. 8.3 shows α, measured between $0.01 < r/R_{\rm vir} < 0.02$, plotted as a function of $M_\star/M_{\rm halo}$. The dark matter inner profile slope shows a tight relationship as a function of $M_\star/M_{\rm halo}$: indeed, much of the scatter apparent when α was plotted as a function of $M_{\rm halo}$ disappears. The grey area indicates the region where the $M_\star/M_{\rm halo}$ ratios are more than 1σ above the $M_\star/M_{\rm halo}$ peak in the abundance matching relation. Real galaxies do not have these star formation efficiencies.

The tight relationship between α and $M_\star/M_{\rm halo}$ points to the conditions in which stellar feedback can create dark matter density cores. At low values of $M_\star/M_{\rm halo}$, the stellar content per halo mass is too small for the feedback energy to modify the DM distribution, and the halo of such galaxies retains a cuspy profile. As the stellar content per halo mass increases, the feedback energy is strong enough to produce expanded dark matter haloes, and thus for increasing values of $M_\star/M_{\rm halo}$ the inner slope of dark matter profiles gets flatter, reaching a maximum of $\alpha = -0.10$ at $M_\star/M_{\rm halo} = 0.5$ per cent. The maximum value of α is even smaller, i.e. the profiles are flatter, if the inner slope is measured closer to the centre. At $3 < r/\epsilon < 10$, $\alpha \sim 0$ at $M_\star/M_{\rm halo} = 0.35$ per cent. At higher masses, the amount of stars formed in the central regions deepens the potential well at the center of the galaxies, opposing the expansion process and leading to increasingly cuspy profiles for higher values of $M_\star/M_{\rm halo}$.

We verified this claim by studying in detail the medium mass version of g15784 for different choices of feedback parameters. We found that the stellar mass within 1 kpc is a good indicator of the minimum of the potential in each galaxy and that, as expected, the cored most version of g15784 (green triangle) has the shallowest potential well. Looking at the evolution of this galaxy, we observe that its SFR decreases with time and correspondingly the $M_\star/M_{\rm halo}$ value within 1 kpc is fairly constant at every redshift, reaching only 0.1 at $z = 0$; the fraction of gas vs stars at the center is always very high, making possible the core creation since there is enough gas per total mass (or stellar mass) to be efficient in flattening the profile.

This process does not occur in the cuspy version g15784 fiducial (red triangle), which has a constant SFR after 11 Gyrs and its $M_\star/M_{\rm halo}$ ratio within 1 kpc increases up to 0.4 at $z = 0$: the increasing amount of stars at the center causes the gas vs stars ratio to become very low, therefore the gas available for the outflows is not sufficient to be effective at flattening the profile because the potential well has been deepened by the stars.

We note that the total amount of gas in the inner 1kpc is similar in

Table 8.2: Best fit parameters and relative errors for the α vs $M_\star/M_{\rm halo}$ relation. The reduced Chi-Square is also listed.

radial range	n	$\log_{10}x_0$	β	γ	χ^2_r
$0.01 < r/R_{\rm vir} < 0.02$	0.132	-2.051	0.593	1.99	1.16
	±0.042	±0.074	±0.086	±0.32	
$1 < r/{\rm kpc} < 2$	0.168	-2.142	0.699	1.56	1.29
	±0.031	±0.133	±0.213	±0.12	
$3 < r/\epsilon < 10$	0.231	-2.209	0.494	1.49	1.28
	±0.043	±0.064	±0.055	±0.55	

both the cored and the cuspy medium mass versions of g15784: it is not the absolute amount of gas which regulates the cusp/core transition, but its relative value compared to the total (or stellar) inner mass. We conclude that stellar mass at the galaxy center and in particular the ratio $M_\star/M_{\rm halo}$ is the most important quantity at indicating the deepening of the gravitational potential which balances the energy released from SNe.

The relationship shown in Fig. 8.3 can be analytically modelled. We use a four parameter, double power law function, whose best fit is shown in Fig. 8.3 as a dashed black line:

$$\alpha(X) = n - \log_{10}\left[\left(\frac{X}{x_0}\right)^{-\beta} + \left(\frac{X}{x_0}\right)^{\gamma}\right], \tag{8.1}$$

where $X = M_\star/M_{\rm halo}$ while β and γ are the low and high star forming efficiency slopes. The best fit parameters, summarized in Table 2, were obtained using a χ^2 minimization fitting analysis. The same dependence, but with different normalization, is obtained for the various criteria used to define the inner radial range, also shown in Table 2.

Fig. 8.4 shows the abundance matching relationship of $M_\star/M_{\rm halo}$ as a function of $M_{\rm halo}$ color coded according to the expected value of DM inner slope when α is measured at $0.01 < r/R_{\rm vir} < 0.02$. The halo mass at which the flattest DM profiles are expected to be found, corresponding to a peak $M_\star/M_{\rm halo} = 0.5$ per cent, is $M_{\rm halo} \approx 10^{10.8}{\rm M}_\odot$. The profile becomes increasingly cuspy, approaching the NFW value for galaxies near the Milky Way mass: only galaxies with $M_\star/M_{\rm halo} > 3.8$ per cent, which is the peak in the abundance matching prediction, are contracted. Such galaxies are outliers in the Universe.

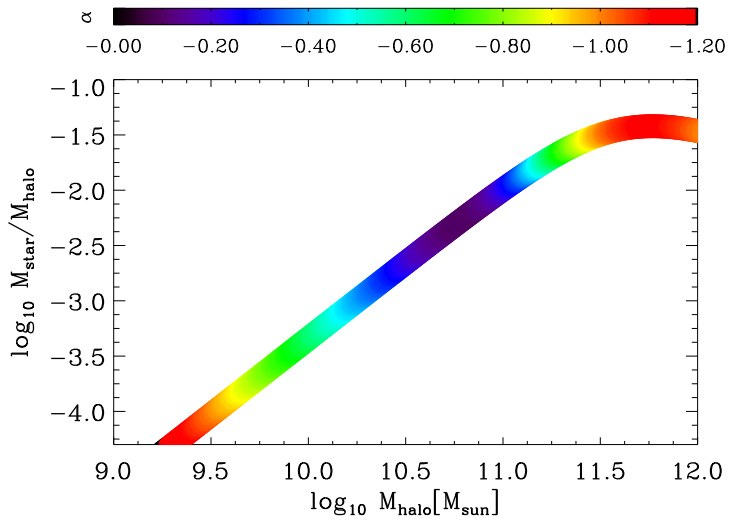

Figure 8.4: The abundance matching prediction color coded according to the expected value of the DM inner slope at every halo mass. We used the best fit parameters of α measured between 0.01 and 0.02 of each galaxy's virial radius.

8.3.3 Core creation

We next examine which mechanism is responsible for the creation of cores, using the three simulations shown in Fig. 8.1 as case studies. As outlined in §8.1, core formation from stellar feedback depends on repeated starbursts that are able to move gas enough to have a dynamical effect on the dark matter (Read & Gilmore 2005; Governato et al. 2010; Macciò et al. 2012; Pontzen & Governato 2012; Teyssier et al. 2013).

The four panels of Fig. 8.5 show how some relevant quantities vary as a function of lookback time. From top to bottom we present: (i) the star formation history, which shows clear starbursts that can drive outflows; (ii) the gas mass within a sphere of 1 kpc from the center of the galaxy, which shows when the gas has been driven out of the galaxy centre; (iii) the distance Δ between the position of the dark matter and gas potential minima, which shows how much the baryonic centre of mass moves around; and (iv) the $M_\star/M_{\rm halo}$ value that determines α.

The medium mass version of g5664 that uses the fiducial MaGICC feedback (red dashed line) has the flattest density profile at $z = 0$, so we expect it to have the most violent history. Indeed, it has a bursty star formation history (multiplied by 100 to get it into the same range as the other galaxy star formation histories), and a star formation efficiency, $M_\star/M_{\rm halo}$, that stays near the optimal value for cores, between $\sim$ 0.35 and 0.5 per cent

throughout its evolution. A couple of the bursts of star formation cause significant gas loss from the inner 1 kpc, which results in consistent offsets between the positions of the center of gas and dark matter distributions.

The medium mass version of g5664 that uses the low feedback MUGS physics (dashed black line) is the most contracted galaxy of this set. Other than a peak of star formation rate at an early time, corresponding to its peak dark matter accretion, its star formation history is a smoothly declining exponential. This early star formation quickly drives the efficiency $M_\star/M_{\rm halo}$ to values higher than 10 per cent, which, according to Fig. 8.3, leads to a cuspy density profile. The high amount of stars already formed 11 Gyrs ago within this galaxy creates a deep potential well which suppresses the effects of stellar feedback, so that little gas flows out of the inner regions and the DM and gas distributions share the same centre of mass throughout the galaxy's evolution.

Perhaps the most interesting case is that of the fiducial high mass g5664 galaxy (red solid line). At $z = 0$ its dark matter profile is slightly contracted compared to the NFW halo, but less contracted than the lower mass MUGS case (dashed black line). Indeed, its star formation efficiency, $M_\star/M_{\rm halo} \sim 5$ per cent at $z = 0$, is lower than the MUGS case, but still high enough to have contracted dark matter. This galaxy shows elevated star formation starting $\sim$6 Gyrs ago, which correlates with an increase of $M_\star/M_{\rm halo}$, increased gas in the centre with fewer outflows and a more constant Δ. Before $z = 0.66$ the star formation efficiency, $M_\star/M_{\rm halo}$, of this galaxy was still ~ 1 per cent, and the feedback energy was still able to cause gas flows and variations in Δ. When we examine the galaxy at that epoch, it indeed had an expanded dark matter profile with $\alpha > -1.0$, measured between 0.01 and 0.02 of the physical virial radius. Immediately after the starburst the star formation efficiency increases, the dark matter and gas start to share the same centre, the outflows from the inner region diminish, and the profile steepens to $\alpha < -1.0$ by $z = 0.66$ (6 Gyrs ago) and finally to $\alpha = -1.8$ by $z = 0$ with a star formation efficiency of $M_\star/M_{\rm halo} \sim 5$ per cent.

8.3.4 Predictions for observed galaxies

Combining the parameters in Table 2 with the Moster et al. (2013) relationship, it is possible to predict the inner density profile slope of a galaxy based on its observed stellar mass. This allows us to make predictions which are independent of the feedback prescription. Using the best fit parameters from the $0.01 < r/R_{\rm vir} < 0.02$ range, we can compute the median expected α dependence on stellar mass for galaxies as massive as $M_{\rm halo} \approx 10^{12}{\rm M}_\odot$ ($M_\star \approx 3.4 \times 10^{10}{\rm M}_\odot$):

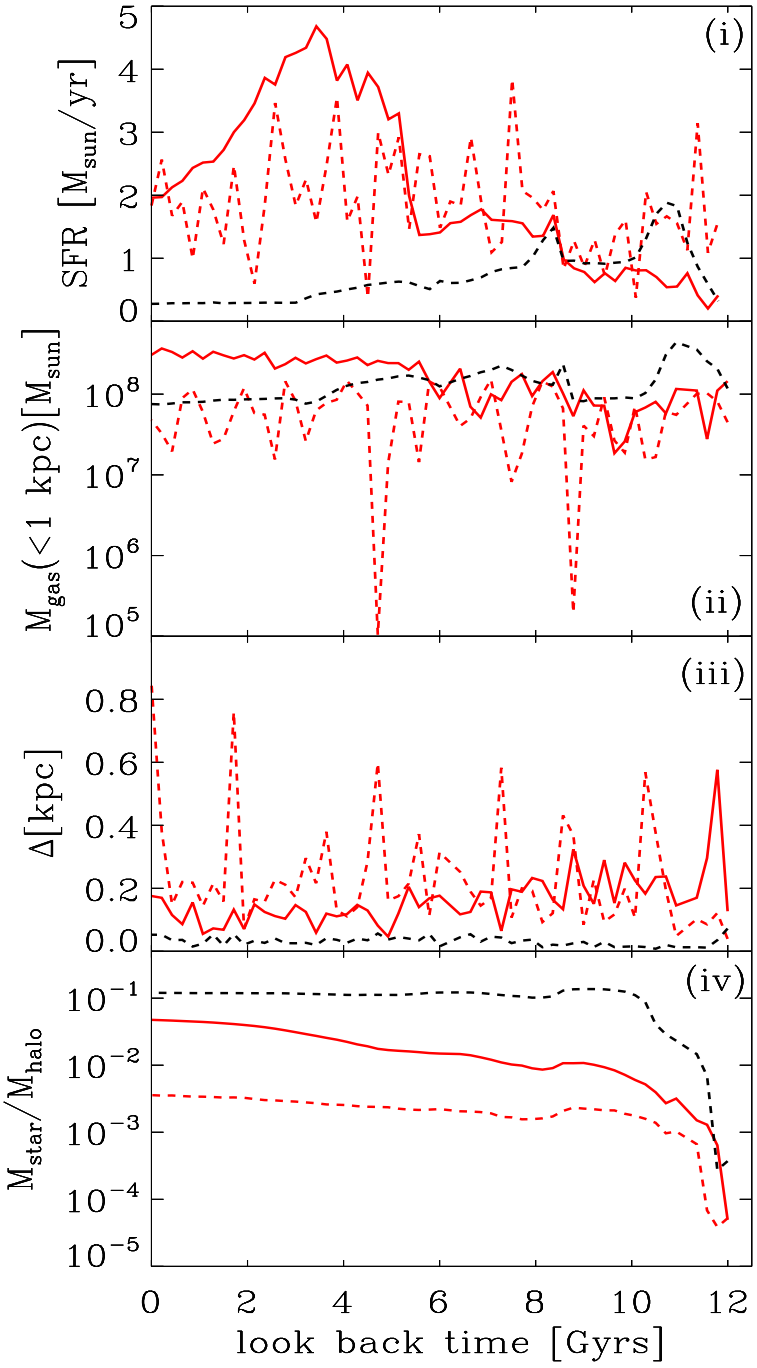

Figure 8.5: For the galaxies in Fig 8.1, we show the evolution of (i) the star formation history; (ii) the gas flows within a 1 kpc sphere centered at the galaxy center; (iii) the relative position between gas and dark matter potential minima and (iv) the $M_\star/M_{\rm halo}$ as a function of lookback time. Note that the SFR of the $M_\star = 2.4 \times 10^8 {\rm M}_\odot$ galaxy (red dashed line) has been multiplied by a factor 100 in order to be shown in the same scale range.

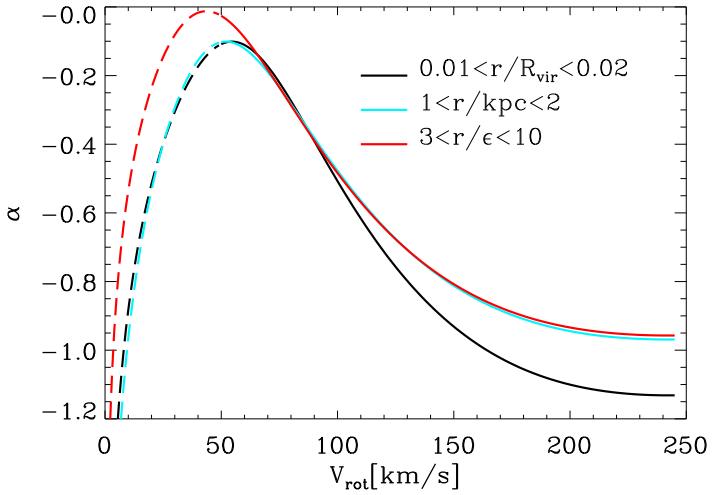

Figure 8.6: Expected relation between galaxies' rotation velocity and inner slope of their dark matter haloes. The three lines correspond to different radial ranges used for measuring α. The dashed lines refer to the linear extrapolation of the baryonic TF relation (Dutton et al. 2010) below $M_\star = 10^9 \mathrm{M}_\odot$.

$$\alpha = 0.132 - \log_{10}\left[\frac{\eta^{2.58}+1}{\eta^{1.99}}\right] \tag{8.2}$$

where

$$\eta = 0.84\left(\frac{M_*}{10^9\mathrm{M}_\odot}\right)^{-0.58} + 0.06\left(\frac{M_*}{10^9\mathrm{M}_\odot}\right)^{0.26} \tag{8.3}$$

The peak of this function occurs at $M_\star = 10^{8.5}\mathrm{M}_\odot$ and the low mass end slope, 0.34, is in good agreement with the one obtained in Governato et al. (2012) for stellar masses between $10^4 < M_\star/\mathrm{M}_\odot < 10^{9.4}$. Our study extends the prediction of cores vs cusps to L* scales and predicts a turnover in the relation between inner slope and galaxy mass for $M_\star > 10^{8.5}\mathrm{M}_\odot$: above this value, the inner slope decreases as $\alpha \propto -0.64 \log_{10} M_\star/\mathrm{M}_\odot$.

Taking a step further, the stellar content of galaxies is then connected to their observed rotation velocity through the Tully-Fisher (TF) relation. Equation 4 of Dutton et al. (2010) parameterizes $V_{\rm rot}$ at 2.2 I-band exponential scale lengths as a function of $M_\star$. Using this $M_\star - V_{\rm rot}$ relation we predict α as a function of $V_{\rm rot}$, the rotation velocity of galaxies. Fig. 8.6 shows, for the different radial ranges where we measure the inner density profile, α as a function of observed rotation velocity for galaxies with $M_{\rm halo} \leqslant 10^{12}\mathrm{M}_\odot$. The dashed lines indicate where the Tully-Fisher relationship was linearly extrapolated for $M_\star < 10^9\mathrm{M}_\odot$.

Fig. 8.6 shows that the galaxies with the flattest inner density profiles are found at $V_{\rm rot} \sim 50\,{\rm km\,s^{-1}}$. α decreases in more massive galaxies where the inner density profiles become more cuspy until they reach the NFW profile.

We note that the position at which the inner slope is measured has an effect on the α values, which alters the best fit parameters reported in Table 2, and consequently determines how α varies with rotation velocity. Thus, Fig. 8.6 has to be interpreted according to the radial range chosen, though the general trends are not changed and the peak of α remains at $V_{\rm rot} \sim 50\,{\rm km\,s^{-1}}$, independent of where the slope is measured.

The major difference between α measured at $0.01 < r/R_{\rm vir} < 0.02$ and the other radial ranges is that the inner slope is steeper for $V_{\rm rot} > 100\,{\rm km\,s^{-1}}$ in the former case. A steeper slope is expected because $0.01 < r/R_{\rm vir} < 0.02$ is further from the galaxy centre than the other two measurements. However, none of the measured α values fall below the NFW expectation as $V_{\rm rot}$ approaches 250 $\,{\rm km\,s^{-1}}$. Thus, dark matter haloes are never contracted in our model, even in the most massive disc galaxies.

8.4 Conclusions

Using 31 simulated galaxies from the MaGICC project, we showed that dark matter density profiles are modified by baryonic processes in the centre of galactic haloes. The inner profile slope depends solely on the mass of stars formed per halo mass and is independent of the particular choice of feedback parameters within our blastwave and early stellar feedback scheme. Similar to previous work, the expansion of the dark matter profile results from supernova-driven outflows that cause fluctuations in the global potential and shift the centre of the gas mass away from the centre of the dark matter mass.

At values of $M_\star/M_{\rm halo} \lesssim 0.01$ per cent, the energy from stellar feedback is not sufficient to modify the DM distribution, and these galaxies retain a cuspy profile. At higher ratios of stellar-to-halo mass, feedback drives the expansion of the DM haloes, resulting in cored profiles. The shallowest profiles form in galaxies with $M_\star/M_{\rm halo} \sim 0.5$ per cent. According to the abundance matching relation (Moster et al. 2013), these galaxies have $M_{\rm halo} \approx 10^{10.8}{\rm M}_\odot$ and $M_\star \approx 10^{8.5}{\rm M}_\odot$. In higher mass haloes, the deepening of the potential due to stars that form in the central regions suppresses supernova-driven outflows and thus lowers expansion, leaving cuspier profiles.

The abundance matching peak of star formation efficiency, $M_\star/M_{\rm halo} =$

3.8 per cent, occurs at $M_{\rm halo} = 10^{11.76}{\rm M}_{\odot}$, which is close to the lowest current estimate of the Milky Way mass. Our model predicts that such a halo will be uncontracted and have an NFW-like inner slope of $\alpha = -1.20$ when the slope is measured between ~ 2 and ~ 4kpc.

We combine our parameterization of α as a function of $M_{\star}/M_{\rm halo}$ with the empirical abundance matching relation to assign a median relationship between α and $M_{\star}$. The inner slope of the dark matter density profile increases with stellar mass to a maximum (most cored profile) at $M_{\star} \approx 10^{8.5}{\rm M}_{\odot}$, before decreasing toward cuspier profiles at higher stellar masses. Below $M_{\star} \approx 10^{8.5}{\rm M}_{\odot}$ the DM inner slope increases with stellar mass as $\alpha \propto 0.34 \log_{10} M_{\star}/{\rm M}_{\odot}$, similar to the relation found in Governato et al. (2012). For $M_{\star} > 10^{8.5}{\rm M}_{\odot}$, dark matter haloes become cuspier, with $\alpha \propto -0.64 \log_{10} M_{\star}/{\rm M}_{\odot}$.

The Tully-Fisher relation allows us to predict the dependence of the DM inner slope on the observed rotation velocity of galaxies. Using our results and the stellar mass TF relation from Dutton et al. (2010), we find that the flattest inner profiles are expected for galaxies with $V_{\rm rot} \sim 50\,{\rm km\,s^{-1}}$. α decreases for more massive galaxies, leading to cuspier profiles and eventually reaching the NFW prediction at the Milky Way mass. We note that, in agreement with our findings, the most clear observational measurements of flattened "core" profiles of disc galaxies (de Blok et al. 2008; Kuzio de Naray et al. 2008b, 2009; Oh et al. 2011b) are found in low surface brightness (LSB) galaxies with $V_{\rm rot} < 100\,{\rm km\,s^{-1}}$.

More massive disc galaxies, being baryon dominated, suffer from larger uncertainties in the disc-halo decomposition of their rotation curves, making it difficult to distinguish if their dark matter profile is cuspy or cored. Some studies conclude that such galaxies, those with $V_{\rm rot} > 150\,{\rm km\,s^{-1}}$, can be described with cored profiles (Borriello & Salucci 2001; Donato et al. 2004; McGaugh et al. 2007), while others find that NFW model provide equally good fits for these high luminosity galaxies (de Blok et al. 2008; Kuzio de Naray et al. 2008b).

More recently, Martinsson et al. (2013) presented rotation-curve mass decompositions of several massive spiral galaxies, and found no significant difference between the quality of a pseudo-isothermal sphere or a NFW model in fitting the DM rotation curves of individual galaxies, given the uncertainties in the contribution of baryons. If high surface brightness discs are sub-maximal (e.g. Courteau & Rix 1999) their haloes are allowed to be cuspy at the center.

An aspect not taken into account in our simulations of galaxy formation is the influence of AGN feedback on the density profile of dark matter haloes.

We acknowledge that this form of feedback starts to be relevant at the high halo mass end, where we observe increasingly cuspy galaxies: the study of the core/cusp problem would thus benefit from a future implementation of this type of feedback.

Our novel prediction for cusp vs core formation can be tested and, at least at the low halo mass end, well constrained using observational data sets. This study can be applied to theoretical modeling of galaxy mass profiles, as well as to modeling of populations of disc galaxies within cold dark matter haloes. We find this encouraging, and hope that our study motivates more systematic analysis of the dependance of α on galaxy mass in real disc galaxies.

Chapter 9

Influence of galaxy formation on dark matter haloes: a mass dependent density profile

We introduce a mass dependent density profile to describe the distribution of dark matter within galaxies, which takes into account the stellar-to-halo mass dependence of the response of dark matter to baryonic processes. The study is based on the analysis of hydrodynamically simulated galaxies from dwarf to Milky Way mass, drawn from the MaGICC project, which have been shown to match a wide range of disk scaling relationships. We find that the best fit parameters of a generic double power-law density profile vary in a systematic manner that depends on the stellar-to-halo mass ratio of each galaxy. Thus, the quantity $M_\star/M_{\rm halo}$ constrains the inner (γ) and outer (β) slopes of dark matter density, and the sharpness of transition between the slopes (α), reducing the number of free parameters of the model to two. Due to the tight relation between stellar mass and halo mass, either of these quantities is sufficient to describe the dark matter halo profile including the effects of baryons. The concentration of the haloes in the hydrodynamical simulations is consistent with N-body expectations up to Milky Way mass galaxies, at which mass the haloes become twice as concentrated as compared with pure dark matter runs.

This mass dependent density profile can be directly applied to rotation curve data of observed galaxies and to semi analytic galaxy formation models as a significant improvement over the commonly used NFW profile.[1]

[1]Note that through this chapter the inner slope of density profile will be indicated as γ, as opposite to the previous chapter in which it was indicated as α.

9.1 Introduction

Over several orders of magnitude in radius, dark matter (DM) halo density profiles arising from N-body simulations are well described by the so-called 'NFW' model (Navarro et al. 1996b; Springel et al. 2008; Navarro et al. 2010), albeit with well known systematic deviations (e.g., Navarro et al. 2004; Springel et al. 2008; Gao et al. 2008; Navarro et al. 2010; Dutton & Macciò 2014). The NFW function consists of two power laws, the inner region where the density is behaving as $\rho \propto r^{-1}$ and the outer part as $\rho \propto r^{-3}$.

The central $\rho \propto r^{-1}$ "cusps" of such model disagree with observations of real galaxies where mass modeling based on rotation curves finds much shallower inner density slopes, known as "cored" profiles (e.g., Moore 1994; Salucci & Burkert 2000; de Blok et al. 2001; Simon et al. 2005; de Blok et al. 2008; Kuzio de Naray et al. 2008b, 2009; Oh et al. 2011b). Cored galaxies are also found within the fainter, dark matter dominated dwarfs spheroidal galaxies surrounding the Milky Way (Walker & Peñarrubia 2011). This *cusp/core discrepancy* is usually seen as one of the major problems of the ΛCDM paradigm at small scales.

The NFW profile is, however, derived from pure DM simulations in which particles only interact through gravity. These simulations neglect hydrodynamical processes that may be relevant in determining the inner halo profile. Many studies have shown how baryons can affect the dark matter (e.g., Tissera & Dominguez-Tenreiro 1998). Gas cooling to the center of a galaxy causes adiabatic contraction (e.g. Blumenthal et al. 1986; Gnedin et al. 2004), whose effect strengthens cusps and exacerbates the mismatch between theoretical profiles and observations. Rather, expanded haloes are required to reconcile observed galaxy scaling relations of both early and late-type galaxies (Dutton et al. 2007, 2013).

Baryons can expand haloes through two main mechanisms (see Pontzen & Governato (2014) for a recent review): outflows driven by stellar or AGN feedback (Navarro et al. 1996a; Mo & Mao 2004; Read & Gilmore 2005; Mashchenko et al. 2006; Duffy et al. 2010; Pontzen & Governato 2012; Martizzi et al. 2013) and dynamical friction (El-Zant et al. 2001; Tonini et al. 2006; Romano-Díaz et al. 2008; Del Popolo 2009, 2010; Goerdt et al. 2010; Cole et al. 2011).

While dynamical friction is effective at expanding high mass haloes hosting galaxy clusters, stellar feedback is most effective at expanding low mass haloes (Governato et al. 2010). Gas cools into the galaxy centre where it forms stars that drive repeated energetic outflows. Such outflows move enough gas mass to create a core in an originally cuspy dark halo, due to

the DM response to the adjusted gravitational potential. Peñarrubia et al. (2012) calculated the energy required to flatten a density profile as a function of halo mass. The cusp/core change can be made permanent if the outflows are sufficiently rapid (Pontzen & Governato 2012).

Simulations from dwarf galaxies (Governato et al. 2010; Zolotov et al. 2012; Teyssier et al. 2013) to Milky Way mass (Macciò et al. 2012) have produced dark matter halo expansion depending on the implementation of stellar feedback. Governato et al. (2012) showed that only simulated galaxies with stellar masses higher than $\sim 10^7 M_\odot$ expand their haloes. They also showed that the inner DM profile slope, γ in $\rho \propto r^{-\gamma}$, flattens with increasing stellar mass, resulting from the increase of available energy from supernovae. An increase in stellar mass may, however, also deepen the potential well in the central region of the halo: indeed, Di Cintio et al. (2014b) showed that above a certain halo mass such a deepened potential well opposes the flattening process.

Di Cintio et al. (2014b) propose that γ depends on the stellar-to-halo mass ratio of galaxies. At $M_\star/M_{\rm halo} \lessapprox 10^{-4}$ there is not enough supernova energy to efficiently change the DM distribution, and the halo retains the original NFW profile, $\gamma \sim -1$. At higher $M_\star/M_{\rm halo}$, γ increases, with the maximum γ (most cored galaxies) found when $M_\star/M_{\rm halo} \sim 3-5\times10^{-3}$. The empirical relation between the stellar and halo mass of galaxies (Moster et al. 2010; Guo et al. 2010) implies that this corresponds to $M_\star \approx 10^{8.5} M_\odot$ and $M_{\rm halo} \approx 10^{11} M_\odot$. In higher mass haloes, the outflow process becomes ineffective at flattening the inner DM density and the haloes have increasingly cuspy profiles.

In this study, we take the next step to provide a mass-dependent parametrization of the entire dark matter density profile within galaxies. Using high resolution numerical simulations of galaxies, performed with the smoothed-particle hydrodynamics (SPH) technique, we are able to study the response of DM haloes to baryonic processes. As with the central density slope γ in Di Cintio et al. (2014b), we find that the density profile parameters depend on $M_\star/M_{\rm halo}$.

This study is based on a suite of hydrodynamically simulated galaxies, drawn from the Making Galaxies In a Cosmological Context (MaGICC) project. The galaxies cover a broad mass range and include stellar feedback from supernovae, stellar winds and the energy from young, massive stars. The galaxies that use the fiducial parameters from Stinson et al. (2013) match the stellar-halo mass relation at $z = 0$ (Moster et al. 2010; Guo et al. 2010) and at higher redshift (Kannan et al. 2013) as well as a range of present observed galaxy properties and scaling relations (Brook et al. 2012b; Stinson et al. 2013). Unlike previous generations of simulations, there is no

catastrophic overcooling, no loss of angular momentum (Brook et al. 2011, 2012a), and the rotation curves do not have an inner peak, meaning that the mass profiles are appropriate for comparing to real galaxies.

We present a profile that efficiently describes the distribution of dark matter within the SPH simulated galaxies, from dwarfs to Milky Way mass. The profile is fully constrained by the integrated star formation efficiency within each galaxy, $M_\star/M_{\rm halo}$, and the standard two additional free parameters, the scale radius $r_{\rm s}$ and the scale density $\rho_{\rm s}$ that depend on individual halo formation histories. After converting $r_{\rm s}$ into r_{-2}, i.e. the point where the logarithmic slope of the profile equals -2, we derive the concentration parameter for this new profile, defined as $c = R_{\rm vir}/r_{-2}$, and show that for high mass galaxies it substantially differs from expectation based on N-body simulations.

This chapter is organized as follows: the hydrodynamical simulations and feedback model are presented in Section 9.2, the main results, including the derivation of profile parameters and galaxies rotation curves, together with a comparison with N-body simulations in Section 9.3 and the conclusions in Section 9.4.

9.2 Simulations

The SPH simulated galaxies we analyze here make up the Making Galaxies in a Cosmological Context (MaGICC) project (Stinson et al. 2013; Brook et al. 2012b), as described in Section 2.2.

Standard formulations of SPH are known to suffer from some weaknesses (Agertz et al. 2007), such as condensation of cold blobs which becomes particularly prominent in galaxies of virial masses $\sim 10^{12}{\rm M}_\odot$. We thus checked our results using a new version of GASOLINE which has a significantly different solver of hydrodynamics than the previous one. Within two simulated galaxies, which represent extreme cases (the cored most case and the highest mass case), we find that the dark matter density profiles are essentially identical to the ones found with the standard version of GASOLINE. As this new hydrodynamical code is not yet published, we have not included any figures here, but these preliminary tests give us confidence that our results are not predicated on the specific of the hydrodynamics solver. Indeed, it has been shown already that similar expansion processes are observed in galaxies simulated with grid-based codes (Teyssier et al. 2013).

The galaxies properties are summarized in Table 1: the sample comprises ten galaxies with five different initial conditions, spanning a wide range in halo mass. The initial conditions of the medium and low mass galaxies are

Table 9.1: Properties of the SPH simulated galaxies used. $M_{\rm halo}$ is the dark matter mass within the virial radius. The increasing symbol size indicates the membership of each galaxy to the low, medium or high mass group.

Mass range	ID	soft [pc]	$M_{\rm halo}$ [$M_\odot$]	$R_{\rm vir}$ [kpc]	$M_\star$ [$M_\odot$]	sym
Low	g1536	78.1	9.4×10^9	60	7.2×10^5	⋅
	g15784	78.1	1.9×10^{10}	77	8.9×10^6	▴
	g15807	78.1	3.0×10^{10}	89	1.6×10^7	▪
Medium	g7124	156.2	5.3×10^{10}	107	1.3×10^8	∗
	g5664	156.2	6.3×10^{10}	114	2.4×10^8	◆
	g1536	156.2	8.3×10^{10}	125	4.5×10^8	●
	g15784	156.2	1.8×10^{11}	161	4.3×10^9	▲
High	g7124	312.5	4.5×10^{11}	219	6.3×10^9	∗
	g5664	312.5	5.6×10^{11}	236	2.7×10^{10}	◆
	g1536	312.5	7.2×10^{11}	257	2.4×10^{10}	●

scaled down variants of the high mass ones. This assures us than any result derived from such sample, and presented in Section 9.3, will not be driven by the specific merger history. It would be desirable, of course, to have a larger statistical sample of simulated galaxies and initial conditions, an issue that we hope to address in the near future.

The main haloes in our simulations were identified using the MPI+OpenMP hybrid halo finder `AHF`[2] (Knollmann & Knebe 2009; Gill et al. 2004a). The virial masses of the haloes are defined as the masses within a sphere containing $\Delta = 92.8$ times the cosmic critical matter density at $z = 0$.

The hydrodynamical simulations use the stochastic star formation recipe described in Stinson et al. (2006) in such a way that, on average, they reproduce the empirical Kennicut-Schmidt Law (Schmidt 1959; Kennicutt 1998).

The stars feed energy back into the interstellar medium (ISM) gas through blast-wave supernova feedback (Stinson et al. 2006) and ionizing feedback from massive stars prior to their explosion as supernovae, referred to as "early stellar feedback" (Stinson et al. 2013).

Early stellar feedback is implemented using 10% of the luminosity emitted by massive stars prior to their explosion as supernovae.

We analyze simulated galaxies that are part of the fiducial run of the MaGICC project, which uses early stellar feedback with $\epsilon_{\rm esf} = 0.1$, a Chabrier

[2]http://popia.ft.uam.es/AMIGA

(2003) initial mass function, a $E_{SN} = 10^{51} erg$ energy from SNe and a gas density threshold of $n_{th} = 9.3\mathrm{cm}^{-3}$. These simulations match the abundance matching relation at $z = 0$ (Moster et al. 2010; Guo et al. 2010), many present observed galaxy properties (Brook et al. 2012b; Stinson et al. 2013) as well as properties at high redshift (Kannan et al. 2013; Obreja et al. 2014).

9.3 Results

We analyze the dark matter density profiles of our SPH simulated galaxies using a five-free parameter α, β, γ profile function. We show how to express α, β and γ as functions of the integrated star formation efficiency $M_\star/M_{\rm halo}$ at z=0.

9.3.1 α, β, γ profile

The NFW profile is a specific form of the so-called (α, β, γ) double power-law model (Merritt et al. 2006; Hernquist 1990; Jaffe 1983):

$$\rho(r) = \frac{\rho_s}{\left(\frac{r}{r_{\rm s}}\right)^{\gamma}\left[1+\left(\frac{r}{r_{\rm s}}\right)^{\alpha}\right]^{(\beta-\gamma)/\alpha}} \tag{9.1}$$

where $r_{\rm s}$ is the scale radius and ρ_s the scale density. $r_{\rm s}$ and ρ_s are characteristics of each halo, related to their mass and formation time (e.g. Prada et al. 2012; Muñoz-Cuartas et al. 2011; Macciò et al. 2007; Bullock et al. 2001). The inner and outer regions have logarithmic slopes $-\gamma$ and $-\beta$, respectively, while α regulates how sharp the transition is from the inner to the outer region. The NFW profile has $(\alpha, \beta, \gamma) = (1, 3, 1)$. In this case, the scale radius equals the radius where the logarithmic slope of the density profile is -2, $r_{\rm s} = r_{-2}$. In the generic five-parameter model,

$$r_{-2} = \left(\frac{2-\gamma}{\beta-2}\right)^{1/\alpha} r_{\rm s} \tag{9.2}$$

9.3.2 Constraining the halo profile via $\mathbf{M_\star/M_{halo}}$

The dark matter halo profiles of each SPH simulated galaxy are computed in spherically averaged radial bins, logarithmically spaced in radius.

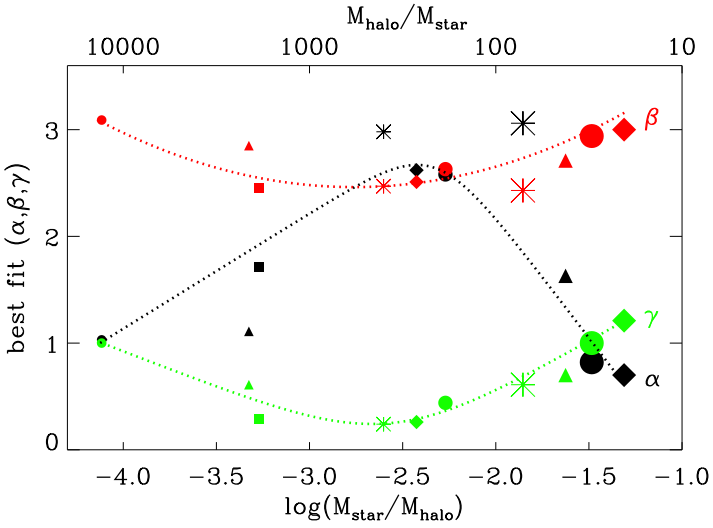

Figure 9.1: Best fit parameters for the inner slope, γ (green), outer slope β (red), and transition α (black) plotted as a function of integrated star formation efficiency, $M_\star/M_{\rm halo}$. The upper x-axis shows the corresponding $M_{\rm halo}/M_\star$ as a reference to the mass to light ratio. The parameters are for the double power law model of the dark matter density profile in Eq. (9.1). Each SPH simulated galaxy is represented by a symbol of a different size and shape as described in Table 1. The dotted lines represent the dependence of α, β and γ on $M_\star/M_{\rm halo}$. Their functional forms are given in Eq. (9.3).

The number of bins $N_{\rm bin}$ in each halo is proportional to the number of particles within the virial radius, so that the best resolved haloes (with $\sim$ 9x10^6 particles) will have an higher $N_{\rm bin}$ with respect to the least resolved ones (with 3.5x10^5 particles).

We only considered bins within $0.01R_{\rm vir} < r < R_{\rm vir}$, as this region fulfills the convergence criterion of Power et al. (2003) in the least resolved simulation. We perform a fitting procedure of the density profile using Eq. (9.1), assigning errors to the density bins depending on the Poisson noise given by the number of particles within each shell, and using a Levenberg-Marquardt technique.

Fig. 9.1 shows how the inner slope γ (green), the outer slope β (red) and the transition parameter α (black) vary as a function of the $M_\star/M_{\rm halo}$ ratio. The symbols, as explained in Table 1, correspond to different initial conditions, while their sizes indicate the mass of the halo. The dotted lines show the best fit for each parameter, which we explain below in Eq. (9.3).

At very low integrated star formation efficiency, we expect to find the

same profile as a dark matter only simulation since star formation is too sporadic to flatten the profile. Indeed, at $\log_{10}(M_\star/M_{\rm halo})$=−4.11 the best fit values are α=1, β=3, and γ=1, exactly an NFW halo.

At higher integrated star formation efficiencies, both the inner (γ) and outer (β) profile slopes decline to lower values than an NFW model, indicating halo expansion. At the same mass, the transition between inner and outer region becomes sharper: α increases as high as 3. Thus, while baryonic processes affect the profiles mainly in the inner region of slope γ, we must take their effects into account when deriving the other parameters α and β.

The star formation efficiency at which the cusp/core transition happens in our simulations is in agreement with the analytic calculation of Peñarrubia et al. (2012), who compared the energy needed to remove a cusp with the energy liberated by SNeII explosions.

The value of the inner slope (γ) varies with integrated star formation efficiency as found in Di Cintio et al. (2014b). The minimum inner slope is at $-2.6<\log_{10}(M_\star/M_{\rm halo})<-2.4$. So, as in Di Cintio et al. (2014b), the dark matter cusps are most efficiently flattened when $M_\star/M_{\rm halo} \sim 3-5\times 10^{-3}$. Above $\log_{10}(M_\star/M_{\rm halo})$=−2.4 (M/L∼250), the parameters turn back towards the NFW values since more mass collapses to the centre than the energy from gas can pull around.

We fit the correlation between α, β, γ and the integrated star formation efficiency using two simple functions. The outer slope, β, is fit with a parabola as a function of $M_\star/M_{\rm halo}$. The inner slope, γ, and the transition parameter, α, are both fit using a double power law model as a function of $M_\star/M_{\rm halo}$ as in Di Cintio et al. (2014b). The best fit are shown as dotted lines in Figure 9.1. Their functional forms are:

$$\begin{aligned}
\alpha &= 2.94 - \log_{10}[(10^{X+2.33})^{-1.08} + (10^{X+2.33})^{2.29}] \\
\beta &= 4.23 + 1.34X + 0.26X^2 \\
\gamma &= -0.06 + \log_{10}[(10^{X+2.56})^{-0.68} + (10^{X+2.56})]
\end{aligned} \tag{9.3}$$

where $X = \log_{10}(M_\star/M_{\rm halo})$.

Eq. (9.3) allows us to compute the entire dark matter profiles based solely on the stellar-to-halo mass ratio of a galaxy. We stress that the mass range of validity of Eq. (9.3) is $-4.1 < \log_{10}(M_\star/M_{\rm halo}) < -1.3$: at lower masses the (α, β, γ) value returns to the usual (1,3,1), NFW prediction, while at masses higher than $10^{12} M_\odot$, i.e. the Milky Way, other effects such as AGN feedback can concur to modify the profile in a way not currently testable with our set of simulations. In the future, having a larger statistical sample

of simulated galaxies would certainly be desirable in order to compute the scatter in the relations defined by Eq. (9.3).

9.3.3 Checking the α, β, γ constraints

Using the constrained values for (α, β, γ) from Eq. (9.3), we re-fit the dark matter density profiles of our haloes with the only standard two-free parameters, $r_{\rm s}$ and $\rho_{\rm s}$. The fit results are shown as dashed red lines in Fig. 9.2, superimposed on the dark matter density profiles of each hydrodynamically simulated galaxy (black lines). The galaxies are ordered according to their mass from top left to bottom right. The best fit values obtained for the scale radius $r_{\rm s}$ and scale density $\rho_{\rm s}$ are shown in the upper-right corner, along with the constrained values used for (α, β, γ). The r.m.s. value of fit, defined as

$$\sigma_{rms} = \sqrt{\frac{1}{N_{\rm bins}} \sum_{k=1}^{N_{\rm bins}} (\log_{10}\rho_{\rm sim,k} - \log_{10}\rho_{\rm fit,k})^2}, \tag{9.4}$$

are shown in the lower-left corner. The average value of σ_{rms} is 0.051 and shows that Eq. (9.3) can accurately describe the structure of simulated dark matter density profiles.

Since we started our analysis using a five-free parameters model, it is possible that some degeneracies may exist, and other combinations of $(\alpha, \beta, \gamma, r_{\rm s}, \rho_s)$ might be equally precise in describing dark matter haloes. We do not claim that our model is unique, but rather that provides a prescription that successfully describes very different dark matter profiles, both cored and cusp ones, in galaxies. Our model, reduced to a two-free parameters profile using the value of $M_\star/M_{\rm halo}$ (or simply $M_\star$) of each galaxy, shows very good precision in reproducing halo density profiles of cosmological hydrodynamically simulated galaxies of any halo mass.

9.3.4 Modeling rotation curves

It is may be easier to compare observations with the dark matter rotation curves, rather than with the density profile. We proceed by deriving the quantity $V_{\rm c}(r) = \sqrt{GM(r)/r}$ for the dark matter component within hydrodynamical simulations, where

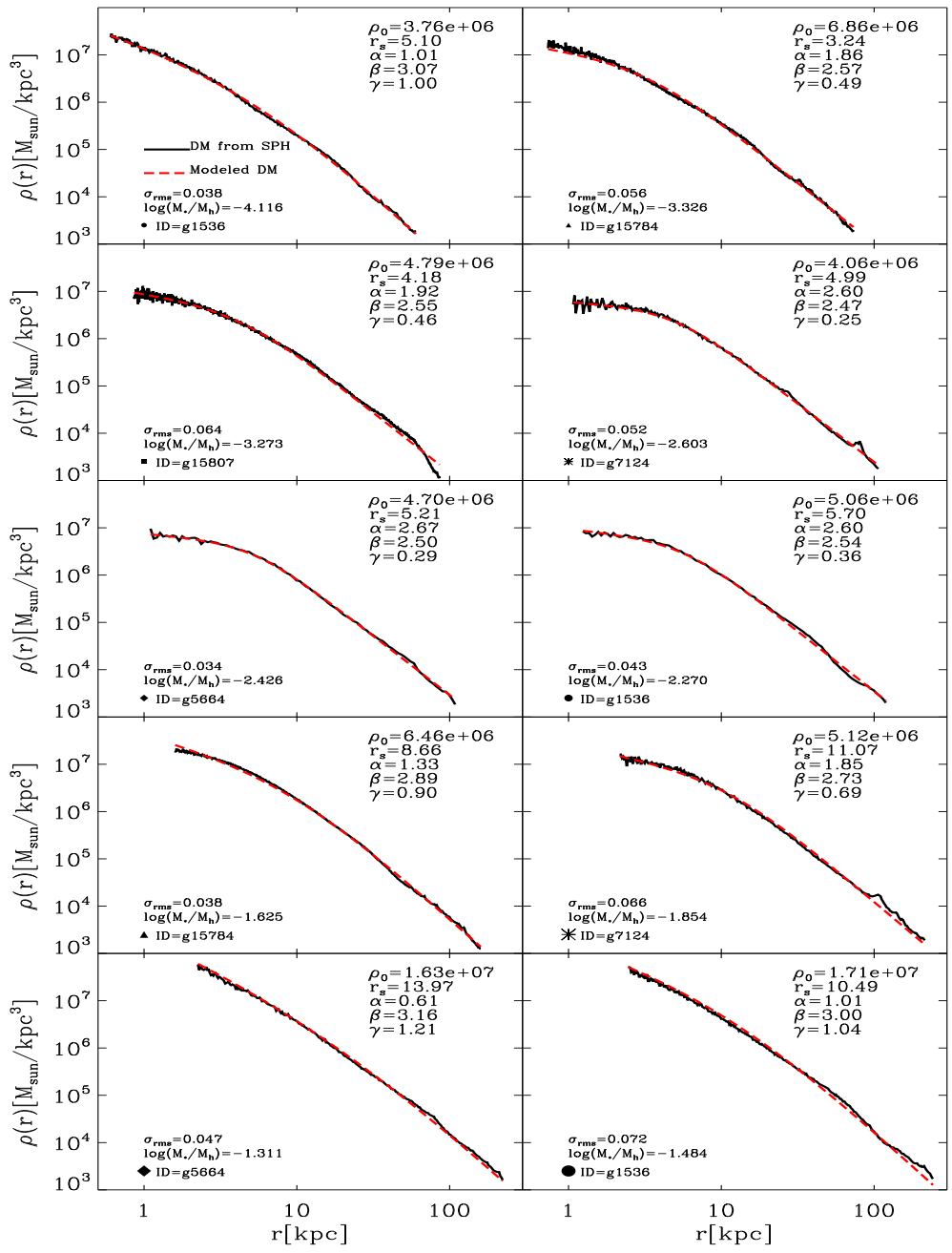

Figure 9.2: Halo dark matter density profiles (black line) and best fit model (dashed red line) for the hydrodynamically simulated galaxies. The profiles start at $0.01R_{\rm vir}$ to ensure convergence and the galaxies are shown in increasing halo mass order, same as in Table 1. The constrained α, β and γ values, from Eq. (9.3), are shown together with the corresponding efficiency $M_\star/M_{\rm halo}$. The two free parameters of the fit, $r_{\rm s}$ and $\rho_{\rm s}$, are also listed as well as the r.m.s value σ_{rms}.

$$M(r) = 4\pi\rho_s \int_0^r \frac{r'^2}{\left(\frac{r'}{r_{\rm s}}\right)^{\gamma}\left[1+\left(\frac{r'}{r_{\rm s}}\right)^{\alpha}\right]^{(\beta-\gamma)/\alpha}} dr' \tag{9.5}$$

The values (α, β, γ) are constrained through Eq. (9.3) for each galaxy, while ρ_s and $r_{\rm s}$ are the best-fit results as listed in Fig. 9.2, such that at the virial radius $M(R_{\rm vir})$ equals $M_{\rm halo}$.

The derived rotation curves for our model are shown as dashed red lines in Fig. 9.3, with galaxies again ordered by mass as in Fig. 9.2. The rotation curves taken directly from simulations, namely using the dark matter component within each hydrodynamically simulated galaxy, are shown as solid black lines. Each velocity curve is normalized to its maximum value V_{max}, and plotted in units of the virial radius.

The smaller panels within each plot show a zoom-in of $V_c(r)$ within $0.1R_{\rm vir}$, in order to better appreciate any difference between the actual simulations (solid black) and our parametrization (dashed red). Within this inner panel we also show as a green dotted-dashed line the rotation curve as derived from the dark matter only runs for each galaxy, scaled by the baryon fraction value. There is a very good agreement between our parametrized dark matter rotation curves and simulated ones, with differences that are below 10 per cent at any radii and for any galaxy. Further, when the contribution from the baryonic component is added to the rotation curves, the difference between the simulations and our parametrization will become even smaller, particularly at the high mass end of galaxy range where baryons dominate. By contrast, large differences can be seen between the rotation curves from dark matter only simulations (green dotted-dashed) and the rotation curves from the baryonic run (solid black) with the largest differences, as much as 50 per cent, being in intermediate mass galaxies. Such differences highlighting the error one would commit by modeling rotation curves of real galaxies using prediction from N-body simulations, with a NFW profile unmodified by baryonic processes. As opposite, our halo model introduces an error in the evaluation of galaxies' rotation curves which is well within observational errors, and can therefore safely be applied to model dark matter haloes within real galaxies.

9.3.5 Constraining the concentration parameter

Now that we have demonstrated the precision of our density profile based on the stellar-to-halo mass ratio as in Eq. (9.3), we examine how one of the free parameters, the scale radius $r_{\rm s}$, varies as a function of integrated star

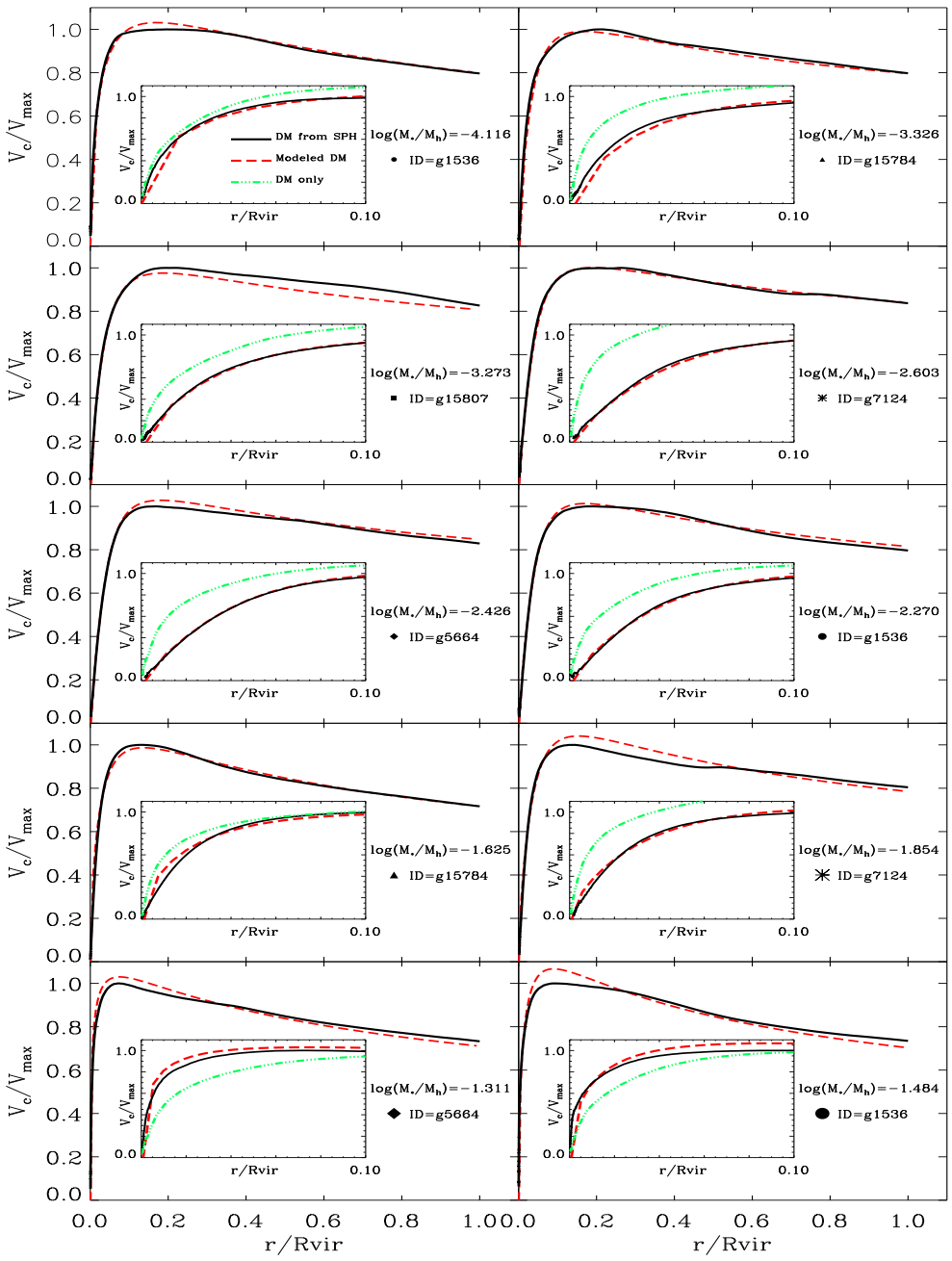

Figure 9.3: Circular velocity curves of dark matter within the galaxies used in this work, $V_{\rm c}(r) = \sqrt{GM(r)/r}$. The dark matter rotation curve from the SPH run is shown as solid black line, while our parametrized model as red dashed line. The small insert within each plot shows a zoom-in of the region within $0.1R_{\rm vir}$, with the addition of the rotation curve from dark matter only run as dotted-dashed green line. The $V_{\rm c}$ of each galaxy is normalized to its maximum values $V_{\rm max}$, and plotted in units of $R_{\rm vir}$.

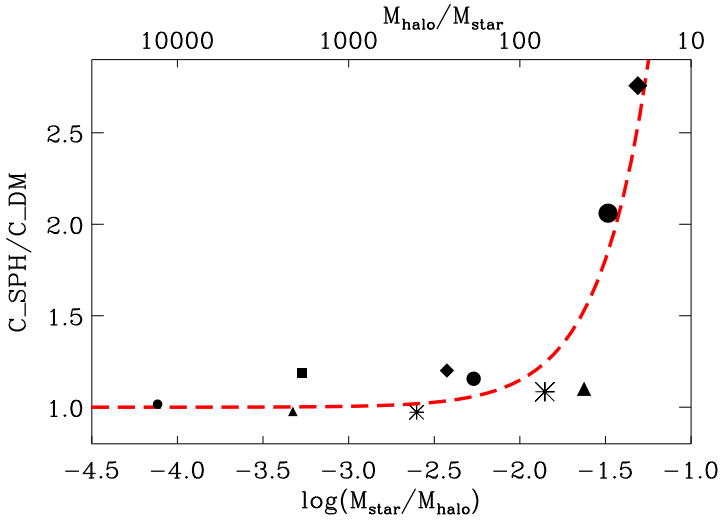

Figure 9.4: Ratio between concentration parameter $c = R_{\rm vir}/r_{-2}$ in the SPH run and dark matter only run for our set of galaxies, as a function of $M_\star/M_{\rm halo}$. The upper x-axis shows the corresponding $M_{\rm halo}/M_\star$ as a reference to the mass to light ratio. $c_{\rm DM}$has been derived fitting a NFW profile to the dark matter only version of each galaxy, while $c_{\rm SPH}$has been computed applying our model profile to the dark matter halo of the galaxies in the hydrodynamical run, and converting the corresponding $r_{\rm s}$into r_{-2}. The dashed red line represent the best model for the $c_{\rm SPH}/c_{\rm DM}$values.

forming efficiency, so that it could be implemented in semi-analytic models of galaxy formation. The concentration parameter of our hydrodynamically simulated galaxies does not always behave the same as in a corresponding dark matter only run.

First, as α, β and γ vary, the definition of $r_{\rm s}$ changes. For consistency, Eq. (9.2) defines a conversion from $r_{\rm s}$ to r_{-2}, the radius at which the logarithmic slope of the profile equals -2. We define $c_{\rm SPH} \equiv R_{\rm vir}/r_{-2}$ as the concentration from the hydrodynamical simulation, and compare it with $c_{\rm DM}$, the NFW concentration from the dark matter only simulation.

Fig. 9.4 shows the ratio between the concentration parameter in the hydrodynamical simulation and the dark matter only one, and how this ratio varies as a function of $M_\star/M_{\rm halo}$. Each simulation is represented by its symbol and size as described in Table 1. The dependence of $c_{\rm SPH}/c_{\rm DM}$ on $M_\star/M_{\rm halo}$ is nearly exponential. The best fit is:

$$c_{\rm SPH}/c_{\rm DM} = 1.0 + 0.00003e^{3.4X} \tag{9.6}$$

where $X = \log_{10}(M_\star/M_{\rm halo}) + 4.5$.

Up to a mass ratio of $\log_{10}(M_\star/M_{\rm halo}) \sim -1.5$ (which corresponds to a halo mass of 10^{12}M$_\odot$), $c_{\rm SPH}$ is essentially the same as $c_{\rm DM}$. Thus, despite of the variation of the inner slope, the transition to the outer slope happens at the same radius r_{-2} as in the dark matter only simulation.

Above $\log_{10}(M_\star/M_{\rm halo}) \sim -1.5$, instead, the difference is striking and the haloes become much more concentrated in the SPH case than the corresponding DM only run. In galaxies about the mass of the Milky Way, the inner region of the dark matter halo becomes smaller in our model, a signature of adiabatic contraction. Indeed, as shown already in Di Cintio et al. (2014b), the increasing amount of stars at the centre of high mass spirals opposes the flattening effect of gas outflows generating instead a profile which is increasingly cuspy and more concentrated. Collisionless simulations in a WMAP3 cosmology find that the typical concentration of a 10^{12} M$_\odot$ halo [$\log_{10}(M_\star/M_{\rm halo}) = -1.5$] is $c \approx 8.5$ (Maccio' et al. 2008); in our model with effective stellar feedback, the inner region of the halo shrinks by a factor of ~ 2, giving a concentration parameter $c_{\rm SPH}$ that can be $2.0 - 2.5$ times higher than the original N-body prediction.

Observations of the Milky Way are best fit with an NFW halo with high concentration parameter $c \approx 18 - 20$ (Battaglia et al. 2005; Catena & Ullio 2010; Deason et al. 2012a; Nesti & Salucci 2013). The data include halo tracers like globular clusters, satellite galaxies, and dynamical observables like blue horizontal branch stars, red giant stars and maser star forming regions used to constrain the Galactic potential. While such a high value of the concentration c is at odds with respect to N-body predictions, our study suggests that the mismatch could be related to the effect of infalling baryons, and that a value of c compatible with the above mentioned works it is indeed expected once such effect is properly taken into account in simulations. Finally, a high concentration could arise possible tensions with the Tully-Fisher relation (Dutton et al. 2011) and the Fundamental Plane (Dutton et al. 2013) for high mass spirals, but this issue has to be explored in more detail once other effects relevant at L* scales, such as feedback from AGN, will be included in the simulations.

9.4 Conclusions

It is well established that baryons affect dark matter density profiles of haloes in galaxies (e.g. Blumenthal et al. 1986; Navarro et al. 1996a; El-Zant et al. 2001; Gnedin et al. 2004; Read & Gilmore 2005; Goerdt et al. 2006; Read et al. 2006; Mashchenko et al. 2006; Tonini et al. 2006; Romano-Díaz et al. 2008; Del Popolo 2009; Governato et al. 2010; Goerdt et al. 2010; Di Cintio et al. 2011; Zolotov et al. 2012; Governato et al.

2012; Macciò et al. 2012; Martizzi et al. 2013; Teyssier et al. 2013). Simple arguments compare the energy available from star formation with the depth of a galactic potential to estimate the degree of the change in the initial dark matter distribution (Peñarrubia et al. 2012; Pontzen & Governato 2012, 2014).

This study describes the dark matter profiles of haloes from a suite of hydrodynamical cosmological galaxy formation simulations that include the effects of stellar feedback. The profiles are modeled using a generic double power law function. We find that the slope parameters of such model (α, β, γ) vary in a systematic manner as a function of the ratio between $M_\star/M_{\rm halo}$, which we call integrated star formation efficiency. Using these fits allows us to propose a star formation efficiency dependent density profile for dark matter haloes that can be used for modeling observed galaxies and in semi-analytic models of galaxy formation.

The star formation efficiency dependent density profile has the form of a double power-law, with inner slope (γ), outer slope (β) and sharpness of transition (α) fully determined by the stellar to halo mass ratio as given in Eq. 9.3. Thus, the five free parameters of the generic model reduce to two, the scale radius $r_{\rm s}$ and scale density $\rho_{\rm s}$, the same free parameters of the commonly used NFW model.

To examine how the scale radii varies as a function of integrated star formation efficiency, we compare the concentration parameter, $c = R_{\rm vir}/r_{-2}$, of the dark matter haloes from galaxies simulated with hydrodynamics prescriptions to those from the corresponding dark matter only simulations. For masses below roughly the Milky Way's the concentrations are similar, indicating that while the profiles may be significantly different from NFW, particularly in terms of inner slope, the radius at which the logarithmic slope of the profile equals -2 is the same as in the NFW model, indicating no net halo response at scales near the scale radius.

However, for Milky Way mass galaxies the haloes from the hydro runs become as much as two times more concentrated than in the pure dark matter runs. Such high concentrations are consistent to what has been derived from observations of Milky Way's dynamical tracers (Battaglia et al. 2005; Catena & Ullio 2010; Deason et al. 2012a; Nesti & Salucci 2013).

Thus, specifying the halo or stellar mass for a galaxy is sufficient to completely describe the shape of dark matter profiles for galaxies ranging in mass from dwarfs to L*, based on the influence of stellar feedback. Importantly, the simulations we utilize in determining these profiles match a wide range of scaling relations Brook et al. (2012b), meaning that their radial mass distributions are well constrained.

The main features of the mass dependent dark matter profile are:

- Baryons affect the profile shape parameters. For galaxies with flat inner profiles γ the sharpness of transition parameter, α, increases from 1 to 3 and corresponds to a small decrease in the slope of the outer profile β.

- At low integrated star formation efficiencies, $M_\star/M_{\rm halo} \lesssim 10^{-4}$ (galaxies with $M_\star \lesssim 5\text{x}10^6 \mathrm{M}_\odot$), dark matter haloes maintain the usual NFW profile as in dark matter only simulations.

- At higher efficiencies the profile becomes progressively flatter. The most cored galaxies are found at $M_\star/M_{\rm halo} \approx 3-5\times10^{-3}$ or $M_\star \sim 10^{8.5}\mathrm{M}_\odot$.

- Galaxies with $M_\star/M_{\rm halo} \gtrsim 5\times10^{-3}$ ($M_\star \gtrsim 10^{8.5}\mathrm{M}_\odot$), become progressively steeper in the inner region as their mass increases.

- The parameters (α,β,γ) returns to the NFW values of (1,3,1) for L* galaxies.

- However such L* galaxies, and more in general galaxies with $M_\star/M_{\rm halo} \gtrsim 0.03$, are up to a factor of 2.5 more concentrated than the corresponding dark matter only simulations.

In an Appendix we show step-by-step how to derive the dark matter profile for any galaxy mass.

Our results show that baryonic effects substantially change the structure of cold dark matter haloes from those predicted from dissipationless simulations, and therefore must be taken into account in any model of galaxy formation.

Of course, our model uses a particular feedback implementation, namely thermal feedback in the form of blast-wave formalism. Yet Teyssier et al. (2013) finds a similar degree of core creation, at least in low mass galaxies, using a different feedback scheme. Both studies are based on the same mechanisms for core creation, i.e. rapid and repeated outflows of gas which result in changes in the potential. Indeed, the simulations closely follow the analytic model of core creation presented in Pontzen & Governato (2012), indicating that the precise details of the feedback implementation are not central to our results, at least not in a qualitative manner. Galaxy formation models which do not include impulsive supernova explosions driving outflows from the central regions will not form cores in this manner.

In a forthcoming study we will present a comprehensive comparison of our predicted density profile with the inferred mass distribution of observed galaxies, with particular emphasis on Local Group members.

9.5 Recipe to derive a mass dependent density profile

We summarize here the steps necessary to derive, for a given halo mass, the corresponding dark matter profile which takes into account the effects of baryons:

- Input the halo mass $M_{\rm halo}$ and the stellar mass $M_\star$ of a galaxy. In case that only one of these two quantities is known, use the abundance matching relation (Brook et al. 2014; Moster et al. 2013; Guo et al. 2011) to derive the second one.
- Specify an overdensity criterion, such that the halo mass is defined as the mass contained within a sphere of radius $R_{\rm vir}$ containing Δ times the critical density of the Universe $\rho_{\rm crit} = 3H^2/8\pi G$:

$$M_{\rm halo} = \frac{4}{3}\pi R_{vir}^3 \Delta \rho_{crit} \tag{9.7}$$

  Common choices of Δ are $\Delta_{200} = 200$ or $\Delta_{\rm vir} = 18\pi^2 + 82x - 39x^2$ with $x = \Omega_m - 1$ at $z = 0$ (Bryan & Norman 1998). In a WMAP3 cosmology $\Delta_{\rm vir} = 92.8$.
- Compute the halo profile parameters (α, β, γ) as a function of integrated star formation efficiency $M_\star/M_{\rm halo}$ using Eq. (9.3). Recall that the range of validity of Eq. (9.3) is $-4.1 < \log_{10}(M_\star/M_{\rm halo}) < -1.3$: at lower efficiencies the (α, β, γ) value returns to the usual (1,3,1), NFW prediction.
- Obtain the concentration parameter $c_{\rm SPH} = R_{\rm vir}/r_{-2}$ via Eq. (9.6), where the quantity $c_{\rm DM}$ is the typical concentration of a halo of mass $M_{\rm halo}$ coming from N-body simulations (Dutton & Macciò 2014; Maccio' et al. 2008). In this way we have derived the r_{-2} at which the logarithmic slope of the profile equals -2.
- Convert such r_{-2} into the corresponding scale radius $r_{\rm s}$ using Eq. (9.2). This is the scale radius that enters into Eq. (9.1).
- Find the scale density $\rho_{\rm s}$ by imposing the normalization $M(< R_{vir}) = M_{\rm halo}$:

$$\rho_s = M_{\rm halo}/4\pi \int_0^{R_{vir}} \frac{r^2}{\left(\frac{r}{r_{\rm s}}\right)^{\gamma}\left[1+\left(\frac{r}{r_{\rm s}}\right)^{\alpha}\right]^{(\beta-\gamma)/\alpha}} dr \qquad (9.8)$$

- The mass dependent density profile can now be obtained through Eq. (9.1) and the corresponding circular velocity via $V_{\rm c}(r) = \sqrt{GM(r)/r}$.
- In case of fitting observed rotation curves of galaxies the scale radius $r_{\rm s}$ and scale density $\rho_{\rm s}$ should be left as the two free parameters of the model.

Chapter 10

Conclusion

In this thesis I explored the Lambda Cold Dark Matter (ΛCDM) small scales problems using two different sets of cosmological simulations of galaxy formation, namely the CLUES (Gottlöber et al. 2010) and the MaGICC ones (Stinson et al. 2013; Brook et al. 2012b). The current cosmological paradigm states that galaxies form within dark matter haloes (White & Rees 1978), in a process highly non linear that can be modeled by using numerical recipes (Springel 2005). As far as the dynamic of the process concerns the large scale structures in the Universe, such as filaments, voids and cluster of galaxies, the only relevant force that drives the evolution of these structures is the gravitational one, and the numerical simulations can be performed simply assuming that collisionless dark matter particles interact through this force. N-body simulation like the Millenium-XXL (Angulo et al. 2012), the Bolshoi (Klypin et al. 2010) and the Multidark run (Riebe et al. 2013) have provided a satisfactory description of the large scale of the Universe when compared to the observed distribution of galaxies (Cross et al. 2001). At smaller, galactic scales, however, the situation is more complicated due to the fact that visible matter undergoes dissipative dynamic processes when clumps into galaxies and stars. A series of problem associated with the formation and evolution of galactic and sub-galactic structures has been identified in the past decade as a possible failure of the ΛCDM paradigm.

In this thesis I reviewed such problems and offered possible solutions and explanations to them. In particular, I focused on the *too big to fail* (TBTF) problem (Boylan-Kolchin et al. 2011) and on the *cusp/core* crisis (de Blok 2010).

The *too big to fail* problem is the discrepancy between the observed kinematic of dwarf spheroidal galaxies around the Milky Way and Andromeda and the kinematic of the most massive subhaloes found in dark matter only simulations, the latter being more dense than what expected from the

measured stellar velocity dispersion of dSPhs (Walker et al. 2007).

I studied this issue by means of constrained cosmological simulations of the Local Group which also include the baryonic physics processes relevant in galaxy formation. These simulations are designed in order to constrain the observed structures at scale larger than few Mpc, while smaller scales are essentially random, therefore reproducing the evolution and formation of the Local Group of galaxies within the correct environment. I showed that the subhaloes lying within the virial radius of the simulated analogues of the Milky Way and Andromeda are affected by baryonic physics (Knebe et al. 2010; Di Cintio et al. 2011). Most of them will form too many stars and will undergo through an adiabatic contraction of their haloes, giving an even worse picture when compared to the observed dSPhs' kinematic; only a few of the subhaloes found in the baryonic (SPH) run of CLUES will experience a decreasing in their central density, possibly due to outflows of gas from their center, bringing them in agreement with observations.

In both cases, the density profile of the simulated subhaloes seem to be better described by an Einasto model (Einasto 1965) rather than the usual NFW (Navarro et al. 1996b), particularly since the subhaloes will experience tidal stripping, which acts at modifying their outer region (Hayashi et al. 2003), once they enter into the main halo of their hosts. I applied the Einasto model to the CLUES subhaloes and I showed that the TBTF problem can be alleviated if one uses this profile allowing for a variation of the shape parameter n_{Ein} (Di Cintio et al. 2013). I found a correlation between such shape parameter and the subhaloes mass, with the biggest subhaloes having a shape parameter as high as $n_{Ein} = 10$, which means that their inner slope is steeper than a NFW model, thus indicating adiabatic contraction, while the smallest subhaloes have on average a shape parameter less than $n_{Ein} = 4$, which is the typical value of dark matter haloes in N-body simulations. This means that the smallest subhaloes have strongly been affected by tides in their outer regions, and some of them have even lost all their gas, further lowering their central density.

In the light of these findings I concluded that using a universal density profile to describe the dark matter haloes of observed dwarf spheroidal galaxies is inconsistent, since both internal (baryonic) and external (tidal stripping) processes can modify the subhaloes density profiles. Asides from the most appropriate density profile to be used, however, the CLUES simulations still produce satellites which are brighter than the most luminous dSphs observed. Unless one accounts for some statistical fluke, this problem has still to be solved, most likely by the inclusion, in the simulations, of proper feedback processes.

The number of satellite galaxies found in numerical simulations within

the virial radius of their host halo is strongly dependent on the host halo mass itself (Wang et al. 2012). Therefore, given the importance of correctly evaluating the mass of the Milky Way galaxy in order to reproduce the observed count and luminosities of its satellite population, I focused on the description of a mass estimator method, based upon dynamical tracers, to calculate such mass (Watkins et al. 2010). I showed that this mass estimator can be safely applied even in the case of Local Group galaxies, in which the two main hosts are near by, possibly influencing each other. The only caveat is to take care in including only dynamical tracers, like globular clusters, halo stars or satellite galaxies, which are actually bound to the considered host: disregarding for this will cause a notable error in the final mass estimation (Di Cintio et al. 2012).

Finally, I explored the TBTF problem using warm dark matter (WDM) simulations of the Local Group, with a dark matter particle mass of 1 keV (Libeskind et al. 2013). While these simulations strongly suppress the counts of subhaloes within the two main galaxies, due to the lack of power at small scales, the result it is actually still affected by the fact that the biggest subhaloes will form too many stars. Moreover, a 1 keV particle does not produce enough bright subhaloes, in the SPH run, to account for all the observed classical dwarf spheroidals of the Milky Way. Recent constraint on warm dark matter particle mass put the limit at $m_{wdm} \geqslant 3.3$ keV (Viel et al. 2013): with such a high mass, the WDM scenario does as bad as the CDM one in solving the small scales problems (Schneider et al. 2014). I further explored the differences between the Local Group of galaxies formed in WDM vs CDM. In WDM, due to the delayed formation and collapse of haloes (Bode et al. 2001; Knebe et al. 2008), the resulting Local Group is more diffuse and still expanding, while in the corresponding CDM the Milky Way and Andromeda galaxies are approaching each other, in agreement with observations. I also showed that, reflecting the formation epoch of haloes and the mass accretion history, WDM haloes have a lower baryon fractions in their inner parts than CDM haloes.

Moreover, I discussed how it is possible to use the simulations of a Local Group to put further constraint on the stellar-to-halo mass relations of galaxies, down to the luminosities of the faintest dwarfs observed (Brook et al. 2014). While this technique has been used extensively to derive an abundance-matching of galaxies down to an halo mass of $M_{\rm halo} = 10^{10.8}{\rm M}_{\odot}$ (Moster et al. 2010; Guo et al. 2010), with our Local Group simulations we have been able to to extrapolate the relation down to $M_{\rm halo} \sim 10^{9.8}{\rm M}_{\odot}$, by using the CLUES halo mass function and by matching it to the observed stellar mass function in the Local Group, which is complete to $M_{\star} \sim 10^{6.5}{\rm M}_{\odot}$. This finding shows that the vast majority of the galaxies in the Local Group, regardless of whether they are satellites or isolated,

are predicted to be housed in haloes whose mass exceeds $10^{10}\mathrm{M}_{\odot}$, in contrast with dynamical measurements of dSphs, which would assign most of these galaxies to a halo of smaller mass. Such assignment assumes, however, that their dark matter halo follows the density profile derived from N-body simulations, the commonly used NFW model.

They way out of this discrepancy may reside in baryonic processes that are neglected when using collisionless simulations to make predictions about observed dwarf galaxies. To reconcile observational data with our abundance-matching prediction one has to assume that some of these galaxies have a central dark matter core, i.e. their halo is expanded.

I explored extensively what are the main mechanisms able to cause an expanded dark matter halo in galaxies, by using hydrodynamical simulations of galaxies from the MaGICC project (Stinson et al. 2013). These galaxies, which spam a wide range in mass, are simulated using feedback from supernovae as well as from young massive stars, in terms of thermal energy. It has been shown that including both sources of feedback it is necessary in order to produce galaxies with the correct amount of stars per halo mass and that match the observed scaling relations (Brook et al. 2012b).

I showed that supernovae driven gas outflows are able to create a flat, cored central density in an initially NFW halo, as a result of the dark matter response to the impulsive variations of the gravitational potential (Pontzen & Governato 2012). This mechanism is dependent on the amount of energy per halo mass, such that the flattening process can be directly related to the $M_{\star}/M_{\mathrm{halo}}$ ratio within each galaxy (Di Cintio et al. 2014b). This process has a peak of efficiency at $M_{\star}/M_{\mathrm{halo}} \sim 0.39\%$, while for higher and lower ratios the profile is cuspy again. At lower ratio the profile is NFW because there is not enough energy from supernovae in order to lead a modification in the dark matter distribution; at higher masses, instead, the supernovae energy is not strong enough to win the deepened potential well caused by the increasing amount of stars.

This finding allows to make predictions for the *cusp/core* transformation in galaxies, with the cored-most galaxies expected at $30 \lesssim V_{\mathrm{circ}}/\mathrm{kms}^{-1} \lesssim 70$, in agreement with observations of disc and low surface brightness galaxies (Kuzio de Naray et al. 2008a; de Blok et al. 2008; Oh et al. 2011a). More massive galaxies are predicted to be cuspy, also in agreement with observations although with a greater uncertainty due to the higher baryonic contribution to the total rotation curve. In our model, some of the satellite galaxies in the Local Group are expected to live within an expanded halo, while some others will retain a cuspy, NFW halo, depending on their stellar-to-halo mass ratio. The evidence for a mixed population of cored and cuspy satellite galaxies within the Local Group is strongly supported

by observations (Walker & Peñarrubia 2011; Wolf & Bullock 2012).

The *cusp/core* crisis, therefore, seems to be solved once one takes into account the relevant processes occurring during the formation of a galaxy. Of course, it would be invaluable to confirm our results using a different feedback scheme and simulation code, although recent studies are going into our same direction (Teyssier et al. 2013).

I further introduced a full density profile able to describe the distribution of dark matter in galaxies, which takes into account the stellar-to-halo mass dependence of the response of dark matter to baryonic processes (Di Cintio et al. 2014a). The main parameters of this profile, like inner and outer slope and concentration parameter, can be fully constrained via the quantity $M_\star/M_{\rm halo}$, reducing the number of free parameters of the model. Knowing the halo or the stellar mass of a galaxy is sufficient to describe the dark matter halo profile including the effects of baryons. I showed that the concentration of the haloes in the hydrodynamical simulations is consistent with N-body expectations up to Milky Way mass galaxies, at which mass the haloes become twice as concentrated as compared with pure dark matter runs, in agreement with recent studies (Nesti & Salucci 2013).

These results suggest that the proposed mass dependent density profile is more adequate than the commonly used NFW one in describing real galaxies, and it can be directly applied to rotation curve data of observed galaxies and to mass modeling of their inner profile.

I showed in this thesis how the main problems of ΛCDM at small scales are connected to each other, the "too big to fail" problem being possibly solved once we understand how and why the "cusp/core" transformation happens in galaxies. According to the common NFW profile, the brightest satellite galaxies of the Milky Way would be placed within haloes of about $M_{\rm halo} \sim 10^9 {\rm M}_\odot$, leaving dark the biggest subhaloes of $M_{\rm halo} \sim 10^{10} {\rm M}_\odot$ and highlighting a disagreement with abundance matching predictions. Rather than a failure of the ΛCDM paradigm at small scales, this issue has to be seen as a proof of the importance of baryonic mechanisms at such scales, and as an evidence for halo expansion within the most luminous dSphs in our galaxy. Expanded, cored haloes, as well as cuspy ones, can be satisfactorily described by means of the mass dependent density profile introduced in this thesis.

Future directions of this research include a complete analysis and comparison of our *cusp/core* prediction with the Local Group galaxies, by applying our mass dependent density profile to their observed velocity dispersions. The goal is to infer the mass distribution of the entire population of the Local Group members, highlighting the connection between abundance matching at these scales and the need for a *cusp/core* transformation.

The prediction for cusp vs core formation can also be applied to the observed rotation curves of galaxies in order to put constraint on the baryonic contribution to their circular velocities.

Running new simulation within the CLUES project using the updated feedback recipe of the MaGICC galaxies, moreover, will allow to explore the Local Group formation within an effective feedback scenario. Several studies can be performed, like understanding what are the physical processes that cause different star formation histories within the observed dwarf spheroidal galaxies and what drives the scatter in the abundance matching relation at very small galaxy masses.

The newly introduced mass dependent density profile can be further used to make comparisons with galaxies in a broad range of masses: in particular the observed abundances and velocities of galaxies within a certain volume can be compared with the theoretical velocity function derived by using our profile.

Finally, it would be imperative to implement such a mass-dependent density profile into semi-analytic models of galaxy formation. The ultimate goal is to start using this density profile as a significant improvement over the NFW model predicted form N-body simulations.

Bibliography

Agertz, O., Moore, B., Stadel, J., et al. 2007, MNRAS, 380, 963

An, J., Evans, N. W., & Deason, A. J. 2012, MNRAS, 420, 2562

Angulo, R. E., Springel, V., White, S. D. M., et al. 2012, MNRAS, 426, 2046

Arraki, K. S., Klypin, A., More, S., & Trujillo-Gomez, S. 2014, MNRAS, 438, 1466

Avila-Reese, V., Colín, P., Valenzuela, O., D'Onghia, E., & Firmani, C. 2001, ApJ, 559, 516

Bahcall, J. N. & Tremaine, S. 1981, ApJ, 244, 805

Baldry, I. K., Driver, S. P., Loveday, J., et al. 2012, MNRAS, 421, 621

Baldry, I. K., Glazebrook, K., & Driver, S. P. 2008, MNRAS, 388, 945

Banerjee, A. & Jog, C. J. 2008, ApJ, 685, 254

Battaglia, G., Helmi, A., Morrison, H., et al. 2005, MNRAS, 364, 433

Behroozi, P. S., Wechsler, R. H., & Conroy, C. 2013, ApJ, 770, 57

Bekki, K. 2008, ApJ, 684, L87

Belokurov, V., Walker, M. G., Evans, N. W., et al. 2008, ApJ, 686, L83

Belokurov, V., Walker, M. G., Evans, N. W., et al. 2009, MNRAS, 397, 1748

Benson, A. 2011, Galacticus: A Semi-Analytic Model of Galaxy Formation, astrophysics Source Code Library

Benson, A. J., Bower, R. G., Frenk, C. S., et al. 2003, ApJ, 599, 38

Benson, A. J., Frenk, C. S., Lacey, C. G., Baugh, C. M., & Cole, S. 2002, MNRAS, 333, 177

Binney, J. & Tremaine, S. 1987, Galactic dynamics (Princeton, NJ, Princeton University Press, 1987, 747 p.)

Blumenthal, G. R., Faber, S. M., Flores, R., & Primack, J. R. 1986, ApJ, 301, 27

Blumenthal, G. R., Faber, S. M., Primack, J. R., & Rees, M. J. 1984, Nature, 311, 517

Bode, P., Ostriker, J. P., & Turok, N. 2001, ApJ, 556, 93

Borriello, A. & Salucci, P. 2001, MNRAS, 323, 285

Bovill, M. S. & Ricotti, M. 2011a, ApJ, 741, 17

Bovill, M. S. & Ricotti, M. 2011b, ApJ, 741, 18

Boylan-Kolchin, M., Bullock, J. S., & Kaplinghat, M. 2011, MNRAS, 415, L40

Boylan-Kolchin, M., Bullock, J. S., & Kaplinghat, M. 2012, MNRAS, 422, 1203

Boylan-Kolchin, M., Springel, V., White, S. D. M., & Jenkins, A. 2010, MNRAS, 406, 896

Brook, C. B., Di Cintio, A., Knebe, A., et al. 2014, ApJ, 784, L14

Brook, C. B., Governato, F., Roškar, R., et al. 2011, MNRAS, 595

Brook, C. B., Miranda, M. S., Gibson, B. K., Pilkington, K., & Stinson, G. S. 2013a, PASA, 30, 42

Brook, C. B., Stinson, G., Gibson, B. K., et al. 2012a, MNRAS, 419, 771

Brook, C. B., Stinson, G., Gibson, B. K., et al. 2013b, ArXiv e-prints

Brook, C. B., Stinson, G., Gibson, B. K., Wadsley, J., & Quinn, T. 2012b, MNRAS, 424, 1275

Brooks, A. M., Kuhlen, M., Zolotov, A., & Hooper, D. 2013, ApJ, 765, 22

Bryan, G. L. & Norman, M. L. 1998, ApJ, 495, 80

Bullock, J. S. 2010, ArXiv e-prints

Bullock, J. S., Kolatt, T. S., Sigad, Y., et al. 2001, MNRAS, 321, 559

Bullock, J. S., Kravtsov, A. V., & Weinberg, D. H. 2000, ApJ, 539, 517

Catena, R. & Ullio, P. 2010, Journal of Cosmology and Astro-Particle Physics, 8, 4

Chabrier, G. 2003, ApJL, 586, L133

Chemin, L., de Blok, W. J. G., & Mamon, G. A. 2011, AJ, 142, 109

Chevalier, R. A. 1974, ApJ, 188, 501

Clowe, D., Bradač, M., Gonzalez, A. H., et al. 2006, ApJ, 648, L109

Cole, D. R., Dehnen, W., & Wilkinson, M. I. 2011, MNRAS, 416, 1118

Cole, S. & et al. 2005, MNRAS, 362, 505

Collins, M. L. M., Chapman, S. C., Rich, R. M., et al. 2014, ApJ, 783, 7

Courteau, S., Dutton, A. A., van den Bosch, F. C., et al. 2007, ApJ, 671, 203

Courteau, S. & Rix, H.-W. 1999, ApJ, 513, 561

Crain, R. A., Theuns, T., Dalla Vecchia, C., et al. 2009, MNRAS, 399, 1773

Cross, N., Driver, S. P., Couch, W., et al. 2001, MNRAS, 324, 825

Davis, M., Efstathiou, G., Frenk, C. S., & White, S. D. M. 1985, ApJ, 292, 371

Dayal, P. & Libeskind, N. I. 2012, MNRAS, 419, L9

de Blok, W. J. G. 2010, Advances in Astronomy, 2010

de Blok, W. J. G., Bosma, A., & McGaugh, S. 2003, MNRAS, 340, 657

de Blok, W. J. G., McGaugh, S. S., Bosma, A., & Rubin, V. C. 2001, ApJ, 552, L23

de Blok, W. J. G., Walter, F., Brinks, E., et al. 2008, AJ, 136, 2648

Deason, A. J., Belokurov, V., Evans, N. W., & An, J. 2012a, MNRAS, 424, L44

Deason, A. J., Belokurov, V., Evans, N. W., et al. 2012b, MNRAS, 425, 2840

Deason, A. J., McCarthy, I. G., Font, A. S., et al. 2011, MNRAS, 415, 2607

Dekel, A. & Silk, J. 1986, ApJ, 303, 39

Del Popolo, A. 2009, ApJ, 698, 2093

Del Popolo, A. 2010, MNRAS, 408, 1808

Del Popolo, A. & Cardone, V. F. 2012, MNRAS, 423, 1060

Devriendt, J. E. G., Guiderdoni, B., & Sadat, R. 1999, A&A, 350, 381

Di Cintio, A., Brook, C. B., Dutton, A. A., et al. 2014a, ArXiv e-prints

Di Cintio, A., Brook, C. B., Macciò, A. V., et al. 2014b, MNRAS, 437, 415

Di Cintio, A., Knebe, A., Libeskind, N. I., et al. 2013, MNRAS, 431, 1220

Di Cintio, A., Knebe, A., Libeskind, N. I., et al. 2012, MNRAS, 423, 1883

Di Cintio, A., Knebe, A., Libeskind, N. I., et al. 2011, MNRAS, 417, L74

Diemand, J., Kuhlen, M., & Madau, P. 2007, ApJ, 657, 262

Diemand, J., Kuhlen, M., Madau, P., et al. 2008, Nature, 454, 735

Domínguez-Tenreiro, R., Obreja, A., Granato, G. L., et al. 2014, MNRAS, 439, 3868

Donato, F., Gentile, G., & Salucci, P. 2004, MNRAS, 353, L17

Duffy, A. R., Schaye, J., Kay, S. T., et al. 2010, MNRAS, 405, 2161

Dunkley, J., Komatsu, E., Nolta, M. R., et al. 2009, ApJS, 180, 306

Dutton, A. A., Conroy, C., van den Bosch, F. C., Prada, F., & More, S. 2010, MNRAS, 407, 2

Dutton, A. A., Conroy, C., van den Bosch, F. C., et al. 2011, MNRAS, 416, 322

Dutton, A. A. & Macciò, A. V. 2014, ArXiv e-prints,1402.7073

Dutton, A. A., Macciò, A. V., Mendel, J. T., & Simard, L. 2013, MNRAS, 432, 2496

Dutton, A. A., van den Bosch, F. C., Dekel, A., & Courteau, S. 2007, ApJ, 654, 27

Einasto, J. 1965, Trudy Inst. Astrofiz. Alma-Ata, 51, 87

El-Zant, A., Shlosman, I., & Hoffman, Y. 2001, ApJ, 560, 636

Evans, N. W., An, J., & Deason, A. J. 2011, ApJ, 730, L26+

Ferrero, I., Abadi, M. G., Navarro, J. F., Sales, L. V., & Gurovich, S. 2012, MNRAS, 425, 2817

Forero-Romero, J. E., Hoffman, Y., Yepes, G., et al. 2011, MNRAS, 417, 1434

Freyer, T., Hensler, G., & Yorke, H. W. 2006, ApJ, 638, 262

Gao, L., Navarro, J. F., Cole, S., et al. 2008, MNRAS, 387, 536

Garrison-Kimmel, S., Boylan-Kolchin, M., Bullock, J. S., & Kirby, E. N. 2014, ArXiv e-prints

Garrison-Kimmel, S., Rocha, M., Boylan-Kolchin, M., Bullock, J. S., & Lally, J. 2013, MNRAS, 433, 3539

Gill, S. P. D., Knebe, A., & Gibson, B. K. 2004a, MNRAS, 351, 399

Gill, S. P. D., Knebe, A., Gibson, B. K., & Dopita, M. A. 2004b, MNRAS, 351, 410

Gnedin, O. Y., Kravtsov, A. V., Klypin, A. A., & Nagai, D. 2004, ApJ, 616, 16

Goerdt, T., Moore, B., Read, J. I., & Stadel, J. 2010, ApJ, 725, 1707

Goerdt, T., Moore, B., Read, J. I., Stadel, J., & Zemp, M. 2006, MNRAS, 368, 1073

Gottlöber, S., Hoffman, Y., & Yepes, G. 2010, in High Performance Computing in Science and Engineering, ed. S. Wagner, M. Steinmetz, A. Bode, M.M. Müller, Springer, 309–323

Governato, F., Brook, C., Mayer, L., et al. 2010, Nature, 463, 203

Governato, F., Zolotov, A., Pontzen, A., et al. 2012, MNRAS, 422, 1231

Graham, A. W., Merritt, D., Moore, B., Diemand, J., & Terzić, B. 2006a, AJ, 132, 2701

Graham, A. W., Merritt, D., Moore, B., Diemand, J., & Terzić, B. 2006b, AJ, 132, 2711

Guo, Q., Cole, S., Eke, V., & Frenk, C. 2011, MNRAS, 417, 370

Guo, Q., White, S., Li, C., & Boylan-Kolchin, M. 2010, MNRAS, 404, 1111

Haardt, F. & Madau, P. 1996, ApJ, 461, 20

Hayashi, E., Navarro, J. F., Taylor, J. E., Stadel, J., & Quinn, T. 2003, ApJ, 584, 541

Hayashi, E. & White, S. D. M. 2008, MNRAS, 388, 2

Hernquist, L. 1990, ApJ, 356, 359

Herpich, J., Stinson, G. S., Macciò, A. V., et al. 2014, MNRAS, 437, 293

Hinshaw, G., Larson, D., Komatsu, E., et al. 2013, ApJS, 208, 19

Hoekstra, H., Yee, H. K. C., & Gladders, M. D. 2004, ApJ, 606, 67

Hoffman, Y. & Ribak, E. 1991, ApJ, 380, L5

Hopkins, P. F., Quataert, E., & Murray, N. 2011, ArXiv e-prints

Hudson, M. J., Gillis, B. R., Coupon, J., et al. 2013, ArXiv e-prints

Ibata, R., Martin, N. F., Irwin, M., et al. 2007, ApJ, 671, 1591

Jaffe, W. 1983, MNRAS, 202, 995

Jarosik, N. & et al. 2011, ApJS, 192, 14

Jenkins, A., Frenk, C. S., White, S. D. M., et al. 2001, MNRAS, 321, 372

Kahn, F. D. & Woltjer, L. 1959, ApJ, 130, 705

Kannan, R., Macciò, A. V., Pasquali, A., Moster, B. P., & Walter, F. 2012, ApJ, 746, 10

Kannan, R., Stinson, G. S., Macciò, A. V., et al. 2013, arXiv.1302.2618

Karachentsev, I. D., Karachentseva, V. E., Huchtmeier, W. K., & Makarov, D. I. 2004, AJ, 127, 2031

Karachentsev, I. D. & Kashibadze, O. G. 2006, Astrophysics, 49, 3

Katz, N. 1992, ApJ, 391, 502

Kay, S. T., Pearce, F. R., Frenk, C. S., & Jenkins, A. 2002, MNRAS, 330, 113

Kazantzidis, S., Mayer, L., Mastropietro, C., et al. 2004, ApJ, 608, 663

Keller, S. C., Mackey, D., & Da Costa, G. S. 2012, ApJ, 744, 57

Keller, S. C., Schmidt, B. P., Bessell, M. S., et al. 2007, PASA, 24, 1

Kendall, M. & Gibbons, J. D. 1990, Rank Correlation Methods, 5th edn. (A Charles Griffin Title)

Kennicutt, Jr., R. C. 1998, in Astronomical Society of the Pacific Conference Series, Vol. 142, The Stellar Initial Mass Function (38th Herstmonceux Conference), ed. G. Gilmore & D. Howell, 1–+

Kirby, E. N., Cohen, J. G., Guhathakurta, P., et al. 2013, ArXiv e-prints

Klypin, A., Gottlöber, S., Kravtsov, A. V., & Khokhlov, A. M. 1999a, ApJ, 516, 530

Klypin, A., Hoffman, Y., Kravtsov, A. V., & Gottlöber, S. 2003, ApJ, 596, 19

Klypin, A., Kravtsov, A. V., Valenzuela, O., & Prada, F. 1999b, ApJ, 522, 82

Klypin, A., Trujillo-Gomez, S., & Primack, J. 2010, ArXiv e-prints

Knebe, A., Arnold, B., Power, C., & Gibson, B. K. 2008, MNRAS, 386, 1029

Knebe, A., Devriendt, J. E. G., Mahmood, A., & Silk, J. 2002, MNRAS, 329, 813

Knebe, A., Gill, S. P. D., Gibson, B. K., et al. 2004, ApJ, 603, 7

Knebe, A., Knollmann, S. R., Muldrew, S. I., et al. 2011a, MNRAS, 415, 2293

Knebe, A., Libeskind, N. I., Doumler, T., et al. 2011b, MNRAS, 417, L56

Knebe, A., Libeskind, N. I., Knollmann, S. R., et al. 2011c, MNRAS, 412, 529

Knebe, A., Libeskind, N. I., Knollmann, S. R., et al. 2010, ArXiv e-prints

Knebe, A., Pearce, F. R., Lux, H., et al. 2013, MNRAS, 435, 1618

Knollmann, S. R. & Knebe, A. 2009, ApJS, 182, 608

Komatsu, E., Dunkley, J., Nolta, M. R., et al. 2009, ApJS, 180, 330

Komatsu, E., Smith, K. M., Dunkley, J., et al. 2011, ApJS, 192, 18

Koposov, S., Belokurov, V., Evans, N. W., et al. 2008, ApJ, 686, 279

Koposov, S. E., Rix, H.-W., & Hogg, D. W. 2010, ApJ, 712, 260

Kravtsov, A. 2010, Advances in Astronomy, 2010

Kroupa, P., Theis, C., & Boily, C. M. 2005, A&A, 431, 517

Kroupa, P., Tout, C. A., & Gilmore, G. 1993, MNRAS, 262, 545

Kuhlen, M., Vogelsberger, M., & Angulo, R. 2012, Physics of the Dark Universe, 1, 50

Kuzio de Naray, R., McGaugh, S. S., & de Blok, W. J. G. 2008a, ApJ, 676, 920

Kuzio de Naray, R., McGaugh, S. S., & de Blok, W. J. G. 2008b, ApJ, 676, 920

Kuzio de Naray, R., McGaugh, S. S., & Mihos, J. C. 2009, ApJ, 692, 1321

Lares, M., Lambas, D. G., & Domínguez, M. J. 2011, AJ, 142, 13

Law, D. R., Majewski, S. R., & Johnston, K. V. 2009, ApJ, 703, L67

Leauthaud, A., Tinker, J., Bundy, K., et al. 2012, ApJ, 744, 159

Libeskind, N. I., Di Cintio, A., Knebe, A., et al. 2013, PASA, 30, 39

Libeskind, N. I., Frenk, C. S., Cole, S., et al. 2005, MNRAS, 363, 146

Libeskind, N. I., Hoffman, Y., Knebe, A., et al. 2012, MNRAS, 421, L137

Libeskind, N. I., Knebe, A., Hoffman, Y., Gottlöber, S., & Yepes, G. 2011a, MNRAS, 418, 336

Libeskind, N. I., Knebe, A., Hoffman, Y., et al. 2011b, MNRAS, 411, 1525

Libeskind, N. I., Yepes, G., Knebe, A., et al. 2010, MNRAS, 401, 1889

Lima Neto, G. B., Gerbal, D., & Márquez, I. 1999, MNRAS, 309, 481

Liu, L., Gerke, B. F., Wechsler, R. H., Behroozi, P. S., & Busha, M. T. 2010, ArXiv e-prints

Liu, L., Gerke, B. F., Wechsler, R. H., Behroozi, P. S., & Busha, M. T. 2011, ApJ, 733, 62

Łokas, E. L. 2009, MNRAS, 394, L102

Lokas, E. L., Kazantzidis, S., & Mayer, L. 2011, ArXiv e-prints

Lokas, E. L., Kazantzidis, S., Mayer, L., & Callegari, S. 2010, ArXiv e-prints

Lovell, M. R., Eke, V., Frenk, C. S., et al. 2012, MNRAS, 420, 2318

LSST Science Collaboration, Abell, P. A., Allison, J., et al. 2009, ArXiv e-prints

Ludlow, A. D., Navarro, J. F., White, S. D. M., et al. 2011, MNRAS, 415, 3895

Macciò, A. V., Dutton, A. A., van den Bosch, F. C., et al. 2007, MNRAS, 378, 55

Macciò, A. V. & Fontanot, F. 2010, MNRAS, 404, L16

Maccio', A. V., Kang, X., & Moore, B. 2008, ArXiv e-prints

Macciò, A. V., Paduroiu, S., Anderhalden, D., Schneider, A., & Moore, B. 2012b, MNRAS, 424, 1105

Macciò, A. V., Stinson, G., Brook, C. B., et al. 2012, ApJL, 744, L9

Martin, N. F., de Jong, J. T. A., & Rix, H.-W. 2008, ApJ, 684, 1075

Martin, N. F., Schlafly, E. F., Slater, C. T., et al. 2013a, ArXiv e-prints

Martin, N. F., Slater, C. T., Schlafly, E. F., et al. 2013b, ApJ, 772, 15

Martinsson, T. P. K., Verheijen, M. A. W., Westfall, K. B., et al. 2013, A&A, 557, A131

Martizzi, D., Teyssier, R., & Moore, B. 2013, MNRAS, 432, 1947

Mashchenko, S., Couchman, H. M. P., & Wadsley, J. 2006, Nature, 442, 539

Mateo, M. L. 1998, ARA&A, 36, 435

McConnachie, A. W. 2012, AJ, 144, 4

McConnachie, A. W., Irwin, M. J., Ferguson, A. M. N., et al. 2005, MNRAS, 356, 979

McGaugh, S. S., de Blok, W. J. G., Schombert, J. M., Kuzio de Naray, R., & Kim, J. H. 2007, ApJ, 659, 149

McKee, C. F. & Ostriker, J. P. 1977, ApJ, 218, 148

Merritt, D., Graham, A. W., Moore, B., Diemand, J., & Terzić, B. 2006, AJ, 132, 2685

Merritt, D., Navarro, J. F., Ludlow, A., & Jenkins, A. 2005, ApJ, 624, L85

Metz, M., Kroupa, P., & Jerjen, H. 2007, MNRAS, 374, 1125

Metz, M., Kroupa, P., & Libeskind, N. I. 2008, ApJ, 680, 287

Mo, H. J. & Mao, S. 2004, MNRAS, 353, 829

Monaco, P., Benson, A. J., De Lucia, G., et al. 2014, MNRAS, 441, 2058

Moore, B. 1994, Nature, 370, 629

Moore, B., Ghigna, S., Governato, F., et al. 1999, ApJ, 524, L19

More, S., Kravtsov, A., Dalal, N., & Gottlöber, S. 2011, ArXiv e-prints

Moster, B. P., Naab, T., & White, S. D. M. 2013, MNRAS, 428, 3121

Moster, B. P., Somerville, R. S., Maulbetsch, C., et al. 2010, ApJ, 710, 903

Muñoz-Cuartas, J. C., Macciò, A. V., Gottlöber, S., & Dutton, A. A. 2011, MNRAS, 411, 584

Munshi, F., Governato, F., Brooks, A. M., et al. 2013, ApJ, 766, 56

Navarro, J. F., Eke, V. R., & Frenk, C. S. 1996a, MNRAS, 283, L72

Navarro, J. F., Frenk, C. S., & White, S. D. M. 1996b, ApJ, 462, 563

Navarro, J. F., Hayashi, E., Power, C., et al. 2004, MNRAS, 349, 1039

Navarro, J. F., Ludlow, A., Springel, V., et al. 2010, MNRAS, 402, 21

Nesti, F. & Salucci, P. 2013, Journal of Cosmology and Astro-Particle Physics, 7, 16

Nickerson, S., Stinson, G., Couchman, H. M. P., Bailin, J., & Wadsley, J. 2011, MNRAS, 415, 257

Obreja, A., Brook, C. B., Stinson, G., et al. 2014, ArXiv e-prints,1404.0043

Oh, K. S., Lin, D. N. C., & Aarseth, S. J. 1995, ApJ, 442, 142

Oh, S., Brook, C., Governato, F., et al. 2011a, ArXiv e-prints

Oh, S.-H., de Blok, W. J. G., Brinks, E., Walter, F., & Kennicutt, Jr., R. C. 2011b, AJ, 141, 193

Onions, J., Knebe, A., Pearce, F. R., et al. 2012, ArXiv e-prints

Parry, O. H., Eke, V. R., Frenk, C. S., & Okamoto, T. 2012, MNRAS, 419, 3304

Peñarrubia, J., Benson, A. J., Walker, M. G., et al. 2010, MNRAS, 406, 1290

Peñarrubia, J., McConnachie, A. W., & Navarro, J. F. 2008, ApJ, 672, 904

Peñarrubia, J., Navarro, J. F., McConnachie, A. W., & Martin, N. F. 2009, ApJ, 698, 222

Peñarrubia, J., Pontzen, A., Walker, M. G., & Koposov, S. E. 2012, ApJ, 759, L42

Peebles, P. J. E. 1980, The large-scale structure of the universe

Penzo, C., Macciò, A. V., Casarini, L., Stinson, G. S., & Wadsley, J. 2014, ArXiv e-prints

Planck Collaboration, Ade, P. A. R., Aghanim, N., et al. 2013, ArXiv e-prints

Pontzen, A. & Governato, F. 2012, MNRAS, 421, 3464

Pontzen, A. & Governato, F. 2014, Nature, 506, 171

Power, C. & Knebe, A. 2006, MNRAS, 370, 691

Power, C., Navarro, J. F., Jenkins, A., et al. 2003, MNRAS, 338, 14

Prada, F., Klypin, A. A., Cuesta, A. J., Betancort-Rijo, J. E., & Primack, J. 2012, MNRAS, 423, 3018

Prada, F., Klypin, A. A., Simonneau, E., et al. 2006, ApJ, 645, 1001

Prada, F., Vitvitska, M., Klypin, A., et al. 2003, ApJ, 598, 260

Prugniel, P. & Simien, F. 1997, A&A, 321, 111

Quinn, T. & Binney, J. 1992, MNRAS, 255, 729

Read, J. I. & Gilmore, G. 2005, MNRAS, 356, 107

Read, J. I., Wilkinson, M. I., Evans, N. W., Gilmore, G., & Kleyna, J. T. 2006, MNRAS, 367, 387

Reed, D., Governato, F., Verde, L., et al. 2005, MNRAS, 357, 82

Reed, D. S., Koushiappas, S. M., & Gao, L. 2011, MNRAS, 415, 3177

Reiprich, T. H. & Böhringer, H. 2002, ApJ, 567, 716

Riebe, K., Partl, A. M., Enke, H., et al. 2013, Astronomische Nachrichten, 334, 691

Riess, A. G., Filippenko, A. V., Challis, P., et al. 1998, AJ, 116, 1009

Romano-Díaz, E., Shlosman, I., Hoffman, Y., & Heller, C. 2008, ApJ, 685, L105

Rubin, V. C., Ford, W. K. J., & . Thonnard, N. 1980, ApJ, 238, 471

Salucci, P. & Burkert, A. 2000, ApJ, 537, L9

Scannapieco, C., Wadepuhl, M., Parry, O. H., & et al. 2012, MNRAS, 423, 1726

Schmidt, M. 1959, ApJ, 129, 243

Schneider, A., Anderhalden, D., Macciò, A. V., & Diemand, J. 2014, MNRAS, 441, L6

Schuberth, Y., Richtler, T., Hilker, M., et al. 2010, A&A, 513, A52

Seigar, M. S., Barth, A. J., & Bullock, J. S. 2008, MNRAS, 389, 1911

Sérsic, J. L. 1963, Boletin de la Asociacion Argentina de Astronomia La Plata Argentina, 6, 41

Sérsic, J. L. 1968, Atlas de galaxias australes

Shen, S., Wadsley, J., & Stinson, G. 2010, MNRAS, 407, 1581

Silk, J. 2003, MNRAS, 343, 249

Simon, J. D., Bolatto, A. D., Leroy, A., Blitz, L., & Gates, E. L. 2005, ApJ, 621, 757

Simon, J. D. & Geha, M. 2007, ApJ, 670, 313

Smoot, G. F., Bennett, C. L., Kogut, A., et al. 1992, ApJ, 396, L1

Somerville, R. S. 2002, ApJ, 572, L23

Sorce, J., Courtois, H., Gottloeber, S., et al. 2014, in American Astronomical Society Meeting Abstracts, Vol. 223, American Astronomical Society Meeting Abstracts, 313.01

Spergel et al., D. N. 2003, ApJS, 148, 175

Spergel et al., D. N. 2007, ApJS, 170, 377

Springel, V. 2005, MNRAS, 364, 1105

Springel, V. & Hernquist, L. 2003, MNRAS, 339, 289

Springel, V., Wang, J., Vogelsberger, M., et al. 2008, MNRAS, 391, 1685

Stinson, G., Seth, A., Katz, N., et al. 2006, MNRAS, 373, 1074

Stinson, G. S., Bailin, J., Couchman, H., et al. 2010, MNRAS, 408, 812

Stinson, G. S., Brook, C., Macciò, A. V., et al. 2013, MNRAS, 428, 129

Stinson, G. S., Brook, C., Prochaska, J. X., et al. 2012, MNRAS, 425, 1270

Stoehr, F., White, S. D. M., Springel, V., Tormen, G., & Yoshida, N. 2003, MNRAS, 345, 1313

Strigari, L. E., Frenk, C. S., & White, S. D. M. 2010, MNRAS, 408, 2364

Strigari, L. E. & Wechsler, R. H. 2012, ApJ, 749, 75

Swaters, R. A., Madore, B. F., van den Bosch, F. C., & Balcells, M. 2003, ApJ, 583, 732

Teyssier, R., Pontzen, A., Dubois, Y., & Read, J. I. 2013, MNRAS, 429, 3068

Tikhonov, A. V., Gottlöber, S., Yepes, G., & Hoffman, Y. 2009, MNRAS, 399, 1611

Tissera, P. B. & Dominguez-Tenreiro, R. 1998, MNRAS, 297, 177

Tollerud, E. J., Boylan-Kolchin, M., Barton, E. J., Bullock, J. S., & Trinh, C. Q. 2011, ApJ, 738, 102

Tollerud, E. J., Boylan-Kolchin, M., & Bullock, J. S. 2014, MNRAS, 440, 3511

Tollerud, E. J., Bullock, J. S., Strigari, L. E., & Willman, B. 2008, ApJ, 688, 277

Tonini, C., Lapi, A., & Salucci, P. 2006, ApJ, 649, 591

Tonry, J. L., Dressler, A., Blakeslee, J. P., et al. 2001, ApJ, 546, 681

Torres, G. 2010, AJ, 140, 1158

van den Bergh, S. 1994, AJ, 107, 1328

van den Bergh, S. 2000, The Galaxies of the Local Group (Cambridge Univ. Press, Cambridge)

Vera-Ciro, C. A., Helmi, A., Starkenburg, E., & Breddels, M. A. 2013, MNRAS, 428, 1696

Viel, M., Becker, G. D., Bolton, J. S., & Haehnelt, M. G. 2013, Phys. Rev. D, 88, 043502

Viel, M., Lesgourgues, J., Haehnelt, M. G., Matarrese, S., & Riotto, A. 2005, Phys. Rev. D, 71, 063534

Vogelsberger, M., Zavala, J., & Loeb, A. 2012, MNRAS, 423, 3740

Wadepuhl, M. & Springel, V. 2011, MNRAS, 410, 1975

Wadsley, J. W., Stadel, J., & Quinn, T. 2004, New Astronomy, 9, 137

Wadsley, J. W., Veeravalli, G., & Couchman, H. M. P. 2008, MNRAS, 387, 427

Walker, M. G., Mateo, M., Olszewski, E. W., et al. 2007, ApJ, 667, L53

Walker, M. G., Mateo, M., Olszewski, E. W., et al. 2009, ApJ, 704, 1274

Walker, M. G. & Peñarrubia, J. 2011, ApJ, 742, 20

Walsh, S. M., Willman, B., & Jerjen, H. 2009, AJ, 137, 450

Wang, J., Frenk, C. S., Navarro, J. F., Gao, L., & Sawala, T. 2012, MNRAS, 424, 2715

Wang, J. & White, S. D. M. 2007, MNRAS, 380, 93

Watkins, L. L., Evans, N. W., & An, J. H. 2010, MNRAS, 406, 264

White, S. D. M. & Rees, M. J. 1978, MNRAS, 183, 341

Willick, J. A., Courteau, S., Faber, S. M., et al. 1997, ApJS, 109, 333

Wojtak, R. & Łokas, E. L. 2010, MNRAS, 408, 2442

Wolf, J. & Bullock, J. S. 2012, ArXiv e-prints arxiv:1203.4240

Wolf, J., Martinez, G. D., Bullock, J. S., et al. 2010, MNRAS, 406, 1220

Woo, J., Courteau, S., & Dekel, A. 2008, MNRAS, 390, 1453

Woodley, K. A., Gómez, M., Harris, W. E., Geisler, D., & Harris, G. L. H. 2010, AJ, 139, 1871

Xu, D. D., Mao, S., Wang, J., et al. 2009, MNRAS, 398, 1235

Xue, X. X., Rix, H. W., Zhao, G., et al. 2008, ApJ, 684, 1143

Zentner, A. R., Kravtsov, A. V., Gnedin, O. Y., & Klypin, A. A. 2005, ApJ, 629, 219

Zolotov, A., Brooks, A. M., Willman, B., et al. 2012, ApJ, 761, 71